LBL-12546

Lawrence Berkeley Laboratory
UNIVERSITY OF CALIFORNIA

COULOMB EFFECTS ON PIONS PRODUCED IN HEAVY-ION REACTIONS

John Peter Sullivan
(Ph.D. thesis)

November 1981

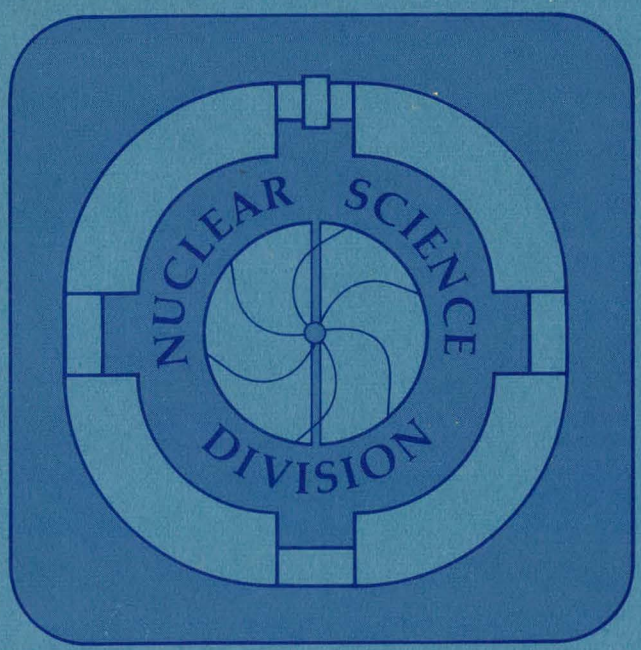

Prepared for the U.S. Department of Energy under Contract W-7405-ENG-48

DISCLAIMER

LBL--12546

DE82 007198

LBL-12546

Coulomb Effects on Pions Produced in Heavy-Ion Reactions

John Peter Sullivan

Nuclear Science Division
Lawrence Berkeley Laboratory
University of California
Berkeley, CA 94720

This work was supported by the Director, Office of Energy Research, Division of Nuclear Physics of the Office of High Energy and Nuclear Physics of the U.S. Department of Energy under Contract W-7405-ENG-48.

ABSTRACT

Coulomb Effects on Pions Produced in Heavy Ion Reactions

By

John Peter Sullivan

Double differential cross sections for the production of π^+ and π^- near the velocity of the incident beam for pion lab angles less than 40 degrees are presented. The experimental apparatus and the techniques are discussed. Beams of ^{20}Ne with E/A from 80 to 655 MeV and ^{40}Ar with E/A = 535 MeV incident on Be, C, NaF, KCl, Cu, and U targets were used. A sharp peak in the π^- spectrum and a depression in the π^+ spectrum were observed at zero degrees near the incident beam velocity. The effect is explained in terms of Coulomb interactions between the pions and fragments of the incident beam. Least squares fits to the data using the Coulomb correction formulas of Gyulassy and Kauffmann and an effective projectile fragment charge are made. The relationship between these data and previously measured pion production and projectile fragmentation data is discussed. The data are also compared to some theoretical models. A simple expression is given for the differential cross section as a function of the projectile mass, target mass, and beam energy.

TABLE OF CONTENTS

ACKNOWLEDGMENTS

The experiments reported in this thesis were done by a collaboration consisting of the Rasmussen and Crowe groups from LBL/UC Berkeley, a group from Michigan State University, a group from the Institute for Nuclear Study at the University of Tokyo, and numerous visitors to LBL. Thanks are due to all of these people who helped to collect and analyze the data, most of whom are listed as authors of references 1,2, and 14.

Some of the collaborators must be singled out for their particular contributions. Tom Ward and Walt Benenson did a large fraction of the work in the early stages of these experiments. Ken Crowe made many valuable suggestions which were used to improve the experimental apparatus and the data analysis. Jim Braley, Tom Buttke, Dan Eggers, Jeff Martoff, Jim Miller, Jean Péter, Mamiko Sasao, and Bill Zajc have all written portions of the computer code used to collect and analyze the data. Ken Frankel did most of the Monte-Carlo calculations. Bill Zajc and Jeff Martoff taught me many things and offered countless useful suggestions. Jim Bistirlich, Roy Bossingham, and Eunice Yoo kept the multi-wire-proportional counters in working order. Without them, many of the experiments reported here would have failed.

The help of the Japanese collaborators (Mamiko Sasao from Osaka along with Masahiro Koike and Osamu Hashimoto from the Institute for Nuclear Study (INS) at the University of Tokyo) is gratefully acknowledged. In addition to all of the useful advice he offered, Osamu Hashimoto has my eternal gratitude for his work on the field map of the spectrometer magnet.

Although he is not listed as an author of any of the experimental papers that came out of these experiments, Phil Siemens offered a variety of suggestions and gave me a great deal of encouragement. He was also the first person to suggest (to me at least) that the structure seen in the pion spectra was a Coulomb effect. Thanks go to Gary Westfall for his help in doing the Firestreak model calculations and to Miklos Gyulassy for helping to apply the Coulomb correction

formulas to the data.

It is impossible to forget the help that John Rasmussen, my research director, has given me. Without his wise advice and constant help, this research project would not have been possible. Finally, I must thank my brothers, Jim and Jeff, my sisters, Jennifer and Julie, and my parents, John and Pat, and all of my friends for their encouragement and moral support which have helped me immensely over the years it has taken to complete this project.

CHAPTER 1

Introduction

A. Introduction

The mechanism of pion production by heavy ion beams has been the subject of considerable recent experimental[1-14] and theoretical[15-30] effort. Much of this interest arose from the hope of investigating long range coherent effects in the nucleus such as "pion condensation"[17,31-34], "Lee-Wick matter"[35], or "quark matter"[36]. Others[15] have suggested that pions could be used to study "shock waves" in colliding nuclei. Pions also offer the possibility of probing the early stages of the interaction of high energy heavy ions because their velocities are normally high and they therefore tend to leave the interaction region quickly. Pions are one of the more commonly produced particles in heavy ion collisions and any complete understanding of these collisions must include an understanding of the pion spectra.

Previous measurements of charged pion production by heavy ion beams generally showed a smooth dependence on pion momentum. However, most of these experiments were restricted to laboratory angles of 15 degrees or greater[9-13] or measured they only relatively high energy pions[3-4]. Emulsion[5-7] and streamer chamber[8] measurements were able to cover small angles and small momenta simultaneously but they reported only smoothly varying pion production cross sections. In these experiments the number of events was generally small, which may have impeded observations of any fine structure in the spectra. In contrast to these smooth spectra, the data which will be discussed in this thesis[1-2] show a sharp peak in the 0 degree π^- spectrum near the beam velocity and a depression in the π^+ spectrum in the same region. This structure has been interpreted as an effect caused by Coulomb interactions between the pions and remnants of the projectile. A large π^-/π^+ ratio had been previously observed near the target (lab) velocity in emulsion experiments with proton[37] and alpha[38] beams and with cosmic rays[39].

This work helped stimulate theoretical treatments[30,40-43] which showed the essential role of Coulomb effects caused by projectile fragments producing the structure in the pion spectra. The analysis of these data and the consequent theoretical discussions showed that detailed measurements of π^- and π^+ differential cross sections could probe the dynamics of charge density evolution in heavy ion collisions. In order to make more accurate and higher resolution measurements, the detection system used in the earlier work was improved using two 3-plane multiwire proportional counters, one on the focal plane of the spectrometer and one behind it. The pions were stopped in a large area 11-element scintillation range telescope after passing through the wire chambers.

This thesis will review the data from the earlier lead slit spectrometer[1] (which used neon beams with energies from 80 to 385 MeV per nucleon) and discuss the experimental techniques used. Then, the experimental apparatus and results from the upgraded spectrometer[2] will be discussed. The measurements with the upgraded spectrometer used neon beams with energies per nucleon from 280 to 655 MeV per nucleon and an argon beam with E/A = 535 MeV. The measurements were performed at small lab angles for pions near the beam velocity. The targets used ranged from Be to U. In all cases, a very strong Coulomb effect in the π^-/π^+ spectrum was observed. Theoretical calculations which approximate the Coulomb effects are also presented and discussed.

B. Definitions of Some Terms

INCLUSIVE CROSS SECTION -- The reactions of particles (or nuclei) a and b such that

$$a + b \rightarrow c + X,$$

where X is one or more particles (or nuclei) of any number and type, is called a one particle inclusive reaction in which the particle c is produced. The angle and momentum distributions of particle c are one-particle inclusive distributions. This definition has been paraphrased from M.L. Perl, High Energy Hadron Physics, p186 (John Wiley

& Sons, New York, 1974). In this thesis a and b correspond to the projectile and target nuclei and c corresponds to a pion. The pion production cross sections reported here are all inclusive cross sections.

LORENTZ INVARIANT CROSS SECTION -- the form of the double differential cross section which is independent of the frame of reference. It can be written as

$$E \frac{d^3\sigma}{dp^3}$$

where

dp^3/E = Lorentz invariant phase space volume

$= p^2 dp d\Omega / E = p dE d\Omega$

This form of the differential cross section has been used throughout this thesis. The units used for the invariant cross section are either $(nb\ c^3)/(MeV^2\ sr)$ or $(\mu b\ c^3)/(MeV^2\ sr)$ which is equivalent to $(b\ c^3)/(GeV^2\ sr)$. For notational convenience the factors of the speed of light, c, (which is one in the units used here) and steradians (sr) have been omitted in some cases.

RAPIDITY -- A kinematic variable which is sometimes used because of its simple behavior under the Lorentz transformation. The usual symbol is y. For instance, the rapidity of a particle in the center of mass is $y_{lab}-y_{cm}$, where y_{lab} is the particle's rapidity in the lab and y_{cm} is the rapidity of the center of mass. The usual kinematic variables (momentum, kinetic energy, etc.) behave in a more complicated manner under the Lorentz transformation.

$$y = 0.5 \ln \left[\frac{E+p_{\|}c}{E-p_{\|}c} \right] = \tanh^{-1}\beta_{\|}$$

where

E = total energy (mass + kinetic) of the particle

$p_{\|}$ = component of momentum parallel to the beam axis

$\beta_{\|} = p_{\|}/E$

C. Units Used

A relatively conventional system of units, with the Boltzmann constant (k) and the speed of light (c) set equal to one, has been used. Masses, momenta, energies, and temperatures have been expressed in MeV and beam energies have been given in MeV per nucleon. Velocities have been quoted in units of the speed of light. Factors of the speed of light have been included (even though it is 1) in most, but not all, cases. The values of some fundamental constants in this system of units are given below.

c = speed of light = 1

k = Boltzmann constant = 1

$\hbar c$ = 197.3 MeV fm

e^2 = elementary charge squared = 1.440 MeV fm

$m_{\pi+} = m_{\pi-}$ = charged pion mass = 139.6 MeV

1 amu = atomic mass unit = 931.5 MeV

CHAPTER 2

Stage-1 Experiment -- The Lead Slit Spectrometer

A. Stage-1 Apparatus

All of the data collected in the first stage of this experiment[1] used Ne beams produced by the Bevalac at Lawrence Berkeley Laboratory. The beam energies per nucleon when extracted from the accelerator ranged from 125 to 400 MeV. In the second stage of the experiment[2] the ranges of the beams incident on the target were measured[44] in order to determine their energies. These measurements showed that the energy loss of the beam in the transport system was significant. Because the configuration of the beam line was the same in the first stage of the experiment as when the beam energies were measured, corrections for the beam's energy loss could be made by assuming that the same amount of material was in the beam line. The resulting beam energies incident on the target range from 101 to 388 MeV per nucleon. The targets used in this first stage of the experiment were NaF, Cu, and U. NaF was used to provide an almost-equal-mass target -- on the average it corresponds to ^{21}Ne.

TABLE 1

Beam energy per Nucleon			Target	
Extracted MeV	at Target MeV	Effective MeV	Material	Thickness gm/cm^2
125	101 ± 5	80 ± 10	NaF	2.14
150	130 ± 4	110 ± 7 118 ± 7	NaF U	2.14 1.90
200	182 ± 3	164 ± 8 172 ± 8	NaF U	2.14 1.90
250	235 ± 3	219 ± 5 214 ± 5 226 ± 5	NaF Cu U	2.14 3.26 1.90
400	388 ± 2	383 ± 3 377 ± 3 381 ± 3	NaF Cu U	1.07 2.05 1.90

Because energy loss of the beam in the targets was not negligible, especially at the lowest energies, the beam energies incident on the target should not be used. Instead, an effective beam energy will be used in the following discussion. This effective beam energy has been averaged over the beam energies at various points in the target weighted by the pion production cross sections, which are decreasing as the beam energy falls. This averaging procedure is discussed in appendix A. The beam energies and targets used in this first stage of the experiment are summarized in table 1.

A schematic diagram of the lead slit spectrometer is shown in figure 1. A large dipole magnet (JANUS) was used to bend pions of interest 180 degrees. Three slits in a lead wall on the focal plane of this 180 degree spectrometer were then used to define the momenta of the particles. Pions were detected by four-element plastic scintillator telescopes, one of which was placed behind each of the three slits. Each telescope consisted of a thin scintillator (0.64cm) followed by a copper absorber, a second thin scintillator (1.27cm), a thick counter (5.08cm) for stopping the pions and, finally, another thin scintillator which was used as a veto counter. The first two thin scintillators in each telescope were used to measure the rate of energy loss of particles entering the telescope (ΔE_1 and ΔE_2). The thickness of the copper absorber between these two thin scintillators was adjusted so that pions in the momentum range specified by the slits in the lead wall and the field in the magnet would stop in the third scintillator (the E counter). The fourth scintillator was used as a veto counter -- that is, to determine whether or not the particle stopped in the E counter. Because of the narrow range of momenta entering each telescope, pions were the only particle type which would trigger the first three scintillators, but not the fourth. By reversing the direction of the field in the magnet, the pion charge which was detected could be reversed.

The energy loss in the first and second scintillators (the ΔE counters) should be about the same for π^+ as for π^-. Their expected behavior in the stopping scintillator (the E counter) is not the

same. When they are stopped, negative pions will be rapidly captured by the nuclei in the stopping material. This capture gives 140 MeV of excitation energy to the nucleus which then decays, producing a very large pulse in the stopping scintillator. When positive pions are stopped, they are not captured. They remain in the scintillator until they decay into muons ($\pi^+ \rightarrow \mu^+$, $t_{1/2}$ = 18 ns). The range of the resulting 4.2 MeV muons is short (about 1.5 mm), so they will generally remain within the scintillator. These muons will then decay into positrons with a half life of 1.5 μs. A time-to-digital converter (TDC) which was started by a pion stopping in the E counter and stopped by a second pulse occurring any time during the following 5 μs was used to detect these delayed muon decays. Wolf et al.[9] used this delayed μ^+ decay to identify positive pions. Because equal detection efficiency for both π^+ and π^- was desired, the very large pulses characteristic of negative pions and the delayed μ^+ decays characteristic of π^+ were not used in the final analysis. Instead, only the energy loss in the first two detectors, the requirement of any signal in the third and no signal in the fourth element were used to identify pions. However, the characteristic signatures of stopped positive and negative pions were used to verify the identity of the detected particles.

For each event which caused a coincidence between the first and second element in one of the scintillator stacks, pulse height (ADC's) and timing (TDC's) information from all of the scintillators were recorded on magnetic tape. The data collection system used a PDP 11/34 computer to provide on-line analysis of the data which it read from CAMAC modules using a microcomputer interface (an MBD-11). In addition to the event data, scalers which monitored the singles counting rates of each scintillator, the ion chamber, and other secondary beam monitors were recorded on magnetic tape at the end of each beam spill (approximately every 5 seconds).

B. Stage-1 Analysis

As mentioned above, pions were identified by their energy loss in the first two scintillators (ΔE_1 and ΔE_2) and by their range. The

momenta were defined by the slits in the lead collimator. The resulting number of pion events was corrected for pion decay in flight, reactions of pions with air, the scintillators, and the copper absorbers, and for multiple Coulomb scattering. Then, using the target thickness, the total number of beam particles incident on the target (measured with an Ar/CO_2 filled ion chamber) and the solid-angle acceptance of each telescope, the differential cross sections were calculated. The calculation or measurement of each of these is discussed below.

Using the values of the vertical (the major) component of the magnetic field along a line perpendicular to the long axis of the magnet and (i.e. parallel to the beam axis) and in its central plane, trajectories of particles through the spectrometer were calculated. The effects of the fringing field were ignored. The range of momenta and angles accepted by each lead slit and scintillator combination calculated from this was used to calculate the unnormalized and uncorrected differential cross sections ($d^2\sigma/dEd\Omega$). These calculations also provided the total path length of particles passing through the system. Using this, the probability of $\pi \rightarrow \mu$ decay in flight could be calculated in order to correct the data for this effect.

A second correction, for pions lost because of nuclear reactions with air, the scintillators, and the copper absorbers, was also made. In order to make this correction, the energy and target dependence of pion reaction cross sections was parameterized[45] as described in appendix A. As discussed in appendix A, the pion reaction formula diverges as the momentum approaches zero. To correct for this, the cross section predicted by the formula at 10 MeV kinetic energy was extrapolated linearly to zero cross section at 0 MeV in order to predict the reaction cross section for pions below 10 MeV. The cross section formula is compared to some experimental values[46-50] in figure 2. In this figure, the points represent data, the solid line shows the cross section formula[45], and the dotted line shows how the formula was extrapolated to zero for very low energy pions. The for-

mula was fit to the average of the π^+ and π^- cross sections. The cross sections for the two pion charges are generally within 10% of the average with the π^- cross section consistently higher. The data of Wilken *et al*[46] and Clough *et al*[47] shown on figure 2 are also averages of π^+ and π^- cross sections. The other data points[48-50] are taken from phase shift analyses of π^+ scattering data. While not perfect, the agreement between the formula and the data is reasonable. The small differences between the π^+ and π^- reaction cross sections were ignored when computing the correction due to reactions with air and with the scintillators. When considering reactions with Cu (which are the source of most of the correction), the π^- cross section was assumed to be 5% greater than the average and the π^+ cross section was assumed to be 5% less than the average. This was done to correct for the neutron excess in Cu.

Finally, a correction for multiple Coulomb scattering of the pions was made. This correction was calculated by a Monte-Carlo program which used a Moliere[51] scattering distribution to calculate the paths of pions going through a series of Coulomb scatterings while passing through the scintillator telescopes.

In general, for each beam, target and pion charge combination studied, data were taken at two different spectrometer field settings. The fields were chosen so that the highest energy pions measured in the lower field run corresponded to the lowest energy pions measured in the higher field runs. This procedure allowed the relative nor-

TABLE 2

Field	p_π	Cu absorber	Acceptance $\Delta\Omega\,\Delta p$	Corrections			
				decay	reaction		Multiple
					π^+	π^-	
KG	MeV/c	cm	msr-Mev/c				Scattering
10.4	103.	0.	29.5	0.72	0.98	0.98	0.85
10.4	134.	0.91	22.8	0.74	0.87	0.86	0.69
10.4	164.	2.12	46.0	0.75	0.73	0.71	0.60
16.0	164.	2.12	45.5	0.80	0.74	0.72	0.60
16.0	222.	4.78	35.1	0.82	0.46	0.43	0.51
16.0	259.	7.39	71.0	0.82	0.31	0.28	0.47

malization of the runs at different field settings to be directly measured. In addition, the magnetic field on the spectrometer was adjusted to send pions of the same energy into each of the three telescopes (in successive runs). This measurement was used to establish the relative acceptance of each detector. The measured values of the relative acceptance were consistent with the trajectory calculations for the first two detectors, but not for the third. The detector which did not agree was used to detect the highest energy pions at any given spectrometer field setting. The particles entering this detector penetrated the fringing field on the downstream side of the magnet during their trajectory. The component of the magnetic field parallel to the beam axis would have a focussing effect (in the vertical direction) on these particles. This explanation is qualitatively consistent with the discrepancy, which required the calculated solid angle for this detector to be increased by a factor of two to bring it into agreement with the results from the other two detectors. The correction factors, the thicknesses of the Cu absorbers, and the acceptances for the two commonly used magnetic field settings are summarized in table 2. The correction factors are defined such that the corrected number of events is the observed number divided by the correction factor. With this definition, the correction factor for pion reactions (for example) corresponds to the fraction of the pions which would <u>not</u> react.

The beam intensity was monitored by the previously mentioned Ar/CO_2-filled ion chamber. To minimize background caused by the beam hitting the ion chamber, it was placed 13 m upstream from the target at the last beam focal point prior to the target. The transmission of the beam from the ion chamber through the final pair of quadrupole focussing magnets to the target was measured with a second ion chamber at normal beam intensities and with plastic scintillators at a reduced beam intensity. The ion chamber was calibrated by counting individual beam particles with a scintillator at reduced beam intensities. By extrapolating this calibration to higher beam intensities, the integrated beam intensity was found and the cross section values were normalized.

Because of the discrepancies in the acceptance calculations and because of the complicated interplay between the slits in the lead wall and the positions of the scintillators in determining the acceptance, the absolute normalization of the results of the first stage of this experiment is believed to be good to only a factor of 2. Since these effects depend largely on the pion energy, rather than the beam energy, the beam energy dependence of the cross section at a particular pion energy is better determined -- to within about 20%. The acceptances were arbitrarily normalized to agree with one another and all beam and target dependent factors are the same for a particular beam energy, so the uncertainty in the relative cross section values at different pion energies is given by the uncertainty in the corrections only. The corrections are not independent of pion energy, so it is not possible to give one number which specifies the relative uncertainty. By combining the uncertainty in the relative cross section values and the statistical errors associated with each point in quadrature, the quantity called the relative uncertainty in the discussion below was obtained. The most accurately determined quantity is the ratio of π^-/π^+ cross sections at a particular beam and pion energy since most of the correction and normalization factors are the same for both pion charges.

C. Results -- Stage 1

A complete set of data obtained at 0 degrees[1] in the lab with the lead slit spectrometer is shown in figure 3. The error bars show the relative uncertainties on the data points -- they do not include the factor of 2 uncertainty in the overall normalization. The lines are to "guide the eye". An angular distribution from 0 and 30 degrees was also measured for 220 MeV/nucleon Ne on a NaF target in 7.5 degree steps and on a U target in 15 degree steps. These distributions are shown in figures 4 and 5. Tables B.1-B.3 in appendix B summarize all of these data. Notice that the units in the tables are different from the units in figure 3 (nbarns are used instead of microbarns). The error bars associated with the cross section measurements in tables B.1-B.3 are relative, and on the π^-/π^+ ratios they

are statistical. These different uncertainties are explained in the preceding section.

D. Discussion of Stage-1 Results

The most striking feature of these data is the large π^-/π^+ ratio for pions with momenta around 135 MeV/c for the ~380 MeV/nucleon Ne beam. This large ratio was seen for all targets studied. If the strong interactions which produce the pions are charge-independent, then, for collisions of nuclei with equal numbers of protons and neutrons (N=Z), the ratio should be about 1. The beam (Ne) has equal numbers of protons and neutrons, but none of the cases studied with the lead slit spectrometer involved targets with N and Z exactly equal, although NaF is close with N=11 and Z=10 on the average. Although the ratios are not expected to be exactly one, it should be close to one. It is reasonable to conclude that this very large π^-/π^+ ratio was caused by Coulomb interactions between the charged pions and other particles involved in the reaction. This conclusion was supported by the fact that the peak occurs at a pion velocity which is approximately the same as the velocity of the incident beam, suggesting that Coulomb interactions between the pions and fragments of the beam moving approximately at the incident beam velocity cause this large ratio. This is demonstrated by figure 6 which shows the π^-/π^+ ratio as a function of the kinetic energy of the pion measured in the rest frame of the incident projectile. The zero-degree data for Ne+NaF at all beam energies have been combined to produce this figure, although the peak is largely defined by the 383 MeV/nucleon data and the lowest energy point for 219 MeV/nucleon.

The lines in figure 6 were calculated (as in ref. 1) by assuming that the peak in the π^-/π^+ ratio can be qualitatively explained in terms of Coulomb distortion of the pion wave functions in the vicinity of the projectile charge. The Coulomb wave for π^- is enhanced near the positive charge of the projectile nucleus and that of the π^+ is reduced. The effects of the target charge were ignored. Specifically, the lines represent the ratio

$$\frac{\sum_{L=0}^{\infty} F_L(-\eta,\rho)}{\sum_{L=0}^{\infty} F_L(\eta,\rho)} \qquad 2.1$$

where

$F_L(\eta,\rho)$ = Coulomb wave function[52]

L = angular momentum quantum number

$\eta = Z\alpha/\beta_\pi$

Z = projectile charge

$\alpha = 1/137$

β_π = pion velocity in the projectile rest frame

$\rho = k_\pi r$

k_π = pion wavenumber in the projectile rest frame

$r = 1.4\text{fm}\ (2Z)^{1/3}$

The solid line is calculated with this expression assuming Z=10 (the full charge of the projectile) and the dashed line assumes Z=5. The data are in reasonable agreement with the calculation which uses Z=5.

To demonstrate the dependence of the pion production cross sections on beam energy in a manner relatively independent of Coulomb effects, the geometric mean ($\sigma = (\sigma_{\pi^+}\sigma_{\pi^-})^{1/2}$) of the π^+ and π^- invariant cross sections has been plotted versus the beam energy per nucleon in the center of mass for three different pion lab energies in figure 7. The range of beam energies studied here starts well below the free nucleon-nucleon threshold energy ($E^*/A = m_\pi c^2/2 = 70$ MeV) and extends to beam energies above this threshold. As expected, the pion production cross sections rapidly rise with increasing beam energy. The rate of increase is greatest for the lowest beam energies. The cross sections rise more rapidly as the beam energies are increased for higher energy pions than for lower energy pions. This difference in beam energy dependence is easy to

understand -- at the higher beam energies the pion production cross sections do not decrease as rapidly (or actually increase) as the pion center of mass energy increases. At the lower beam energies, the cross sections consistently fall with increasing center of mass energy of the pion. Figure 7 also shows the prediction of the firestreak model[23], which is close to the data at the lowest beam energy measured (E_{beam}/A = 80 MeV). At the highest beam energy measured ($E_{beam}/A \simeq$ 380 MeV), the firestreak model is close to the data for 134 and 164 MeV/c pions, but overpredicts the cross section for 103 MeV pions by about 50%. For beam energies between these two extremes the agreement between the model and the data is worse. The firestreak model, as is well known[13,23,29], generally overpredicts the pion production cross sections by about a factor of 2. In the case of these data, the agreement between the model and the data is better at higher pion energies. The fact that the agreement between the model and the data depends on the pion energy means that the model is not correctly predicting the slope of the energy spectrum. The firestreak model predicts a spectrum which falls more rapidly than the 0 degree data at the higher beam energies studied. As will be discussed later, the normalization of the data from the lead slit spectrometer is higher than the later data by a factor of about 1.7. Inclusion of this factor would make the agreement between the firestreak model and the data in figure 7 somewhat worse, but it would bring the disagreement between the data and the model into agreement with the discrepancy observed for other sets of data[13,23,29].

For Ne+NaF and Ne+U at $E_{beam}/A \simeq$ 220 MeV, angular distributions between 0 and 30 degrees were measured. These are shown in figures 4 and 5. Except for the lowest energy pions, the angular distributions are essentially isotropic. The lowest energy pions measured at 0 degrees are very close to the projectile velocity, which causes a depression in the π^+ distribution and a peak in the π^- distribution, as discussed above. The π^- and π^+ distributions become more similar as the lab angle increases from 0 to 30 degrees, although the lowest energy pions seem to be influenced even at 30 degrees.

For all beam and pion energies studied in this experiment, the pion production cross sections monotonically rise as the target mass is increased. At the highest beam energy studied in this part of the experiment, the cross section for a given pion energy increases linearly with $A^{2/3}$, where A is the target mass. At the lower beam energies, the cross sections at a fixed pion energy do not increase as rapidly with the target mass. This can be seen from figure 7. The expected separations of the curves for the different targets if the cross sections scale with $A^{2/3}$ are shown on the figure. The actual separations of the curves are consistent with this $A^{2/3}$ scaling for the higher beam energies, but the curves move closer together as the beam energy decreases. This different scaling behavior could be caused by the lack of data for other pion energies and angles. If the total cross section at each beam energy had been measured, it might scale in a more consistent manner.

Particle production in relativistic heavy ion collisions is frequently described in terms of a participant-spectator model. The number of participant nucleons is usually calculated geometrically. The number of pions emerging from the participant region, as well as their energy and angular distribution, depends more strongly on the model. The dependence of the pion double differential cross sections on the target mass is demonstrated in figure 7. If the target mass dependence of the differential cross sections could be explained by a purely geometric factor, the curves for different targets on the semilog scale of figure 7 would be separated by a constant factor. Because the separation varies with the beam energy, no purely geometric factor can explain the behavior.

As shown by Hüfner and Knoll[20], the inclusive cross section for nucleons is the same in their rows on rows model as in the fireball model and in the Glauber model for high energy proton-nucleus scattering. This total cross section can be written as

$$\pi R_t^2 A_p + \pi R_p^2 A_t \qquad 2.2$$

where

A_t, R_t = mass number and radius of the target

A_p, R_p = mass number and radius of the projectile.

The total number of pions produced and their energy and angular distributions depend on the beam and target masses, but unlike the nucleon cross sections, it depends strongly on the beam energy even in the models which describe the nucleon cross sections in terms of a function, like equation 2.2, which is independent of beam energy. If the total pion production cross section at any fixed beam energy is assumed to be proportional to the total nucleon cross section, which is not necessarily true, then the total pion cross sections would scale with the geometric factor given in equation 2.2. However, even if the total cross sections scale with a simple geometric factor, the energy and angular distributions depend on the beam and target masses and the beam energy, so the pion cross sections at some fixed pion lab energy will not necessarily scale in the same manner. The scaling behavior of the pion cross sections will be discussed further in chapter 6.

CHAPTER 3

Why Build a New Apparatus?

A. Theoretical Interest

After the data from the lead slit spectrometer experiment[1] were published, a number of theoretical studies and speculations concerning Coulomb effects on the charged particle spectra in heavy ion reactions appeared. Some of these are summarized below.

Libbrecht and Koonin[40] suggested that the broad peak at 90 degrees in the center of mass in the π^+ spectrum, which was reported independently by Wolf *et al.*[9] and Chiba *et al.*[10], could be explained as a Coulomb effect. Their classical Monte Carlo calculation indicated that the Coulomb repulsion between the combined participant and spectator parts of the colliding nuclei and the positive pions could produce a peak similar to the experimentally observed effect. In their model, the peak at 90 degrees in the center of mass did not occur if the colliding nuclei were assumed to pass through one another (i.e. if the nuclei are transparent). When a fraction of the charge in the participant region of the colliding nuclei was distributed along a line between the receding nuclei, a peak in the π^+ spectrum qualitatively similar to the observed peaks was predicted. The assumption of a line charge is not very realistic, but the calculation suggests that the presence of some of the protons from the participant region in the intermediate rapidity region is necessary to produce the peak. Libbrecht and Koonin also pointed out that this problem is similar to the focussing of long range alpha particles observed in fission[53]. Their calculation predicted a large π^-/π^+ ratio for beam velocity pions, although the predicted ratio was much higher than the experimental value. This failure is attributed to the "use of undisturbed nuclear charge distributions (no target or projectile fragmentation) and classical mechanics." If the velocity dispersion of the projectile (and target) fragments and the possibility of tunneling had been included, the predicted π^-/π^+ ratio might be reduced.

The model used by Libbrecht and Koonin[40] was improved upon by Cugnon and Koonin[30] by using a Monte Carlo model of the collision between the two heavy ions. The Monte Carlo model approximates the interaction between two heavy ions with a series of nucleon-nucleon collisions. The calculation was done in two steps. First, the Monte Carlo calculation of the space-time evolution of the nucleons in the colliding nuclei was done several times for various impact parameters. The distribution of nucleons was approximated by three expanding Gaussian charge distributions, one each describing the projectile and target fragments and one describing the participant charge. With these approximate descriptions of the charge evolution, the effects on the pion spectra were calculated by relativistic classical trajectory calculations. This calculation improved upon the earlier calculation[40] by using a more reasonable nucleon space-time distribution and by using better approximations to the shape of the pion spectra in the absence of Coulomb effects than were used earlier. With this model they were able to approximately explain the peak in the π^+ differential cross section at 90 degrees in the center of mass and the projectile velocity pion data. However, their π^-/π^+ ratio at rest in the center of mass for Ar+Ca at E/A = 1.05 GeV is considerably higher than that measured by Frankel et al[14].

Bertsch[41] showed that Coulomb effects can also cause the π^+ cross sections to be greater than the π^- cross sections, as observed at low beam energies and/or higher pion energies. When the beam energy is low, the Coulomb potential energy gained by removing one positive charge from the nucleus ($p \rightarrow n\pi^+$, with the π^+ leaving the nucleus), versus the potential energy lost by adding a positive charge to the nucleus ($n \Rightarrow p\pi^-$, with the π^- leaving the nucleus) is enough to cause an excess of positive pions for pion velocities far from the beam velocity.

Gyulassy and Kauffmann[42] developed a set of approximate equations to describe Coulomb effects on the charged particle spectra. Their equations include quantum and relativistic effects to first order in $Z\alpha$, where Z is the nuclear charge and α is the fine structure con-

stant. In their model, the charged pion cross sections are written in terms of an uncharged pion cross section evaluated at its momentum before being shifted by a Coulomb impulse ($\vec{dp}$), this is then modified by a Coulomb phase space distortion factor (D($\vec{p}$))

$$\sigma_{\pm} = \sigma_0(\vec{p} \mp \vec{dp}) \; D(\vec{p}) \qquad 3.1$$

Where $\sigma_{+,0,-}$ refers to the differential cross section ($d^3\sigma/dp^3$) for the production of π^+, π^0, π^-, respectively. The calculation of $\vec{dp}$ and D will be discussed in detail in chapter 6. They also include a nuclear temperature in their calculations. The use of this finite temperature removes the singularity in the π^-/π^+ ratio at the beam velocity which is predicted by some other models. For small values of the momentum (relative to the charged center causing the Coulomb effect), the phase space distortion factor dominates and the π^- cross section is much larger than the π^+ cross section, as seen in the 380 MeV/nucleon Ne data near the beam velocity. With these equations, they were able to quantitatively reproduce the π^-/π^+ ratios observed in the first part of this experiment for 380 MeV/nucleon Ne+NaF. For large momenta, the momentum shift dominates and (assuming the cross section decreases as the momentum increases as in most models) the π^+ cross section is larger than the π^- cross section. This limit corresponds to the situation Bertsch[41] discussed. In addition, their calculations qualitatively reproduced the peak in the π^+ spectrum at 90 degrees in the center of mass reported by Wolf *et al.*[9] and Chiba *et al.*[10]

Ko and Siemens[43] studied the production of negative pions from the target directly into bound atomic orbitals around the beam particle. The cross section for this process was estimated and found to be similar to, although probably less than, the observed cross sections. Unfortunately, the cross section is dominated by production in the 1s orbital (n=principal quantum number=1, L=angular momentum quantum number=0) and rapidly falls off as the n and L are increased. Because of the high capture probability for pions in the 1s orbital (which has a large overlap with the nucleus), these pions would probably not be observed. They point out an interesting extension of

this experiment which would involve measurements of the pionic x-rays from transitions between the atomic orbitals in coincidence with the beam fragments. The cross section for such a process would, in their model, be greatly enhanced by collective transitions involving many neutrons in the target.

B. Experimental Reasons to Continue the Experiments

Although the peak in the π^- spectrum (hole in the π^+ spectrum) is easily understood as a Coulomb effect, this sharp structure was not anticipated. Previously measured pion spectra in heavy ion reactions[3-13] were relatively smooth. Because the spectra were expected to be smooth, the spectrometer was not designed for high resolution measurements. Furthermore, because the purpose of the first stage of the experiment was to measure pion production at threshold, the data for pions around the beam velocity was not as complete as it could have been. These experimental reasons, combined with the theoretical interest sparked by the results of the first stage of the experiment, made a finer spacing of points in the pion energy spectrum and an angular distribution for pions around the peak seem desirable. Both data and theory suggested that detailed measurements of π^- and π^+ differential cross sections could probe the dynamics of charge density evolution in heavy ion collisions. Furthermore, it was clear that Coulomb effects were not always insignificant and that a better understanding of them was needed in order to make corrections for them in experiments studying more exotic processes. A device capable of measuring low energy π^+ and π^- spectra with essentially equal efficiency would be uniquely useful for this purpose. In order to make these more comprehensive and higher resolution measurements of the pion spectra around the beam velocity, the detection system employed in the first part of the experiment was improved by using two 3-plane multi-wire proportional counters, one near the focal plane of the spectrometer and one behind it. The pions were stopped in a large area 11-element plastic scintillation range telescope after passing through the wire chambers. Most of the rest of this thesis will be devoted to a discussion of the methods

used, the results of, and the interpretation of the results from this upgraded spectrometer.

CHAPTER 4

Upgraded Spectrometer

A. Stage-2 Apparatus

As in the first stage of these experiments, all of the data from the second stage of the experiments were collected at the BEVALAC at the Lawrence Berkeley Laboratory. Beams of ^{20}Ne with E/A from 280 to 655 MeV and ^{40}Ar with E/A = 535 MeV were used. Targets used in one part of the experiment or another were Be, C, NaF, KCl, Cu, U. Target thicknesses ranged from 0.4 to 2.2 gm/cm^2, with about 1 gm/cm^2 the most common thickness. Table 3 lists all of the beam and target combinations used.

A schematic diagram of the upgraded spectrometer is shown in figure 7. The configuration is similar to that used in the first stage

TABLE 3

Summary of Some Experimental Parameters

Beam	E_{beam}/A accelerated MeV	E_{beam}/A Center of Target MeV	Target	gm/cm^2	p_π MeV/c	Resolution σ_p MeV/c	Resolution σ_θ deg.
Ne	300	280	C	0.56	116	2.5	2.0
		281	NaF	0.60	116	2.5	2.1
		282	Cu	0.45	117	2.6	2.4
Ne	400	380	NaF	1.07	138	2.6	2.2
		382	Cu	0.91	139	2.7	2.6
		385	U	0.52	139	2.9	2.7
Ne	425	405	C	1.12	144	3.6	2.5
		400	NaF	2.19	143	4.2	3.0
		407	U	1.92	144	3.8	4.8
Ne	500	482	C	1.12	159	2.4	1.9
		483	NaF	1.07	160	2.3	2.0
		485	Cu	0.91	160	2.2	2.3
		487	U	0.52	160	2.6	2.4
Ar	557	533	C	0.56	169	2.3	1.7
		534	KCl	0.50	170	2.2	1.8
Ne	670	654	Be	1.17	192	3.1	2.1
		655	NaF	1.07*	192	3.0	2.2

* Most data were taken with a 0.41 gm/cm^2 target, but the higher momentum data were taken with this thicker target.

of the experiment. The same magnet and beam line were used in both cases. The position of the target inside the magnet was also similar. In place of the lead slits used to define the momenta of the particles in the earlier experiments, a multi-wire proportional counter (MWPC) was placed on the focal plane of the spectrometer. A second MWPC, approximately at the outer edge of the magnet's coils, was followed by a stack of 11 plastic scintillators which was capable of stopping pions with momenta up to 200 MeV/c. The two MWPCs were used to define the trajectories of the particles in the magnetic field. Because the first MWPC was on an approximate focal plane, the position at which the particle hit this wire chamber approximately gave the radius of curvature of the particle in the magnetic field (and therefore its momentum). The second MWPC served to complete the definition of the particle's trajectory. The first two scintillators in the range telescope were thin (0.64cm) and were used to measure the rate of energy loss of the particles. The pions of interest were then stopped in one or another of the next eight elements of the scintillator stack, which were from 2.5 to 3.8 cm thick. The last scintillator in the stack was 1.3 cm thick and was used as a veto counter.

The data were collected in three sets of runs. The configuration shown in figure 7 was used with the 300, 400, 500 MeV/nucleon Ne beams and the 557 MeV/nucleon Ar beam. The 425 MeV/nucleon Ne data were collected with the entire apparatus rotated 15 degrees from this configuration so that the spectrometer acceptance was centered at 15 rather than 0 degrees. The 670 MeV/nucleon Ne data were collected with the magnet in the zero degree configuration shown in figure 7 and with the magnet rotated to 30 degrees. The data from the two different angles were combined. The configuration of the range stack was also different during the 670 MeV/nucleon runs. The first scintillator was thinner (0.32 cm instead of 0.64 cm), and a brass plate (8 gm/cm^2 thick) was inserted between the last stopping scintillator and the veto counter. The first scintillator was thinner than it was in the other runs in order to measure lower energy pions. The brass plate was added in order to increase the maximum pion

momentum which could be measured by stopping pions between 200 and 300 MeV/c. These pions would have triggered the veto counter if the brass plate had not stopped them. For many of the beam and target combinations used, data were collected with several different field settings on the magnet. The data from these separate fields were combined to give the final results.

For each event which caused an event trigger, the addresses of all wires which were hit and the pulse heights (ADCs) and timing signals (TDCs) from each element of the scintillator stack were recorded on magnetic tape. The event trigger consisted of two parts. The first part came from the MWPCs and was called the "fast out". This signal was generated for each event in which at least one wire in both MWPCs was triggered. The second part of the event trigger came from the scintillators in the range stack. This signal was called "S" and was generated by a coincidence of the first three scintillators in the range stack and the "gate". The "gate" was set up to allow "S" signals to occur only when the computer was not busy reading out a previous event and the beam was on. When there was a coincidence between "fast out" and "S", an event trigger was generated. The Q system, developed at LAMPF in Los Alamos, was used to control the data acquisition. This system ran on a PDP 11/45 and used a microcomputer interface (an MBD-11) to read the data from each event from a pair of CAMAC crates. The computer system also provided on-line analysis of a sample of the data as it was collected.

B. Data Analysis -- Stage 2

A field map of all three components of the magnetic field of the spectrometer magnet was measured in order to calculate pion orbits in the magnet and thus find the positions at which these orbits would cross the MWPC planes. A Monte Carlo program was used to generate the starting parameters of the trajectories. A least squares fit was then made which provided the radius of curvature (ρ), the angle (θ), and the vertical position of the particle at the target (z_0) as a Chebyshev polynomial function of the wire chamber hit positions. The fitting method is described by Alder *et al.*[54]. Energy loss of the

pions in air and the MWPCs was included in the orbit calculations, so this small correction was included in the algorithm used to calculate ρ, θ, and z_0.

For each event on magnetic tape, the addresses of the MWPC wires which fired were used to find the trajectory of the particle. If a single trajectory was found, the algorithm described above was used to calculate ρ, θ, and z_0 for the particle. Some events ($\sim$ 20%) were rejected because the calculated quantities indicated that the particle did not originate at the target. Monte Carlo calculations indicated that many muons from decay in flight of pions fell into this category, although this did not account for all of the rejected events. Background events from reactions of the beam with the air in the spectrometer and with other material in the beam line (both upstream and downstream) are the most reasonable explanation for the rest of these bad events. For those events which appeared to have originated at the target, momentum-dependent cuts on the energy loss in the first and second scintillators and on the range of the particle in the scintillator stack were then used to identify pions.

Protons in the momentum range studied were of such low energies that they were not able to pass through the first two scintillators and therefore did not generate event triggers. Protons which did not come from the target (i.e. background) and still passed the target traceback cut described above could be clearly separated from pions in most cases by the combined ΔE and range cuts. Furthermore, corrections due to protons which were not associated with the target should be included in the blank target subtraction.

The arguments against any significant electron contamination in the results are similar to those against protons. The difference is that electrons which came from the target would be able to cause event triggers. However, in the momentum region studied, the range of an electron with the same momentum as a pion is much longer than that of the pion and the ΔE signals are generally less. Because the production cross sections for high energy electrons which could con-

taminate the data are much smaller than the pion cross sections, the most significant source of high energy electrons is probably the conversion (in the target) of high energy gamma rays from π^0 decay (i.e. $\pi^0 \rightarrow 2\gamma$, $\gamma \rightarrow e^+e^-$). If this is true, then the electron background should be greater for heavier and/or thicker targets since higher Z nuclei are more efficient at gamma ray conversion. This effect, at least qualitatively, was observed in the data. However, even when many electron events do occur, they are easily separated from the pions so the electron contamination of the present results should be negligible.

Muons were not separated from the pions as clearly as other particles. The cross sections for muon production are not significant compared to the pion production cross sections. The major source of muon contamination is from the decay of pions. These events are not as cleanly separated from pions as the other events since most of these $\pi \rightarrow \mu$ decays occur after the pions have left the target. As a result, the momentum (which is calculated by assuming that the particle originated at the target) is generally incorrect. Many muons fail the target traceback cuts. For those that pass this cut, most are rejected by the dE/dx and range cuts. A Monte Carlo calculation of the muons which pass all of the cuts indicated that less than 3% of the "good" events were actually muons.

C. Acceptance and Efficiency Calculations

The acceptance and efficiency of the spectrometer were calculated with the same Monte Carlo program as was used to generate events for the polynomial fits. Pion events were generated with a uniform distribution in momentum space, and a Gaussian beam spot approximately the same size as the actual beam spots was assumed. Pions were allowed to decay into muons while going through the spectrometer (with the appropriate half-life). If a decay did occur, the muon was followed through the spectrometer. When the calculated orbit of a pion or muon passed through both MWPCs and then hit the first scintillator in the range stack, a multiple-scattering, energy loss code was used to follow the particle through the scintillator stack.

Pions were allowed to react with carbon nuclei in the scintillators using the same analytic approximations to the πC total cross sections[45] as were used in the first stage of the experiment. The rest of the treatment of the pions reactions differed from the earlier analysis.

The new analysis was not as complete as the old analysis in one sense -- it did not include the reactions of pions with protons in the scintillators or with the air. These factors were omitted because they are smaller corrections than the πC reaction correction and because the omission would save computing time. Computing time is saved for several reasons. First, it was saved since it was not necessary to calculate the reaction probability for each step in the integration of the trajectory through the magnetic field. Computing time was also saved by ignoring the reactions of pions with the protons in the scintillators. The most important reason that this was necessary is that the reaction probability of pions with protons is a factor of three different for π^+ and π^-. In order to calculate both corrections, a separate calculation for each pion charge would have been needed. Because the amount of computing time consumed by the Monte Carlo acceptance calculations was already very large ($\tilde{}$ 3 months of CPU time on a VAX 11/780), it was not reasonable to do separate calculations for the two pion charges. The error introduced by these approximations is small and will be discussed further in the section below which deals with the normalization.

In most respects the newer treatment of pion reactions was more complete than the older treatment -- if a pion reacted with a nucleus in the scintillator stack, it was not automatically assumed to be rejected by the analysis as was previously assumed. Instead, an effort was made to continue following the path of the pion. To do this, the total πC reaction cross section was divided into three parts. These parts, and the associated percentages of the total cross section were elastic (39%), inelastic π,π' (31%), and absorption (30%). The formula used to calculate the total πC reaction cross sections[45] is described in appendix A. The agreement between

the formula and some of the available data[46-50] is shown in figure 2. As explained in chapter 2 and appendix A, this cross section formula diverges as the pion momentum approaches zero. In the analysis of the data from the lead slit spectrometer the formula was extrapolated to zero as shown by the dashed line in figure 2. In the analysis of the data from the upgraded spectrometer, this correction was (inadvertently) omitted. However, because the Monte Carlo program considered the pions to have stopped when their kinetic energies were reduced to 0.5 MeV (momentum = 11.8 MeV/c), the region where the calculated cross section became very large was never reached. The probability of a pion reaction between 50 MeV/c and 11.8 MeV/c, the region where the formula was too large, is less than 0.5%, so this error did not effect the results significantly.

The elastic scattering cross section was assumed to be 39% of the total cross section. Some measured ratios[49,55,56] of the elastic scattering cross sections to the total cross section are summarized in table 4. The data, which show no significant variation for pion momenta between 128 and 310 MeV/c, are consistent with the 39% ratio which was used in the analysis. The elastic scattering angular distribution was assumed to be a Gaussian function of the center of mass scattering angle. Specifically, the function used was

$$\left[\frac{d\sigma}{d\Omega}\right]_{CM} = \frac{\sigma_{el}}{2\pi w_\theta^2} \exp\left[-\theta_{CM}^2/(2w_\theta^2)\right] \qquad 4.1$$

The total elastic scattering cross section is σ_{el} and w_θ is the standard deviation, which was assumed to be 0.3 radian (17.2 degrees).

TABLE 4

p_π MeV/c	$R(\frac{\text{elastic}}{\text{total}})$	Reference
128	0.38	Moinester *et al.* (ref 49)
156	0.40±0.06	Crozen *et al.* (ref 55)
179	0.37±0.04	"
219	0.37±0.02	Binon *et al.* (ref 56)
254	0.37±0.02	"
287	0.37±0.02	"
310	0.37±0.02	"

This function was normalized such that

$$\int_0^{2\pi} d\phi \int_0^{\pi} \sin\theta d\theta \left[\frac{d\sigma}{d\Omega}\right]_{CM} = 2\pi \int_0^{\pi} \sin\theta d\theta \left[\frac{d\sigma}{d\Omega}\right]_{CM} \qquad 4.2$$

$$= \frac{\sigma_{el}}{w_\theta^2} \int_0^{\pi} \sin\theta d\theta \exp[-\theta^2/(2w_\theta^2)]$$

$$\simeq \frac{\sigma_{el}}{w_\theta^2} \int_0^{\infty} \theta d\theta \exp[-\theta^2/(2w_\theta^2)] = \sigma_{el}$$

where the approximation that only small values of θ contribute significantly to the cross section has been used in the last step. In that case $\sin\theta \simeq \theta$ and the upper limit of the integral can be changed from π to ∞. Figure 8 compares this function with the data of Binon et al.[56] for pions with momenta of 220 MeV/c. The agreement is reasonable in the regions where the cross section is large. The general shape of the elastic scattering angular distribution is similar for pion momenta between 100 and 400 MeV/c[48-50,56-60]. The depth of the slight minimum seen in the 220 MeV/c data near θ_{CM} = 65 degrees is generally greater and its location varies with pion momentum.

The inelastic πC cross section was divided into 2 parts. The first involves π,π' reactions and the other part consists of pion absorption. The sum of these two parts was assumed to make up 61% of the total cross section. This can be compared to the data summarized in table 4 ($R(\frac{\text{inelastic}}{\text{total}}) = 1-R(\frac{\text{elastic}}{\text{total}})$) which shows that this is consistent with the data.

The inelastic π,π' cross section is assumed to make up 31% of the total cross section and pion absorption is assumed to make up 30% of the total cross section. This division of the inelastic cross section is consistent with the measurements of absorption of 231 MeV/c positive pions by carbon reported by Bellotti et al.[61] and with the π^+ and π^- absorption data reported by Navon et al.[60] for 225 MeV/c pions. Both sets of authors report at 50% of the inelastic cross section consisted of pion absorption.

The assumed form of the inelastic double differential cross section was

$$\left[\frac{d^2\sigma}{dEd\Omega}\right]_{CM} = \frac{1}{\Delta E}\,\frac{0.31\sigma_{tot}}{2\pi w_\theta^2}\,\exp[\,-\theta^2/(2w_\theta^2)\,] \qquad 4.3$$

for $T_\pi - \Delta E < T_\pi' < T_\pi$

and

$$\left[\frac{d^2\sigma}{dEd\Omega}\right]_{CM} = 0$$

for T_π outside the range specified above. The variables above are

$0.31\sigma_{tot}$ = total π,π' inelastic cross section

T_π = initial CM kinetic energy of the pion

T_π' = final CM kinetic energy of the pion

$$\Delta E = 12 \text{ MeV}\left[\frac{T_\pi}{150 \text{ MeV}}\right]$$

and the other symbols are defined as in equation 4.1. In other words, the CM angular distribution was assumed to be independent of the pion energy and to be the same as the angular distribution for elastic scattering. An equal probability of any CM energy loss between 0 and ΔE, where ΔE = 12 MeV for 150 MeV pions was assumed. This differential cross section does not agree with the data as well as the assumed form for the elastic scattering cross section does. The energy loss distribution is not flat as was assumed, but has a relatively complicated structure[48,56,59] including a peak corresponding to the excitation a of 4.44 MeV level in the carbon nucleus. However, the cross sections decrease rapidly with excitation energy. The data analyzed with the assumed form of the cross section should not be sensitive to details of the energy loss distribution. The angular distribution for inelastic π,π' reactions was not the same as for elastic scattering. Like elastic scattering, it is generally forward peaked. This forward peaking increases as the pion (lab) momentum is reduced from ~250 MeV/c -- which corresponds to the entire region of the data reported here.

In summary, a relatively detailed treatment of pion reactions with carbon nuclei was used in the newer analysis. Reactions with nuclei other than C were ignored, but this should not introduce a large error. The uncertainties in the final results introduced by these methods will be discussed in the section on the overall normalization. The magnitudes of the total πC reaction cross sections and of the three parts it was divided into (elastic ; inelastic π,π' ; absorption) which were used in this analysis are consistent with the data. The assumed shapes of the differential cross sections are similar to the data. The final results of this experiment should not be sensitive to the exact shapes of the differential cross sections.

For each Monte Carlo event, the MWPC wires which would be expected to fire were calculated from the positions where the orbits of the particles crossed the planes of the wires chamber. A probability distribution taken from the analysis of the real data was used to decide how many adjacent wires would fire in each MWPC plane. This probability distribution included the possibility that the plane would misfire. Table 6 shows the probability distribution used for some of the runs. Any wire which was not working during the actual experiment was then removed from this list of wires which would fire. The table above gives zero probability of no wires firing in some of the planes. This does not mean that the plane never misfired, but that the number of times the plane misfired could be explained by the wires which were not working during the experiment. This procedure allowed the wire chamber efficiency to be incorporated into the acceptance calculation.

Table 6

Expected Number of Wires for each MWPC Plane

Plane#	0 wires	1 wire	2 wires	3 wires	4 wires	5+ wires
1	0.2%	62.6%	33.1%	2.4%	0.7%	1.1%
2	0.0%	50.1%	39.7%	8.0%	1.1%	1.1%
3	0.0%	83.6%	13.6%	1.2%	0.6%	1.0%
4	3.3%	89.6%	5.3%	0.8%	0.4%	0.6%
5	0.0%	50.3%	40.1%	8.0%	1.4%	0.3%
6	0.6%	63.1%	31.5%	3.6%	0.6%	0.6%

The Monte Carlo method was not completely successful in calculating the MWPC efficiency. It consistently overestimated the efficiency of the wire chamber. The method for deciding how many wires in each plane would fire assumed that the probability for each plane was independent. Because it was still possible to analyze events where only one MWPC plane misfired and the probability of two planes misfiring simultaneously was small, very few Monte Carlo events did not fire enough wires to be analyzed. The calculated distribution of the number of adjacent wires which would fire was consistent with the data, but there were more events in the real data with more than one plane misfiring simultaneously. This suggests that there was some correlation between a misfire in one plane and in another. A possible explanation for this is that the wire chambers are less efficient for lightly ionizing particles and, for these particles, the probability of many planes misfiring is larger. In the final analysis, a correction of the difference in the efficiency calculated by the Monte Carlo analysis and the efficiency seen in the real data was applied to the overall normalization. The correction was about 5%. Although the Monte Carlo analysis did not totally reproduce the observed wire chamber efficiency, it should approximate some of the momentum and angle dependent parts of the efficiency by specifically including the wires which did not work. In general, a group of bad wires will affect some parts of the acceptance more than others -- this is at least approximately included in the present analysis.

From the calculated energy loss of the particles in each scintillator, the expected ADC signals were calculated. Using this, along with the MWPC wires which would fire, a set of simulated event data were created. These data were then analyzed in the same manner as the real data.

The analysis of the Monte Carlo events, which included events in which $\pi \rightarrow \mu$ decays and πC reactions would occur, therefore incorporated into the acceptance calculations corrections for events lost due to decay in flight of pions and pion reactions with carbon nuclei in the scintillators. Only those Monte Carlo events which would have

caused an event trigger were analyzed. To summarize the efficiency of the system, the events were divided into three categories. The categories were pions which neither decayed into muons nor reacted, pions which reacted, and pions which decayed into muons. As an example, table 7 summarizes the efficiency of the spectrometer and analysis system for these three types of events for the configuration used with the 300, 400, 500 MeV/nucleon Ne beams and the 557 MeV/nucleon Ar beam. The magnetic field settings listed in the table were the most commonly used values. In table 7, "% of total" refers to the fraction of the total event triggers caused by particles in the category and "% good" refers to the fraction of that type of event which were considered good events. In other words, "% good" refers to the efficiency of the spectrometer and the analysis for that type of event. Notice that the sum of the percentages of each type of event is 101% for the 11.65 KG field, this is due to rounding errors. The muon contamination, or the fraction of the "good" events which were muons, is given in the last column of table 7. The true muon contamination may be slightly larger than this because Monte Carlo events were only generated over a finite range of momenta and angles. Muons from the decay of pions outside this range may have contributed to the muon contamination of the data, but the total contamination should be less than about 3%. As shown by table 7, the system was less than 100% efficient even for pions which neither reacted nor decayed in flight. This was due to the combined effects of multiple scattering, wire chamber inefficiency, small misalignments of the scintillators, and inefficiencies in the analysis

TABLE 7

Summary of Monte Carlo Analysis

B Field KG	pions which did not react		pions which reacted		muons		μ contamination
	% of total	% good	% of total	% good	%of total	% good	
11.65	83%	91%	8%	70%	10%	14%	1.7%
13.4	78%	93%	13%	66%	9%	17%	2.0%
15.1	74%	87%	18%	55%	8%	14%	1.6%
16.1	70%	81%	22%	50%	8%	12%	1.5%

programs.

Since the Monte Carlo events were generated with a probability proportional to dp^3 (the momentum space volume), dividing the number of real data events in each bin corrected for blank target background by the corresponding number of Monte Carlo events gives the differential cross section $d^3\sigma/dp^3$ except for the overall factor which converts the relative yield into the cross section. The cross section so determined includes corrections due to $\pi \rightarrow \mu$ decay, wire chamber inefficiency, π reactions with C nuclei in the scintillators, multiple-Coulomb scattering in the scintillators, effects due to the finite size of the beam spot, and any inefficiencies in the analysis programs. The statistical uncertainties associated with the Monte Carlo events were never larger than 5% and have been included in the quoted statistical errors.

D. Normalization

With the upgraded spectrometer, as with the lead slit spectrometer, the beam intensity was monitored with an Ar/CO_2 ion chamber 13 meters upstream from the target. The ion chamber was not recalibrated. For the beam energies at which a calibration from the earlier runs was not available, the calibration from a nearby energy

TABLE 8

Normalization and Correction Factors and Their Uncertainties

Factor	Typical Value	Estimated Uncertainty
Beam intensity	10^7/pulse	±25%
Computer dead time	20%	±5%
MWPC inefficiency	5-10%	±3%
Target traceback	20%	±6%
dE/dx cuts	5-10%	±3%
Range cuts	15-40%	±10%
Spectrometer acceptance		±10%
Overall uncertainty		±30%

was scaled to the necessary beam energy using the ratio of dE/dx in argon for the two beams. Using the ion chamber, the total number of beam particles was found and the cross section values were normalized. The uncertainty in the absolute normalization is about 30%. The factors contributing to this uncertainty are listed in table 8.

Secondary reactions of pions and of the beam in the target and effects due to neutrons from the capture of stopped negative pions by nuclei in the scintillator stack were neglected. The correction due to secondary reactions would increase the π^+ and π^- cross sections by less than 3%. The correction due to stopped negative pions would increase the π^- cross sections by less than 10%. Reactions of pions with air and with the protons in the scintillators were also neglected. These corrections would increase the cross sections by less than 5%.

A comparison of the normalization of the data which appears here with data from other groups and the consistency of some of the different data sets among themselves will be discussed in chapter 5. Table 12 (in chapter 5) summarizes these relative normalizations. All of the disagreements between the normalizations of the results presented here and those of other groups are within the combined uncertainties of the normalizations which are compared.

E. Resolution

In comparing cross sections with sharp structure one must take experimental resolution into account. The beam velocity peaks and valleys of the data have widths larger than the resolution, but effects due to the resolution cannot be ignored. This effect was treated by folding the calculated resolution function into the theoretically calculated cross sections, as described in appendix D. Factors contributing to the resolution were the size of the beam spot; the spatial resolution of the MWPC's; multiple Coulomb scattering in the target, air, and the MWPC's; the size of the data bins; and the uncertainty introduced by the use of the polynomial fit used to calculate the momenta of the particles. The combined

TABLE 9

Factors Contributing to Resolution
380 MeV/A Ne + NaF → π , p = 132 MeV/c , θ = 0

Factor	Contribution to: σ_p (MeV/c)	σ_θ (deg.)
Size of beam spot +MWPC resolution +Polynomial fit	2.24	0.51
Energy loss/Multiple scattering in the target	1.17	1.38
Multiple scattering in air and the MWPCs	0.78	0.56
Beam Divergence	--	1.00
Bin size	1.13	1.15
TOTAL	2.88	2.19

contributions of the size of the beam spot, the spatial resolution of the MWPCs, and the polynomial fit used to calculate the momenta and angles to the resolution were determined by the analysis of the Monte Carlo events. The contributions of energy loss in the target to the momentum resolution and of the size of the data bins to the momentum/angular resolution were calculated by finding the rms deviation from the momentum at the center of the target or the momentum/angle at the center of the data bin, respectively. The effects of multiple scattering in the target were calculated assuming that the pion originated at the center of the target. The divergence of the beam was estimated, not measured. All contributions to the resolution were then combined quadratically to get the overall resolution. In general, the size of the beam spot, which is included in the part of the resolution calculated by the Monte Carlo analysis, made the largest contribution to the momentum resolution, and multiple scattering in the target made the largest contribution to the angular resolution. An example, which breaks down the various contributions to the resolution, is shown in table 9. The case chosen was Ne + NaF at E/A = 380 MeV and a pion momentum near the beam velocity. This represents neither the best nor the worst resolution

obtained in these experiments. Table 3 summarizes the resolution for all of the beam and target combinations reported here for pions at the beam velocity. The momentum and angular resolution given in table 3 correspond to σ_p and θ_0 which are defined in appendix D.

Due to uncertainties in the absolute magnitude of the magnetic field used during the experiment and the position of the beam spot on the target, there is an additional 1.5% uncertainty in the magnitude of the momentum. The beam ranges were measured with aluminum and/or copper wedges and Polaroid film, and the beam energies were calculated from the ranges[44]. All beam and pion energies given for the upgraded spectrometer are values at the center of the target.

CHAPTER 5

Results from the Upgraded Spectrometer

A. Summary of Results

The peak in the π^- spectrum near the beam velocity and the corresponding hole in the π^+ spectrum which were seen with the lead slit spectrometer were confirmed with the upgraded spectrometer for the ~400 MeV per nucleon Ne beam. These features of the projectile velocity pion spectra were also seen for all of the other beam and target combinations studied. Figures 10-15 show cuts through the peak in the π^- spectra and the hole in the π^+ spectra for each of the nearly-equal-mass projectile-target combinations studied with the upgraded spectrometer. The vertical error bars are statistical. The horizontal error bars on the graphs of the cross section vs. angle show the angular resolution (σ_θ) and, on the graphs of cross section vs. momentum, show the momentum resolution (σ_p). The values of σ_p and σ_θ for all projectile-target combinations are summarized in table 3 and defined in appendix D. The solid curves are least squares fits to the data based on Gyulassy and Kauffmann's[42] theoretical expressions. These solid curves have had the resolution of the spectrometer folded into them using the method described in appendix D. The dashed curves are the same functions before folding with the resolution and the dotted curves are the fits to the pion spectra in the absence of Coulomb effects. Figures 16-32 show the data for all projectile-target combinations studied as plots of Lorentz invariant cross section vs. lab momentum at fixed lab angles from 0 degrees up to the maximum angle measured in each case. As in figures 10-15, the vertical error bars are statistical and the solid curves are least squares fits with the experimental resolution folded in. Tables of all data are given in appendix E.

In order to provide a better overview of the data, perspective views of the three dimensional surface defined by the data and contour plots describing the same surfaces are shown in figures 33-42 for each nearly-equal-mass projectile-target combination except for 400 MeV per nucleon Ne+NaF. The 400 MeV data were omitted because

the beam energy is so close to 380 MeV per nucleon (for which a plot was made) and because the resolution is worse (due to a thicker target) than it is for the 380 MeV data. The plots are of the Lorentz invariant cross section as a function of rapidity ($y=\tanh^{-1}\beta_{||}$) and perpendicular momentum in units of the pion mass ($p_{\perp}/m_{\pi}c$). These perspective and contour plots were drawn by a set of computer routines[62]. Only the labels on the original plots were modified. All data points were weighted equally in making these plots. Because the statistical uncertainties were not used to produce the plots and are not displayed on them, caution is necessary when drawing conclusions based on these figures alone. They should be used along with the two dimensional graphs which show the statistical uncertainties.

Two figures are shown for each case in which these plots were made. First, a perspective representation of the surface defined by the data, along with a contour "key" to the surface, is shown. The contour "key" is a contour plot of the data plotted with the same orientation of the axes as the perspective plot. The direction from which the surface is viewed in these perspective plots is not the same in all cases because the direction which provides the best view is not always same. The π^- data are all viewed from the same perspective angle, but the π^+ are viewed from two different perspective angles (both of which differ from the angle used for π^-). The π^+ data for beam energies per nucleon less than 400 MeV have been viewed from one angle and the data for higher beam energies have been viewed from a second angle.

In addition to the perspective representations of the data and the associated contour "keys", contour plots with a more standard orientation of the axes were drawn. It is simpler to compare the different data sets with these contour plots since the orientation of the axes is the same in each case. The interval between the contour lines in the contour plots was chosen to correspond to approximately twice the (one standard deviation) statistical uncertainty on the data points. Because these uncertainties vary from point to point, it is not possible to do this exactly. The choice of the contour

intervals was particularly complicated in some cases where several data sets taken with different settings of the field on the spectrometer magnet were combined. In some of these cases the statistical uncertainties in one region of momentum and angle are significantly different from those in another region. The data for Ne+NaF at E/A=655 MeV provide an especially good example of this. On figure 15 a sudden change in the size of the error bars can be seen on the graph of cross section vs. momentum for π^+ and on the graph of cross section vs. angle for π^-. In all cases the contour interval was chosen to be larger than the statistical uncertainty on any data point.

For all projectile-target combinations in which beam velocity pions were studied, a peak in the π^- differential cross section (and in the π^-/π^+ ratio) was observed slightly lower than the velocity of the incident beam. The shifts of the peak from the momentum associated with the beam velocity tended to decrease as the beam energy increased, but the changes were within the experimental uncertainties. The uncertainty in the absolute value of the momentum was 1.5% of the pion's lab momentum, which translates into an uncertainty of roughly 2 MeV/c in the values of the momentum shift. For the Ar beam, this pion momentum shift was 2.0±1.7 MeV/c in the rest frame of the incident beam. When the 654 MeV per nucleon Ne+Be data are omitted, the corresponding shift for Ne is 3.2±2.0 MeV/c. The shift for Ne+Be is 7.2 MeV/c, which is much different from the shift observed in all other cases. The reason for this difference is unclear, but an experimental difficulty encountered while collecting the 655 MeV per nucleon Ne data at beam velocity should be noted. After the beam had been tuned and the location of the beam spot had been checked, but before any of the data were collected, a modification (by the Bevatron operators) which caused the beam spot to move by ~1 cm was made. This change was discovered after the Ne+NaF $\rightarrow \pi^-$ data at beam velocity were taken, but before any other data were collected. Before continuing the runs, the beam was retuned. A correction to the Ne+NaF $\rightarrow \pi^-$ data which were taken during this period was made, so there should not be any difference between the NaF and Be data due

to this problem. However the large difference between the downshift seen for Be and that seen for NaF should be viewed with caution, since the beam was retuned between the two runs. The depression in the π^+ cross section near the beam velocity is broader than the corresponding π^- peak but has approximately the same downshift as does the π^- peak.

Table 10 gives the half widths, $\Gamma_i/2$, of the peaks in the π^- spectra and the pion momentum shifts for each of the projectile-target combinations in the projectile velocity reference frame. The widths are defined as the half widths at half maximum, measured above a smooth background. The smooth background was defined by the source function which is described in chapter 6 (see eq. 6.14). The resolution of the spectrometer had been subtracted in quadrature from these widths. The 405 MeV per nucleon Ne+C and the 407 MeV per nucleon Ne+U data have been omitted from table 10 because pions at the beam velocity were not measured -- although the data include pions very close to the beam velocity. In table 10 the widths of the peaks are

TABLE 10

Widths and Momentum Downshifts of the Peaks in the π^- Spectra

E_{beam}/A	Beam	Target	$dp_{\parallel}$ MeV/c	$\Gamma_{\parallel}/2$ MeV/c	$\Gamma_{\perp}/2$ MeV/c
280	Ne	C	3.0	7	10
281	Ne	NaF	3.5	8	10
282	Ne	Cu	4.0	9	13
380	Ne	NaF	3.5	9	8
382	Ne	Cu	3.5	11	11
385	Ne	U	3.5	12	10
400	Ne	NaF	3.5	11	9
482	Ne	C	3.0	8	10
483	Ne	NaF	3.0	8	10
485	Ne	Cu	2.5	9	10
487	Ne	U	2.5	13	13
533	Ar	C	2.5	5	7
534	Ar	KCl	1.5	6	11
654	Ne	Be	7.2	10	18
655	Ne	NaF	2.1	6	8

expressed in terms of parallel and perpendicular momentum; if they has been defined in terms of pion kinetic energies in the beam velocity reference frame, the full widths at half maximum would generally be less than 1 MeV.

B. Comparison of Stage-1 Data with Stage-2 Data

For the ≃ 380 MeV per nucleon Ne beam data were taken with both the lead slit spectrometer (the "stage-1" data) and the upgraded spectrometer (the "stage-2" data) for NaF, Cu, and U targets. The shapes of the spectra seen with the two different spectrometer configurations are in reasonable agreement, but the normalizations do not agree. The cross sections from the lead slit spectrometer are consistently higher than those from the upgraded spectrometer. The data sets are compared in figures 43-45 and the ratios are summarized in table 11. The average ratio is 1.7. This difference is consistent with the factor of 2 uncertainty in the overall normalization of the stage-1 data and the 30% uncertainty in the normalization of the stage-2 data.

C. Comparison of Stage-2 Data with Data from Other Groups

Some of the data from the upgraded spectrometer overlap the data of Nakai et al[11]. Specifically, the data for Ne + C and Ne + NaF $\rightarrow \pi^+$ at E/A = 400 MeV can be compared. As demonstrated by figures 46 and 47, the ratio of the present data to Nakai et al's data is 1.2

TABLE 11

Ratio of Stage-1 to Stage-2 Normalization
≃ 380 MeV/nucleon Ne Data

Target	Pion Charge	Ratio
NaF	-	1.6
	+	2.0
Cu	-	1.8
	+	1.8
U	-	1.4
	+	1.4

for Ne + NaF → π^+ and 0.9 for Ne + C → π^+. To get these ratios the data from the beam which was 425 MeV per nucleon when extracted from the Bevatron were used. At the center of the target this beam was degraded to 400 MeV per nucleon for the NaF target and 405 MeV for C. Nakai *et al.* give their beam energy as 400 MeV per nucleon, but that is probably the energy when extracted from the Bevatron, in which case the present ≃ 380 MeV per nucleon data should be compared to it. Unfortunately, these 380 MeV per nucleon data do not extend out to 30 degrees. The ratio of the present 400 MeV per nucleon Ne + NaF →π^+ data to the 380 MeV per nucleon data is 1.1 when averaged over all data from 8 to 20 degrees. The data at smaller angles were omitted from the average because they are more strongly influenced by the hole in the projectile velocity π^+ spectrum. If the 400 MeV per nucleon Ne data are used to extrapolate the 380 MeV per nucleon out to 30 degrees, then the ratio of the 380 MeV per nucleon Ne+NaF→ π^+ data to the data of Nakai *et al.* is 1.3. These differences in normalizations between the present 380 MeV and 400 MeV per nucleon Ne data and the 400 MeV per nucleon Ne data of Nakai *et al.* are all within the uncertainties on the overall normalizations (30% in each case).

Some of the ≃400 MeV per nucleon Ne+NaF data from the upgraded spectrometer also overlap some of the data of Nagamiya *et al.*[13,63] for lab angles of 20 and 30 degrees. Figure 47 compares the two data sets for Ne+NaF → π^+ at a lab angle of 30 degrees. This figure also

TABLE 12

Ratios of Other Normalizations to the Normalization of the Stage 2 data ≃ 400 MeV per nucleon Ne beam

Reference	Target	Pion Charge	θ (deg.)	Ratio
Nakai *et al.*[11]	C	+	30	0.9
	NaF	+	30	1.3
Nagamiya *et al.*[13,63]	NaF	+	30	1.2
	NaF	-	20	1.25
	NaF	-	30	1.2

shows the data of Nakai et al[11]. The data from the upgraded spectrometer (labeled Sullivan et al) are from the beam which was 400 MeV per nucleon at the center of the target. The other data sets probably used a 400 MeV per nucleon beam at extraction from the Bevatron and may have had somewhat lower energy within the target. Figure 48 compares the Ne+NaF $\rightarrow \pi^-$ data from the upgraded spectrometer with the data of Nagamiya et al. at a lab angle of 20 degrees. Here, the data from the beams which were 380 and 400 MeV per nucleon at the center of the target can both be compared to Nagamiya et al's data. There is no discernible difference between the 380 and 400 MeV data. Finally, the 400 MeV per nucleon (center of target) data for Ne+NaF $\rightarrow\pi^-$ at 30 degrees can be compared to the data of Nagamiya et al. This comparison is made in figure 49. In general, there is no significant difference in the shape of the data from Nagamiya et al. and the present results, but the normalization of their data is higher by about 20%. The ratios of the normalization from Nakai et al.[11] and Nagamiya et al.[13,63] to the normalization of the data from the upgraded spectrometer are summarized in table 12. In all of the cases listed in table 12 the normalization differences are within the combined uncertainties on the overall normalizations (30% in each case).

CHAPTER 6

Discussion of Results

A. Beam Energy, Projectile/Target Mass Dependence of Cross Sections

The dependence of the pion production cross sections on the beam energy for various projectile/target combinations is shown in figure 50 for three different pion (lab) momenta. This updated version of figure 7 combines the data taken with the lead slit spectrometer (the "stage 1" data) and the data from the upgraded spectrometer (the "stage 2" data). As discussed earlier (chapter 5, section B), the normalizations of these two data sets do not agree. Therefore, the cross sections displayed in figure 50 which were obtained with the lead slit spectrometer have been divided by 1.7.

Each of the three sections of figure 50 shows the Lorentz invariant cross section for pion production vs. the beam energy per nucleon in the (nucleon-nucleon) center of mass for some fixed pion momentum. For reference, the beam energy per nucleon in the lab is also given. In order to approximately remove the Coulomb effects, the geometric mean ($\sigma = [\sigma_+ \sigma_-]^{1/2}$) of the π^- and π^+ cross sections has been used in the figure. This figure demonstrates the main features of the beam energy and projectile/target mass dependence of the data. The pion cross sections rapidly rise with increasing beam energy. The cross sections also consistently increase as the mass of the target is increased. Figure 50 also compares the firestreak model[23] (the dashed lines) for Ne+Ne to the data. As discussed in chapter 2, the firestreak model predicts pion cross sections which are consistently higher than the measured cross sections. The agreement between the Ne+NaF data in figure 50 and the firestreak model is best at the lowest beam energies.

In chapter 2 the scaling of the pion cross sections with the target mass was discussed. The curves shown in figure 7 were compared with an $A^{2/3}$ dependence on the target mass. As discussed then, the cross sections at the higher beam energies are consistent with the $A^{2/3}$ dependence while the cross sections at lower beam energies are

not. It is clear that any geometric scaling law should depend in a symmetric manner on both the projectile and the target mass. The geometric factors relevant to the cross sections for nucleons were discussed in chapter 2, but the expected dependence of the pion cross sections on geometric factors is more model-dependent and more complicated.

One reasonable method to estimate the dependence of the pion cross sections on the projectile and target mass is to follow the procedure used by Sternheim and Silbar[64] for pion production in proton-nucleus collisions. They used the isobar model to find the expected dependence of the π^+, π^0, and π^- cross sections on the target mass. By assuming the two-step process $NN \rightarrow N\Delta$, then $\Delta \rightarrow N\pi$, a simple evaluation of the appropriate Clebsch-Gordan coefficients gives the proportions of the three pion charges expected from the various possible combinations of neutron and proton collisions. For np and pp collisions they give these proportions as

$$\begin{aligned} pp &\rightarrow np\pi^+ \qquad d\sigma = \tfrac{5}{6}d\sigma_{iso} \\ &\rightarrow pp\pi^0 \qquad d\sigma = \tfrac{1}{6}d\sigma_{iso} \end{aligned} \tag{6.1}$$

$$\begin{aligned} np &\rightarrow nn\pi^+ \qquad d\sigma = \tfrac{1}{12}d\sigma_{iso} \\ &\rightarrow np\pi^0 \qquad d\sigma = \tfrac{1}{3}d\sigma_{iso} \\ &\rightarrow pp\pi^- \qquad d\sigma = \tfrac{1}{12}d\sigma_{iso} \end{aligned} \tag{6.2}$$

where $d\sigma_{iso}$ is the cross section for the production of pions (summed over all pion charges) in pp collisions. By analogy to the pp case, the proportions of the three pion charges in neutron-neutron collisions is

$$\begin{aligned} nn &\rightarrow np\pi^- \qquad d\sigma = \tfrac{5}{6}d\sigma_{iso} \\ &\rightarrow nn\pi^0 \qquad d\sigma = \tfrac{1}{6}d\sigma_{iso} \end{aligned} \tag{6.3}$$

Next, the numbers of possible nn, np, and pp collisions must be counted. The geometric cross section for a neutron from the projectile to react with the target is πR_t^2. The total geometric cross section for neutrons to be knocked out of the projectile nucleus is just

the number of neutrons in the projectile times this geometric cross section $N_p \pi R_t^2$. This cross section can be broken up into two parts, corresponding to neutrons whose first pion producing reaction is with a proton or a neutron from the target. Many of the possible nucleon-nucleon collisions will not produce pions, but this model only calculates the relative numbers of pions produced so this overall normalization factor can be ignored. This model also ignores the possibility that a nucleon which has already been involved in a pion producing collision with another nucleon can be involved in the production of a second pion. This is reasonable since the probability of producing a pion is small and because in the energy range studied here the energy loss involved in making the pion will make this probability even smaller. The number of interactions of neutrons in the projectile with protons and neutrons in the target should be proportional to

$$\frac{N_t}{A_t} N_p \pi R_t^2 \qquad \text{nn interactions} \tag{6.4}$$

$$\frac{Z_t}{A_t} N_p \pi R_t^2 \qquad \text{np interactions}$$

After also considering the interactions of protons from the projectile plus protons and neutrons from the target, the number of nucleon-nucleon pion producing collisions should be proportional to

$$\text{pp collisions} : \pi \left[\frac{Z_t}{A_t} Z_p R_t^2 + \frac{Z_p}{A_p} Z_t R_p^2 \right] \tag{6.5}$$

$$\text{nn collisions} : \pi \left[\frac{N_t}{A_t} N_p R_t^2 + \frac{N_p}{A_p} N_t R_p^2 \right] \tag{6.6}$$

$$\text{np collisions} : \pi \left[\frac{Z_t}{A_t} N_p R_t^2 + \frac{N_t}{A_t} Z_p R_t^2 + \frac{Z_p}{A_p} N_t R_p^2 + \frac{N_p}{A_p} Z_t R_p^2 \right] \tag{6.7}$$

Using these proportions of the various combinations of nucleon-nucleon collisions and the proportions of the three pion charges expected to be produced, the following scaling laws for the three pion charges emerge.

$$Y_+ \propto \frac{\pi r_0^2}{12} (A_t^{-1/3} + A_p^{-1/3}) (10Z_pZ_t + Z_tN_p + N_tZ_p) \quad 6.8$$

$$Y_0 \propto \frac{\pi r_0^2}{12} (A_t^{-1/3} + A_p^{-1/3}) (2Z_pZ_t + 4Z_tN_p + 4N_tZ_p + 2N_pN_t) \quad 6.9$$

$$Y_- \propto \frac{\pi r_0^2}{12} (A_t^{-1/3} + A_p^{-1/3}) (10N_pN_t + Z_tN_p + N_tZ_p) \quad 6.10$$

In equations 6.8-6.10 the radii of the projectile and target have been replaced by $r_0A^{1/3}$.

Several tests can be applied to these scaling laws to make sure they are reasonable. If there are no neutrons in the projectile or the target ($N_t=N_p=0$), which means that only pp collisions are possible, then the cross section for π^- production is zero and the π^+/π^0 ratio is 5/1, as in elementary pp collisions (see equation 6.1). A similar limit exists for $Z_p=Z_t=0$. If both the projectile and target have equal numbers of protons and neutrons, then equal cross sections for π^+, π^0, and π^- are predicted, as expected for this isospin symmetric case. These formulas also predict the same relative numbers of the various pion charges for the proton-nucleus case as given by Sternheim and Silbar[64]. For reference, the geometric factors in equations 6.8-6.10 have been evaluated for all of the projectile-target combinations studied here. The results are listed in table 13 where r_0 = 1.2 fm has been assumed. Although the scaling factors are given in barns, these numbers are actually just proportional to the

TABLE 13

Predicted Geometric Scaling of Pion Cross Sections

Beam	Target	Y_+	Y_-	$R(\pi^-/\pi^+)$
Ne	Be	1.57	1.57	1.00
	C	2.19	2.19	1.00
	NaF	3.33	3.61	1.08
	Cu	8.25	9.53	1.16
	U	23.1	33.9	1.47
Ar	C	3.63	4.28	1.18
	KCl	8.88	11.1	1.25

pion production cross sections, they must be multiplied by a beam-energy-dependent factor related to the fraction of nucleon-nucleon interactions which actually produce pions.

The measured differential pion production cross sections, which are shown in figure 50, do not scale with this scaling law. As discussed in chapter 2, this does not mean that the total cross sections do not agree with this model. The angular and energy distributions depend upon the projectile and target mass. It is therefore of some interest to compare the target/projectile mass dependence predicted equations 6.8-6.10 to the integrated cross sections of Nagamiya et al[13]. The cross sections in reference 13 were obtained by interpolating and extrapolating the measured differential cross sections. Table 14 compares the π^-/π^+ total cross section ratio predicted by equations 6.8 and 6.10 with the data of Nagamiya et al. The measured π^-/π^+ ratio is in all cases greater than or equal to the predicted value, but the uncertainty associated with the experimental values is about 30%, so the differences may not be significant.

TABLE 14

π^-/π^+ Predicted vs. Measured[13] Integrated Cross Section Ratios

$R(\pi^-/\pi^+)$ predicted	$R(\pi^-/\pi^+)$ measured	Reaction	E/A (MeV)
1.08	1.12 1.14	Ne+NaF	400 800
1.16	1.16	Ne+Cu	800
1.43	1.86 1.53	Ne+Pb	400 800
1.25	1.46	Ar+KCl	800
1.69	1.95	Ar+Pb	800

The predicted projectile and target mass dependence of the pion cross sections can also be compared to the experimental data of Nagamiya et al[13]. The ratios of the total cross sections for various projectile and target combinations to the cross sections for Ne+NaF which were measured by Nagamiya et al. are compared to the ratios

TABLE 15

Predicted vs. Measured[13]

Projectile/Target Mass Dependences of Integrated Pion Production Cross Sections

E/A (MeV)	Ratio	π^+ Measured	π^+ Predicted	π^- Measured	π^- Predicted
400	Ne+Cu/Ne+NaF	1.82	2.47	--	2.64
	Ne+Pb/Ne+NaF	2.73	6.24	4.53	8.23
800	Ne+Cu/Ne+NaF	2.14	2.47	2.17	2.64
	Ne+Pb/Ne+NaF	3.81	6.24	5.12	8.23
	Ar+KCl/Ne+NaF	2.78	2.66	3.41	3.08
	Ar+Pb/Ne+NaF	6.11	10.11	10.5	15.3
	C+C/Ne+NaF	--	0.43	0.39	0.39
	C+Pb/Ne+NaF	--	4.22	2.85	5.57

predicted by equations 6.8 and 6.10 in table 15. For the lighter target-projectile combinations the scaling law reproduces the data well. The ratio of the Ne+Cu to Ne+NaF cross section is approximately reproduced. The ratios of the data involving the Pb target to the Ne+NaF data are not reproduced very well (but the 30% uncertainty on the experimental numbers should be remembered). The difference between the predicted and measured ratios of Ne+Pb/Ne+NaF and Ar+Pb/Ne+NaF may be partially due to reabsorption of the pions by the lead nucleus. It is also important to notice that the ratios Ne+Cu/Ne+NaF and Ne+Pb/Ne+NaF are not the same at the two beam energies. If this difference is not just due to experimental uncertainty, then it means that the scaling of the cross sections depends upon more than simple geometric factors.

B. Comparison of Some Theoretical Calculations to the Data

Figure 51 compares Cugnon and Koonin's[30] calculation of the expected π^- and π^+ differential cross sections at 0 degrees with the combined data from the two versions of the pion spectrometer. The cross sections from the lead-slit spectrometer have all been divided by 1.7 to bring the normalizations of the two data sets into agreement. Cugnon and Koonin's calculation was based on a Monte Carlo program which calculated the space-time evolution of the nucleons involved in the collision. The calculation is summarized in chapter

3. Statistical uncertainties associated with the Monte Carlo calculation have probably caused some of the fine structure in the theoretical curves shown in figure 51. Aside from the normalization, which is not in agreement with the data, the shapes of the π^- peak and the π^+ hole are roughly reproduced by the calculation, although the measured π^- peak is narrower than the calculated one. The shape of the spectrum at high pion momentum does not appear to agree with the data, but more data at higher pion momenta would be necessary to confirm this. The calculation seems to reproduce the π^-/π^+ ratio reasonably well throughout the regions in which there are data.

Although the 380 MeV per nucleon data do not extend into the center-of-mass velocity, where Cugnon and Koonin predict a π^-/π^+ ratio of about 5, this large π^-/π^+ ratio is probably not correct. The Ne+NaF data at E/A = 655 MeV (see figure 15, where the center-of-mass velocity corresponds to a lab momentum of 83 MeV/c) show neither a depression in the π^+ spectrum nor a peak in the π^- spectrum at the center-of-mass velocity, and the π^-/π^+ ratio at the CM velocity is only about 1.5. It is reasonable to assume that the data at E/A = 380 MeV, which are shown in figure 51, are similar. For Ar+Ca at E/A = 1.05 GeV, Cugnon and Koonin predict the π^-/π^+ ratio to be about 5.5. The observed value is 1.5[14]. The reasons for the large disagreement are not understood.

The 655 MeV per nucleon Ne+NaF data is the only data set reported in this thesis which covers pions at the center of mass velocity. As shown in figure 37, a slight enhancement of the invariant cross section at the rapidity of the center of mass (y_{cm}=0.55) was seen in the π^- data at $p_\perp \simeq 0.4 m_\pi c$. This feature is similar in location and shape to the enhancements of the π^+ cross section reported for Ar+Ca at E/A = 1.05 GeV[9] and Ne+NaF at E/A = 800 MeV[10]. This is the first time that this structure has been reported in the π^- data and, assuming that the same process causes each of these independently reported enhancements, it implies that this structure is not a Coulomb effect, contrary to the suggestions of several authors[40,42].

The theory of Gyulassy and Kauffmann[42] has been used to make least squares fits which parameterize the data. The solid lines in figures 10-32 are from these fits. The details of the fitting procedure will be given in the following section. The Gyulassy and Kauffmann (GK) formulas will be summarized in this section. In their work, GK have developed approximate Coulomb correction equations which use a perturbative approach to treat both quantum and relativistic effects due to the field of a thermally expanding charge distribution. The charged pion cross section is expressed in terms of an uncharged pion cross section (the "source function") which is evaluated at a momentum which has been shifted by a Coulomb impulse ($\vec{\delta p}$), then modified by a Coulomb phase space distortion factor. The "non-perturbative extrapolation" of the GK model has been used in this analysis.

$$\sigma_{\pm}(\vec{p}) = \sigma_0(\vec{p} \mp \vec{\delta p})\ G(\pm\delta D/\pi) \qquad 6.10$$

where

$\sigma_0(\vec{p})$ = the uncharged pion source function ($d^3\sigma/dp_\pi^3$)

$\vec{p}$ = the observed momentum of the particle

$\vec{\delta p}$ = the Coulomb impulse

δD = the phase space distortion factor, and

$G(\eta) = 2\pi\eta/[\exp(2\pi\eta) - 1]$.

The uncharged pion source function is evaluated at a shifted momentum, where the momentum shift is given by GK as

$$\delta p_\mu(\vec{p}) = \sum_i Z_i \alpha (q - E'_i u_i/c)_\mu \frac{E'_i R_i \hbar c}{(\hbar c)^2 + (p'_i c R_i)^2} \qquad 6.11$$

where the parameters associated with the charged fragments are

Z_i = charge on fragment i

R_i = mean inverse radius of fragment i

T_i = temperature of fragment i in MeV

$\beta_{Ti}^2 = \dfrac{\pi T_i}{2m_p c^2} = T_i/597\text{MeV}$ = mean square thermal velocity of protons

u_i = 4-velocity of fragment i = $\gamma_i(1,\vec{\beta_i})$, $\gamma_i = (1-\beta_i^2)^{-1/2}$

and the kinematic variables are

E_i = energy of particle i in the rest frame of charge i

(mass + kinetic) = $q_\mu u^\mu = \gamma_i[(E/c) , \vec{p} \cdot \vec{\beta_i}]$

$E'_i = E_i(1 - \beta_{Ti}^2)^{-1/2}$

q = 4-momentum of particle in the frame in which δp_μ is being evaluated = $(E/c,\vec{p})$

$p'_i = [(E'_i/c)^2 - (m_\pi c)^2]^{1/2}$, and

$\alpha = 1/137$.

In this analysis, the mean inverse radii are assumed to be

$$R_i = \frac{2}{3} r_0 A_i^{1/3}$$

where A_i is the mass number and r_0 is taken somewhat arbitrarily as 1.4 fm. The factor 2/3 relates the mean inverse radius of a uniformly charged sphere to its radius.

The source function is then modified by a phase space distortion factor as shown in equation 6.10. In that equation

$$\delta D(p) = \pi\alpha\left(\sum_i Z_i \frac{E'_i}{p'_i c}\right)\mathcal{F}(p'_i) \qquad 6.12$$

where the variables have the same meanings as above, and the form factor is taken to be

$$\mathcal{F}(p'_i) = [(\pi p'_i R/\hbar)^2 + 1]^{-1/2}. \qquad 6.13$$

This form factor is not identical to that derived by GK for an exponential charge distribution, but it closely approximates their expression, has the same limits as $p \to 0$ and $p \to \infty$, and is simpler to evaluate.

If the Coulomb correction equations above are applied to the case of a single charged particle leaving a nucleus whose temperature is zero, they become a little simpler. If the limit of $\rho = pR/\hbar \to 0$ is also taken, then the momentum shift (δp) approaches zero and the phase space shift (δD) approaches $\pi Z\alpha/\beta$, where β is the velocity of

the charged particle which is leaving the nucleus. In this case the observed cross section as defined by equation 6.10 reduces to

$$\sigma_{\pm}(\vec{p}) = \sigma_0(\vec{p})\ G(\pm Z\alpha/\beta).$$

This is the non-relativistic method which is commonly used to make Coulomb corrections to beta decay spectra[65-67]. In this same limit, the ratio of negatively charged particles to positive particles will reduce to

$$R = G(-Z\alpha/\beta)/G(+Z\alpha/\beta).$$

Equation 2.1, which was used to calculate the lines in figure 6, also approaches this expression as $\rho \rightarrow 0$. Specifically,

$$\lim_{\rho \rightarrow 0} \sum_{L=0}^{\infty} \frac{F_L(\eta,\rho)}{\rho} = G(\eta)$$

where

$\eta = Z\alpha/\beta$, and

and $F_L(\eta,\rho)/\rho$ $(L=0,\infty)$ are the solutions to the radial part of the Schrödinger equation for a particle in a Coulomb field[52].

C. Least Squares Fitting Method

As mentioned above, the Gyulassy and Kauffmann[42] Coulomb correction equations were used to make least squares fits to the data. The lines in figures 10-32 are based on these fits. Their equations are given in equations 6.10-6.13, where the sums are over all charge distributions. The model used in the least squares fitting procedure assumed that there were projectile and target fragments at relatively low temperatures. The temperatures were parameterized in terms of a thermal velocity (β_{Ti}) as shown below equation 6.11. A hot central charge distribution is assumed for all of the charge not contained in the projectile and target fragments.

The analysis used here differs from that of Gyulassy and Kauffmann in a few details. First, the form factor (eq. 6.13) used here is not the same as their form factor, although the differences are small. The other differences are discussed below.

Gyulassy and Kauffmann used the fireball model[22] for their uncharged pion source function. It is not possible to quantitatively describe the data presented here with the fireball model's single Boltzmann thermal source since, in contrast to the predictions of this model, the measured differential cross sections do not always fall with increasing center of mass energy of the pion. Gyulassy and Kauffmann compared their calculations to the π^-/π^+ ratio, which is not sensitive to the source function. They were able to accurately reproduce the π^-/π^+ ratios from reference 1, although the same model reproduced neither the π^- nor the π^+ differential cross section. Here, in order to obtain reasonable fits to the data, a source function expressed by the lowest three terms in a momentum expansion about the center of mass was used. A Boltzmann factor exponential with the pion "temperature" (E_0 in their notation) estimated from Nagamiya *et al.*[13] was used to give the correct asymptotic behavior.

$$\sigma_0(p,\theta) = N\left[1 + (p_{cm}/m_\pi c)^2(c_1 + c_2 P_2[\cos\theta_{cm}])\right]\exp(-E_{cm}/T) \qquad 6.14$$

where

p_{cm}, E_{cm} = momentum and total energy (mass + kinetic) of the pion in the nucleon-nucleon center of mass.

N = normalization parameter

c_1, c_2 = source shape parameters

$P_2(\cos\theta) = (3\cos^2\theta - 1)/2$

T = slope parameter or temperature of the source

For $c_1 = c_2 = 0$, this expression reduces to a central thermal pion source. Notice that the temperature in equation 6.14 (which is taken from Nagamiya *et al.*[13]) is not necessarily the same as the temperatures used in equations 6.11 and 6.12. The total cross section obtained by integrating equation 6.14 over all momenta and angles is

$$\sigma_{tot} = 4\pi N m_\pi^2 T\left[K_2(m_\pi/T) + \frac{3c_1 T}{m_\pi}K_3(m_\pi/T)\right] \qquad 6.15$$

where K_2 and K_3 are modified Bessel functions.

The third manner in which the fitting procedure used here differed from that of Gyulassy and Kauffmann was in the interpretation of the parameter β_T which is used in equations 6.11 and 6.12. In the first attempts to make fits to the data, β_T was used as a free parameter. The β_T values obtained for the projectile and target fragments with this procedure correspond to nucleon temperatures which were unreasonably small, of the order of 1 MeV, which implies that the fragments will be bound and will not expand. This result prompted the reinterpretation of the parameter β_T. Instead of being the r.m.s. expansion velocity of a Boltzmann distribution of nucleons, it has been reinterpreted as the r.m.s. velocity dispersion of the projectile fragments. The velocity (or momentum) dispersion of the projectile fragments has been studied for several projectile particles and energies[68-70]. The parallel momentum dispersion has been fit by the general expression

$$\left\langle p_{\parallel}^2 - \langle p_{\parallel} \rangle^2 \right\rangle^{1/2} = \sigma_0 \left[\frac{A_f (A-A_f)}{A-1} \right]^{1/2} \qquad 6.16$$

where A is the mass of the projectile and A_f is the mass of the fragment. Table 16 lists the values of σ_0 for the systems studied in references 68-70. Here, a value of 86 MeV/c has been assumed, although pion producing reactions may not be representative of normal fragmentation reactions. The parameter β_T used in the fitting procedure was calculated by assuming an expression of the same form as equation 6.16. Specifically, the formula used was

$$\beta_T = \frac{0.16}{A_f} \left[\frac{A_f (A-A_f)}{A-1} \right]^{1/2} \qquad 6.17$$

where $0.16 = \sqrt{3}\sigma_0/931.5\text{MeV}$. The factor $\sqrt{3}$ was obtained by assuming that the momentum dispersion of the two momentum components perpendicular to the beam was the same as the parallel dispersion, then adding the three components in quadrature. The mass numbers in this equation were calculated from the charges by assuming that the charge-to-mass ratios of the projectile and target fragments were the same as the original nuclei.

TABLE 16

σ_0 from Projectile Fragmentation Data

Authors	E/A MeV	Beam	Target	σ_0 MeV/c
Greiner et al.[68]	1050	C	various[a]	70±2[b]
	2100	C	various[a]	74±2[b]
	2100	O	various[a]	86±2[b]
Viyogi et al.[69]	213	Ar	C	94±5
Van Bibber et al.[70]	92.5	O	Al	86
	92.5	O	Au	80

a) Averaged over targets from Be to Pb. The authors say that σ_0 does not depend on the target mass above the 5% level.

b) Notice that their definition of the parameter differs from the definition used here by a factor of 2; the values quoted here are one-half of the values given in the original reference.

The normalization parameter (N in eq. 6.14), the source shape parameters (c_1 and c_2 in equation 6.14), and the charge on the projectile fragment (Z_{eff}) were used as parameters in the least squares fit of this function to the data. The shift of the peak in the π^- spectrum (or hole in the π^+ spectrum) from the velocity of the incident beam (see the values of $dp_{||}$ in table 10) was estimated graphically and was held fixed during the the fitting procedure.

The charge on the target fragment was calculated by assuming that the same number of nucleons were knocked out of the target as were knocked out of the projectile. The charge-to-mass ratio of both the projectile and target fragments were assumed to be the same as in the initial nuclei. The charge and mass of the hot central charge distribution were then calculated by charge and baryon number conservation. The charge of the pion was included in the charge balance equation. For the projectile and target fragments, the parameter β_{Ti} was fixed according to the measured velocity dispersion of projectile fragments[68-70] (see eq. 6.17). The temperature of the central charge distribution in equations 6.11 and 6.12 was taken to be $T=2E^*/3$,

where E^* is the beam energy per nucleon in the nucleon-nucleon center of mass. The temperature in the source function (eq. 6.14) was taken from Nagamiya *et al.*[13]. Source shape parameters c_1 and c_2 for π^+ were taken from the corresponding π^- fits.

In table 17 and figures 52-54 the values of the parameters found in the fits are shown. The uncertainty associated with each parameter in Table 17 was determined by calculating how much the parameter had to be changed, with all other parameters freely adjustable, in order to increase the chi-squared (x^2) by one from its value at the minimum[71]. These errors are due to statistical uncertainties in the data. They do not include uncertainties due to any systematic errors in the data or due to the assumptions involved in the fitting expression. Because the source shape parameters (c_1 and c_2) for the π^+ fits were taken from the corresponding π^- fits, the number of parameters that were varied during the complete error analysis was smaller for π^+ than for π^-. As a result, the errors associated with the π^+ parameters are generally smaller than for π^-. The errors given for c_1 and c_2 are from the π^- fits.

TABLE 17

Parameters from Least Squares Fits to Pion Data

E/A	System	Z_{eff}	N $\mu b/MeV^3$	T[a] MeV	c_1	c_2	x^2/N[b]
280	Ne+C→π-	6.4±.2	0.11±.01	30	2.9±.5	0.±.4	1.7
	→π+	3.8±.2	0.11±.01	"			2.1
281	Ne+NaF→π-	5.6±.2	0.19±.01	"	2.1±.6	1.0±.5	2.0
	→π+	3.1±.2	0.16±.01	"			1.3
282	Ne+Cu→π-	4.3±.3	0.47±.04	"	1.4±.7	1.3±.7	1.6
	→π+	1.8±.3	0.40±.02	"			1.1
380	Ne+NaF→π-	4.6±.1	0.20±.01	36	1.7±.1	1.0±.1	2.6
	→π+	3.3±.1	0.15±.01	"			2.3
382	Ne+Cu→π-	3.4±.1	0.43±.02	"	1.1±.2	0.0±.1	1.6
	→π+	2.3±.1	0.37±.01	"			1.3
385	Ne+U→π-	2.7±.2	1.62±.15	"	0.6±.2	0.0±.1	1.5
	→π+	1.5±.3	0.91±.04	"			0.9
405	Ne+C→π-	3.2±.3	0.11±.01	39	1.1±.2	0.0±.1	2.3
	→π+	4.2±.3	0.11±.01	"			1.5
400	Ne+NaF→π-	4.3±.1	0.12±.01	"	1.6±.1	0.0±.1	2.4
	→π+	2.5±.1	0.11±.01	"			3.5
407	Ne+U→π+	1.3±.6	0.93±.12	"	0.2±.3	0.0±.2	0.9
	→π+	1.0±.6	0.50±.03	"			1.6
482	Ne+C→π-	5.0±.1	0.09±.01	45	1.1±.2	0.0±.1	1.4
	→π+	3.5±.1	0.08±.01	"			2.1
483	Ne+NaF→π-	4.4±.1	0.16±.01	"	0.8±.1	0.0±.1	2.2
	→π+	2.9±.1	0.14±.01	"			1.9
485	Ne+Cu→π-	3.5±.1	0.43±.01	"	0.1±.1	0.2±.1	2.1
	→π+	2.2±.1	0.31±.01	"			2.4
487	Ne+U→π-	3.1±.2	1.54±.04	"	0.0±.1	0.0±.1	1.0
	→π+	1.8±.3	0.63±.03	"			1.2
533	Ar+C→π-	6.3±.1	0.16±.01	50	0.7±.1	0.0±.1	1.4
	→π+	8.4±.4	0.12±.01	"			2.7
534	Ar+KCl→π-	4.4±.2	0.44±.01	"	0.1±.1	0.0±.1	1.4
	→π+	4.2±.3	0.27±.01	"			3.2
654	Ne+Be→π-	3.1±.1	0.07±.01	56	0.6±.2	0.0±.1	2.2
	→π+	3.1±.1	0.06±.01	"			3.2
655	Ne+NaF→π-	1.9±.1	0.16±.01	"	0.6±.1	0.0±.1	3.7
	→π+	3.6±.1	0.15±.01	"			3.9

a) Temperature in source function (eq. 6.14)

b) Chi-squared per degree of freedom of the fit

D. Results of Fits

The solid curves of figures 10-32 show the results of the least squares fits to the pion data. The resolution of the spectrometer has been folded into these curves using the method described in appendix D. The dashed lines in figures 10-15 show the same fitting function before folding with the resolution, and the dotted lines show the uncharged pion source function (eq. 6.14) to which the Coulomb corrections were applied. The fits were made as a function of momentum and angle, so the comparisons of the calculations and the data in figures 10-15 represent only two cuts through the two-dimensional surface centered on the π^- peak and the π^+ hole near beam velocity.

The effective projectile fragment Z values (Z_{eff}) in table 17 and figure 52 show a slight decrease with bombarding energy for the lighter targets, reversing for heavy targets. Some of the values of Z_{eff} have been omitted from figure 52 because the fits were poor near the projectile velocity peak or depression and Z_{eff} is sensitive to the quality of the fit in this region. For the nearly equal mass Ne+NaF collisions, the Z_{eff} values for π^- are typically about half the initial charge of the neon projectile, while the values for π^+ are more nearly a third of the initial charge. As the mass of the target increases, Z_{eff} generally decreases for both π^+ and π^-. For the neon beam the effective charge on the projectile fragment for π^+ is less than for π^- in almost all cases. This difference can be qualitatively understood in that a beam velocity π^+ arises from a smaller average impact parameter than π^-, as noted by GK[42]. This difference between π^+ and π^- was not seen in all cases, but in the cases were it was not seen, the fitting procedure was not as successful as in the cases where the difference was seen. There is another possible explanation for the difference in Z_{eff} values between π^+ and π^-. By charge conservation, the charge of the rest of the system must be two units larger when a π^- is produced than when a π^+ is produced. The division of these two charges among the rest of the system is very model dependent, but it is reasonable to assume that it

will result in Z_{eff} values for π^- which are larger than for π^+.

The use of a single value of Z_{eff} to represent the Coulomb effects is an approximation. A better treatment would be to average over the cross sections for the production of each of the possible projectile fragments, weighted by the probability of simultaneously producing a pion. This was done by Radi et al.[72], who show that the single value of Z_{eff} needed to reproduce the same Coulomb effect as the more complicated averaging procedure can vary rapidly with pion momentum. This is demonstrated by figure 55, which shows the single value of Z_{eff} needed to reproduce the Coulomb effects due to the averaging procedure as a function of pion momentum in the projectile velocity reference frame for Ne+C at E/A = 280 MeV. From this figure, it is clear that the fits to the data will be most successful when a small range of pion momenta is covered. The 655 MeV per nucleon Ne data covers a larger range of pion momenta than the other data sets, which explains (at least partially) the failure of the fitting procedure in this case.

The values of the normalization parameter in the uncharged pion source function (N in eq. 6.14) found by the fitting procedure are given in table 17. As in the fireball model[22], these values of N are almost independent of beam energy, suggesting that it is just a geometric factor. To illustrate the beam energy dependence of the source function and to display it in a manner independent of c_1 and c_2, figure 53 shows the values of the Lorentz invariant form of the source function ($Ed^3\sigma/dp^3$) evaluated for pions at rest in the center of mass [$N' = Nm_\pi \exp(-m_\pi/T)$] vs. the kinetic energy per nucleon of the beam in the center of mass (E^*). Since N is nearly independent of beam energy, the beam energy dependence of N' is contained largely in the Boltzmann factor $\exp(-m_\pi/T)$.

The values of N' can be parameterized by the simple semi-empirical expression

$$N'_{\pm} = N_0 Y_{\pm} \exp\left[\frac{-m_\pi}{aE^*}\right] \qquad 6.18$$

where Y_+ and Y_- are geometric factors defined by equations 6.8 and 6.10, respectively. The curves in figure 53 are based on this expression with $N_0 = 2\times10^{-6}$ $c^3MeV^{-2}sr^{-1}$, $a = 0.872$, and $r_0 = 1.2$ fm in equations 6.8 and 6.10. This parameterization assumes that the cross sections for the production of pions at rest in the center of mass depends on a geometric factor which depends only on the mass number, the neutron number, and the proton number of the beam and target times a Boltzmann factor. In the fireball model[22], aE^* would correspond to the temperature and the parameter "a" would be about 2/3 (i.e. $E^* \simeq (3/2)T$). Figure 54 attempts to put all of the values of N' on a universal line by plotting $\log(N'_\pm/Y_\pm)$ vs. $(2E^*/3)^{-1}$. The solid line, which is the least squares fit to the data, is based on the same parameters as were used in figure 53. The dashed line shows the slope of a line based on equation 6.18 with $a = 2/3$, which means that the slope is $-m_\pi$. The parameterization of N' is reasonable successful except for the U target. This failure for U is due (mostly) to the failure of the geometric scaling factors ($Y_\pm$) for heavier targets. As discussed in section 6A, this problem may be partially caused by the reabsorption of the pions in the large spectator fragments.

The values of c_1, which are related to the departure of the source function from a Boltzmann distribution, consistently decrease with increasing target mass and with increasing beam energy. Because the calculated cross section can be negative for c_1 less than zero, it has been restricted to positive values. When c_2 is zero, the source function is isotropic in the center of mass. A positive value of c_2 indicates a source function that is forward-backward peaked in the center of mass. To avoid sideward peaking of the source function and because the calculated cross section can be negative for c_2 less than zero, it has also been restricted to positive values. The fitted values of c_2 are generally consistent with zero, but they are poorly determined since the data are concentrated at low center-of-mass angles.

CHAPTER 7
Conclusions

In summary, strong Coulomb effects on the charged pion spectra were observed near the beam velocity and, by inference, near the target velocity. For light projectiles incident on light targets, these effects can be explained quantitatively in terms of Coulomb interactions between the pions and cold projectile fragments using Gyulassy and Kauffmann's[42] Coulomb correction formulas. The present treatment of Coulomb effects differs from that of Gyulassy and Kauffmann in that a different expression has been used for the uncharged pion source function (see eq. 6.14) and their formulas for thermal averaging are reinterpreted in terms of an average over the velocity dispersion of the projectile fragments. The shift of the peak in the π^- spectrum from the incident beam velocity and the approximate widths of these peaks are consistent with previously measured projectile fragmentation data[68-70]. It has also been demonstrated that the effective charge on the projectile fragment is less for π^+ near the beam velocity than for π^-. This difference is consistent with the expectation that positive pions near beam velocity tend to come from more central collisions[42,72]. Using the same methods, qualitative agreement is achieved for heavier targets and projectiles. The differences between the fitting function used here and the data are due, at least in part, to an incomplete treatment of impact parameter averaging. It has also been demonstrated that the beam energy, projectile mass, and target mass dependence of the pion cross sections, after correcting for Coulomb effects, can be qualitatively understood in terms of a beam-energy-independent geometric factor multiplied by a Boltzmann factor which contains the beam energy dependence.

The Ne + NaF $\rightarrow \pi^-$ data at E/A = 655 MeV cover a larger region of momentum and angle than the other data sets. These 655 MeV per nucleon π^- data show an enhancement of the invariant cross section at 90 degrees in the center of mass which is similar to the enhancements seen by Wolf *et al.*[9] and Chiba *et al.*[10] in the π^+ data at higher beam energies. This feature was not seen in the Ne + NaF $\rightarrow \pi^+$ data at

400 MeV per nucleon[11]. This is the first time this enhancement has been seen in the π^- data and it is also the lowest beam energy at which it has been seen. Because it has now been seen for both pion charges, the theoretical explanations of the structure as a Coulomb effect[40,42] seem to be ruled out. This conclusion could be made with greater confidence if measurements of both the π^+ and π^- spectrum had been made in the 90 degree center of mass region. Unfortunately, the Ne + NaF $\rightarrow \pi^+$ data at E/A = 655 MeV do not cover as large an angular range as the π^- data, so the region of the enhancement at 90 degrees in the center of mass was not covered for positive pions.

For most of the projectile-target combinations studied, the data reported here cover a relatively small region of momentum and angle, but this band includes the region in which the Coulomb effects are expected to be greatest. In the projectile-velocity region the Coulomb effects can be explained reasonably. The situation for pions near the center-of-mass velocity is worse. The theoretical models which have been used to explain the projectile velocity data fail near the center-of-mass velocity. In order to study some of the more exotic phenomena associated with the charged particle spectra in heavy ion interactions, Coulomb effects must be understood in all momentum regions and taken into account.

This work was supported by the Director, Office of Energy Research, Division of Nuclear Physics of the Office of High Energy and Nuclear Physics of the U.S. Department of Energy under Contract W-7405-ENG-48.

APPENDIX A

Target Thickness Corrections

The cross section is related to the number of pions produced by a weighted average of the range of cross sections which occur as the beam loses energy in the target.

$$\frac{1}{x_t}\int_0^{x_t}\sigma(x)\,dx = \frac{AN_\pi}{\rho x_t N_a N_b} \qquad \text{(thick target)} \qquad \text{A.1}$$

where

$\sigma(x)$ = cross section at position x in the target

A = atomic mass of target

ρ = density of target

N_a = Avogadro's number = 6.023×10^{23}

N_b = number of incident beam particles

x_t = thickness of target

N_π = number of pions observed

If the energy loss of the beam in the target is small, so that the cross section can be treated as a constant, then equation A.1 reduces to the usual relationship between cross section and the number of produced particles.

$$\sigma_{thin} = \frac{AN_\pi}{\rho x_t N_a N_b} \qquad \text{(thin target)} \qquad \text{A.2}$$

where σ_{thin} is used to denote cross section calculated by ignoring energy loss in the target.

One way to approach the problem of correcting the thick target data would be to estimate the cross section at the incident beam energy. Call this method A. A second approach would be to estimate an "effective beam energy" at which with the thin target formula (eq. A.2) is applicable. Call this method B. The equations relevant to both methods will be worked out below.

First, try method A (adjust the cross sections to agree with the incident beam energy). The beam energy as position x in the target can be written as:

$$E_{beam}(x) = E_0 - \int_0^x \left[\frac{dE}{dx'} \right] dx' \qquad A.3$$

where E_0 is the incident beam energy. Next, assume that the cross section varies exponentially with beam energy, specifically:

$$\sigma(E_{beam}) = \sigma_0 \exp[(E_{beam} - E_0)/E_\sigma] \qquad A.4$$

where

E_{beam} = beam energy

E_σ = a slope parameter

σ_0 = the cross section at the incident beam energy

Using equation A.4 to describe the beam energy dependence of the cross section, with $E_{beam}(x)$ given by equation A.3, equation A.1 can be rearranged to give the cross section at the incident beam energy

$$\sigma_0 = \frac{AN_\pi}{\rho x_t N_a N_b} = \frac{\sigma_{thin}}{I} \qquad A.5$$

where σ_{thin} is the cross section calculated by ignoring energy loss in the target and the dimensionless quantity

$$I = \frac{\int_0^{x_t} \exp \left[\frac{-\int_0^x \left[\frac{dE}{dx'}\right] dx'}{E_\sigma} \right] dx}{x_t} \qquad A.6$$

which is a function of the target material, the charge and velocity of the projectile, the target thickness, and E_σ has been defined for notational convenience. The simplest approximation is to assume that dE/dx is constant throughout the target, then equation A.6 can be rewritten as

$$I \simeq \frac{E_\sigma}{\Delta E_t} \left[1 - \exp (-\Delta E_t / E_\sigma) \right] \qquad A.7$$

where ΔE_t is the energy loss of the beam in the target.

Now, try method B. That is, correct the beam energy so that it corresponds to the beam energy at which the cross section is equal to the cross section calculated with the thin target formula (equation A.2). This effective beam energy can be found by equating σ_{thin} and $\sigma(E_e)$, where E_e is the effective beam energy and $\sigma(E_e)$ is given by equation A.4.

$$\sigma(E_e) = \exp\left[(E_e - E_0)/E_\sigma \right] = \sigma_{thin} \qquad A.8$$

Next, use equation A.5 to replace σ_0 with σ_{thin}/I and solve for the effective beam energy

$$E_e = E_0 + E_\sigma \ln(I) \qquad A.9$$

The same dimensionless factor I, defined in equation A.7, is used in methods A and B. It ranges from 0 for $E_\sigma = 0$ (a cross section rising at an infinite rate with the beam energy) to 1 for $E_\sigma \rightarrow \infty$ (a cross section independent of beam energy). Since I is always between 0 and 1, σ_0, the cross section estimated (with eq. A.5) at the incident beam energy, will always be greater than or equal to the cross section calculated with the thin target formula. Similarly, this range of values of I means that the effective beam energy calculated with equation A.9 is always less than or equal to the incident beam energy.

Method B (eq. A.9) has been used to calculate the effective beam energies for each beam energy and target combination studied with the lead slit spectrometer. These energies have been used in the main body of this thesis along with the differential cross sections calculated with the thin target formula (eq. A.2). The parameter E_σ, which specifies the slope of the cross section as a function of beam energy, was evaluated from the uncorrected data. In principle, the corrections could be estimated with this value of E_σ and then an improved value of E_σ could be found from the corrected data and an improved correction could be made. However, the second iteration did not have a significant effect in the case of these data. The effective beam energy is most poorly determined at the lowest beam energy because it was not possible to determine E_σ as accurately since it is

at one extreme of the data and because the correction is largest for the lower beam energies. For this reason, a relatively large uncertainty (10 MeV per nucleon) has been associated with the 80 MeV per nucleon effective beam energy.

APPENDIX B

Data Tables from the Lead Slit Spectrometer

Table B.1 Ne + NaF → π + X Data, Benenson *et al.*

T_{beam}/A	p_π	θ_π	$E_\pi \frac{d^3\sigma}{dp_\pi^3}$ $\frac{nb\ c^3}{sr\ MeV^2}$				$R(\pi^-/\pi^+)$	
MeV	MeV/c	deg.	π^-	±	π^+	±	R	±
80.	103.	0.	1.19	0.38	1.78	0.40	0.67	0.24
80.	134.	0.	0.76	0.37	1.23	0.37	0.62	0.34
80.	164.	0.	0.45	0.20	0.92	0.23	0.49	0.22
110.	103.	0.	13.2	3.3	8.8	2.1	1.50	0.40
110.	134.	0.	12.9	3.7	12.3	3.6	1.05	0.37
110.	164.	0.	9.0	2.9	8.2	2.0	1.11	0.39
110.	222.	0.	--	--	0.0	2.6	--	--
110.	259.	0.	--	--	0.84	1.11	--	--
164.	103.	0.	82.5	15.3	30.6	7.7	2.69	0.56
164.	134.	0.	67.0	14.0	57.7	12.5	1.16	0.25
164.	164.	0.	50.6	13.3	63.9	12.5	0.79	0.19
164.	222.	0.	16.7	6.2	30.2	10.4	0.55	0.23
164.	259.	0.	14.6	5.6	21.4	7.4	0.68	0.26
219.	103.	0.	357.	56.	74.	12.	4.82	0.38
219.	134.	0.	310.	48.	173.	26.	1.79	0.09
219.	164.	0.	256.	39.	208.	32.	1.23	0.04
219.	222.	0.	191.	40.	158.	32.	1.20	0.09
219.	259.	0.	114.	29.	132.	34.	0.86	0.05
219.	103.	7.5	--	--	86.	19.	--	--
219.	134.	7.5	--	--	171.	31.	--	--
219.	164.	7.5	--	--	157.	25.	--	--
219.	222.	7.5	--	--	146.	32.	--	--
219	259.	7.5	--	--	123.	32.	--	--
219.	103.	15.	306.	48.	92.	15.	3.33	0.31
219.	134.	15.	310.	39.	166.	26.	1.87	0.14
219.	164.	15.	192.	32.	176.	27.	1.09	0.08
219.	222.	15.	126.	27.	145.	31.	0.87	0.10
219.	259.	15.	69.	32.	112.	29.	0.62	0.07
219.	103.	22.5	--	--	107.	27.	--	--
219.	134.	22.5	--	--	171.	31.	--	--
219.	164.	22.5	--	--	162.	25.	--	--
219.	222.	22.5	--	--	128.	29.	--	--
219.	259.	22.5	--	--	88.	24.	--	--
219.	103.	30.	215.	35.	107.	19.	2.00	0.17
219.	134.	30.	215.	34.	180.	28.	1.20	0.08
219.	164.	30.	200.	33.	178.	26.	1.12	0.08
219.	222.	30.	175.	36.	207.	43.	0.84	0.07
219.	259.	30.	83.	21.	127.	32.	0.65	0.06

Table B.1 Ne + NaF → π + X Data, Benenson et al.

T_{beam}/A	p_π	θ_π	$E_\pi \frac{d^3\sigma}{dp_\pi^3}$ $\frac{nb\ c^3}{sr\ MeV^2}$				$R(\pi^-/\pi^+)$	
MeV	MeV/c	deg.	π^-	±	π^+	±	R	±
383.	98.	0.	1860.	292.	605.	104.	3.08	0.24
383	103.	0.	1780.	270.	401.	63.	4.43	0.17
383.	108.	0.	1890.	285.	510.	80.	3.70	0.20
383.	118.	0.	2210.	341.	401.	62.	5.53	0.30
383.	130.	0.	3790.	576.	420.	65.	9.03	0.35
383.	134.	0.	3820.	577.	385.	61.	9.92	0.52
383.	164.	0.	1720.	252.	691.	105.	2.49	0.06
383.	222.	0.	1410.	281.	1000.	209.	1.40	0.05
383.	259.	0.	1660.	420.	1410.	353.	1.17	0.04

Table B.2 Ne + Cu → π + X Data, Benenson et al.

T_{beam}/A	p_π	θ_π	$E_\pi \frac{d^3\sigma}{dp_\pi^3}$ $\frac{nb\ c^3}{sr\ MeV^2}$				$R(\pi^-/\pi^+)$	
MeV	MeV/c	deg.	π^-	±	π^+	±	R	±
214.	103.	0.	660.	102.	183.	33.	3.62	0.38
214.	134.	0.	635.	98.	351.	58.	1.81	0.14
214.	164.	0.	510.	87.	386.	59.	1.32	0.10
214.	222.	0.	261.	55.	253.	62.	1.03	0.11
214.	259.	0.	214.	56.	190.	49.	1.13	0.11
377.	103.	0.	3730.	575.	998.	152.	3.74	0.13
377.	108.	0.	4060.	621.	1120.	176.	3.63	0.19
377.	130.	0.	5340.	801.	996.	152.	5.36	0.17
377.	134.	0.	4800.	734.	1060.	160.	4.52	0.16
377.	164.	0.	2810.	439.	1400.	226.	2.01	0.14
377.	222.	0.	2220.	448.	1600.	322.	1.38	0.06
377.	259.	0.	2450.	615.	2060.	516.	1.19	0.04

Table B.3 Ne + U → π + X Data, Benenson et al.

T_{beam}/A	p_π	θ_π	$E_\pi \frac{d^3\sigma}{dp_\pi^3}$ $\frac{nb\ c^3}{sr\ MeV^2}$				$R(\pi^-/\pi^+)$	
MeV	MeV/c	deg.	π^-	±	π^+	±	R	±
118.	103.	0.	77.	42.	27.	21.	2.85	2.74
118.	134.	0.	78.	31.	9.	55.	8.33	48.7
118.	164.	0.	41.	19.	45.	20.	0.91	0.54
118.	222.	0.	--	--	0.	16.	--	--
118.	259.	0.	--	--	2.	13.	--	--
172.	103.	0.	575.	128.	144.	71.	4.00	2.01
172.	134.	0.	577.	117.	125.	94.	4.62	3.52
172.	164.	0.	359.	66.	240.	64.	1.50	0.37
226.	103.	0.	1920.	327.	326.	90.	5.90	1.46
226.	134.	0.	1700.	281.	655.	117.	2.59	0.32
226.	164.	0.	1400.	226.	799.	226.	1.75	0.44
226.	222.	0.	605.	136.	437.	104.	1.38	0.24
226.	259.	0.	512.	140.	401.	112.	1.28	0.19
226	103.	15.	--	--	197.	92.	--	--
226.	134.	15.	--	--	605.	145.	--	--
226.	164.	15.	--	--	457.	100.	--	--
226.	103.	30.	--	--	290.	75.	--	--
226.	134.	30.	--	--	368.	94.	--	--
226.	164.	30.	--	--	347.	67.	--	--
381.	98.	0.	11800.	1790.	2150.	292.	5.49	4.53
381.	103.	0.	9810.	1510.	1810.	290.	5.42	0.34
381.	108.	0.	10100.	1540.	2140.	354.	4.70	0.30
381.	118.	0.	--	--	1940.	310.	--	--
381.	130.	0.	--	--	1950.	311.	--	--
381.	134.	0.	10200.	1570.	2110.	329.	4.84	0.29
381.	164.	0.	6430.	1110.	2240.	387.	2.88	0.35
381.	222.	0.	5030.	1020.	2620.	540.	1.92	0.11
381.	259.	0.	5170.	1290.	3310.	1020.	1.56	0.29

APPENDIX C

Pion Reaction Cross Section Formula

All of the corrections for the reactions of pions with nuclei in this thesis were based on a parameterization of the cross section given in A.S. Carroll et al.[45] Because the definitions of some of the parameters in the original reference were slightly confusing and because, as a result, the formula used here may not exactly correspond to the intentions of the authors, the equations used here will be defined as explicitly as possible. It should be noted that any disagreement between the cross sections predicted by the formulas used here and those of the original authors is small. The confusion in interpreting the equation stems from two sources. First, the parameter μ is never defined and second, the symbol Γ_1 has two related, but different definitions. Here, μ has been defined as the reduced mass of the pion-nucleus system ($\mu = m_\pi M/(M_\pi+M)$, with M=the mass of the nucleus). It is possible, if not probable, that the mass of the pion was the intended definition. Because the masses of the nuclei involved are much larger than the pion mass, the difference between the two interpretations is very small ($\sim$1%). The confusion in the definition of Γ_1 stems from the fact that, when used in the cross section formula, it is a function of pion momentum, but when its value is given, the symbol refers to the value of Γ_1 at a particular momentum. The exact form of the equation used in the present analysis follows.

$$\sigma_{tot} = \frac{2\pi\Gamma_1}{k^2 E_1}\left\{\tan^{-1}\left[\frac{E_0+E_1 L_{max}^2-E}{\Gamma/2}\right] - \tan^{-1}\left[\frac{E_0-E}{\Gamma/2}\right]\right\} \qquad B.1$$

where the kinematic quantities (all in the CM) are

$$k = \left[(T_\pi+\mu)^2 - \mu^2\right]^{1/2}/\hbar c$$

T_π = pion kinetic energy

$$E = T_\pi + m_\pi + m$$

$$\mu = m_\pi M/(M+m_\pi)$$

m_π = pion mass

M = mass of nucleus

m = nucleon mass (931.5 MeV)

$L_{max} = kR + 1$

$R = (1.20\text{fm})\ A^{1/3}$

and the parameters used in the fit to the data are

$E_0 = 1227\ \text{MeV} - (16\ \text{MeV})A^{1/3}$

$E_1 = (15\ \text{MeV})A^{-2/3}$

$$c = \hbar c \frac{-67\ \text{MeV} + (54\ \text{MeV})A^{1/3}}{\left[(E_0 - m_\pi + \mu - m)^2 - \mu^2 \right]^{1/2}}$$

$\Gamma_1 = ck$

$\Gamma_2 = -9\ \text{MeV} + (55\ \text{MeV})A^{1/3}$

$\Gamma = \Gamma_1 + \Gamma_2$

As an example, this formula has been evaluated for pion momenta between 50 and 300 MeV/c for reactions with carbon nuclei. The results are shown in the table below.

p_π MeV/c	σ_{tot} mbarn
50.	155.1
100.	213.2
150.	344.2
200.	530.3
250.	665.4
300.	673.1

The parameters for the πC reaction cross section used above were

$E_0 = 1190.4\ \text{MeV}$

$E_1 = 2.862\ \text{MeV}$

$c = 51.52\ \text{MeV fm}$

$\Gamma_2 = 116.92\ \text{MeV}$

$R = 3.19$ fm

There is another problem with this formula -- the cross section does not approach zero as the pion momentum approaches zero. Instead, it becomes infinite. This divergence is due to the k^{-1} ($\Gamma_1/k^2 = c/k$) dependence of the factor which multiplies the $\tan^{-1}$ terms. This unusual behavior is caused by an approximation used to derive the formula. A sum over partial waves from 0 to L_{max} was approximated with an integral in order to put the expression in the form used here. For small values of momentum, only one or two partial waves contribute and this approximation is no longer valid. As demonstrated by figure 7, the problem is not serious above $\simeq$ 50 Mev/c.

APPENDIX D

Equations Related to the Resolution

The effects of the resolution of the spectrometer were treated by folding the resolution of the spectrometer into the theoretical curves when they were compared to the data. This method was chosen because the procedure is relatively simple and does not involve any assumptions which are not easily justified. The alternative would be to attempt to correct the data for the effects of the resolution. To do this, it would be necessary to assume some analytic expression to describe the data. The correction would then depend on this expression. A related problem would be to separate statistical fluctuations from true peaks and valleys. For these reasons, the resolution was folded into the theoretical curves rather than attempting to correct the data. Except for the regions of momentum and angle close to the projectile velocity peaks and valleys in the pion spectra, the spectrometer resolution did not have a significant effect on the observed data.

The discussion which follows is expressed in terms of the "true" cross section and the "measured" cross section. The "true" cross section refers to the cross section which would be observed with infinitely good resolution. For practical applications it refers to the theoretical expression for the cross section which is compared to the data. The "measured" cross section refers to the "true" cross section after it has been smeared by the resolution. Similarly, the expressions "initial" and "final" momentum are used. The "initial" momentum refers to the "true" momentum of the particle and the "final" momentum refers to the "measured" momentum of the particle, which may differ from the "initial" momentum due to the finite resolution of the spectrometer. Similar definitions have been used for the "initial" and "final" angle. The "error" in the angle or momentum refers to the difference between their "initial" and "final" values. The symbols used for these various quantities are

σ_{true} = the true or theoretical differential cross section

σ_{meas} = the measured differential cross section

θ_i = the true angle, before resolution effects

θ_f = the measured angle, after resolution effects

p_i = the true momentum

p_f = the measured momentum

$q = p_i - p_f$

$\cos\alpha = \vec{p_i} \cdot \vec{p_f} / (p_i p_f)$

The angular resolution was expressed in terms of a Gaussian function of the scattering angle α

$$g(\alpha)\,\sin\alpha\,d\alpha\,d\beta \simeq g(\alpha)\,\alpha\,d\alpha\,d\beta \qquad D.1$$

$$= \frac{\exp(-\alpha^2/\theta_0^2)}{\pi\theta_0^2}\,\alpha\,d\alpha\,d\beta$$

where the angle α is measured relative to the direction of the pion momentum vector, β is the azimuthal angle, and θ_0 is the rms value of α. The small angle approximation has been used to replace $\sin\alpha$ with α. The normalization of this function is

$$\frac{1}{\pi\theta_0^2}\int_0^{2\pi} d\beta \int_0^{\pi} \alpha\,d\alpha\,\exp(-\alpha^2/\theta_0^2) \simeq \frac{2}{\theta_0^2}\int_0^{\infty} \alpha\,d\alpha\,\exp(-\alpha^2/\theta_0^2) \qquad D.2$$

$$\simeq 1$$

where the assumption that large values of α do not contribute significantly to the integral has been used to change the upper limit on α from π to ∞.

The momentum resolution function was also assumed to be Gaussian. The form used was

$$f(q)\,dq = \frac{\exp(-q^2/2\sigma_p^2)}{\sqrt{2\pi}\,\sigma_p}\,dq \qquad D.3$$

where q is the difference between the true momentum and the measured momentum and σ_p is the rms value of q. The normalization of this

function is

$$\frac{1}{\sqrt{2\pi}\,\sigma_p}\int_{-\infty}^{\infty}\exp(-q^2/2\sigma_p^2)\,dq = 1 \qquad \text{D.4}$$

The error in the pion angle (α) is measured relative to the pion momentum vector. To express this difference between the true and calculated angle of the pion in the lab coordinate system, a coordinate transformation (rotation through θ, where θ is the lab angle of the pion) is necessary. After this rotation, the lab angle of the pion is given by

$$\sin^2\theta_i = \frac{p_x^2 + p_y^2}{p^2} = \frac{p_\perp^2}{p^2} \qquad \text{D.5}$$

$$= \sin^2\alpha\sin^2\beta + [\sin\alpha\cos\beta\cos\theta_f - \cos\alpha\sin\theta_f]^2$$

The observed cross section at some p and θ will be, for the resolution functions used here

$$\sigma_{meas}\begin{bmatrix} p_f \\ \theta_f \end{bmatrix} = \int_0^{2\pi} d\beta \int_0^{\infty} \alpha\, d\alpha\, g(\alpha) \int_{-\infty}^{\infty} dq\, f(q)\, \sigma_{true}\begin{bmatrix} p_f+q \\ \theta_i(\alpha,\beta,\theta_f) \end{bmatrix} \qquad \text{D.6}$$

where $g(\alpha)$, $f(q)$, and θ_i are given by equations D.1, D.3, and D.5, respectively.

As a simple example which illustrates the important properties of these expressions, they have been applied to the case of a Gaussian peak centered at zero degrees and a lab momentum p_0.

$$\sigma_{true} = N \exp\left[-\frac{p_\perp^2}{\Gamma_\perp^2} - \frac{(p_\parallel - p_0)^2}{2\,\Gamma_\parallel^2}\right] \qquad \text{D.7}$$

Given this form of the "true" cross section, that is the cross section which would be observed with infinitely good resolution, the measured cross section would be

$$\sigma_{meas} = N' \exp\left[-\frac{p_\perp^2}{\sigma_\perp^2 + \Gamma_\perp^2} - \frac{(p_\parallel - p_0)^2}{2(\sigma_\parallel^2 + \Gamma_\parallel^2)}\right] \qquad \text{D.8}$$

where

$$N' = \frac{N}{(1+\sigma_\perp^2/\Gamma_\perp^2)\,(1+\sigma_\parallel^2/\Gamma_\parallel^2)^{1/2}} \qquad \text{D.9}$$

and

$$\sigma_{\perp} = p_0 \sin\theta_0$$

In this case, the resolution adds quadratically to the width of the peak in each direction and the height of the peak is reduced by a factor which is a function of the ratios of the resolution to the width of the peak in each direction. This expression only applies at zero degrees, where equation D.5 reduces to a simpler expression, but it demonstrates the qualitative effect of the resolution on the observed spectra.

APPENDIX E

Data Tables from the Upgraded Spectrometer

TABLE E.1	Ne+C → π^- + X E/A = 280 MeV					$Ed^3\sigma/dp^3$ $\mu b\ c^3/(sr\ MeV^2)$
P_π MeV/c	θ_π lab. degrees 0	4	8	12	16	20
89	--	.22 ±.05	.24 ±.05	.20 ±.04	--	--
92	.35 ±.05	.50 ±.06	.27 ±.04	.32 ±.05	.28 ±.04	--
96	.52 ±.06	.36 ±.05	.36 ±.05	.33 ±.05	.31 ±.04	.27 ±.04
99	.49 ±.06	.47 ±.03	.38 ±.05	.29 ±.04	.23 ±.03	.20 ±.03
102	.78 ±.08	.62 ±.04	.46 ±.05	.33 ±.04	.28 ±.04	.22 ±.03
105	.94 ±.09	.75 ±.04	.38 ±.03	.34 ±.04	.24 ±.03	.19 ±.03
109	1.11 ±.10	.83 ±.04	.46 ±.03	.30 ±.04	.36 ±.04	--
112	1.29 ±.10	.82 ±.04	.45 ±.03	.36 ±.04	.33 ±.04	--
115	1.13 ±.09	.72 ±.04	.36 ±.03	.30 ±.02	--	--
119	.83 ±.07	.64 ±.03	.40 ±.03	.29 ±.03	--	--
122	.69 ±.06	.48 ±.03	.37 ±.03	.27 ±.03	--	--
125	.44 ±.04	.51 ±.03	.37 ±.03	.25 ±.03	.26 ±.03	--
129	.48 ±.05	.49 ±.03	.37 ±.03	.32 ±.03	.26 ±.02	--
132	.41 ±.04	.34 ±.03	.29 ±.03	.31 ±.03	.24 ±.02	--
135	.43 ±.05	.36 ±.03	.31 ±.03	.27 ±.03	.22 ±.02	--
139	--	--	.29 ±.04	.24 ±.02	.22 ±.02	.22 ±.02
142	--	--	--	--	.17 ±.02	.19 ±.02

TABLE E-2 $Ne+NaF \rightarrow \pi^- + X$ E/A = 281 MeV $Ed^3\sigma/dp^3$ $\mu b\ c^3/(sr\ MeV^2)$

p_π MeV/c	θ_π lab. degrees 0	4	8	12	16	20
89	.44 ±.10	.43 ±.08	.45 ±.08	.37 ±.06	--	--
92	.53 ±.08	.74 ±.08	.59 ±.07	.51 ±.07	.54 ±.07	.24 ±.04
96	.74 ±.09	.64 ±.07	.66 ±.07	.65 ±.08	.48 ±.06	.51 ±.07
99	.91 ±.09	.73 ±.05	.77 ±.08	.52 ±.06	.50 ±.06	.37 ±.05
102	1.03 ±.10	.93 ±.05	.80 ±.08	.60 ±.07	.48 ±.06	.33 ±.05
105	1.42 ±.13	1.13 ±.06	.79 ±.08	.62 ±.06	.41 ±.05	.33 ±.04
109	1.62 ±.14	1.22 ±.06	.79 ±.05	.42 ±.05	.47 ±.06	--
112	1.86 ±.14	1.19 ±.06	.72 ±.05	.65 ±.06	.58 ±.06	--
115	1.47 ±.12	1.16 ±.06	.64 ±.04	.58 ±.04	--	--
119	1.30 ±.11	.96 ±.05	.71 ±.05	.47 ±.05	--	--
122	1.12 ±.10	.80 ±.04	.61 ±.04	.49 ±.04	--	--
125	.82 ±.07	.89 ±.05	.59 ±.05	.43 ±.04	.38 ±.04	--
129	.64 ±.06	.83 ±.05	.51 ±.05	.51 ±.05	.44 ±.04	--
132	.56 ±.05	.65 ±.05	.52 ±.04	.50 ±.04	.39 ±.04	--
135	.61 ±.07	.58 ±.05	.49 ±.04	.45 ±.04	.39 ±.03	.36 ±.03
139	--	--	.41 ±.05	.40 ±.03	.33 ±.03	.38 ±.03
142	--	--	--	--	.23 ±.03	.30 ±.02

TABLE E.3	Ne+Cu → π^- + X E/A = 282 MeV					$Ed^3\sigma/dp^3$ $\mu b\ c^3/(sr\ MeV^2)$
p_π	θ_π lab. degrees					
MeV/c	0	4	8	12	16	20
91	1.12 ±.20	1.61 ±.20	1.02 ±.16	1.10 ±.17	1.06 ±.16	.66 ±.13
96	1.74 ±.21	1.07 ±.16	1.53 ±.17	1.30 ±.16	1.23 ±.15	.93 ±.14
101	1.71 ±.20	1.90 ±.12	1.68 ±.18	1.36 ±.15	1.19 ±.15	1.09 ±.13
106	2.54 ±.25	2.20 ±.14	1.48 ±.11	1.32 ±.14	1.06 ±.13	1.06 ±.14
111	2.98 ±.25	2.32 ±.13	1.64 ±.12	1.50 ±.15	1.18 ±.14	--
116	2.59 ±.23	1.99 ±.12	1.30 ±.10	1.24 ±.10	--	--
121	1.97 ±.20	1.56 ±.10	1.48 ±.11	1.20 ±.11	--	--
126	1.57 ±.16	1.63 ±.10	1.31 ±.13	1.04 ±.11	.82 ±.09	--
131	1.33 ±.14	1.30 ±.12	.96 ±.11	1.21 ±.11	1.04 ±.10	--
136	1.39 ±.21	1.07 ±.13	1.10 ±.10	.85 ±.10	.73 ±.08	.71 ±.07
141	--	--	--	1.26 ±.16	.68 ±.09	.65 ±.06

TABLE E.4 — Ne+C → π^+ + X, E/A = 280 MeV — $Ed^3\sigma/dp^3$ μb $c^3/(sr\ MeV^2)$

p_π MeV/c	θ_π lab. degrees 0	4	8	12	16	20
92	.055 ±.013	.071 ±.016	.071 ±.012	.092 ±.012	.079 ±.017	--
96	.048 ±.010	.032 ±.007	.081 ±.011	.103 ±.014	.106 ±.016	.093 ±.018
101	.010 ±.017	.056 ±.007	.074 ±.013	.074 ±.011	.100 ±.015	.120 ±.015
106	.052 ±.013	.058 ±.007	.050 ±.009	.075 ±.011	.115 ±.013	.091 ±.014
111	.014 ±.013	.030 ±.008	.068 ±.008	.080 ±.014	.149 ±.014	--
116	.020 ±.011	.042 ±.006	.076 ±.006	.109 ±.008	--	--
121	.029 ±.013	.057 ±.006	.081 ±.008	.086 ±.011	--	--
126	.057 ±.009	.076 ±.008	.100 ±.011	.122 ±.013	.124 ±.009	--
131	.071 ±.012	.094 ±.009	.094 ±.012	.120 ±.014	.141 ±.011	--
136	.141 ±.015	.078 ±.013	.123 ±.010	.126 ±.011	.108 ±.010	.118 ±.010
141	--	--	--	.131 ±.018	.113 ±.010	.129 ±.009

TABLE E.5	Ne+NaF → π^+ + X E/A = 281 MeV					$Ed^3\sigma/dp^3$ $\mu b\ c^3/(sr\ MeV^2)$
p_π	θ_π lab. degrees					
MeV/c	0	4	8	12	16	20
91	.074 ±.023	.068 ±.026	.105 ±.021	.157 ±.023	.120 ±.030	--
96	.088 ±.019	.056 ±.018	.105 ±.019	.154 ±.025	.130 ±.026	.162 ±.033
101	.022 ±.028	.087 ±.012	.091 ±.022	.134 ±.021	.169 ±.028	.205 ±.028
106	.052 ±.020	.106 ±.012	.111 ±.022	.157 ±.022	.183 ±.023	.168 ±.027
111	.050 ±.023	.073 ±.014	.111 ±.014	.128 ±.024	.176 ±.021	--
116	.064 ±.021	.091 ±.012	.134 ±.011	.170 ±.015	--	--
121	.101 ±.024	.116 ±.011	.145 ±.015	.159 ±.019	--	--
126	.095 ±.017	.121 ±.015	.153 ±.020	.170 ±.021	.190 ±.017	--
131	.107 ±.021	.141 ±.016	.128 ±.020	.152 ±.023	.202 ±.019	.133 ±.015
136	.222 ±.028	.168 ±.024	.201 ±.019	.179 ±.019	.187 ±.018	.189 ±.018
141	--	--	--	.188 ±.031	.182 ±.018	.190 ±.015

TABLE E.6 — Ne+Cu → π^+ + X, E/A = 282 MeV, $Ed^3\sigma/dp^3$ μb $c^3/(sr\ MeV^2)$

p_π MeV/c	θ_π lab. degrees 0	4	8	12	16	20
91	.220 ±.086	.112 ±.097	.335 ±.078	.463 ±.080	.341 ±.115	--
96	.359 ±.081	.163 ±.071	.429 ±.077	.369 ±.086	.396 ±.101	.301 ±.115
101	.076 ±.115	.366 ±.050	.351 ±.089	.369 ±.076	.553 ±.107	.417 ±.089
106	.239 ±.086	.348 ±.048	.313 ±.061	.363 ±.076	.421 ±.077	.350 ±.091
111	.187 ±.095	.275 ±.056	.377 ±.055	.266 ±.087	.466 ±.072	--
116	.262 ±.086	.248 ±.046	.289 ±.036	.455 ±.052	--	--
121	.266 ±.093	.383 ±.043	.377 ±.053	.355 ±.069	--	--
126	.289 ±.064	.372 ±.057	.435 ±.074	.454 ±.079	.443 ±.056	--
131	.361 ±.081	.418 ±.061	.359 ±.078	.313 ±.086	.439 ±.066	--
136	.553 ±.089	.161 ±.080	.383 ±.060	.419 ±.067	.378 ±.062	.398 ±.063
141	--	--	--	.478 ±.114	.331 ±.060	.391 ±.054

TABLE E.7 — $Ne+NaF \rightarrow \pi^- + X$ — $E/A = 380$ MeV — $Ed^3\sigma/dp^3$ $\mu b\ c^3/(sr\ MeV^2)$

P_π MeV/c	θ_π lab. degrees 0	4	8	12	16	20
106	1.14 ±.17	.88 ±.07	1.07 ±.09	.91 ±.08	.87 ±.09	.54 ±.07
110	1.21 ±.11	1.05 ±.08	.77 ±.07	.89 ±.08	.81 ±.08	.80 ±.08
113	1.21 ±.10	1.07 ±.07	.97 ±.08	.81 ±.07	.76 ±.08	.71 ±.08
117	1.33 ±.06	1.22 ±.04	1.04 ±.05	.95 ±.05	.77 ±.04	.68 ±.04
121	1.53 ±.06	1.34 ±.04	1.08 ±.04	.92 ±.04	.85 ±.04	.85 ±.04
125	1.82 ±.07	1.50 ±.03	1.13 ±.04	.91 ±.03	.82 ±.03	.80 ±.03
129	2.26 ±.07	1.66 ±.03	1.14 ±.03	.98 ±.03	.79 ±.03	.75 ±.03
133	2.62 ±.07	1.73 ±.03	1.03 ±.03	.98 ±.03	.87 ±.03	.83 ±.04
137	2.53 ±.08	1.63 ±.03	.98 ±.02	.87 ±.03	.86 ±.04	--
141	2.04 ±.06	1.46 ±.03	1.02 ±.02	.94 ±.03	.83 ±.03	.71 ±.06
145	1.61 ±.05	1.28 ±.02	1.00 ±.02	.87 ±.03	.77 ±.04	.80 ±.07
149	1.48 ±.05	1.25 ±.03	.94 ±.02	.81 ±.02	.77 ±.03	--
153	1.21 ±.04	1.09 ±.02	.90 ±.02	.84 ±.03	.84 ±.04	.60 ±.06
157	1.03 ±.04	.97 ±.03	.87 ±.02	.78 ±.03	.73 ±.04	.62 ±.06
161	1.03 ±.06	.91 ±.04	.75 ±.03	.67 ±.03	.70 ±.05	.61 ±.04
165	.90 ±.05	.98 ±.03	.82 ±.03	.70 ±.03	.67 ±.02	.69 ±.04
169	.90 ±.04	.84 ±.02	.76 ±.02	.70 ±.02	.65 ±.02	.63 ±.04
174	.85 ±.04	.78 ±.03	.72 ±.03	.69 ±.03	.62 ±.03	--
178	.64 ±.05	.79 ±.04	.75 ±.03	.63 ±.03	.60 ±.02	.48 ±.02
182	.67 ±.05	.73 ±.04	.70 ±.04	.60 ±.04	.54 ±.02	.61 ±.02
189	.72 ±.09	.77 ±.06	.71 ±.05	.61 ±.05	.51 ±.04	--

TABLE E.8 — Ne+Cu → π^- + X, E/A = 382 MeV — $Ed^3\sigma/dp^3$ μb $c^3/(sr\ MeV^2)$

p_π MeV/c	θ_π lab. degrees 0	4	8	12	16	20
105	1.20 ±.27	2.03 ±.24	1.79 ±.23	1.97 ±.25	1.39 ±.23	1.16 ±.22
109	1.90 ±.27	1.73 ±.20	1.99 ±.23	2.04 ±.25	2.04 ±.26	2.14 ±.29
113	2.44 ±.28	2.47 ±.24	1.86 ±.22	1.66 ±.20	1.49 ±.21	1.83 ±.24
117	2.59 ±.29	2.04 ±.13	1.97 ±.18	1.91 ±.18	1.54 ±.16	1.46 ±.16
120	2.91 ±.23	2.18 ±.12	1.85 ±.15	2.17 ±.18	1.65 ±.16	1.75 ±.17
124	2.50 ±.19	2.16 ±.11	2.09 ±.16	1.72 ±.15	1.59 ±.14	1.65 ±.16
128	3.07 ±.22	2.40 ±.11	2.07 ±.12	1.57 ±.14	1.55 ±.13	2.00 ±.22
132	3.65 ±.23	2.56 ±.11	1.90 ±.11	1.61 ±.13	1.66 ±.15	1.68 ±.24
136	3.65 ±.23	2.53 ±.11	1.73 ±.10	1.61 ±.10	1.87 ±.22	--
140	2.93 ±.21	2.20 ±.11	1.74 ±.09	1.87 ±.12	--	--
144	2.29 ±.18	2.07 ±.10	1.73 ±.10	1.61 ±.12	--	--
148	2.33 ±.19	2.10 ±.11	1.68 ±.11	1.41 ±.12	1.35 ±.13	--
152	1.78 ±.16	1.78 ±.10	1.46 ±.10	1.49 ±.11	1.35 ±.13	--
156	1.59 ±.15	1.64 ±.11	1.62 ±.11	1.55 ±.12	1.34 ±.12	--
160	2.16 ±.23	1.69 ±.15	1.19 ±.12	1.08 ±.11	1.45 ±.12	1.07 ±.10
164	1.14 ±.23	1.83 ±.16	1.43 ±.13	1.24 ±.09	1.07 ±.10	1.15 ±.09
168	1.35 ±.21	1.51 ±.17	1.27 ±.16	1.19 ±.15	1.03 ±.09	1.16 ±.09
173	1.83 ±.35	1.29 ±.20	1.52 ±.21	1.22 ±.18	1.12 ±.16	--
178	--	--	1.43 ±.29	1.30 ±.18	.86 ±.13	.80 ±.12
182	--	--	--	--	.80 ±.16	1.11 ±.14

TABLE E.9	Ne+U → π^- + X E/A = 385 MeV				Ed$^3\sigma$/dp^3 μb c^3/(sr MeV^2)	
P_π	θ_π lab. degrees					
MeV/c	0	4	8	12	16	20
106	4.59 ±.90	6.10 ±.77	6.17 ±.81	6.39 ±.89	6.38 ±.93	5.94 ±.96
112	6.73 ±.91	5.97 ±.75	5.15 ±.75	5.71 ±.75	5.31 ±.77	7.07 ±.91
118	8.19 ±.97	6.33 ±.48	5.43 ±.69	6.23 ±.76	5.51 ±.70	4.88 ±.71
124	6.49 ±.83	6.32 ±.48	4.44 ±.42	4.73 ±.62	4.06 ±.57	5.98 ±.84
130	9.36 ±.97	7.00 ±.52	5.63 ±.46	4.43 ±.60	5.87 ±.74	--
136	8.68 ±.92	5.42 ±.48	5.19 ±.43	4.25 ±.39	--	--
142	7.27 ±.84	4.94 ±.42	4.73 ±.42	4.37 ±.52	--	--
148	4.40 ±.69	5.85 ±.46	5.63 ±.60	4.25 ±.50	3.05 ±.44	--
154	3.97 ±.61	3.79 ±.48	5.01 ±.52	3.33 ±.46	3.76 ±.44	--
160	5.66 ±.93	4.17 ±.56	3.82 ±.44	3.26 ±.40	3.09 ±.39	3.06 ±.35
166	--	--	--	4.05 ±.75	3.34 ±.42	2.72 ±.30

TABLE E.10 — $Ne+NaF \rightarrow \pi^+ + X$, E/A = 380 MeV — $Ed^3\sigma/dp^3$ $\mu b\ c^3/(sr\ MeV^2)$

p_π MeV/c	θ_π lab. degrees 0	4	8	12	16	20
105	.20 ±.05	.19 ±.03	.22 ±.03	.30 ±.04	.26 ±.04	.24 ±.04
109	.21 ±.04	.20 ±.03	.26 ±.03	.27 ±.04	.34 ±.05	.36 ±.05
113	.21 ±.04	.16 ±.03	.25 ±.03	.26 ±.03	.29 ±.04	.32 ±.04
117	.17 ±.03	.15 ±.01	.24 ±.02	.32 ±.03	.33 ±.03	.33 ±.02
120	.19 ±.02	.16 ±.01	.22 ±.02	.28 ±.02	.34 ±.03	.33 ±.03
124	.12 ±.01	.16 ±.01	.21 ±.01	.28 ±.02	.30 ±.02	.37 ±.03
128	.14 ±.02	.16 ±.01	.22 ±.01	.29 ±.02	.35 ±.02	.35 ±.03
132	.14 ±.01	.16 ±.01	.22 ±.01	.28 ±.02	.39 ±.02	.41 ±.03
136	.13 ±.01	.16 ±.01	.23 ±.01	.31 ±.02	.41 ±.03	--
140	.14 ±.01	.19 ±.01	.24 ±.01	.33 ±.02	.43 ±.03	--
144	.19 ±.02	.17 ±.01	.27 ±.01	.29 ±.02	--	--
148	.19 ±.02	.20 ±.01	.28 ±.01	.31 ±.02	.32 ±.03	--
152	.18 ±.02	.23 ±.01	.30 ±.02	.34 ±.02	.36 ±.03	--
156	.23 ±.02	.26 ±.01	.30 ±.02	.35 ±.02	.38 ±.03	--
160	.32 ±.04	.28 ±.02	.30 ±.02	.31 ±.03	.37 ±.03	.34 ±.02
164	.28 ±.03	.30 ±.02	.30 ±.02	.32 ±.02	.36 ±.03	.41 ±.02
168	.30 ±.03	.31 ±.02	.35 ±.02	.38 ±.02	.35 ±.02	.37 ±.02
173	.34 ±.04	.33 ±.03	.35 ±.03	.36 ±.02	.43 ±.03	.25 ±.02
177	--	--	.35 ±.04	.36 ±.03	.37 ±.02	.31 ±.02

TABLE E.11 — $Ne+Cu \rightarrow \pi^+ + X$, E/A = 382 MeV, $Ed^3\sigma/dp^3$ in $\mu b\ c^3/(sr\ MeV^2)$

P_π MeV/c	θ_π lab. degrees 0	4	8	12	16	20
107	.61 ±.10	.61 ±.07	.71 ±.08	.77 ±.11	.83 ±.11	1.00 ±.12
113	.56 ±.10	.46 ±.07	.76 ±.09	.70 ±.09	.61 ±.10	.98 ±.11
119	.63 ±.08	.59 ±.04	.60 ±.07	.76 ±.08	.98 ±.09	.76 ±.11
125	.50 ±.07	.57 ±.04	.54 ±.05	.66 ±.07	.76 ±.08	1.00 ±.13
131	.45 ±.06	.61 ±.05	.58 ±.05	.72 ±.07	.99 ±.10	--
136	.40 ±.06	.61 ±.05	.55 ±.04	.77 ±.05	--	--
142	.55 ±.07	.56 ±.04	.66 ±.05	.69 ±.07	--	--
148	.52 ±.07	.60 ±.05	.65 ±.07	.69 ±.07	.69 ±.07	--
154	.58 ±.07	.63 ±.06	.66 ±.06	.85 ±.07	.90 ±.07	--
160	.61 ±.10	.64 ±.07	.82 ±.06	.68 ±.06	.81 ±.07	.80 ±.05
166	--	--	--	.64 ±.11	.80 ±.06	.90 ±.05

TABLE E.12 — $Ne+U \rightarrow \pi^- + X$ — E/A = 385 MeV — $Ed^3\sigma/dp^3$ $\mu b\ c^3/(sr\ MeV^2)$

P_π MeV/c	θ_π lab. degrees 0	4	8	12	16	20
106	1.73 ±.52	1.46 ±.33	1.73 ±.34	1.83 ±.52	1.64 ±.44	2.11 ±.41
112	.48 ±.47	.82 ±.35	1.66 ±.42	1.06 ±.36	1.63 ±.53	1.75 ±.38
118	1.27 ±.34	1.44 ±.19	1.87 ±.35	1.70 ±.36	1.77 ±.32	.28 ±.46
124	1.51 ±.35	1.16 ±.19	1.41 ±.29	1.90 ±.34	1.77 ±.32	2.46 ±.49
130	1.46 ±.32	1.67 ±.23	1.43 ±.23	1.80 ±.30	2.08 ±.42	--
136	1.69 ±.36	1.24 ±.25	1.66 ±.23	1.58 ±.34	--	--
142	1.78 ±.36	1.40 ±.21	1.59 ±.26	1.98 ±.36	--	--
148	2.09 ±.38	1.27 ±.26	1.76 ±.35	1.38 ±.36	1.38 ±.38	--
153	1.62 ±.40	1.48 ±.32	2.06 ±.35	2.04 ±.37	2.25 ±.34	--
159	1.74 ±.49	1.56 ±.35	1.87 ±.27	1.50 ±.34	1.16 ±.36	2.21 ±.28
165	--	--	--	--	1.81 ±.29	2.05 ±.25

TABLE E.13 — Ne+C → π^- + X, E/A = 405 MeV — $Ed^3\sigma/dp^3$ $\mu b\ c^3/(sr\ MeV^2)$

p_π MeV/c	θ_π lab. degrees 0	4	8	12	16	20	24	28	32
106	.76 ±.13	.82 ±.08	.58 ±.07	.60 ±.09	--	--	--	--	--
112	.70 ±.11	.81 ±.07	.71 ±.07	.67 ±.08	.59 ±.07	--	--	--	--
117	.69 ±.11	.85 ±.07	.57 ±.06	.48 ±.07	.58 ±.07	--	--	--	--
123	.76 ±.10	.98 ±.07	.87 ±.09	.63 ±.08	.64 ±.08	.51 ±.06	--	--	--
129	1.10 ±.13	.98 ±.07	.60 ±.07	.49 ±.07	.49 ±.06	.35 ±.05	.49 ±.06	--	--
134	1.17 ±.14	.93 ±.09	.79 ±.08	.57 ±.06	.54 ±.06	.52 ±.06	.53 ±.06	--	--
140	--	.65 ±.08	.50 ±.07	.47 ±.06	.46 ±.05	.51 ±.05	.43 ±.05	.45 ±.05	--
146	--	--	.32 ±.05	.55 ±.06	.49 ±.06	.55 ±.06	.45 ±.05	.48 ±.05	.46 ±.05
152	--	--	--	.44 ±.06	.51 ±.06	.51 ±.06	.54 ±.05	.45 ±.05	.43 ±.04
157	--	--	--	--	--	--	--	.39 ±.04	.44 ±.04

TABLE E-14 $Ne+NaF \rightarrow \pi^- + X$ E/A = 400 MeV $Ed^3\sigma/dp^3$ $\mu b\ c^3/(sr\ MeV^2)$

P_π MeV/c	θ_π lab. degrees 0	4	8	12	16	20	24	28	32
90	.58 ±.14	.52 ±.08	.46 ±.07	.55 ±.10	--	--	--	--	--
93	.62 ±.14	.73 ±.09	.76 ±.10	.57 ±.10	.59 ±.10	--	--	--	--
97	.72 ±.14	.81 ±.08	.77 ±.09	.64 ±.09	.65 ±.10	.64 ±.10	--	--	--
101	.84 ±.14	.89 ±.09	.80 ±.10	.67 ±.11	.73 ±.10	.70 ±.09	--	--	--
105	.86 ±.16	.98 ±.12	.83 ±.11	1.04 ±.12	.84 ±.10	.70 ±.09	.79 ±.09	--	--
109	.63 ±.13	1.03 ±.12	1.15 ±.13	.80 ±.10	.78 ±.10	.77 ±.10	.67 ±.09	--	--
113	1.07 ±.10	.98 ±.05	.94 ±.05	.82 ±.05	.79 ±.10	.59 ±.08	.70 ±.08	.71 ±.09	--
117	1.06 ±.09	1.14 ±.05	.93 ±.05	.81 ±.05	.83 ±.05	.78 ±.10	.82 ±.09	.61 ±.07	.61 ±.08
121	1.20 ±.10	1.10 ±.06	.86 ±.05	.78 ±.05	.81 ±.05	.76 ±.05	.78 ±.08	.73 ±.08	.55 ±.06
125	1.46 ±.14	1.17 ±.07	.66 ±.05	.91 ±.09	.78 ±.07	.82 ±.07	--	--	--
131	1.69 ±.15	1.51 ±.09	.84 ±.08	.84 ±.08	.78 ±.07	.67 ±.06	.69 ±.06	--	--
136	1.81 ±.14	1.35 ±.05	.93 ±.04	.69 ±.04	.71 ±.04	.77 ±.07	.63 ±.06	--	--
142	1.87 ±.26	.86 ±.08	.88 ±.08	.74 ±.06	.62 ±.05	.69 ±.05	.72 ±.06	.75 ±.06	--
147	1.32 ±.11	1.15 ±.06	.73 ±.04	.67 ±.04	.66 ±.04	.66 ±.06	.59 ±.05	.52 ±.05	.50 ±.05
153	1.14 ±.08	1.05 ±.04	.84 ±.05	.68 ±.04	.69 ±.04	.65 ±.03	.65 ±.05	.60 ±.05	.54 ±.04
159	.95 ±.06	.88 ±.04	.81 ±.04	.76 ±.04	.71 ±.04	.63 ±.04	.46 ±.05	.48 ±.04	.52 ±.04
169	.70 ±.08	.77 ±.06	.66 ±.05	.62 ±.05	.61 ±.05	.51 ±.05	.64 ±.05	--	--
176	--	.48 ±.05	.61 ±.05	.63 ±.05	.51 ±.04	.53 ±.04	.49 ±.04	.55 ±.04	--
184	--	--	.45 ±.05	.53 ±.05	.53 ±.04	.54 ±.04	.55 ±.04	.49 ±.04	--
191	--	--	--	.47 ±.05	.43 ±.04	.44 ±.04	.44 ±.04	.40 ±.03	--

TABLE E.15 — Ne+U → π^- + X, E/A = 407 MeV — $Ed^3\sigma/dp^3$ μb $c^3/(sr\ MeV^2)$

p_π MeV/c	θ_π lab. degrees 0	4	8	12	16	20	24	28	32
106	4.75 ±1.24	4.97 ±.74	4.19 ±.77	4.07 ±.91	--	--	--	--	--
112	4.48 ±1.14	4.48 ±.65	5.53 ±.73	5.11 ±.87	3.92 ±.72	--	--	--	--
117	4.55 ±1.11	3.97 ±.59	3.96 ±.64	3.21 ±.67	4.58 ±.81	2.91 ±.68	--	--	--
123	4.26 ±.90	3.93 ±.52	3.64 ±.71	4.11 ±.83	3.90 ±.73	3.45 ±.63	--	--	--
128	3.10 ±.83	5.87 ±.69	3.35 ±.69	3.07 ±.76	3.82 ±.66	2.31 ±.58	2.68 ±.60	--	--
134	3.25 ±.83	4.53 ±.76	4.51 ±.76	3.20 ±.58	2.67 ±.53	3.25 ±.61	2.88 ±.51	--	--
140	--	--	2.19 ±.60	3.46 ±.62	2.68 ±.50	2.57 ±.45	2.78 ±.49	2.05 ±.43	--
146	--	--	1.75 ±.53	2.75 ±.55	2.99 ±.56	2.54 ±.49	2.45 ±.44	2.75 ±.50	1.79 ±.44
151	--	--	--	--	2.66 ±.53	3.15 ±.57	2.01 ±.41	2.52 ±.44	2.29 ±.38
157	--	--	--	--	--	1.80 ±.53	2.10 ±.43	1.79 ±.37	2.49 ±.41

TABLE E.16 — $Ne+C \rightarrow \pi^+ + X$ — E/A = 405 MeV — $Ed^3\sigma/dp^3$ $\mu b\ c^3/(sr\ MeV^2)$

P_π MeV/c	θ_π lab. degrees 0	4	8	12	16	20	24	28	32
107	.35 ±.07	.18 ±.03	.23 ±.04	.41 ±.06	--	--	--	--	--
112	.14 ±.04	.17 ±.03	.19 ±.03	.26 ±.04	.20 ±.04	--	--	--	--
118	.12 ±.03	.16 ±.03	.16 ±.03	.17 ±.04	.32 ±.05	--	--	--	--
123	.11 ±.04	.16 ±.02	.16 ±.04	.30 ±.05	.32 ±.04	.26 ±.04	--	--	--
129	.07 ±.02	.13 ±.03	.20 ±.04	.31 ±.04	.25 ±.04	.29 ±.04	.34 ±.04	--	--
135	.10 ±.03	.17 ±.03	.24 ±.03	.22 ±.03	.27 ±.04	.34 ±.04	.38 ±.04	--	--
140	--	--	.25 ±.03	.22 ±.03	.23 ±.03	.23 ±.03	.31 ±.04	.33 ±.03	--
146	--	--	.21 ±.03	.29 ±.04	.33 ±.04	.29 ±.04	.34 ±.04	.35 ±.03	.41 ±.04
152	--	--	--	.24 ±.03	.24 ±.04	.38 ±.04	.36 ±.04	.33 ±.03	.35 ±.03
158	--	--	--	--	--	--	--	.34 ±.03	.31 ±.03

TABLE E.17 $Ne+NaF \rightarrow \pi^+ + X$ E/A = 400 MeV $Ed^3\sigma/dp^3$ $\mu b\ c^3/(sr\ MeV^2)$

P_π MeV/c	θ_π lab. degrees 0	4	8	12	16	20	24	28	32
94	.28 ±.07	.26 ±.05	.26 ±.05	.30 ±.06	.20 ±.07	--	--	--	--
99	.28 ±.08	.37 ±.05	.31 ±.05	.41 ±.06	.33 ±.06	.39 ±.06	--	--	--
104	.30 ±.07	.25 ±.04	.30 ±.05	.33 ±.07	.36 ±.06	.42 ±.07	.43 ±.06	--	--
109	.29 ±.04	.32 ±.03	.32 ±.03	.39 ±.04	.36 ±.06	.32 ±.05	.49 ±.07	--	--
115	.27 ±.05	.33 ±.03	.33 ±.03	.38 ±.04	.36 ±.06	.48 ±.06	.46 ±.06	.36 ±.06	--
120	.16 ±.03	.25 ±.03	.25 ±.03	.30 ±.03	.43 ±.04	.42 ±.05	.49 ±.05	.39 ±.06	.33 ±.04
126	.19 ±.04	.24 ±.02	.18 ±.02	.39 ±.05	.38 ±.04	.46 ±.04	.38 ±.05	.37 ±.05	.44 ±.04
131	.20 ±.02	.26 ±.02	.32 ±.02	.37 ±.03	.37 ±.04	.36 ±.04	.39 ±.04	--	--
137	.14 ±.02	.21 ±.01	.26 ±.02	.31 ±.02	.30 ±.04	.39 ±.04	.49 ±.04	--	--
143	.11 ±.03	.21 ±.02	.22 ±.02	.26 ±.02	.34 ±.02	.32 ±.03	.42 ±.04	.39 ±.03	--
148	.19 ±.03	.19 ±.02	.23 ±.02	.35 ±.03	.41 ±.03	.35 ±.02	.43 ±.04	.41 ±.03	.39 ±.03
154	--	--	--	.19 ±.03	.27 ±.04	.44 ±.04	.41 ±.04	.37 ±.03	.41 ±.03
160	.20 ±.02	.28 ±.02	.31 ±.02	.38 ±.03	.37 ±.02	.31 ±.02	.31 ±.03	.29 ±.03	.42 ±.03
170	.21 ±.04	.26 ±.03	.31 ±.03	.29 ±.03	.32 ±.03	.33 ±.03	.40 ±.03	.35 ±.03	--
177	--	.24 ±.03	.27 ±.03	.29 ±.03	.34 ±.03	.30 ±.03	.32 ±.03	.36 ±.03	--
185	--	--	.23 ±.03	.27 ±.03	.36 ±.03	.37 ±.03	.34 ±.03	.37 ±.03	--
192	--	--	--	.24 ±.03	.29 ±.03	.35 ±.03	.34 ±.03	.34 ±.03	--

TABLE E.18 — $Ne+U \rightarrow \pi^+ + X$ — $E/A = 407$ MeV — $Ed^3\sigma/dp^3$ $\mu b\ c^3/(sr\ MeV^2)$

p_π MeV/c	θ_π lab. degrees 0	4	8	12	16	20	24	28	32
107	1.36 ±.49	1.87 ±.39	.81 ±.33	1.45 ±.45	--	--	--	--	--
112	.93 ±.42	1.23 ±.35	1.68 ±.34	.31 ±.34	.91 ±.37	--	--	--	--
118	.66 ±.27	1.46 ±.30	.95 ±.28	.96 ±.43	1.42 ±.40	.82 ±.42	--	--	--
124	.71 ±.39	1.44 ±.25	.99 ±.39	1.64 ±.45	1.38 ±.37	2.16 ±.42	--	--	--
129	.57 ±.23	.63 ±.32	1.23 ±.35	2.09 ±.41	1.10 ±.33	.87 ±.29	--	--	--
135	.99 ±.41	1.12 ±.30	1.37 ±.29	.81 ±.31	1.64 ±.39	.94 ±.31	1.42 ±.35	--	--
141	--	--	1.71 ±.36	1.78 ±.38	1.25 ±.31	.80 ±.31	1.33 ±.35	1.55 ±.30	--
147	--	--	--	1.55 ±.36	1.49 ±.33	1.31 ±.31	1.75 ±.32	1.15 ±.26	--
153	--	--	--	--	.61 ±.37	1.68 ±.36	1.32 ±.30	1.10 ±.28	1.21 ±.24
158	--	--	--	--	.54 ±.24	.43 ±.30	1.16 ±.24	1.35 ±.28	1.31 ±.25

TABLE E.19 — $Ne+C \rightarrow \pi^- + X$, E/A = 482 MeV — $Ed^3\sigma/dp^3$ $\mu b\ c^3/(sr\ MeV^2)$

p_π MeV/c	θ_π lab. degrees 0	4	8	12	16	20
119	--	.77 ±.09	.72 ±.10	.75 ±.11	.80 ±.12	.56 ±.10
123	.86 ±.12	.98 ±.11	.74 ±.10	.97 ±.12	.76 ±.11	.83 ±.11
127	.97 ±.12	.99 ±.10	1.03 ±.11	.82 ±.10	.69 ±.10	.68 ±.10
132	1.10 ±.12	.93 ±.07	.91 ±.10	.94 ±.11	.86 ±.11	.78 ±.11
136	1.27 ±.13	1.07 ±.07	.86 ±.09	.77 ±.09	.74 ±.09	.61 ±.09
141	1.39 ±.14	1.15 ±.07	1.03 ±.10	.91 ±.10	.71 ±.09	.98 ±.13
145	1.91 ±.16	1.32 ±.08	1.03 ±.07	.70 ±.08	.81 ±.10	--
150	2.18 ±.17	1.51 ±.08	.98 ±.06	.83 ±.09	1.12 ±.13	--
154	2.81 ±.20	1.68 ±.08	.93 ±.06	.85 ±.09	--	--
158	2.55 ±.18	1.48 ±.08	.78 ±.06	.84 ±.08	--	--
163	2.26 ±.17	1.43 ±.08	1.08 ±.07	.70 ±.07	--	--
167	1.45 ±.13	1.23 ±.07	.96 ±.08	.77 ±.07	--	--
172	1.21 ±.11	1.21 ±.07	.82 ±.07	.73 ±.06	.66 ±.06	--
176	1.16 ±.11	.87 ±.07	.81 ±.07	.64 ±.06	.66 ±.06	--
181	1.13 ±.12	.80 ±.07	.67 ±.06	.69 ±.06	.63 ±.05	--
185	--	--	.84 ±.10	.60 ±.06	.70 ±.05	.48 ±.04
190	--	--	--	--	.53 ±.06	.60 ±.05

TABLE E.20 Ne+NaF → π^- + X E/A = 483 MeV $Ed^3\sigma/dp^3$ $\mu b\ c^3/(sr\ MeV^2)$

P_π MeV/c	θ_π lab. degrees 0	4	8	12	16	20
118	1.05 ±.13	1.22 ±.10	1.52 ±.12	1.47 ±.12	1.53 ±.14	1.25 ±.12
123	1.44 ±.13	1.80 ±.13	1.48 ±.12	1.41 ±.12	1.33 ±.12	1.28 ±.11
127	1.78 ±.14	1.55 ±.11	1.44 ±.11	1.45 ±.11	1.38 ±.11	1.44 ±.12
132	1.95 ±.14	1.62 ±.07	1.67 ±.12	1.57 ±.12	1.40 ±.11	1.26 ±.11
136	2.18 ±.14	1.71 ±.07	1.56 ±.11	1.49 ±.11	1.36 ±.10	1.25 ±.10
140	2.36 ±.15	1.86 ±.08	1.63 ±.11	1.48 ±.11	1.27 ±.10	--
145	2.76 ±.17	2.20 ±.08	1.48 ±.07	1.43 ±.10	1.37 ±.10	--
149	3.21 ±.18	2.40 ±.09	1.79 ±.07	1.33 ±.09	--	--
154	3.88 ±.21	2.46 ±.09	1.48 ±.06	1.29 ±.06	--	--
158	3.78 ±.20	2.25 ±.08	1.48 ±.06	1.28 ±.08	--	--
163	2.91 ±.17	2.08 ±.08	1.64 ±.07	1.20 ±.07	--	--
167	2.30 ±.14	1.95 ±.07	1.33 ±.08	1.23 ±.07	.82 ±.05	--
172	2.22 ±.13	1.95 ±.07	1.44 ±.08	1.12 ±.06	1.08 ±.06	--
176	1.77 ±.11	1.51 ±.08	1.22 ±.07	1.22 ±.07	1.07 ±.06	--
181	1.79 ±.13	1.46 ±.08	1.16 ±.07	1.15 ±.06	1.05 ±.06	--
185	--	1.42 ±.23	1.20 ±.09	1.08 ±.06	1.06 ±.05	--

TABLE E.21 — $Ne+Cu \rightarrow \pi^- + X$, E/A = 485 MeV, $Ed^3\sigma/dp^3$ $\mu b\ c^3/(sr\ MeV^2)$

p_π MeV/c	θ_π lab. degrees 0	4	8	12	16	20
118	--	3.13 ±.30	3.78 ±.37	3.05 ±.33	3.19 ±.37	2.49 ±.32
122	3.10 ±.36	3.78 ±.35	3.12 ±.33	3.34 ±.35	3.11 ±.34	3.14 ±.32
126	4.08 ±.38	3.96 ±.32	3.87 ±.34	3.30 ±.31	3.86 ±.35	2.97 ±.32
131	3.82 ±.37	3.34 ±.19	3.44 ±.30	2.93 ±.31	3.37 ±.32	2.27 ±.26
135	3.70 ±.34	3.72 ±.20	3.51 ±.29	3.39 ±.31	2.93 ±.28	1.91 ±.24
140	3.75 ±.35	3.87 ±.20	3.66 ±.30	3.67 ±.31	2.90 ±.27	--
144	4.73 ±.38	4.29 ±.21	3.25 ±.19	2.66 ±.25	2.96 ±.29	--
149	4.72 ±.38	4.27 ±.20	3.67 ±.20	2.74 ±.24	--	--
153	6.27 ±.44	4.13 ±.21	2.90 ±.17	2.53 ±.27	--	--
158	5.83 ±.41	4.18 ±.20	2.63 ±.16	2.76 ±.21	--	--
162	5.79 ±.43	3.68 ±.20	3.07 ±.18	2.54 ±.21	--	--
167	4.32 ±.35	3.20 ±.18	2.91 ±.23	2.39 ±.20	1.55 ±.15	--
171	3.90 ±.31	3.58 ±.19	2.69 ±.20	1.98 ±.17	2.04 ±.17	--
176	2.95 ±.27	2.98 ±.21	2.48 ±.19	2.53 ±.18	1.84 ±.16	--
180	3.11 ±.32	2.59 ±.20	2.51 ±.20	2.36 ±.17	2.03 ±.15	1.28 ±.12
185	--	--	2.31 ±.24	2.18 ±.16	1.87 ±.14	1.50 ±.12
189	--	--	--	--	1.50 ±.16	1.82 ±.13

TABLE E.22	Ne+U → π^- + X E/A = 487 MeV					Ed$^3\sigma$/dp^3 μb c^3/(sr MeV^2)
p_π	θ_π lab. degrees					
MeV/c	0	4	8	12	16	20
120	9.9 ±1.6	14.7 ±1.6	8.3 ±1.4	8.1 ±1.4	8.5 ±1.5	10.0 ±1.4
127	11.8 ±1.6	12.7 ±1.3	11.7 ±1.4	9.9 ±1.4	11.2 ±1.4	10.9 ±1.4
133	10.5 ±1.5	11.3 ±.9	10.7 ±1.3	9.8 ±1.3	8.7 ±1.2	7.8 ±1.2
140	13.0 ±1.6	11.0 ±.8	9.8 ±.8	10.3 ±1.2	8.0 ±1.1	--
147	12.2 ±1.6	12.3 ±.9	9.8 ±.9	7.9 ±1.1	--	--
154	16.1 ±1.7	12.3 ±.9	8.8 ±.8	7.0 ±.7	--	--
160	15.4 ±1.7	10.5 ±.9	7.7 ±.8	7.6 ±.9	--	--
167	7.8 ±1.3	8.6 ±.8	7.5 ±1.0	5.7 ±.9	4.9 ±.7	--
174	8.6 ±1.2	8.1 ±.9	8.9 ±.9	6.0 ±.8	5.6 ±.8	--
181	6.9 ±1.6	7.1 ±1.1	6.2 ±.9	5.9 ±.7	5.9 ±.7	--
188	--	--	--	4.9 ±1.2	4.4 ±.7	4.7 ±.6

TABLE E.23 — $Ne+C \rightarrow \pi^+ + X$, E/A = 482 MeV — $Ed^3\sigma/dp^3$ $\mu b\ c^3/(sr\ MeV^2)$

p_π MeV/c	θ_π lab. degrees 0	4	8	12	16	20
121	.23 ±.04	.39 ±.05	.29 ±.04	.39 ±.05	.54 ±.06	.55 ±.07
128	.24 ±.04	.32 ±.04	.40 ±.05	.44 ±.05	.45 ±.05	.59 ±.07
134	.21 ±.04	.23 ±.02	.32 ±.04	.33 ±.04	.47 ±.05	.35 ±.05
141	.16 ±.03	.25 ±.02	.27 ±.02	.34 ±.04	.38 ±.05	.71 ±.09
148	.22 ±.03	.19 ±.02	.34 ±.03	.42 ±.04	.46 ±.06	--
154	.13 ±.03	.19 ±.02	.30 ±.02	.36 ±.03	--	--
161	.23 ±.03	.20 ±.02	.34 ±.02	.43 ±.04	--	--
168	.23 ±.03	.22 ±.02	.34 ±.03	.40 ±.04	.34 ±.03	--
174	.26 ±.04	.32 ±.03	.37 ±.03	.43 ±.03	.47 ±.03	--
181	.25 ±.05	.28 ±.04	.36 ±.03	.45 ±.03	.51 ±.03	--
188	--	--	--	.40 ±.05	.43 ±.03	.44 ±.03

TABLE E.24	Ne+NaF → π^+ + X E/A = 483 MeV					$Ed^3\sigma/dp^3$ $\mu b\ c^3/(sr\ MeV^2)$
p_π	θ_π lab. degrees					
MeV/c	0	4	8	12	16	20
118	--	.52 ±.06	.70 ±.08	.90 ±.10	.73 ±.09	.84 ±.10
122	.42 ±.07	.55 ±.08	.62 ±.08	.69 ±.09	.79 ±.09	.75 ±.09
126	.42 ±.07	.58 ±.07	.49 ±.07	.66 ±.08	.61 ±.08	.69 ±.09
131	.46 ±.07	.44 ±.06	.58 ±.07	.70 ±.08	.76 ±.08	.78 ±.09
135	.44 ±.06	.43 ±.04	.56 ±.06	.80 ±.08	.87 ±.08	.62 ±.08
140	.39 ±.06	.44 ±.03	.51 ±.06	.75 ±.08	.76 ±.08	--
144	.39 ±.05	.36 ±.04	.59 ±.04	.53 ±.06	.89 ±.09	--
148	.36 ±.05	.45 ±.03	.55 ±.04	.52 ±.06	--	--
153	.30 ±.05	.36 ±.03	.53 ±.04	.68 ±.04	--	--
157	.35 ±.05	.41 ±.03	.55 ±.04	.75 ±.06	--	--
162	.36 ±.05	.37 ±.03	.67 ±.04	.65 ±.06	--	--
166	.38 ±.05	.38 ±.03	.67 ±.06	.76 ±.06	.58 ±.05	--
171	.37 ±.05	.50 ±.04	.72 ±.05	.57 ±.05	.65 ±.05	--
175	.45 ±.06	.56 ±.05	.68 ±.06	.66 ±.05	.70 ±.05	--
180	.56 ±.07	.43 ±.05	.68 ±.05	.68 ±.05	.73 ±.05	--
184	--	--	.52 ±.06	.64 ±.05	.69 ±.05	--

TABLE E.25 — Ne+Cu → π^+ + X, E/A = 485 MeV — $Ed^3\sigma/dp^3$ $\mu b\ c^3/(sr\ MeV^2)$

p_π MeV/c	θ_π lab. degrees 0	4	8	12	16	20
120	1.04 ±.19	1.32 ±.18	1.49 ±.18	1.57 ±.20	1.81 ±.22	1.71 ±.22
127	.91 ±.17	1.32 ±.15	1.29 ±.16	1.57 ±.18	1.72 ±.19	1.60 ±.20
133	1.10 ±.17	1.15 ±.10	1.37 ±.16	1.28 ±.16	1.89 ±.20	1.07 ±.17
140	.89 ±.15	.94 ±.09	1.04 ±.09	1.19 ±.16	1.59 ±.19	1.98 ±.28
147	.77 ±.13	1.10 ±.09	1.27 ±.10	1.16 ±.14	1.90 ±.21	--
154	.96 ±.14	.94 ±.08	1.15 ±.09	1.34 ±.10	--	--
160	.95 ±.13	.87 ±.08	1.29 ±.09	1.47 ±.13	--	--
167	1.03 ±.14	.90 ±.08	1.22 ±.13	1.36 ±.13	1.10 ±.11	--
174	1.29 ±.15	1.06 ±.12	1.38 ±.12	1.16 ±.11	1.20 ±.12	--
180	.82 ±.18	1.06 ±.15	1.01 ±.11	1.41 ±.12	1.43 ±.11	.77 ±.09
187	--	--	--	1.18 ±.17	1.17 ±.11	1.32 ±.10

TABLE E.26	Ne+U → π^+ + X E/A = 487 MeV					$Ed^3\sigma/dp^3$ $\mu b\ c^3/(sr\ MeV^2)$
P_π	θ_π lab. degrees					
MeV/c	0	4	8	12	16	20
123	1.75 ±.70	2.74 ±.68	2.00 ±.59	2.55 ±.62	3.17 ±.60	2.81 ±.71
131	2.37 ±.64	1.96 ±.36	3.18 ±.55	2.88 ±.57	3.66 ±.60	2.83 ±.66
140	2.83 ±.60	1.74 ±.35	2.66 ±.34	2.81 ±.57	2.41 ±.62	--
149	1.93 ±.53	1.93 ±.33	2.43 ±.36	2.78 ±.39	--	--
158	2.22 ±.47	1.75 ±.31	2.53 ±.31	3.39 ±.49	--	--
167	2.31 ±.51	2.38 ±.33	3.47 ±.48	2.58 ±.45	2.02 ±.44	--
176	2.29 ±.57	1.07 ±.50	2.81 ±.46	3.11 ±.46	1.82 ±.42	--
185	--	--	2.85 ±.85	2.85 ±.56	2.81 ±.40	1.79 ±.37

TABLE E.27 — $Ar+C \rightarrow \pi^- + X$, E/A = 533 MeV — $Ed^3\sigma/dp^3$, $\mu b\ c^3/(sr\ MeV^2)$

p_π MeV/c	θ_π lab. degrees 0	4	8	12	16	20
91	1.34 ±.28	1.33 ±.26	1.71 ±.28	1.63 ±.30	1.00 ±.24	.78 ±.20
98	1.39 ±.28	1.65 ±.16	1.86 ±.28	2.00 ±.27	1.56 ±.26	1.26 ±.23
104	2.50 ±.34	2.18 ±.18	1.71 ±.17	1.81 ±.24	1.44 ±.23	--
110	2.20 ±.30	2.47 ±.18	2.04 ±.17	2.20 ±.27	--	--
117	2.64 ±.31	2.14 ±.16	2.06 ±.17	1.79 ±.20	--	--
123	2.06 ±.26	2.48 ±.18	2.22 ±.23	1.91 ±.21	1.93 ±.18	--
130	2.14 ±.17	2.22 ±.14	2.24 ±.15	2.09 ±.15	2.18 ±.15	1.82 ±.21
136	2.50 ±.24	2.45 ±.17	2.30 ±.19	1.97 ±.15	1.77 ±.14	1.88 ±.12
143	2.77 ±.25	2.92 ±.14	2.40 ±.20	1.73 ±.19	1.73 ±.17	1.60 ±.18
148	4.25 ±.33	3.40 ±.16	2.25 ±.20	2.16 ±.20	1.75 ±.18	--
153	4.45 ±.32	3.57 ±.16	2.41 ±.13	2.07 ±.18	1.99 ±.17	--
158	6.10 ±.36	4.02 ±.16	2.24 ±.12	1.94 ±.16	--	--
163	9.23 ±.47	4.35 ±.17	2.45 ±.13	1.82 ±.11	--	--
167	10.55 ±.52	4.14 ±.17	2.42 ±.13	1.75 ±.14	--	--
172	7.28 ±.39	3.95 ±.16	2.05 ±.12	1.93 ±.14	--	--
177	4.51 ±.29	3.52 ±.15	2.25 ±.15	1.81 ±.14	1.22 ±.11	--
182	3.48 ±.26	2.95 ±.14	2.45 ±.16	1.75 ±.14	1.94 ±.13	--
187	3.35 ±.23	2.44 ±.15	2.00 ±.14	1.74 ±.13	1.72 ±.11	--
191	2.92 ±.24	2.22 ±.15	1.71 ±.13	1.86 ±.12	1.53 ±.11	--
196	--	--	1.46 ±.22	1.59 ±.16	1.69 ±.12	--

TABLE E.28 — Ar+KCl → π^- + X, E/A = 534 MeV — $Ed^3\sigma/dp^3$ $\mu b\ c^3/(sr\ MeV^2)$

p_π MeV/c	θ_π lab. degrees 0	4	8	12	16	20
124	--	4.61 ±.51	4.74 ±.60	5.43 ±.55	4.50 ±.54	3.40 ±.55
129	4.90 ±.55	5.66 ±.51	4.62 ±.49	4.44 ±.53	4.60 ±.56	4.64 ±.55
134	4.73 ±.61	4.98 ±.49	4.54 ±.55	4.93 ±.56	5.29 ±.62	4.10 ±.51
139	5.30 ±.60	4.87 ±.35	4.82 ±.50	4.51 ±.46	4.22 ±.50	4.29 ±.48
143	5.00 ±.63	5.73 ±.34	5.09 ±.49	4.34 ±.51	4.19 ±.46	3.90 ±.46
148	7.94 ±.78	6.39 ±.37	5.32 ±.52	4.52 ±.51	3.97 ±.46	--
153	6.82 ±.72	6.39 ±.37	5.41 ±.35	4.54 ±.45	4.31 ±.43	--
158	8.95 ±.72	7.42 ±.37	5.04 ±.32	4.14 ±.39	--	--
163	12.15 ±.87	7.62 ±.40	4.68 ±.32	3.66 ±.29	--	--
168	14.11 ±.90	6.80 ±.38	5.08 ±.32	4.00 ±.38	--	--
172	12.01 ±.79	6.98 ±.37	3.83 ±.32	3.87 ±.37	--	--
177	6.71 ±.64	6.36 ±.36	4.36 ±.38	3.55 ±.35	--	--
182	5.68 ±.62	5.43 ±.34	4.49 ±.37	3.80 ±.36	--	--
187	4.86 ±.49	4.63 ±.36	4.02 ±.37	3.30 ±.34	3.38 ±.29	--
192	4.50 ±.52	3.88 ±.35	3.79 ±.33	3.41 ±.29	3.32 ±.27	--
196	--	--	3.29 ±.59	3.16 ±.42	2.99 ±.28	--

TABLE E.29 $Ar+C \rightarrow \pi^+ + X$ $Ed^3\sigma/dp^3$

E/A = 533 MeV $\mu b\ c^3/(sr\ MeV^2)$

P_π MeV/c	θ_π lab. degrees 0	4	8	12	16	20
128	.29 ±.06	.35 ±.06	.43 ±.08	.60 ±.07	.89 ±.08	.86 ±.09
135	.33 ±.05	.22 ±.05	.44 ±.06	.72 ±.07	.61 ±.07	.89 ±.08
142	.19 ±.04	.22 ±.03	.35 ±.06	.57 ±.06	.72 ±.07	.79 ±.07
149	.14 ±.04	.14 ±.03	.40 ±.05	.62 ±.06	.62 ±.06	--
157	.07 ±.04	.16 ±.03	.32 ±.03	.60 ±.06	--	--
164	.08 ±.04	.15 ±.03	.28 ±.03	.59 ±.04	--	--
171	.16 ±.04	.17 ±.02	.33 ±.03	.57 ±.05	--	--
178	.17 ±.05	.17 ±.02	.36 ±.04	.51 ±.05	--	--
185	.17 ±.03	.22 ±.03	.42 ±.04	.59 ±.05	.79 ±.05	--
193	.22 ±.04	.20 ±.03	.38 ±.04	.55 ±.04	.70 ±.04	--

TABLE E.30 — $Ar+KCl \rightarrow \pi^+ + X$, E/A = 534 MeV, $Ed^3\sigma/dp^3$ $\mu b\ c^3/(sr\ MeV^2)$

p_π MeV/c	θ_π lab. degrees 0	4	8	12	16	20
128	1.14 ±.23	1.33 ±.22	1.05 ±.27	1.35 ±.24	2.09 ±.29	2.05 ±.29
135	1.10 ±.21	.69 ±.18	1.16 ±.21	2.00 ±.25	1.51 ±.26	2.15 ±.29
142	.87 ±.16	.97 ±.12	.87 ±.20	1.61 ±.22	1.66 ±.24	1.91 ±.24
149	.64 ±.17	.62 ±.13	1.22 ±.19	1.73 ±.20	1.77 ±.23	--
156	.76 ±.16	.71 ±.10	.96 ±.12	1.55 ±.20	--	--
164	.37 ±.16	.71 ±.10	.96 ±.12	1.59 ±.13	--	--
171	.80 ±.17	.67 ±.09	.92 ±.11	1.39 ±.16	--	--
178	.55 ±.17	.89 ±.10	1.05 ±.15	1.42 ±.17	--	--
185	.91 ±.14	.81 ±.12	1.20 ±.15	1.35 ±.17	1.76 ±.16	--
192	.73 ±.15	.69 ±.13	1.31 ±.16	1.29 ±.13	1.57 ±.15	--

TABLE E.31 — Ne+Be → π^- + X — E/A = 654 MeV — $Ed^3\sigma/dp^3$ μb $c^3/(sr\ MeV^2)$

P_π MeV/c	θ_π lab. degrees 0	4	8	12	16	20
146	--	1.10 ±.13	.95 ±.12	.73 ±.10	.97 ±.13	--
151	--	1.33 ±.14	1.15 ±.13	1.03 ±.12	.99 ±.13	.93 ±.13
156	1.31 ±.15	1.49 ±.15	1.08 ±.12	.88 ±.11	1.00 ±.13	.89 ±.12
161	1.44 ±.14	1.80 ±.17	1.76 ±.16	1.03 ±.12	1.08 ±.13	.90 ±.12
166	1.50 ±.14	1.64 ±.11	1.49 ±.15	.94 ±.12	1.09 ±.13	1.19 ±.13
170	1.73 ±.15	1.60 ±.10	1.48 ±.14	1.34 ±.14	1.25 ±.14	1.18 ±.13
175	1.86 ±.15	1.61 ±.10	1.41 ±.14	1.24 ±.14	1.07 ±.13	1.32 ±.18
180	2.23 ±.17	1.68 ±.10	1.30 ±.09	1.19 ±.13	1.02 ±.12	--
185	2.05 ±.16	1.57 ±.10	1.19 ±.08	.92 ±.11	--	--
190	1.66 ±.15	1.46 ±.09	1.14 ±.08	.97 ±.12	--	--
195	1.77 ±.14	1.24 ±.08	1.02 ±.07	1.19 ±.11	--	--
200	1.51 ±.13	1.12 ±.08	.88 ±.07	.79 ±.08	--	--

TABLE E.32a	Ne+NaF → π^- + X E/A = 655 MeV					Ed$^3\sigma$/dp^3 μb c^3/(sr MeV^2)
P_π	θ_π lab. degrees					
MeV/c	0	4	8	12	16	20
74	2.10 ±.25	2.55 ±.26	2.36 ±.25	2.56 ±.21	2.23 ±.20	1.75 ±.19
78	2.28 ±.24	2.37 ±.17	2.17 ±.23	2.62 ±.21	2.50 ±.22	2.36 ±.20
82	2.38 ±.24	2.36 ±.16	2.40 ±.16	2.43 ±.20	2.60 ±.20	3.08 ±.40
87	2.57 ±.23	2.30 ±.15	2.17 ±.14	2.80 ±.18	2.44 ±.41	2.43 ±.38
91	2.61 ±.22	2.50 ±.15	2.06 ±.14	2.86 ±.20	--	3.33 ±.43
96	2.29 ±.20	2.42 ±.13	2.45 ±.14	2.42 ±.13	2.50 ±.12	2.72 ±.20
100	2.66 ±.18	2.41 ±.17	2.45 ±.13	2.47 ±.13	2.42 ±.17	2.72 ±.18
106	2.81 ±.30	3.20 ±.21	2.45 ±.20	2.54 ±.19	2.13 ±.18	2.46 ±.19
110	2.77 ±.28	2.52 ±.19	3.06 ±.23	2.41 ±.19	2.58 ±.20	2.44 ±.19
115	2.74 ±.28	2.83 ±.19	2.77 ±.19	2.84 ±.22	2.68 ±.20	3.13 ±.32
123	2.49 ±.20	2.50 ±.12	2.72 ±.13	2.41 ±.13	1.88 ±.24	2.37 ±.16
128	2.35 ±.18	2.55 ±.11	2.30 ±.11	2.33 ±.12	2.05 ±.23	2.13 ±.21
132	2.35 ±.15	2.34 ±.11	2.27 ±.11	2.39 ±.11	2.33 ±.10	2.23 ±.22
136	2.16 ±.17	2.38 ±.14	2.36 ±.12	2.69 ±.12	2.37 ±.21	2.25 ±.21
140	2.52 ±.28	2.40 ±.20	2.46 ±.21	2.13 ±.20	1.99 ±.21	1.89 ±.20

TABLE E.32b	Ne+NaF → π^- + X E/A = 655 MeV					$Ed^3\sigma/dp^3$ $\mu b\ c^3/(sr\ MeV^2)$
p_π MeV/c	θ_π lab. degrees 0	4	8	12	16	20
144	2.40 ±.26	2.35 ±.17	2.08 ±.22	2.25 ±.20	2.21 ±.20	2.10 ±.19
149	2.49 ±.30	2.13 ±.19	2.56 ±.27	2.07 ±.21	2.23 ±.20	2.41 ±.23
153	2.03 ±.22	2.03 ±.13	2.25 ±.13	1.86 ±.13	2.25 ±.14	2.00 ±.16
157	2.42 ±.26	1.93 ±.12	2.34 ±.12	2.26 ±.13	2.24 ±.15	2.00 ±.14
161	2.51 ±.14	2.30 ±.13	2.14 ±.11	2.02 ±.10	2.15 ±.14	1.95 ±.13
165	2.71 ±.13	2.39 ±.11	2.45 ±.11	2.09 ±.10	2.21 ±.12	1.98 ±.10
170	2.87 ±.14	2.62 ±.10	2.35 ±.10	2.22 ±.10	2.23 ±.12	1.97 ±.10
174	3.27 ±.15	2.59 ±.09	2.25 ±.11	2.21 ±.10	2.06 ±.10	2.17 ±.11
178	2.90 ±.28	2.63 ±.22	1.32 ±.20	1.41 ±.16	--	--
182	3.41 ±.17	2.64 ±.12	2.17 ±.09	2.02 ±.12	2.05 ±.16	1.56 ±.40
187	4.30 ±.22	2.73 ±.11	2.02 ±.08	2.06 ±.14	2.03 ±.15	1.76 ±.36
191	4.04 ±.23	2.71 ±.13	2.23 ±.11	2.08 ±.18	--	2.35 ±.33
196	2.67 ±.18	2.25 ±.11	1.77 ±.10	2.06 ±.16	--	1.50 ±.29
201	2.76 ±.18	1.88 ±.10	1.67 ±.09	1.58 ±.11	--	--

TABLE E.32c	Ne+NaF → π^- + X E/A = 655 MeV					$Ed^3\sigma/dp^3$ $\mu b\ c^3/(sr\ MeV^2)$
P_π	θ_π lab. degrees					
MeV/c	24	28	32	36	40	44
74	2.84 ±.44	2.67 ±.37	--	--	--	--
78	2.05 ±.43	2.62 ±.36	2.21 ±.36	--	--	--
82	3.18 ±.38	2.65 ±.38	3.30 ±.39	3.00 ±.35	--	--
87	2.34 ±.38	2.26 ±.35	2.91 ±.34	3.05 ±.33	--	--
91	2.35 ±.38	1.98 ±.35	3.14 ±.32	2.93 ±.31	2.90 ±.30	--
96	2.73 ±.22	3.20 ±.34	2.75 ±.30	2.91 ±.29	2.77 ±.26	--
100	2.89 ±.26	3.22 ±.27	2.99 ±.40	2.59 ±.35	3.38 ±.32	--
106	3.65 ±.33	2.81 ±.32	3.62 ±.32	--	--	--
110	3.56 ±.32	3.61 ±.34	3.03 ±.29	2.91 ±.29	--	--
115	3.00 ±.31	3.26 ±.30	2.96 ±.29	3.18 ±.29	--	--
123	2.74 ±.19	2.69 ±.20	2.74 ±.21	2.84 ±.19	2.83 ±.19	--
128	2.76 ±.19	2.69 ±.18	2.57 ±.19	2.64 ±.17	2.66 ±.16	2.22 ±.14
132	2.19 ±.35	2.80 ±.17	2.62 ±.17	2.43 ±.15	2.68 ±.15	2.29 ±.12
136	2.04 ±.34	1.85 ±.31	2.54 ±.18	2.18 ±.16	2.63 ±.15	--
140	2.79 ±.39	2.08 ±.33	2.38 ±.32	--	--	--

TABLE E.32d	Ne+NaF → π^- + X E/A = 655 MeV					$Ed^3\sigma/dp^3$ $\mu b\ c^3/(sr\ MeV^2)$
p_π	θ_π lab. degrees					
MeV/c	24	28	32	36	40	44
144	2.25 ±.36	2.67 ±.39	1.69 ±.28	--	--	--
149	2.47 ±.38	2.07 ±.34	2.28 ±.32	1.84 ±.28	--	--
153	1.84 ±.28	2.10 ±.29	1.94 ±.27	2.49 ±.30	--	--
157	2.07 ±.14	2.24 ±.26	1.89 ±.31	1.79 ±.27	2.21 ±.29	--
161	2.03 ±.12	1.63 ±.21	2.13 ±.28	1.68 ±.24	1.82 ±.23	--
165	2.25 ±.13	2.07 ±.22	2.20 ±.21	1.81 ±.26	2.16 ±.25	--
170	1.71 ±.17	2.19 ±.19	1.78 ±.16	1.59 ±.24	1.71 ±.23	1.50 ±.20
174	1.94 ±.18	2.15 ±.18	2.07 ±.16	1.82 ±.22	1.62 ±.19	1.42 ±.18
178	--	2.16 ±.26	1.79 ±.23	1.58 ±.20	1.59 ±.19	1.68 ±.17
182	1.71 ±.41	1.53 ±.37	1.59 ±.18	1.57 ±.17	1.34 ±.17	1.85 ±.18
187	1.70 ±.32	1.78 ±.30	1.36 ±.26	1.02 ±.16	1.52 ±.22	--
191	1.68 ±.29	1.19 ±.22	1.45 ±.24	1.40 ±.22	1.80 ±.24	--
196	1.53 ±.25	1.25 ±.27	1.18 ±.22	1.41 ±.21	1.23 ±.18	--
201	1.66 ±.28	1.33 ±.25	1.00 ±.24	1.43 ±.23	1.04 ±.17	1.20 ±.26

TABLE E.33	Ne+Be → π^+ + X E/A = 654 MeV					$Ed^3\sigma/dp^3$ $\mu b\ c^3/(sr\ MeV^2)$
P_π MeV/c	θ_π lab. degrees 0	4	8	12	16	20
146	--	.33 ±.04	.40 ±.05	.43 ±.05	.40 ±.05	--
151	--	.36 ±.05	.43 ±.05	.45 ±.05	.64 ±.06	.55 ±.06
156	.42 ±.05	.37 ±.04	.35 ±.04	.48 ±.05	.59 ±.06	.55 ±.06
161	.33 ±.04	.38 ±.05	.43 ±.05	.43 ±.05	.50 ±.05	.59 ±.06
166	.35 ±.04	.39 ±.03	.45 ±.05	.54 ±.06	.64 ±.06	.61 ±.06
171	.29 ±.04	.33 ±.03	.35 ±.04	.44 ±.05	.81 ±.07	.73 ±.06
176	.27 ±.04	.31 ±.03	.36 ±.04	.55 ±.05	.67 ±.06	.69 ±.08
181	.25 ±.04	.23 ±.02	.36 ±.03	.45 ±.05	.58 ±.06	--
186	.28 ±.04	.24 ±.02	.40 ±.03	.41 ±.05	--	--
191	.21 ±.03	.29 ±.03	.41 ±.03	.47 ±.05	--	--
196	.25 ±.03	.35 ±.03	.39 ±.03	.70 ±.05	--	--
201	.31 ±.04	.27 ±.02	.44 ±.03	.68 ±.05	--	--

TABLE E.34a	Ne+NaF → π^+ + X E/A = 658 MeV					$Ed^3\sigma/dp^3$ $\mu b\ c^3/(sr\ MeV^2)$
p_π MeV/c	θ_π lab. degrees 0	4	8	12	16	20
74	1.34 ±.20	1.23 ±.18	1.25 ±.17	1.44 ±.17	1.19 ±.16	1.36 ±.16
78	1.18 ±.19	1.21 ±.12	1.33 ±.16	1.39 ±.17	1.21 ±.16	1.41 ±.16
83	1.50 ±.17	1.45 ±.12	1.46 ±.12	1.29 ±.15	1.70 ±.17	1.77 ±.23
87	1.32 ±.15	1.45 ±.11	1.34 ±.10	1.74 ±.12	1.90 ±.25	--
92	1.28 ±.14	1.49 ±.10	1.32 ±.10	1.56 ±.13	1.34 ±.21	--
96	1.42 ±.13	1.38 ±.09	1.29 ±.10	1.31 ±.10	1.34 ±.11	--
100	1.41 ±.17	1.43 ±.12	1.45 ±.10	1.64 ±.11	1.22 ±.16	1.73 ±.17
106	1.33 ±.21	1.72 ±.15	1.29 ±.19	1.54 ±.18	1.70 ±.19	1.24 ±.17
110	1.27 ±.19	1.39 ±.13	1.31 ±.16	1.34 ±.18	1.79 ±.20	1.64 ±.19
115	1.73 ±.20	1.49 ±.14	1.24 ±.13	1.15 ±.18	1.71 ±.20	--
120	1.20 ±.17	1.38 ±.12	1.57 ±.12	1.32 ±.13	--	--
124	1.27 ±.16	1.05 ±.11	1.35 ±.11	1.33 ±.16	--	--
129	1.43 ±.17	1.31 ±.11	1.16 ±.11	1.11 ±.13	1.32 ±.13	--
134	1.17 ±.15	1.01 ±.12	1.61 ±.15	1.28 ±.13	1.62 ±.12	--
138	--	1.00 ±.20	1.30 ±.16	1.62 ±.16	--	--

TABLE E.34b	Ne+NaF → π^+ + X E/A = 658 MeV					$Ed^3\sigma/dp^3$ $\mu b\ c^3/(sr\ MeV^2)$
p_π	θ_π lab. degrees					
MeV/c	0	4	8	12	16	20
146	--	.84 ±.08	.89 ±.08	1.01 ±.09	.95 ±.10	--
151	--	.88 ±.09	1.08 ±.09	.93 ±.09	1.27 ±.11	1.31 ±.11
156	.99 ±.10	.83 ±.08	.98 ±.08	.91 ±.09	1.24 ±.11	1.31 ±.11
161	.76 ±.07	.84 ±.08	1.09 ±.09	.96 ±.09	1.35 ±.11	1.27 ±.11
166	.78 ±.08	.88 ±.06	1.07 ±.09	1.11 ±.10	1.10 ±.10	1.29 ±.10
171	.79 ±.08	.79 ±.05	.91 ±.08	1.06 ±.09	1.44 ±.11	1.45 ±.11
176	.80 ±.07	.76 ±.05	.81 ±.07	1.11 ±.09	1.52 ±.11	1.54 ±.14
181	.57 ±.07	.73 ±.05	.93 ±.06	1.13 ±.09	1.26 ±.10	--
186	.61 ±.06	.70 ±.05	.86 ±.05	1.03 ±.09	1.21 ±.11	--
190	.58 ±.06	.65 ±.05	.91 ±.05	1.04 ±.09	--	--
195	.68 ±.06	.66 ±.04	.88 ±.05	1.56 ±.10	--	--
200	.61 ±.06	.60 ±.04	.88 ±.05	1.10 ±.07	--	--

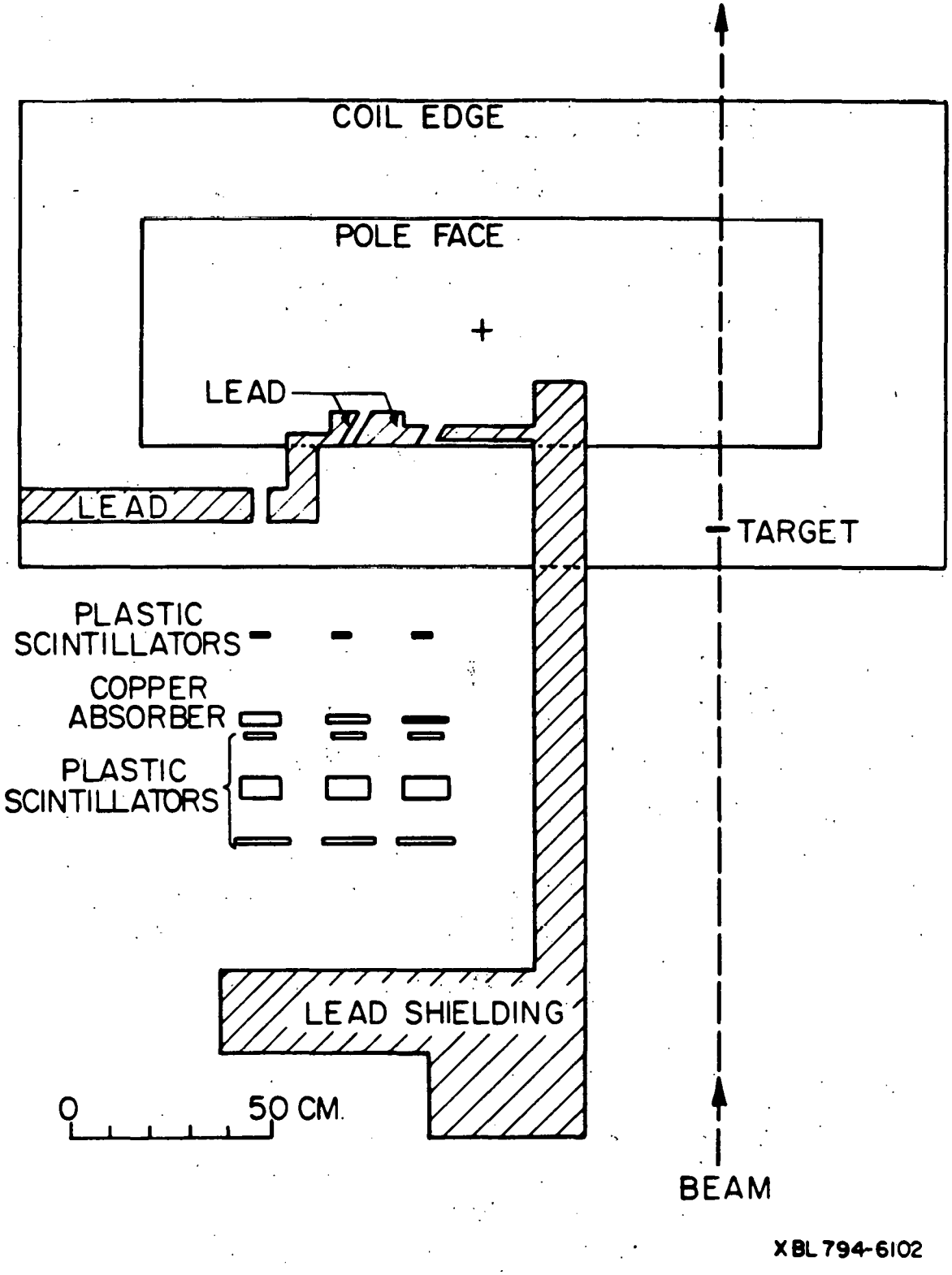

Fig. 1 -- Schematic diagram of the lead slit spectrometer

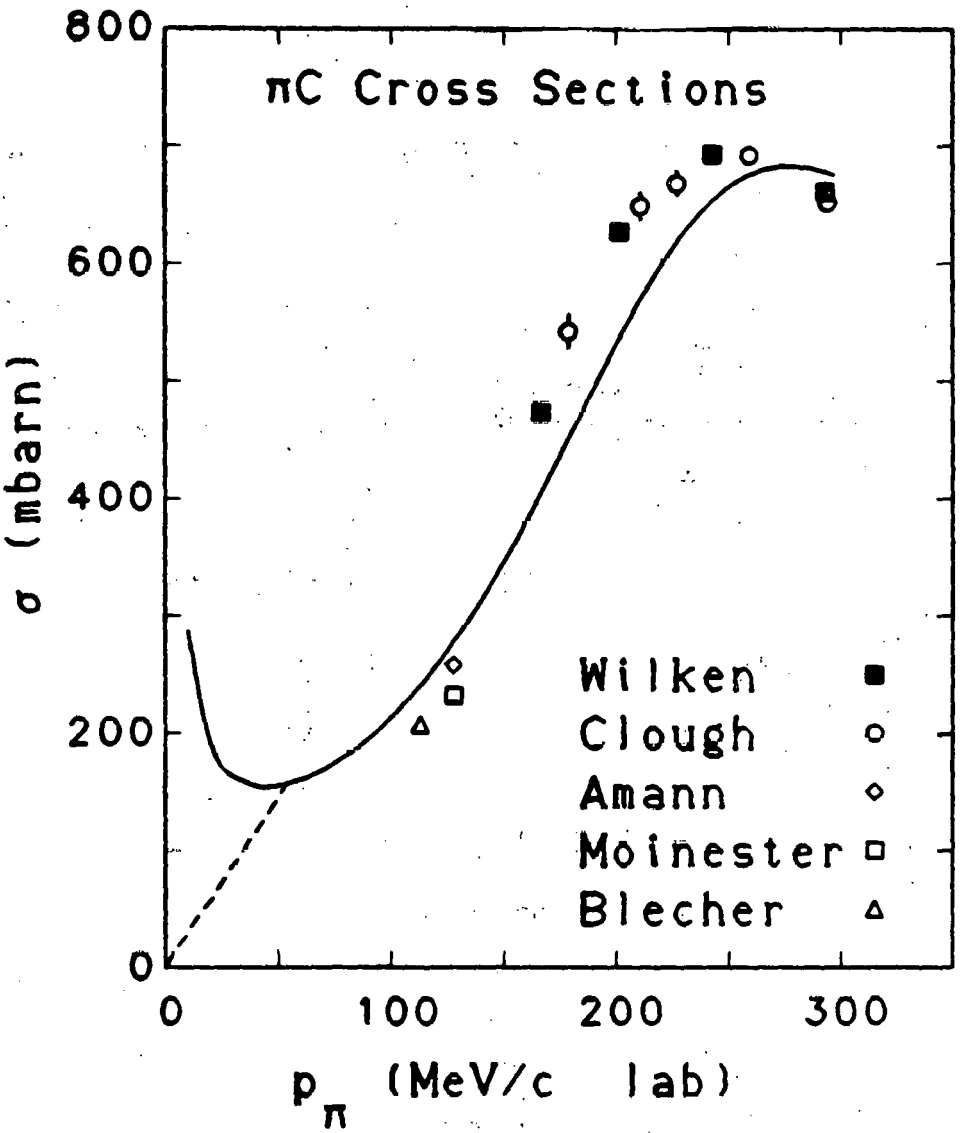

Fig. 2 -- Comparison of the pion reaction cross section formula[45] described in appendix C (solid line) and some measured total cross sections. The first author is shown for each of the experimental measurements[46-50]. The dashed line shows how the formula was extrapolated to $p_\pi = 0$. This extrapolation was necessary because the cross section formula diverges for small pion momenta.

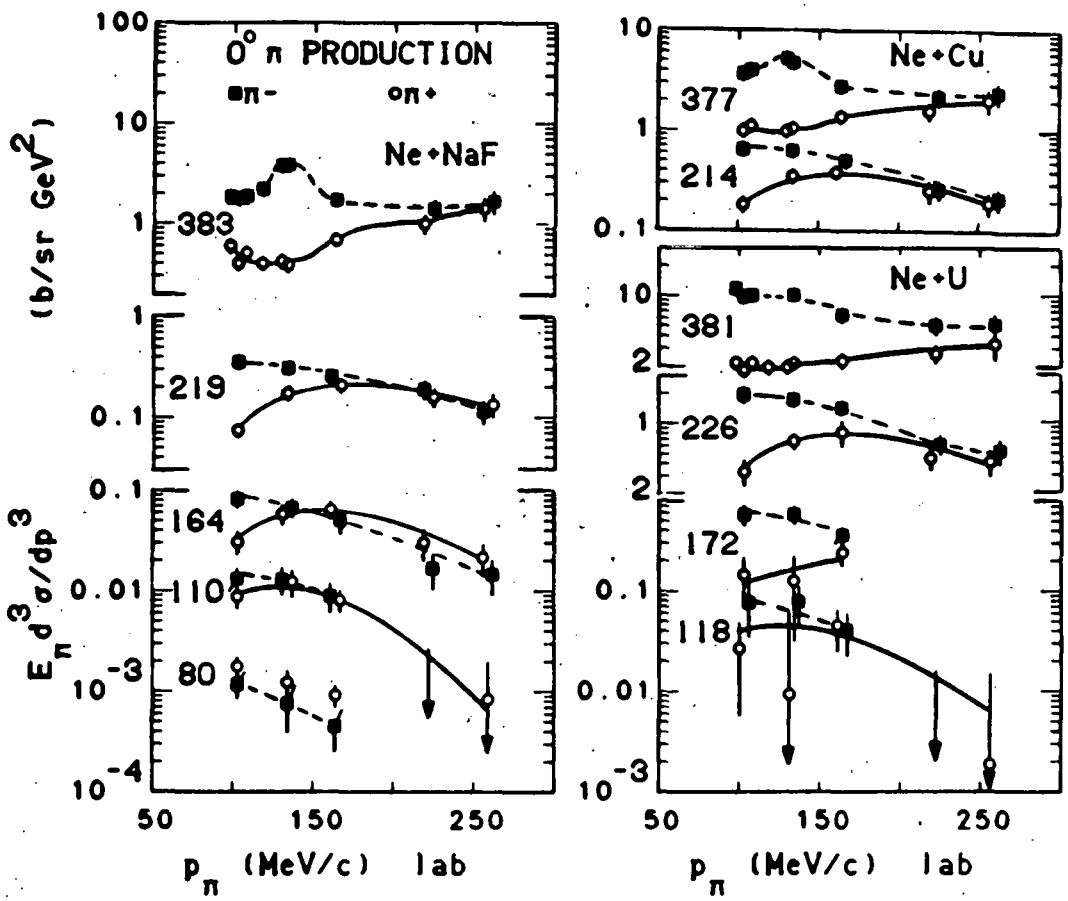

Fig. 3 -- A summary of the data collected with the lead slit spectrometer at $\theta_{lab} = 0$. The Lorentz invariant cross section vs. pion lab momentum is plotted. The numbers next to each set of points refer to the beam energy per nucleon in MeV. The lines are to guide the eye. The error bars are the relative errors -- they do not include the uncertainty in the normalization.

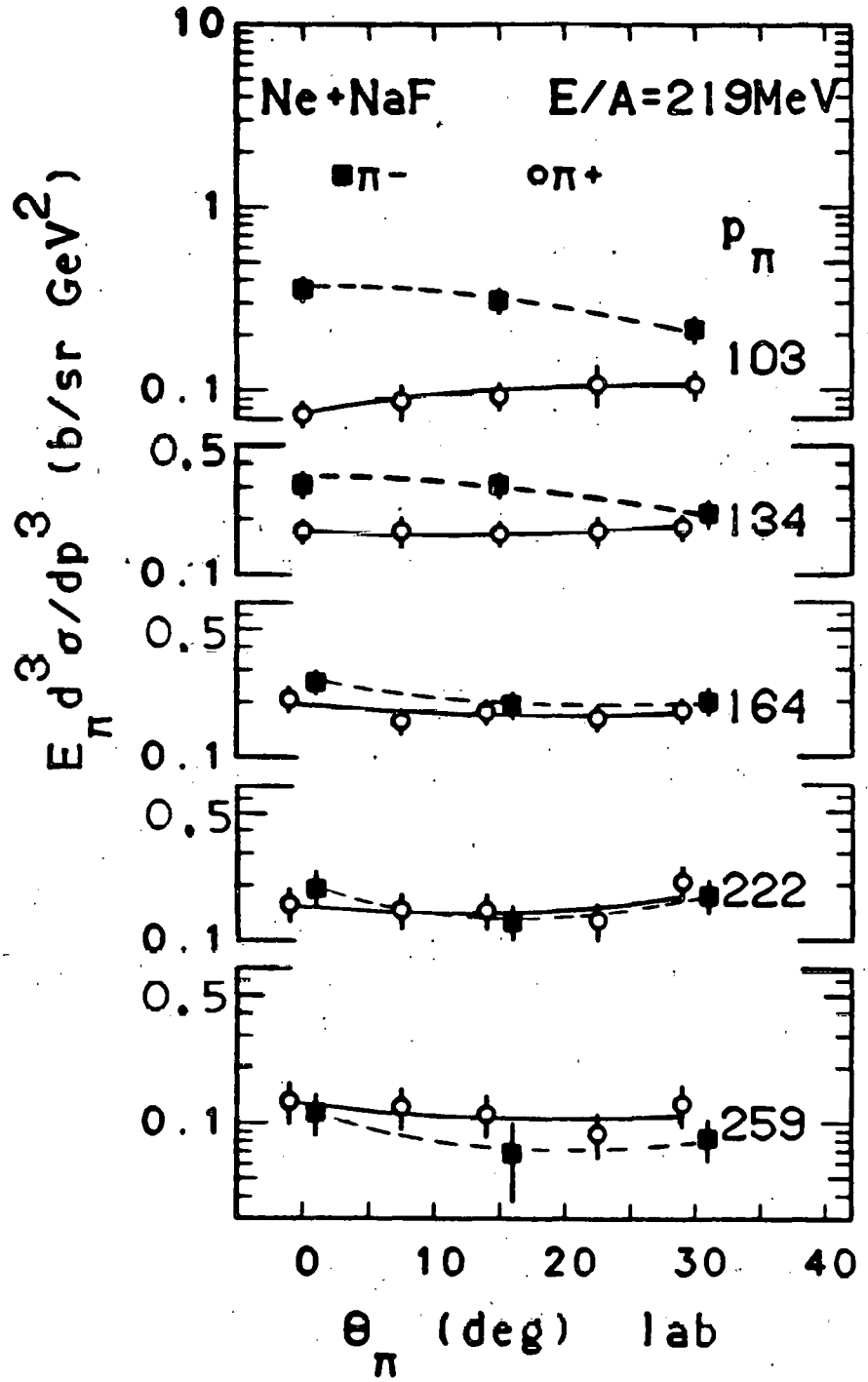

Fig. 4 -- The Lorentz invariant cross section vs. pion lab angle for Ne+NaF → π at E/A = 219 MeV. The numbers next to each set of points refer to the lab momentum of the pion in MeV/c. The lines are to guide the eye. The error bars are relative errors -- they not not include the uncertainty in the normalization.

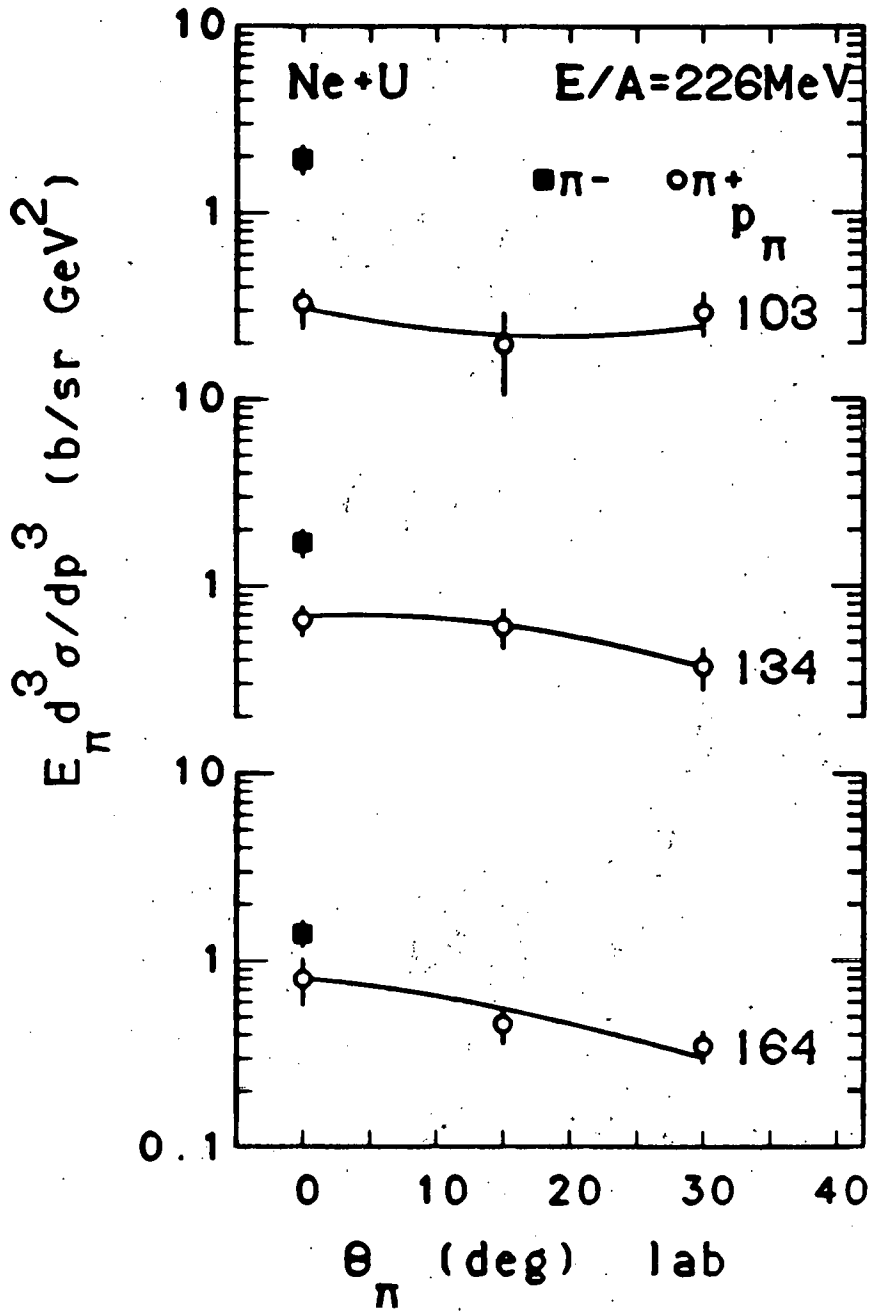

Fig. 5 -- The Lorentz invariant cross section vs. pion lab angle for Ne + U → π at E/A = 226 MeV. The numbers next to each set of points refer to the lab momentum of the pion in MeV/c. The lines are to guide the eye. The error bars are relative errors -- they not not include the uncertainty in the normalization.

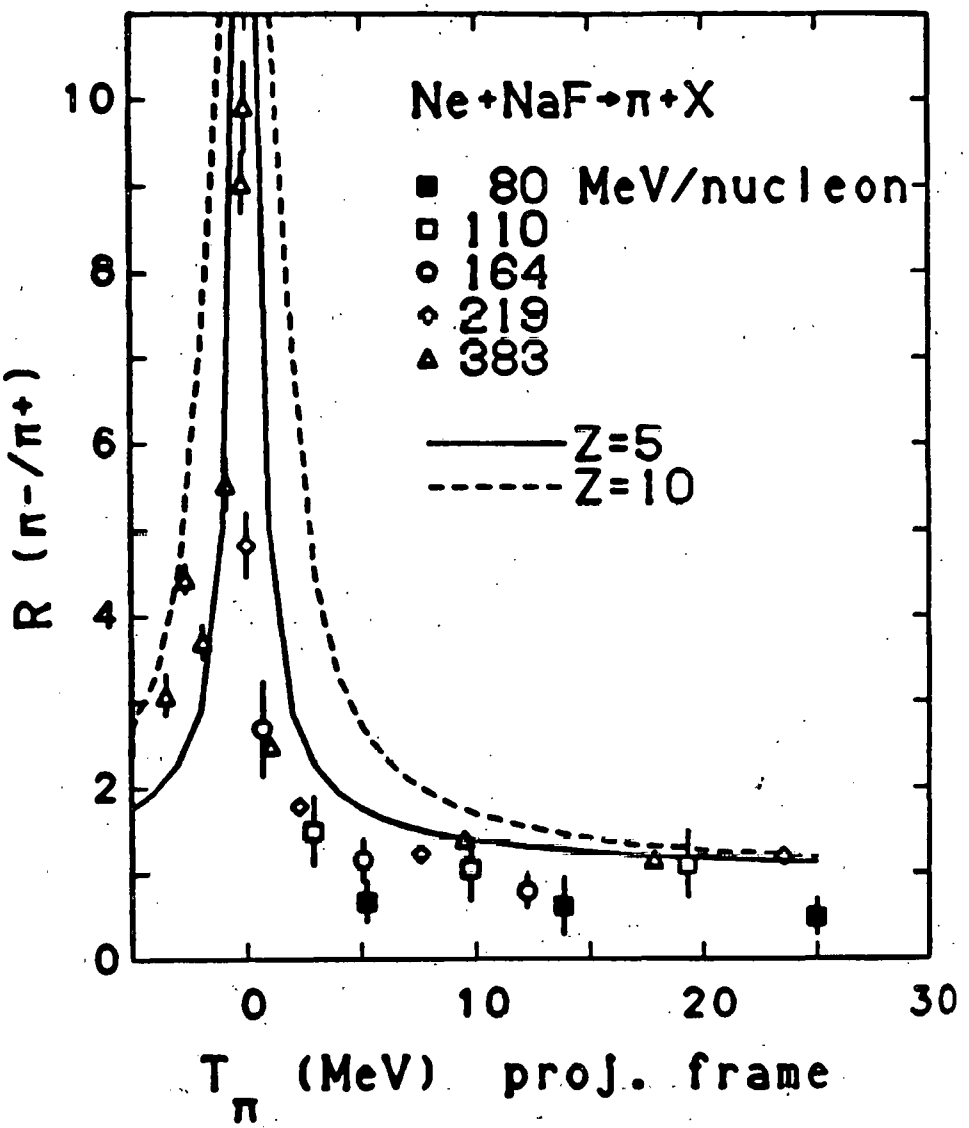

Fig. 6 -- The π^-/π^+ ratio as a function of the kinetic energy of the pion in the rest frame of the incident projectile for Ne+NaF at the indicated beam energies. The lines are based on equation 2.1 assuming that the charge on the projectile fragment is 5 (solid line) and 10 (dashed line). The error bars on the data points are statistical.

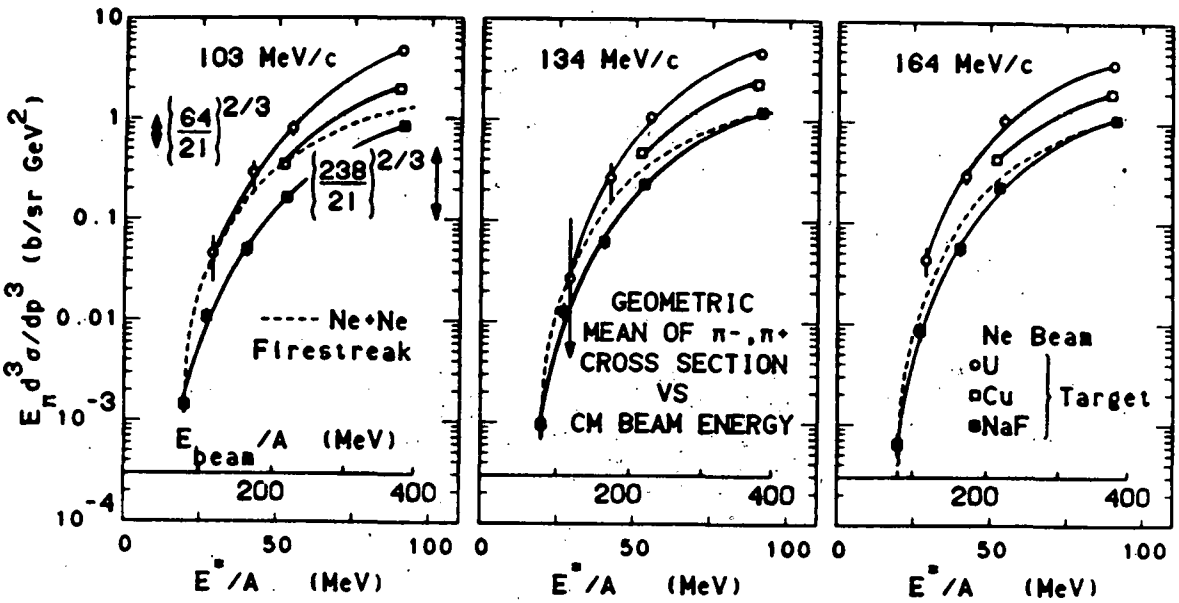

Fig. 7 -- The Lorentz invariant cross section as a function of the Ne beam energy per nucleon in the nucleon-nucleon center of mass at three different pion lab momenta. In order to approximately remove the Coulomb effects, the geometric mean of the π^+ and π^- cross sections has been plotted. The arrows on the left hand side of the figure show the expected separation of the curves for different targets if the cross sections scaled with the target mass to the 2/3 power. The solid lines serve only to guide the eye. The dashed lines show the predictions of the firestreak model[23] for Ne+Ne. The error bars on the data points do not include the uncertainty in the overall normalization.

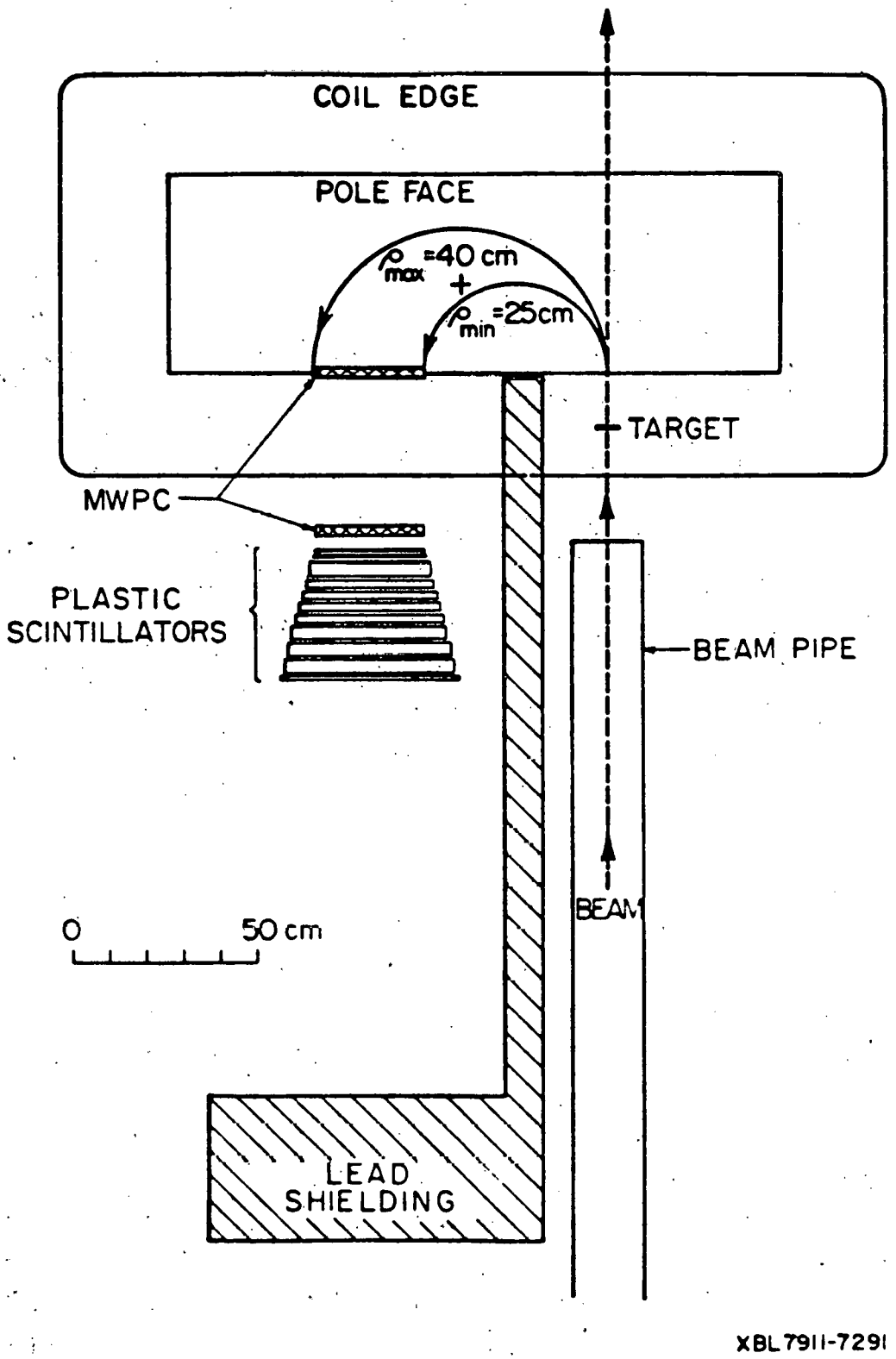

Fig. 6 -- Schematic diagram of the spectrometer used in the second stage of the experiments (the "upgraded spectrometer").

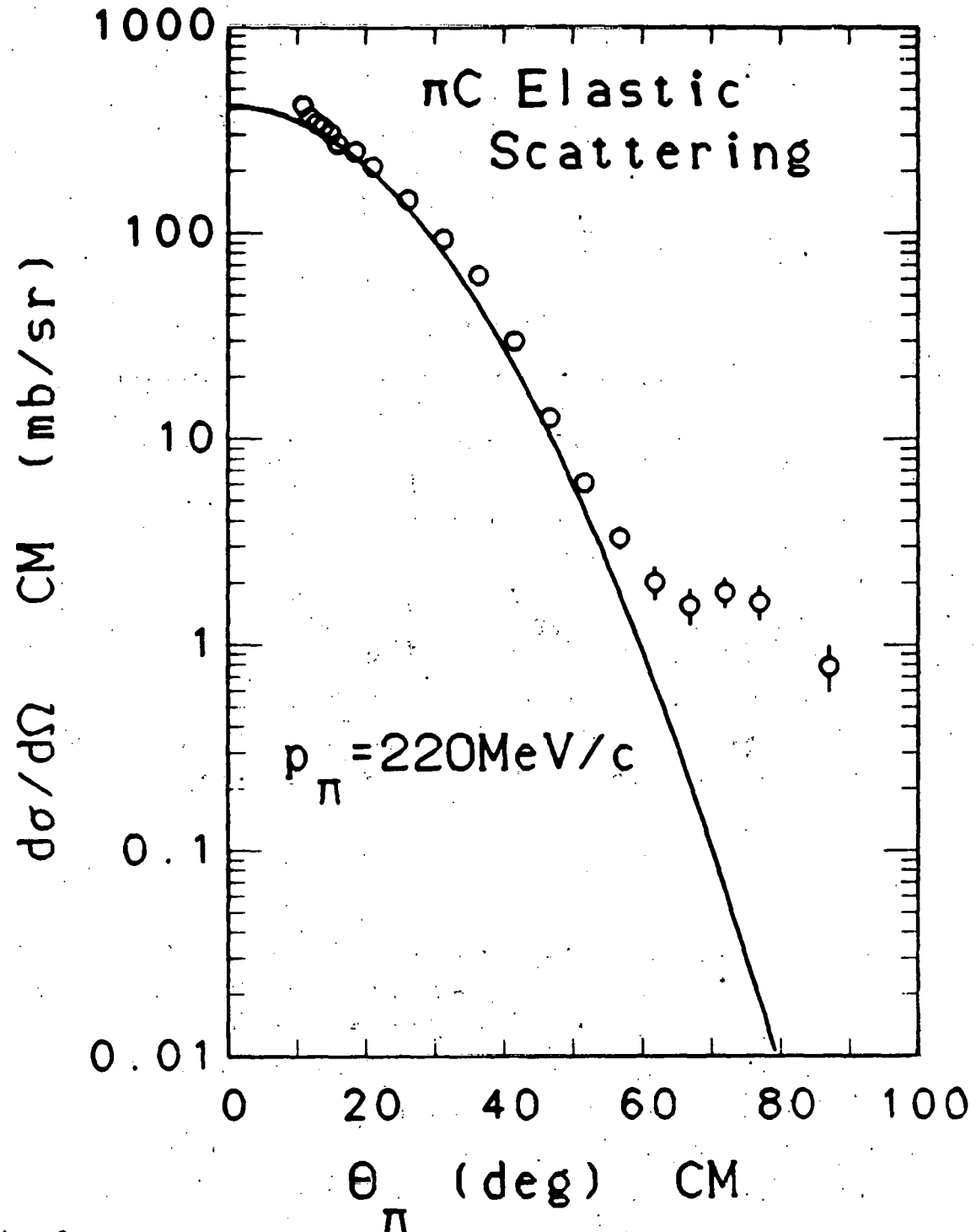

Fig. 9 -- Comparison of the assumed (Gaussian) form of the elastic scattering differential cross section for pions scattered by a carbon target with the measurements of Binon et al.[56] for pions with lab momenta of 220 MeV/c. The assumed form of the differential cross section is given by equation 4.1.

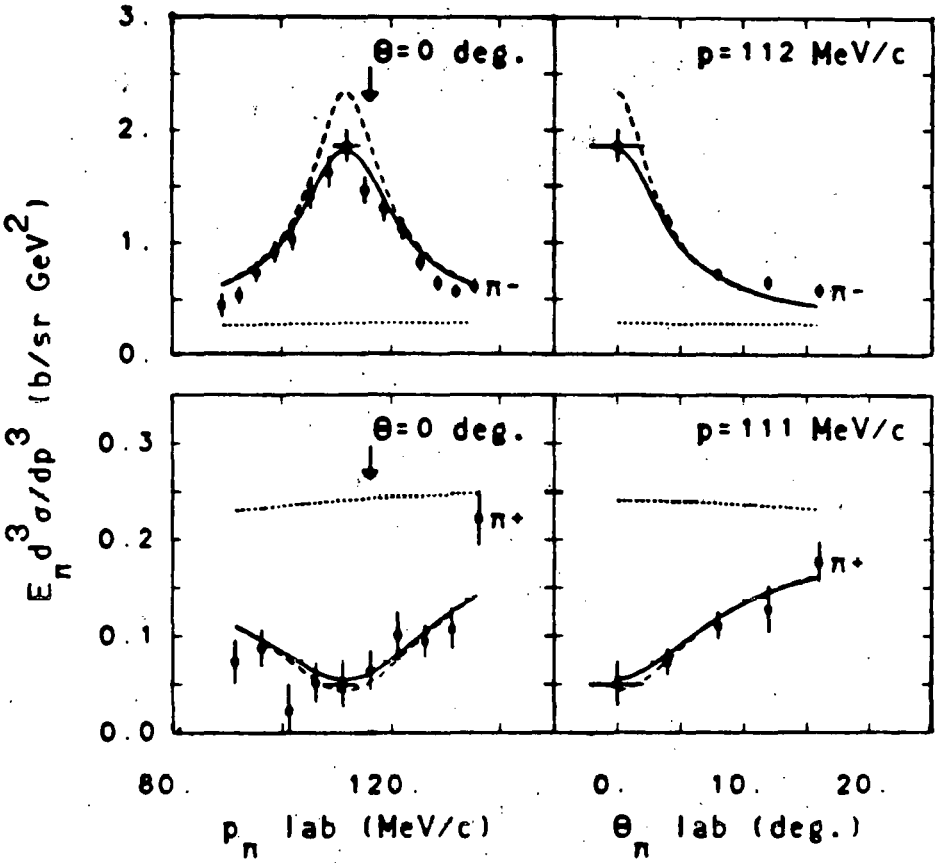

Fig. 10 -- Lorentz invariant cross section cuts for Ne+NaF $\rightarrow\pi^{\pm}$ at E/A = 281 MeV. The left side of the graph shows the cross section vs. momentum at 0 degrees in the lab for π^- (top) and π^+ (bottom). The right side shows the cross section vs. lab angle at a fixed lab momentum near the peak in the π^- spectrum. The solid line is from a least squares fit of a function based on the Coulomb correction equations of Gyulassy and Kauffmann[42]. This solid line has the experimental resolution folded into it. The dashed line is the same function before folding with the resolution. The dotted line shows the cross section predicted by the uncharged pion source function to which the Coulomb effects were applied. The arrows on the left-hand graphs mark the velocity of the incident beam.

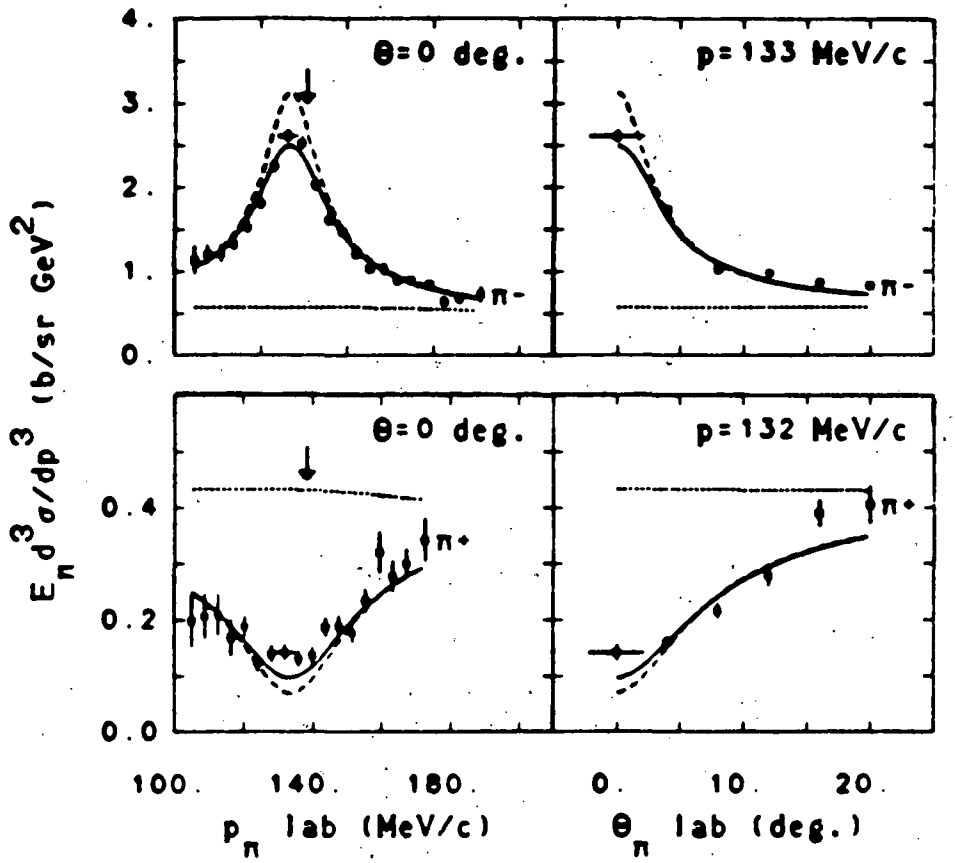

Fig. 11 -- Lorentz invariant cross section cuts for Ne+NaF $\rightarrow\pi^{\pm}$ at E/A = 380 MeV. See the caption for figure 10 for further details.

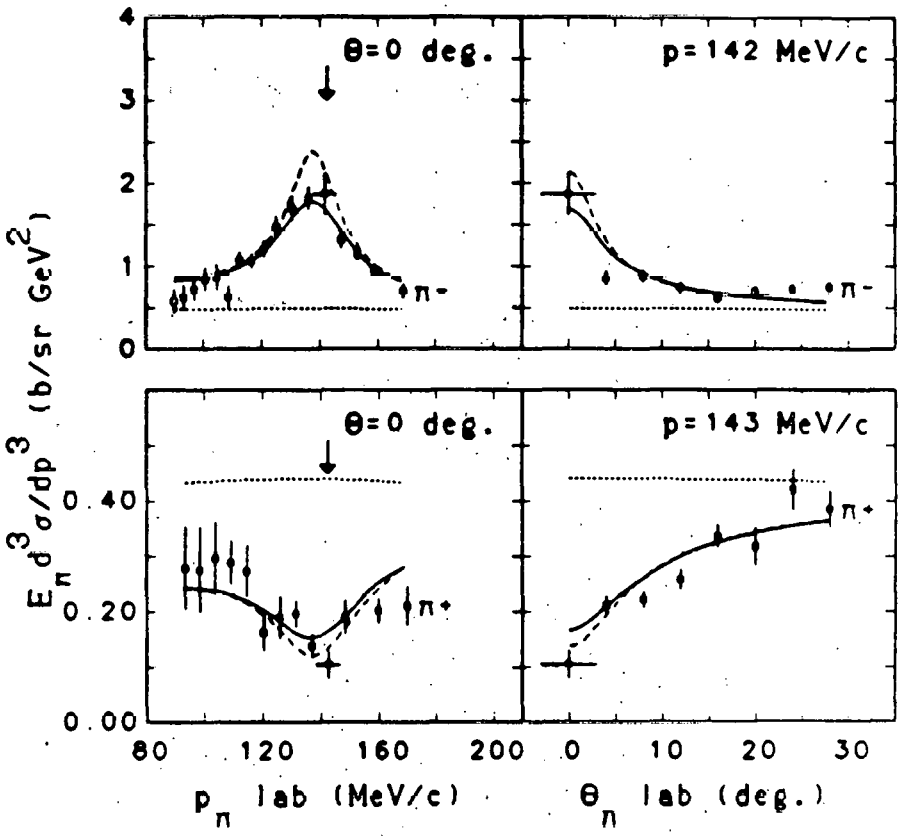

Fig. 12 -- Lorentz invariant cross section cuts for Ne+NaF $\rightarrow \pi^{\pm}$ at E/A = 400 MeV. See the caption for figure 10 for further details.

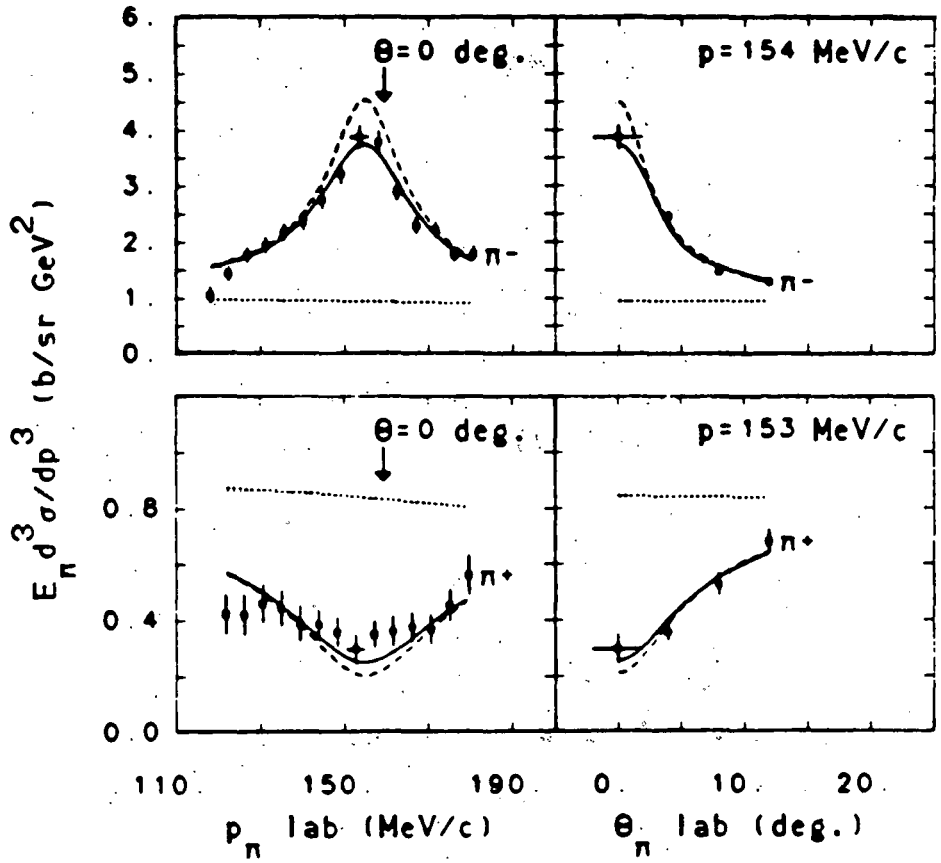

Fig. 13 -- Lorentz invariant cross section cuts for Ne+NaF $\rightarrow\pi^{\pm}$ at E/A = 483 MeV. See the caption for figure 10 for further details.

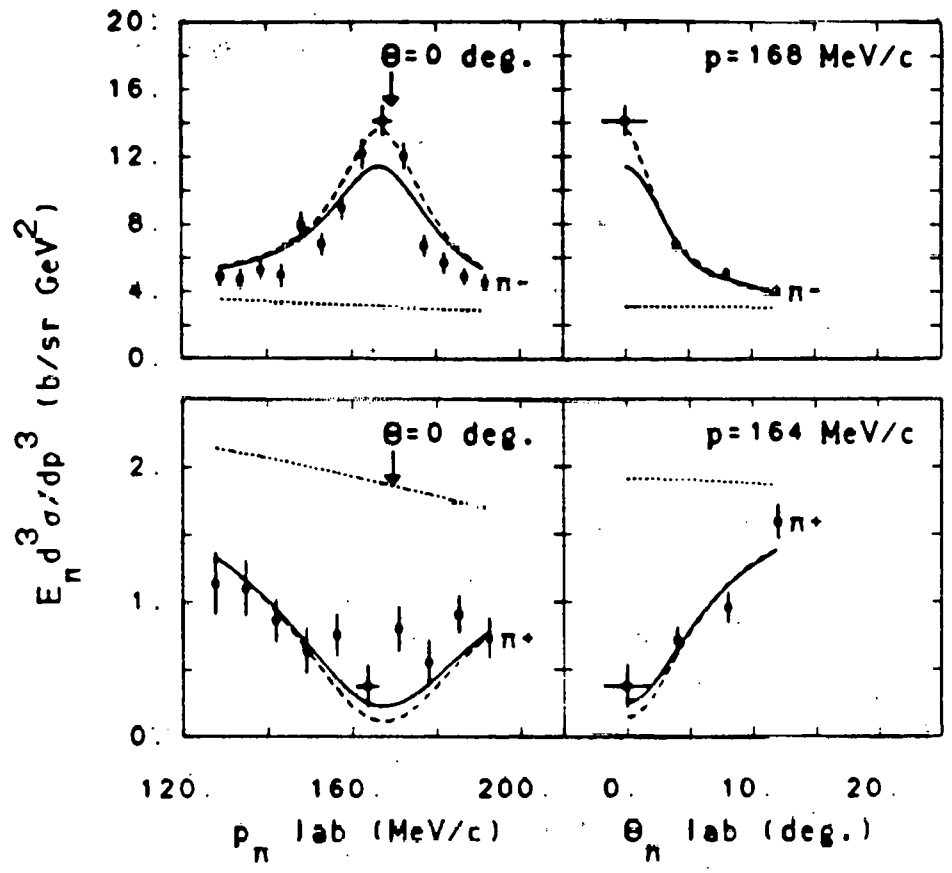

Fig. 14 -- Lorentz invariant cross section cuts for Ar+KCl $\rightarrow \pi^{\pm}$ at E/A = 534 MeV. See the caption for figure 10 for further details.

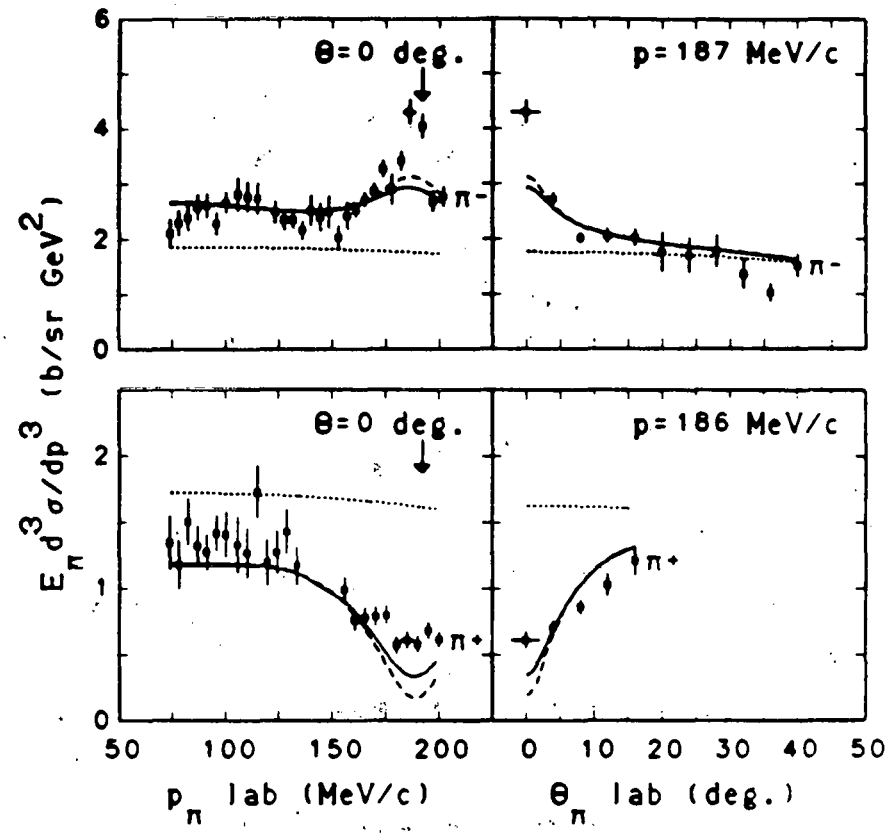

Fig. 15 -- Lorentz invariant cross section cuts for Ne+NaF $\rightarrow\pi^{\pm}$ at E/A = 655 MeV. See the caption for figure 10 for further details.

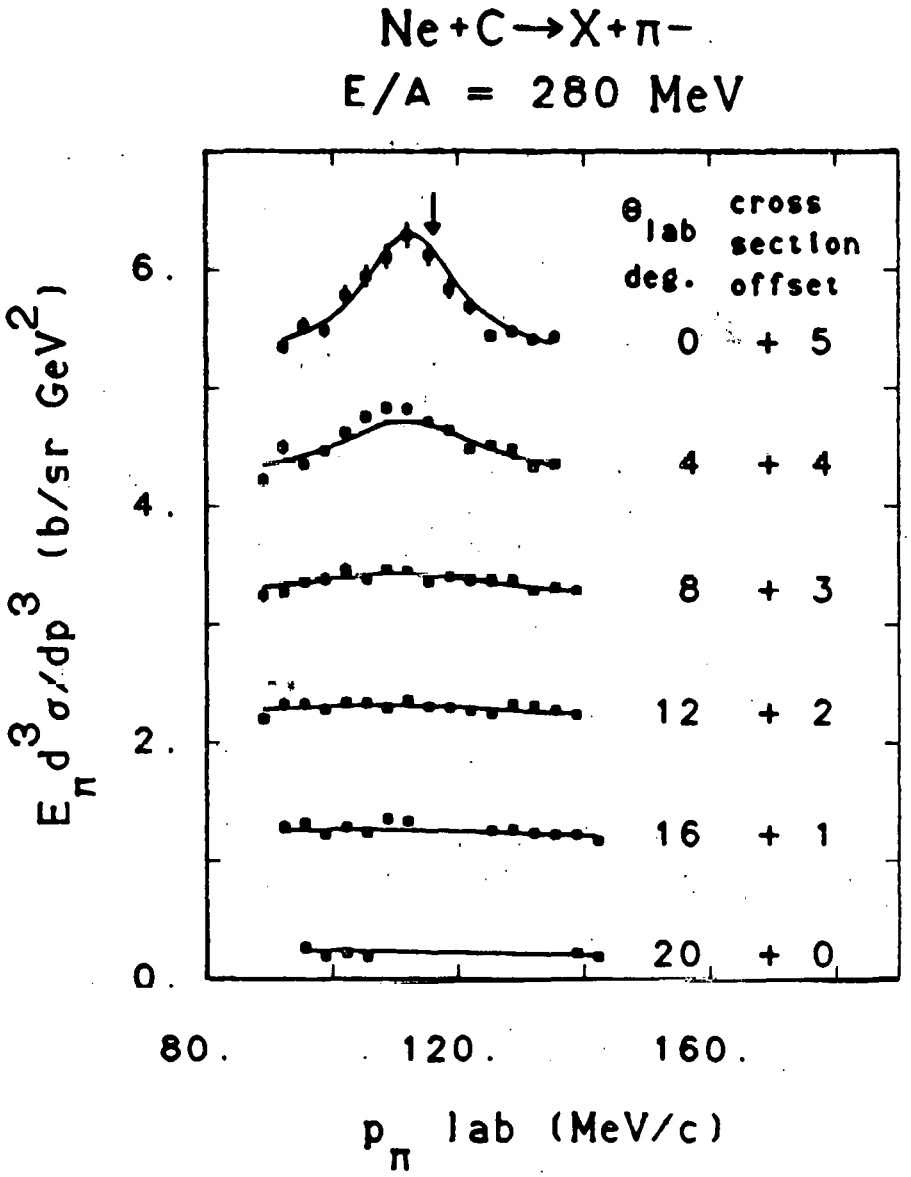

XBL 815-9938

Fig. 16A -- Lorentz invariant cross section vs. lab momentum for Ne+C $\rightarrow\pi^-$ at E/A = 280 MeV. Each set of data points is at a fixed lab angle, which is shown on the right side of the figure. A cross section offset has been added to the data at each angle (except the 20 degree data) in order to display it all on the same graph. This offset is given on the right side of the figure. The solid line is from a least squares fit of a function based on the Coulomb correction equations of Gyulassy and Kauffmann[42]. This function has been folded with the resolution of the spectrometer. The arrow marks the velocity of the incident beam.

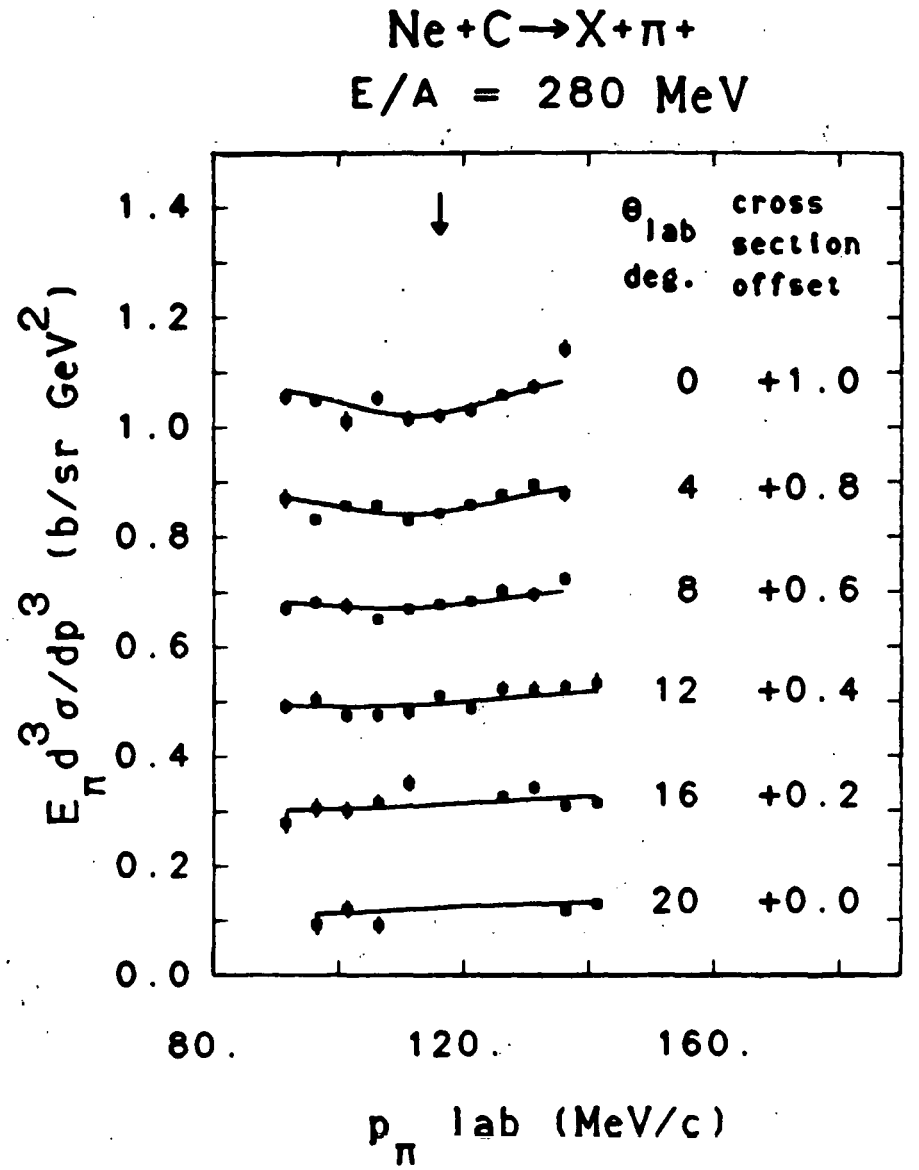

Fig. 16B -- Lorentz invariant cross section vs. lab momentum for Ne+C → π^+ at E/A = 280 MeV. See also the caption for figure 16A.

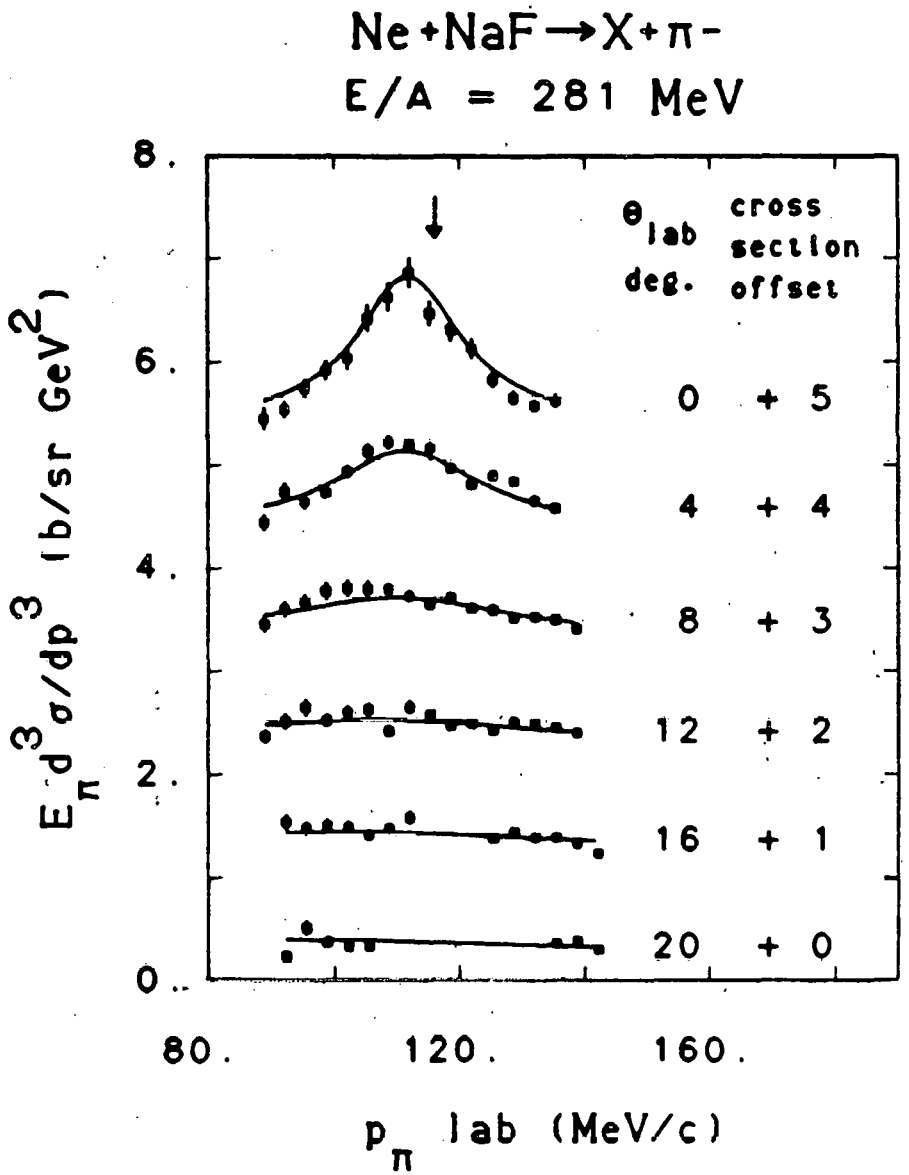

Fig. 17A -- Lorentz invariant cross section vs. lab momentum for Ne+NaF → π^- at E/A = 281 MeV. See also the caption for figure 16A.

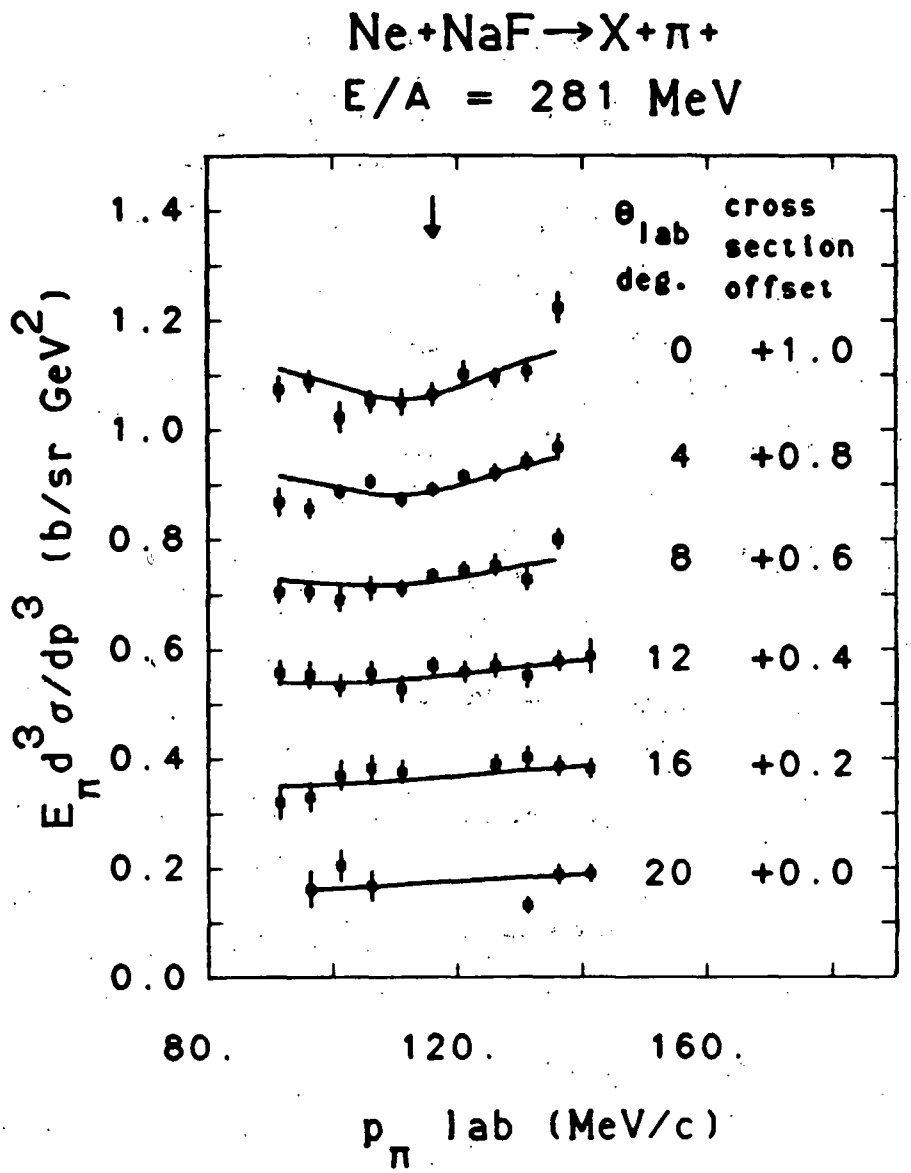

Fig. 17B -- Lorentz invariant cross section vs. lab momentum for Ne+NaF → π^+ at E/A = 281 MeV. See also the caption for figure 16A.

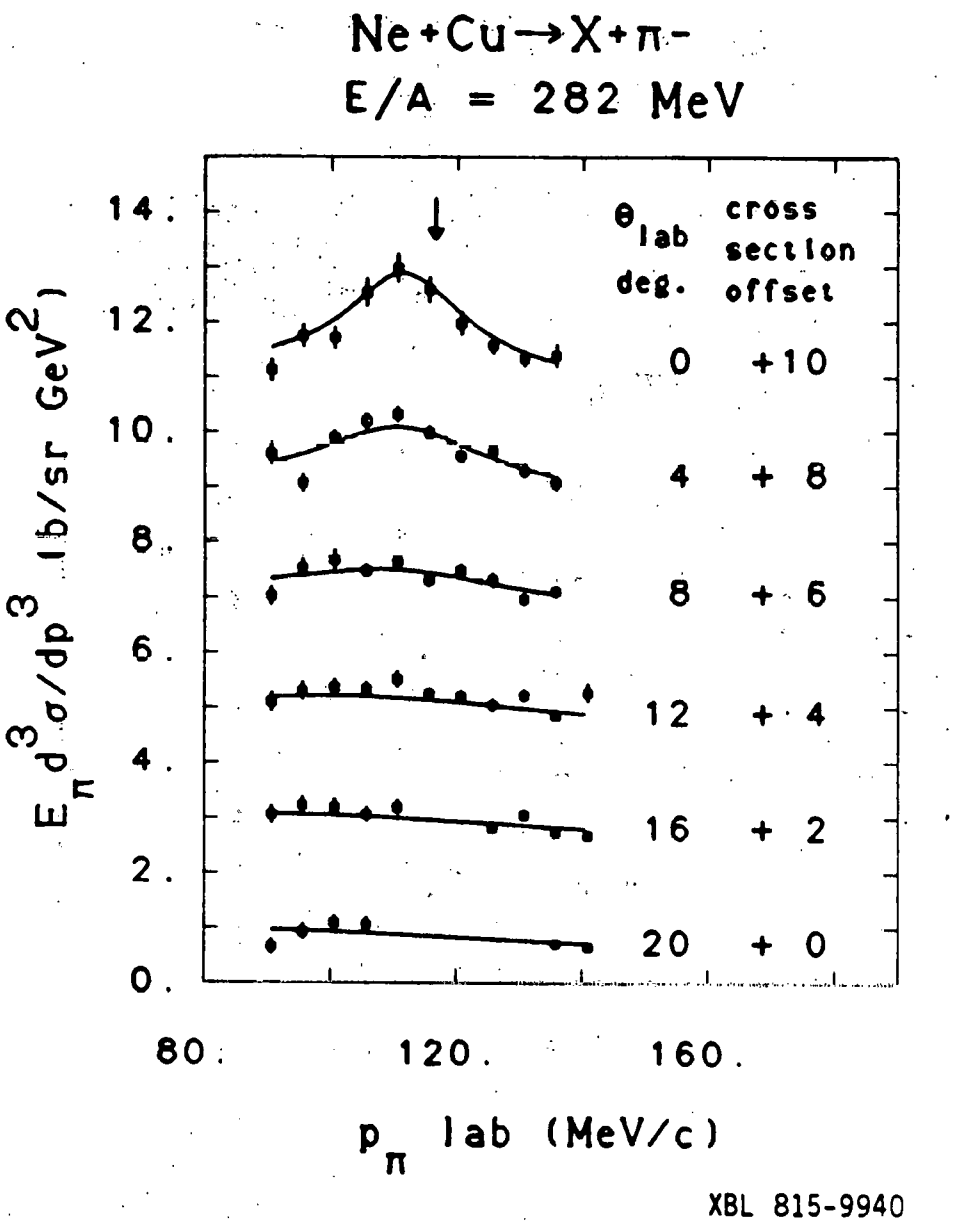

Fig. 18A -- Lorentz invariant cross section vs. lab momentum for Ne+Cu → π^- at E/A = 282 MeV. See also the caption for figure 16A.

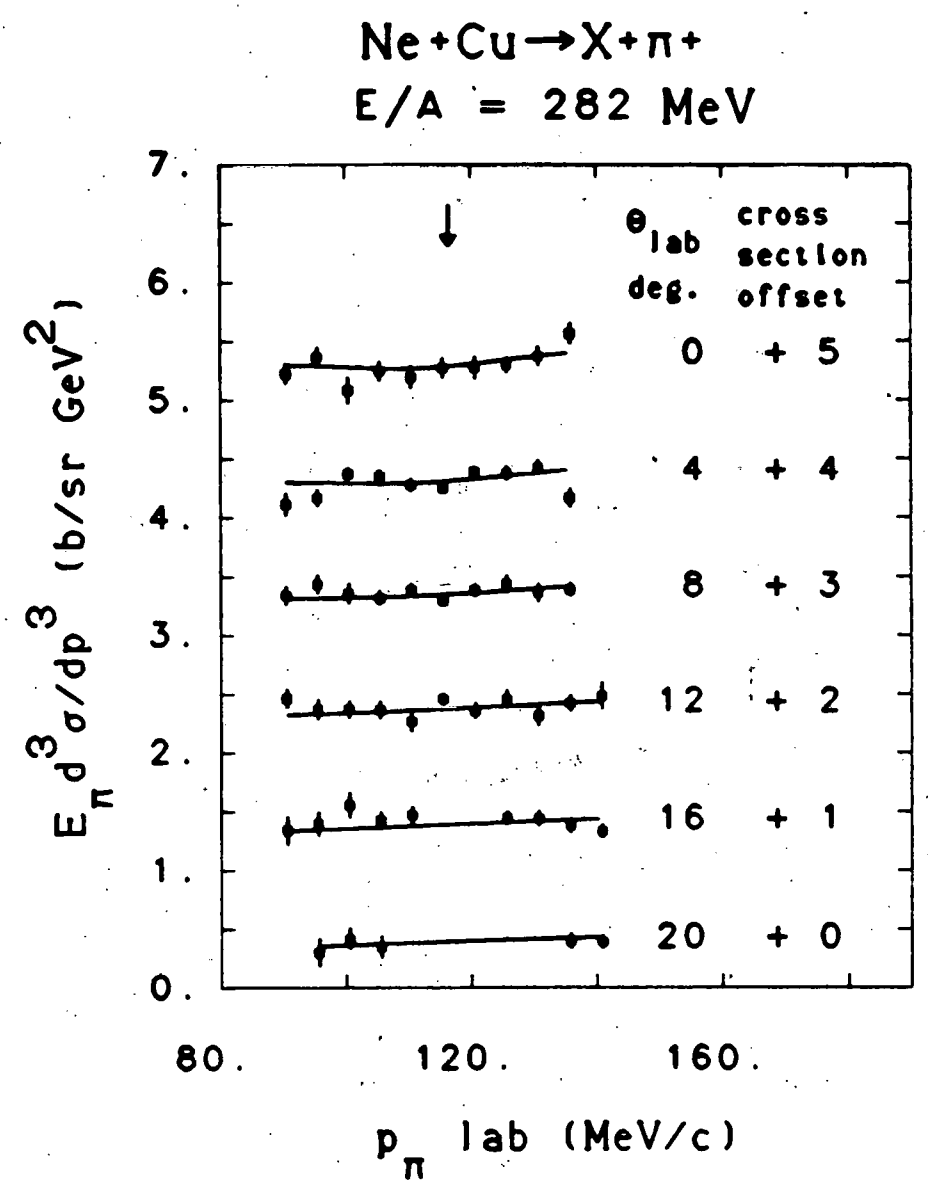

Fig. 18B -- Lorentz invariant cross section vs. lab momentum for Ne+Cu → π^+ at E/A = 282 MeV. See also the caption for figure 16A.

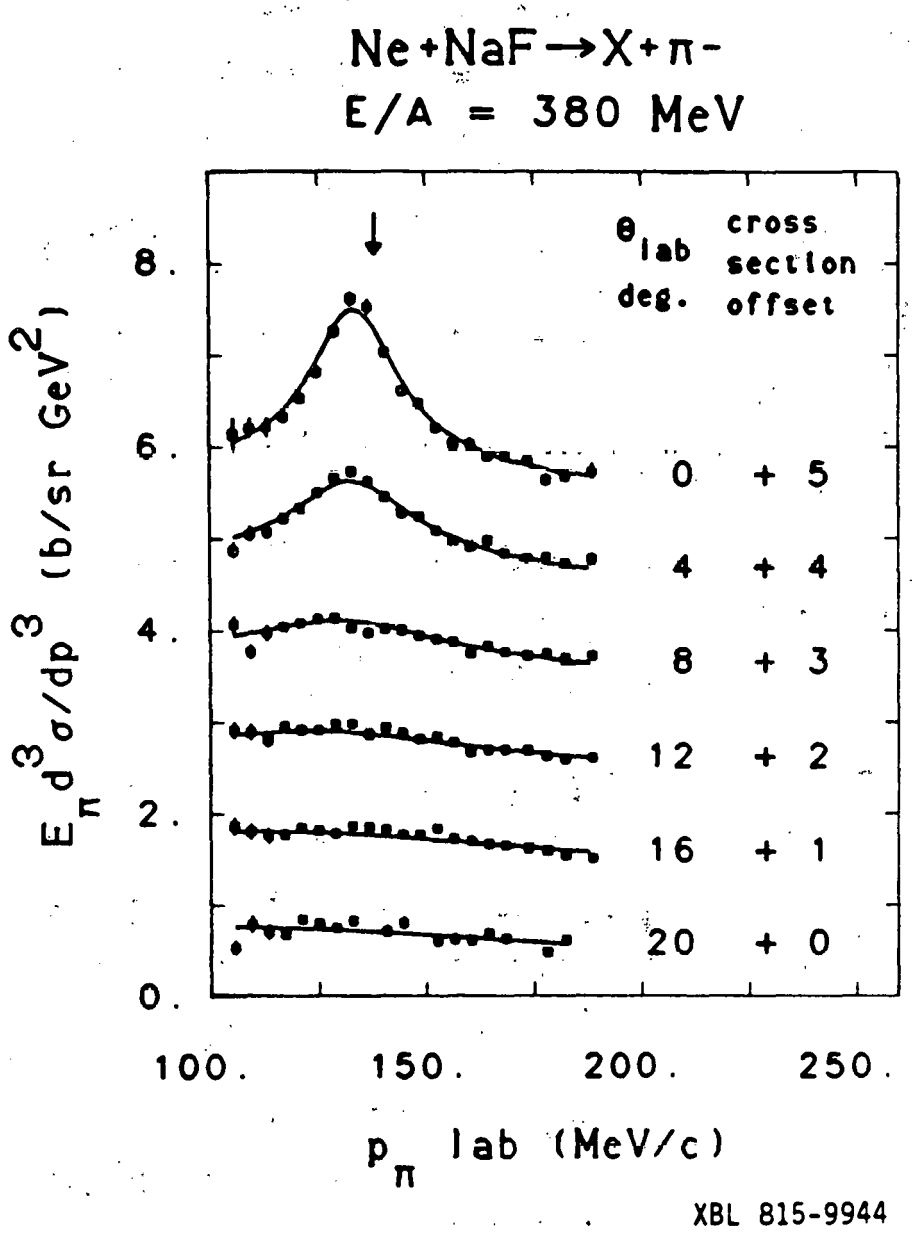

Fig. 19A -- Lorentz invariant cross section vs. lab momentum for Ne+NaF → π^- at E/A = 380 MeV. See also the caption for figure 16A.

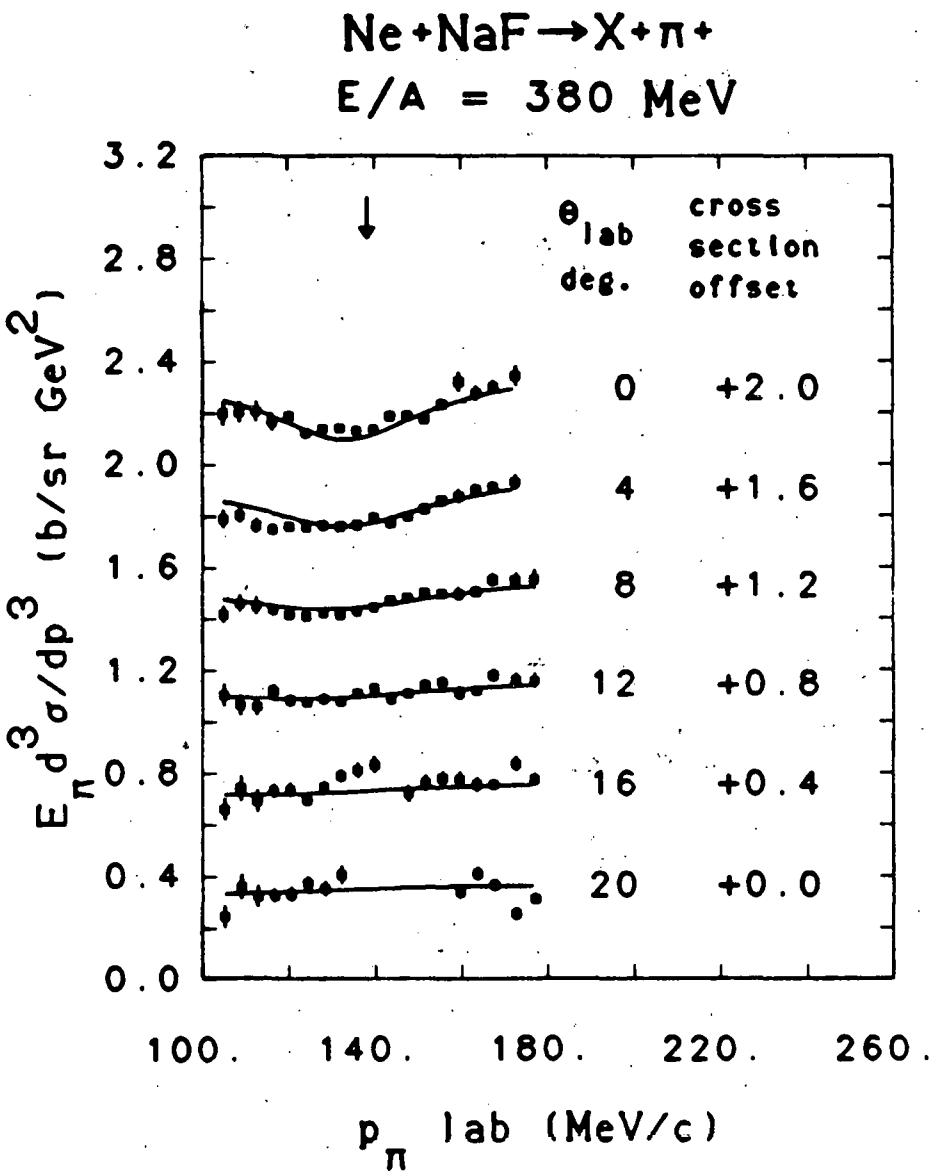

Fig. 19B -- Lorentz invariant cross section vs. lab momentum for Ne+NaF → π^+ at E/A = 380 MeV. See also the caption for figure 16A.

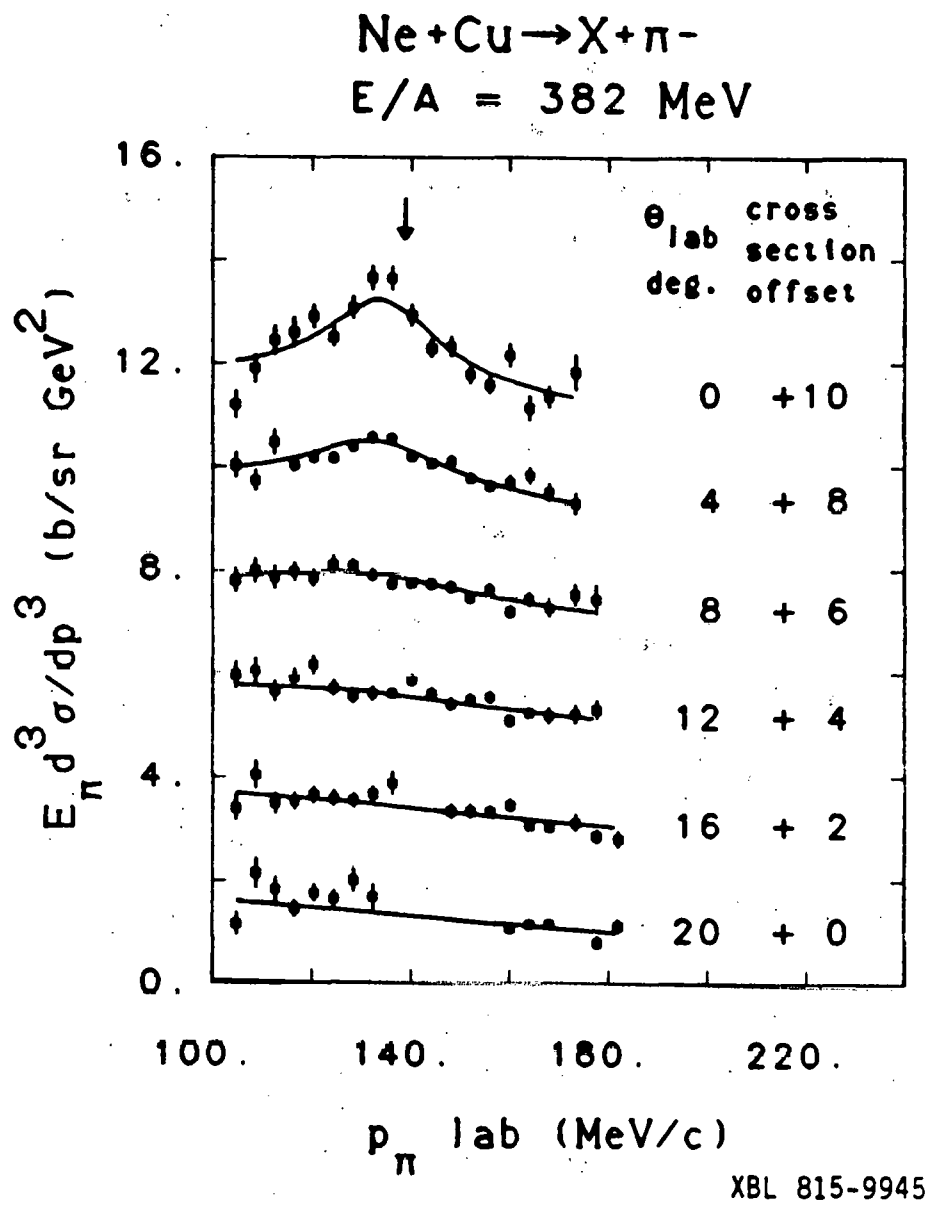

Fig. 20A -- Lorentz invariant cross section vs. lab momentum for Ne+Cu → π^- at E/A = 382 MeV. See also the caption for figure 16A.

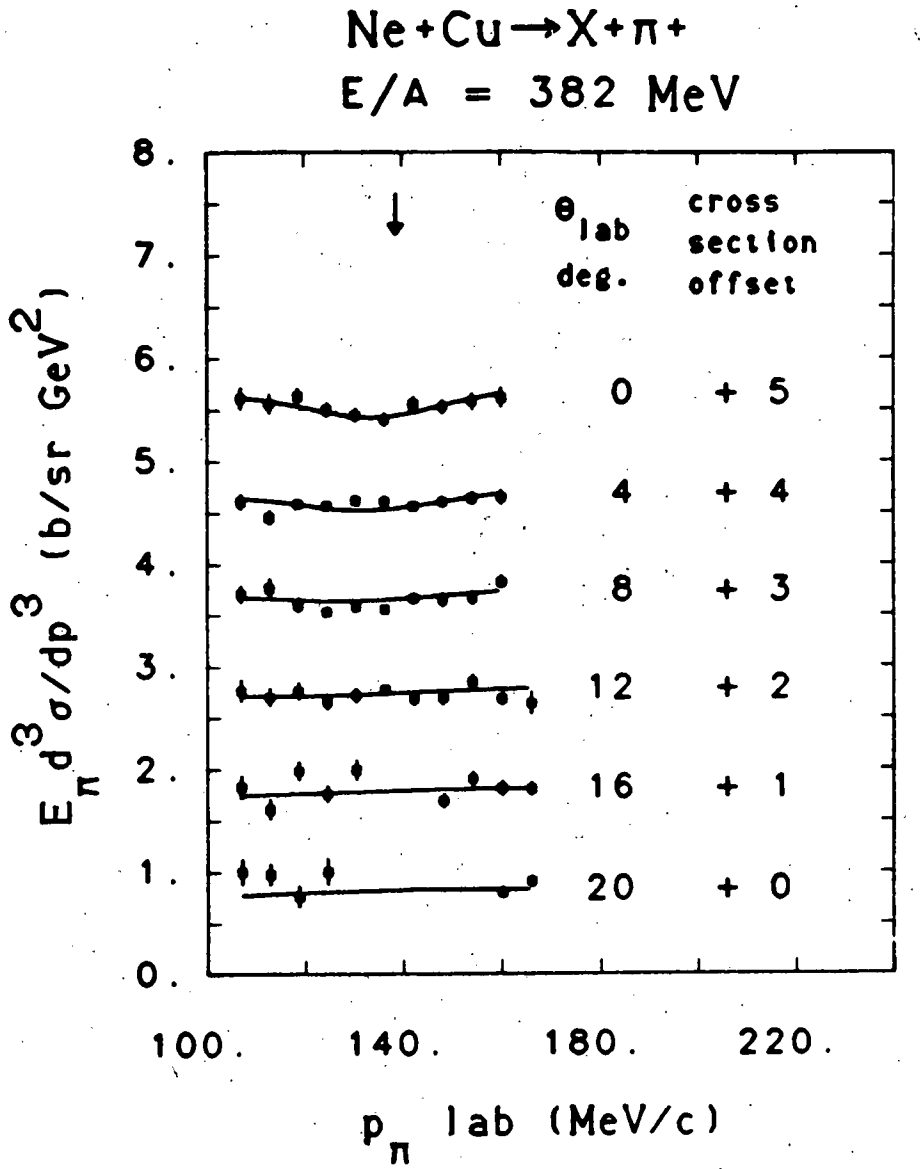

XBL 815-9948

Fig. 20B -- Lorentz invariant cross section vs. lab momentum for Ne+Cu → π^+ at E/A = 382 MeV. See also the caption for figure 16A.

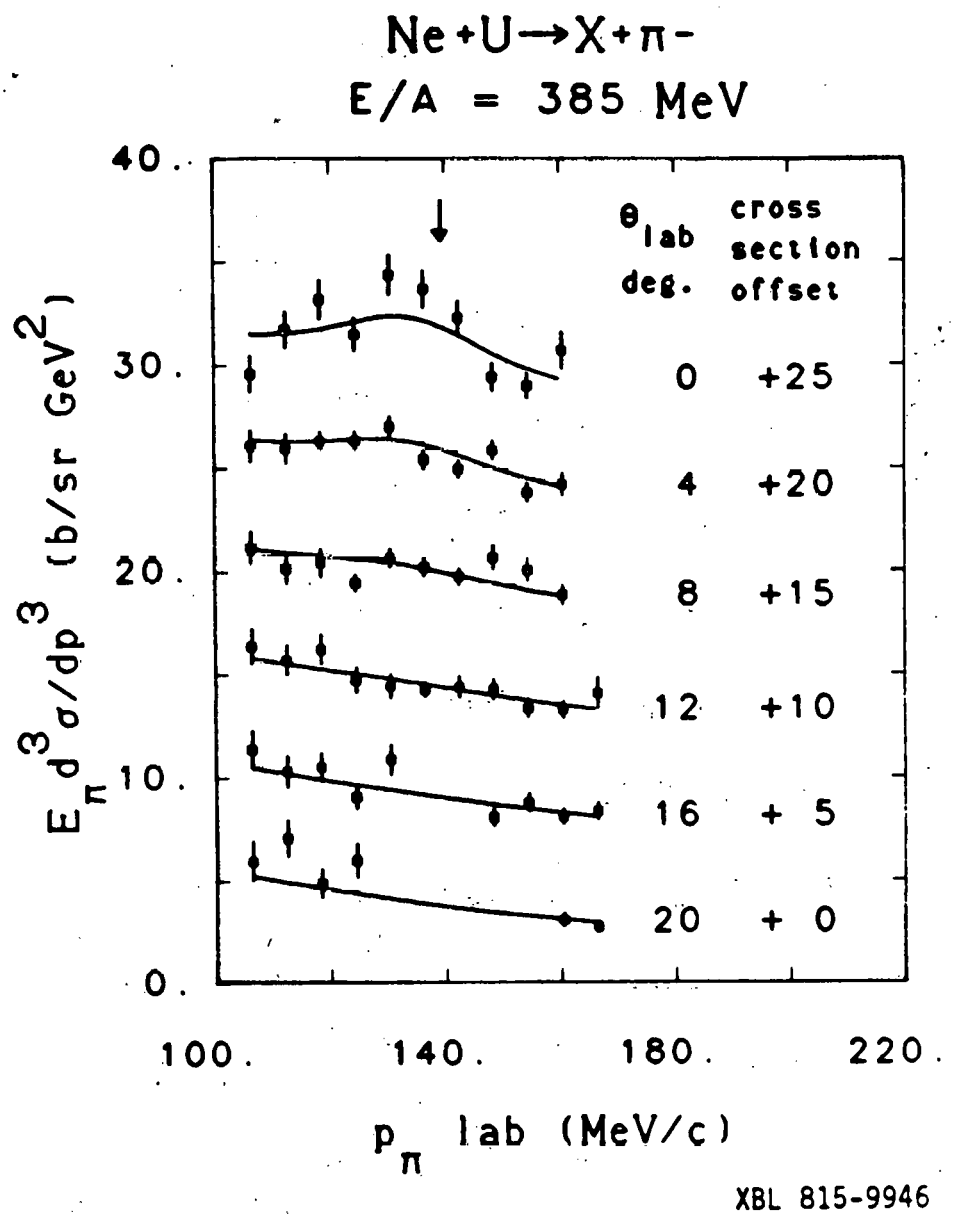

Fig. 21A -- Lorentz invariant cross section vs. lab momentum for Ne+U → π^- at E/A = 385 MeV. See also the caption for figure 16A.

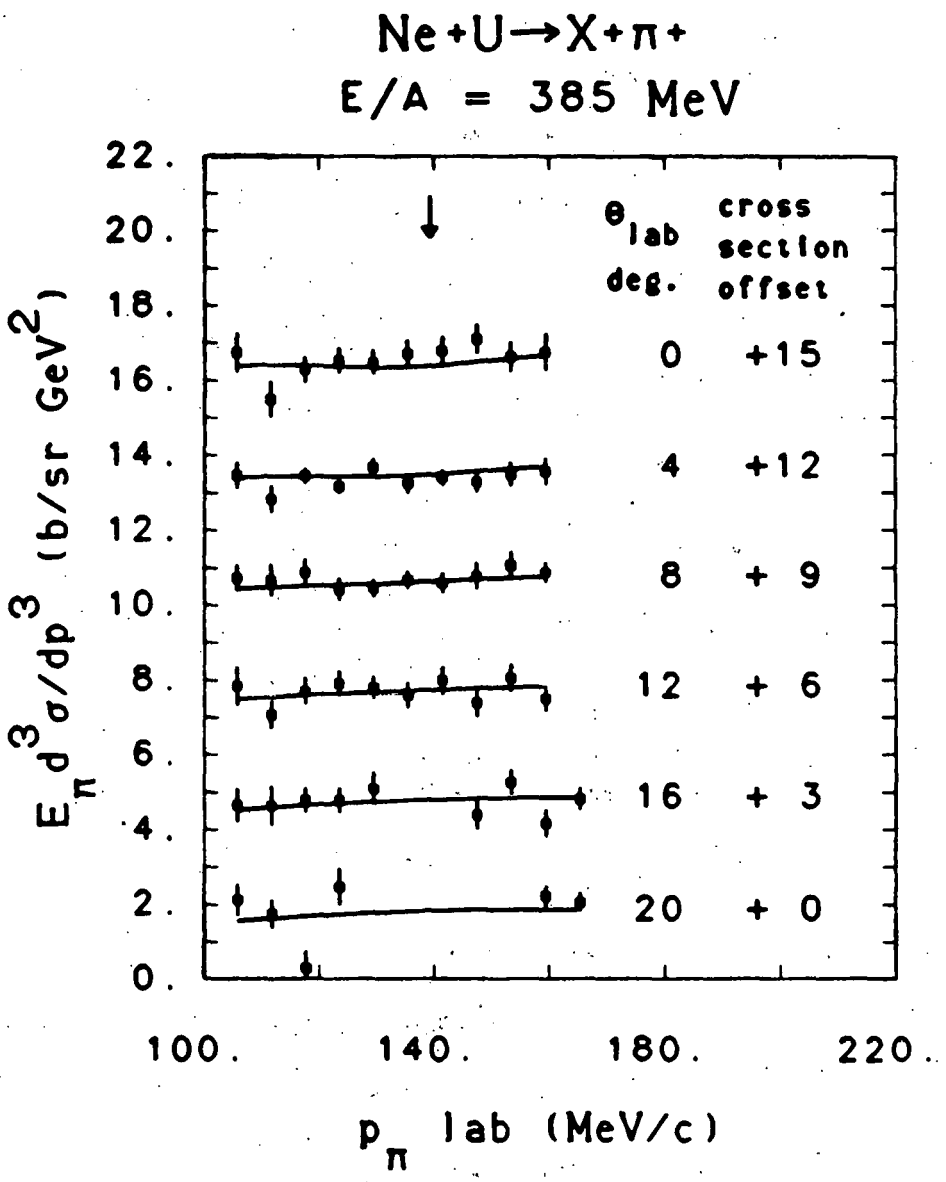

XBL 815-9949

Fig. 21B -- Lorentz invariant cross section vs. lab momentum for Ne+U → π^+ at E/A = 385 MeV. See also the caption for figure 16A.

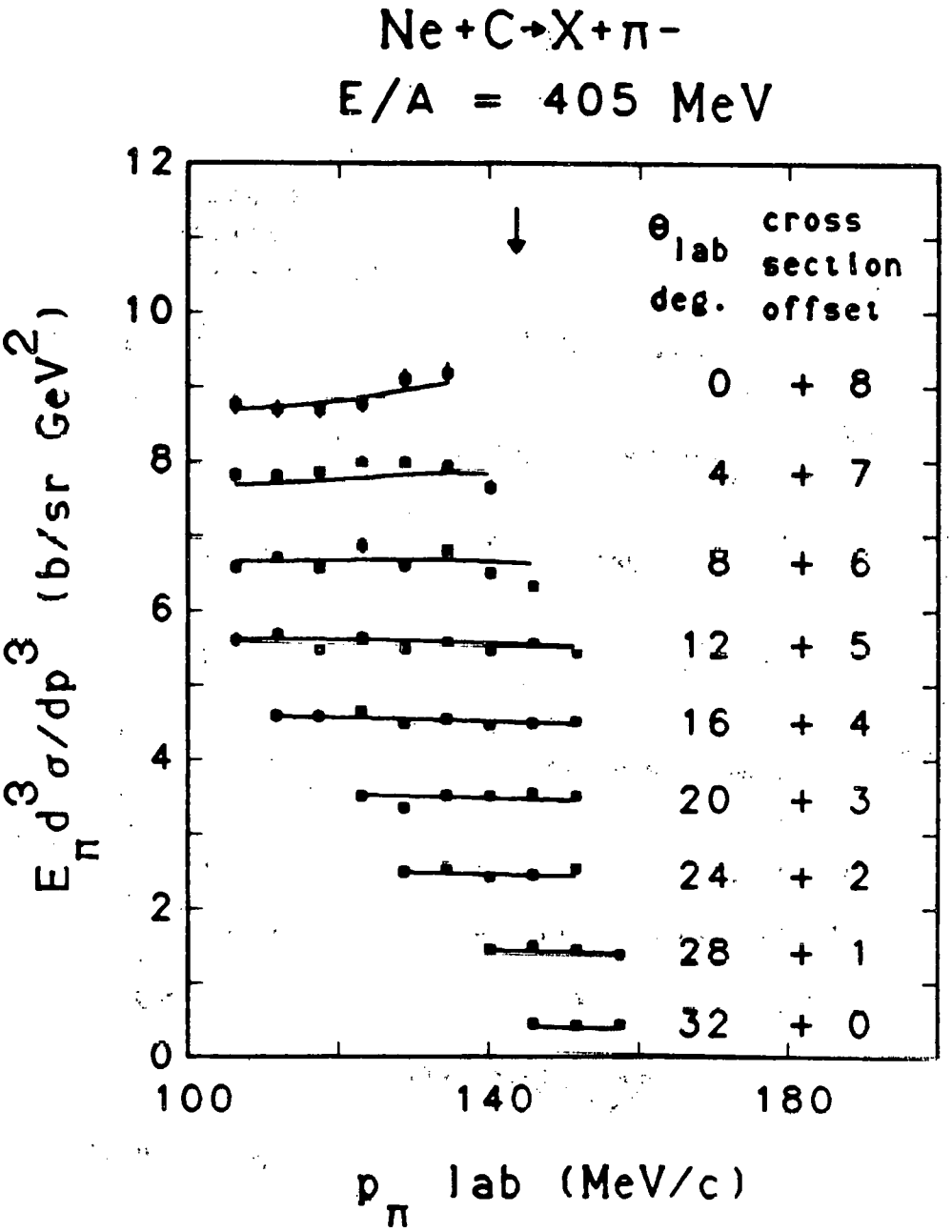

Fig. 22A -- Lorentz invariant cross section vs. lab momentum for Ne+C → π^- at E/A = 405 MeV. See also the caption for figure 16A.

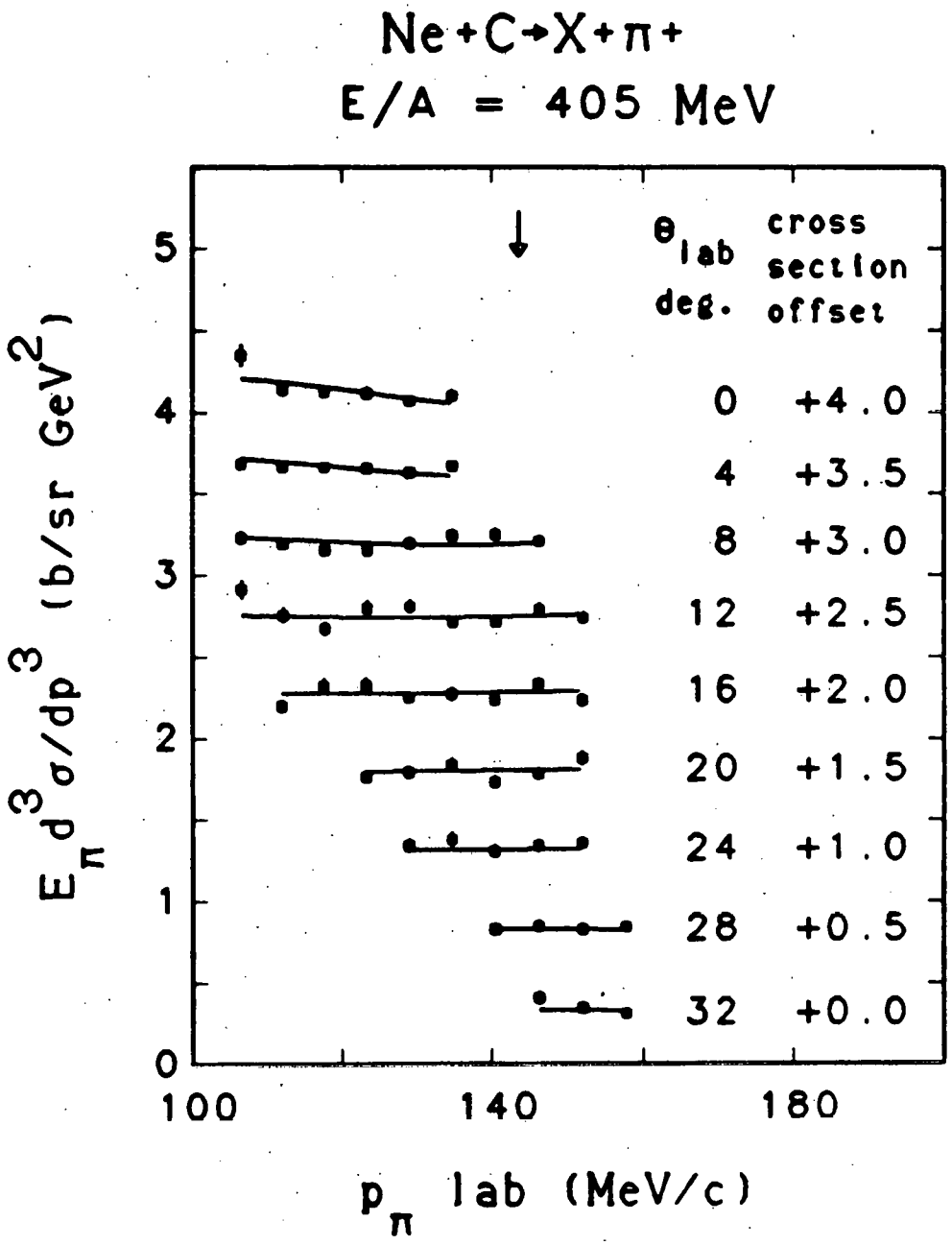

Fig. 22B -- Lorentz invariant cross section vs. lab momentum for Ne+C → π^+ at E/A = 405 MeV. See also the caption for figure 16A.

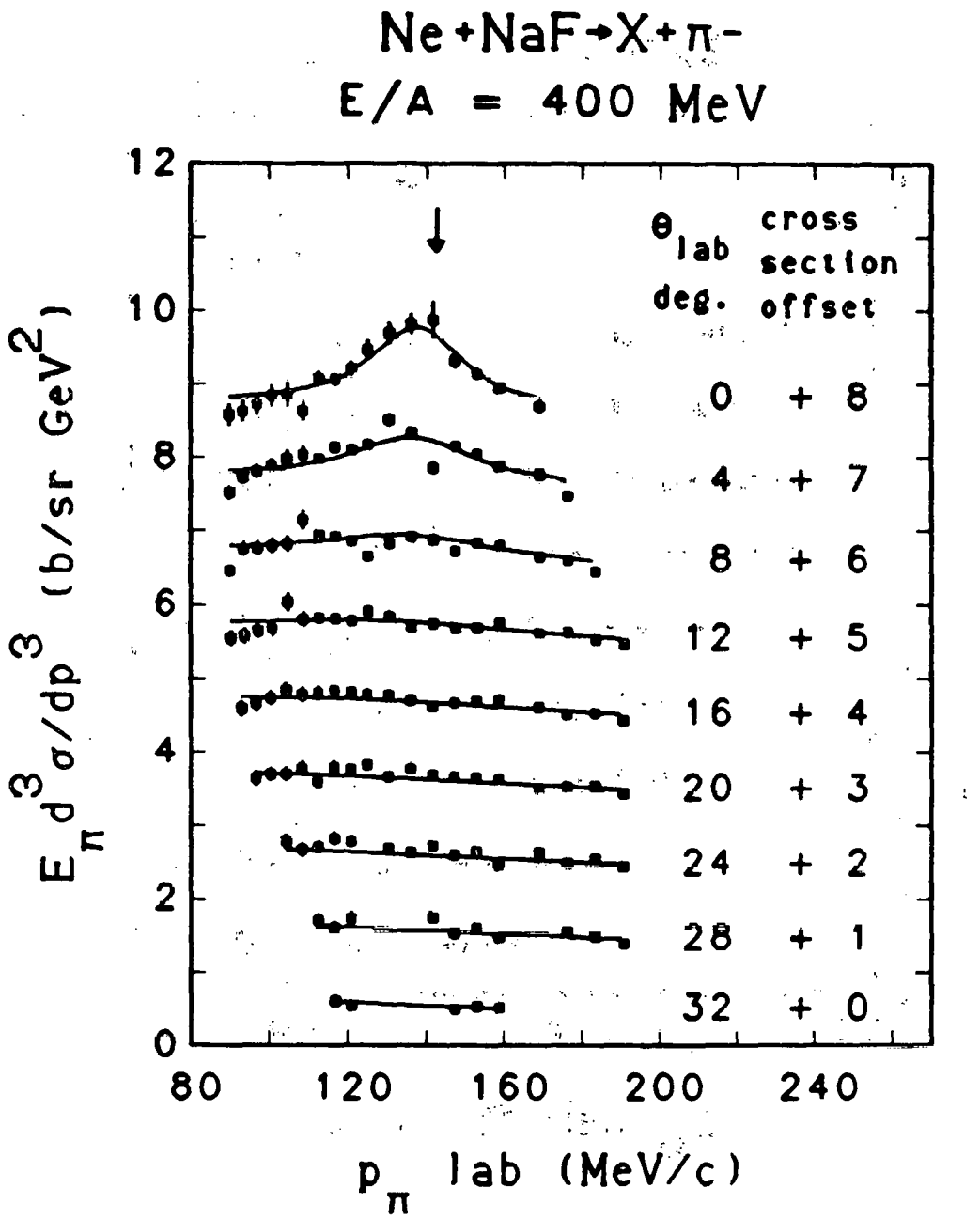

Fig. 23A -- Lorentz invariant cross section vs. lab momentum for Ne+NaF → π^- at E/A = 400 MeV. See also the caption for figure 16A.

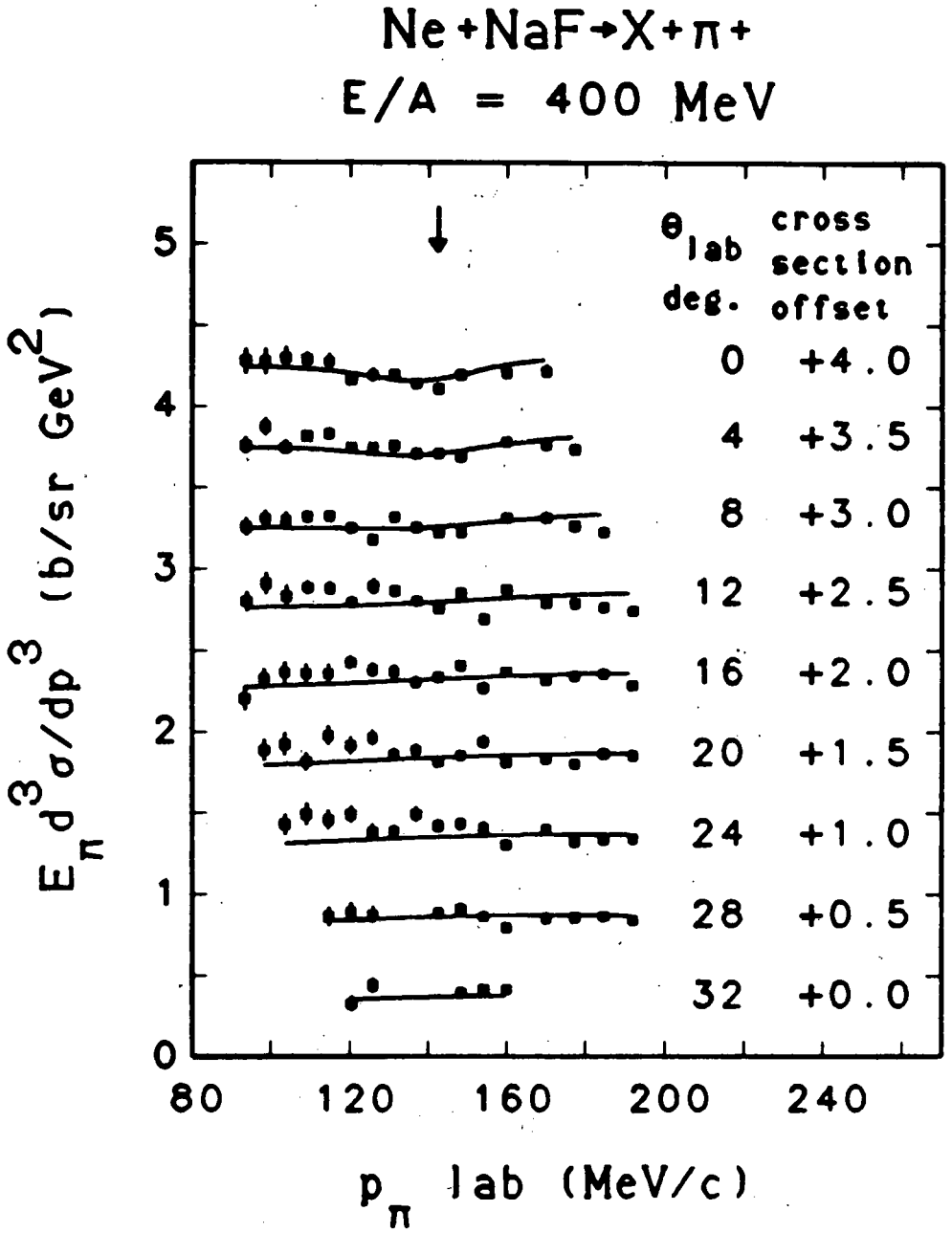

Fig. 23b -- Lorentz invariant cross section vs. lab momentum for Ne+NaF → π^+ at E/A = 400 MeV. See also the caption for figure 16A.

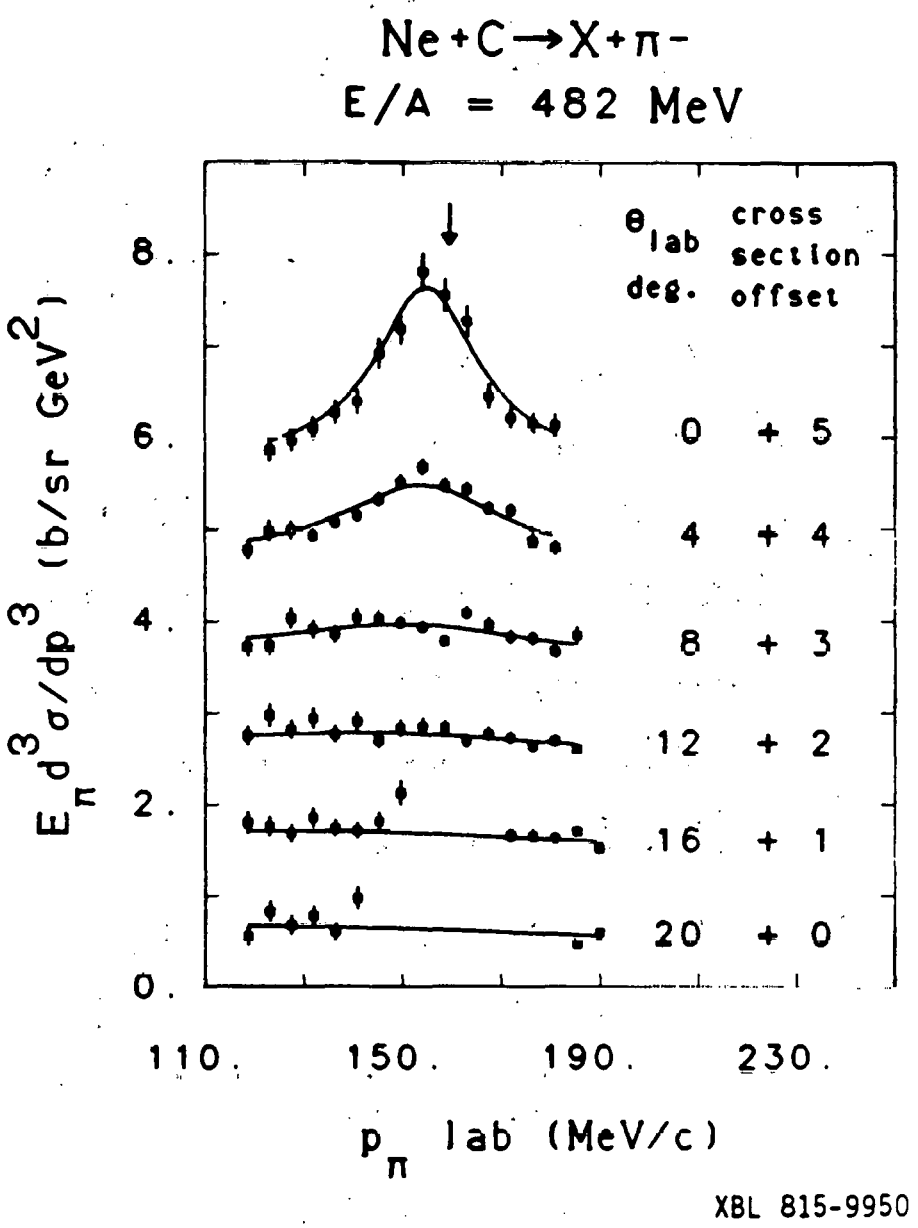

Fig. 25A -- Lorentz invariant cross section vs. lab momentum for Ne+C → π^- at E/A = 482 MeV. See also the caption for figure 16A.

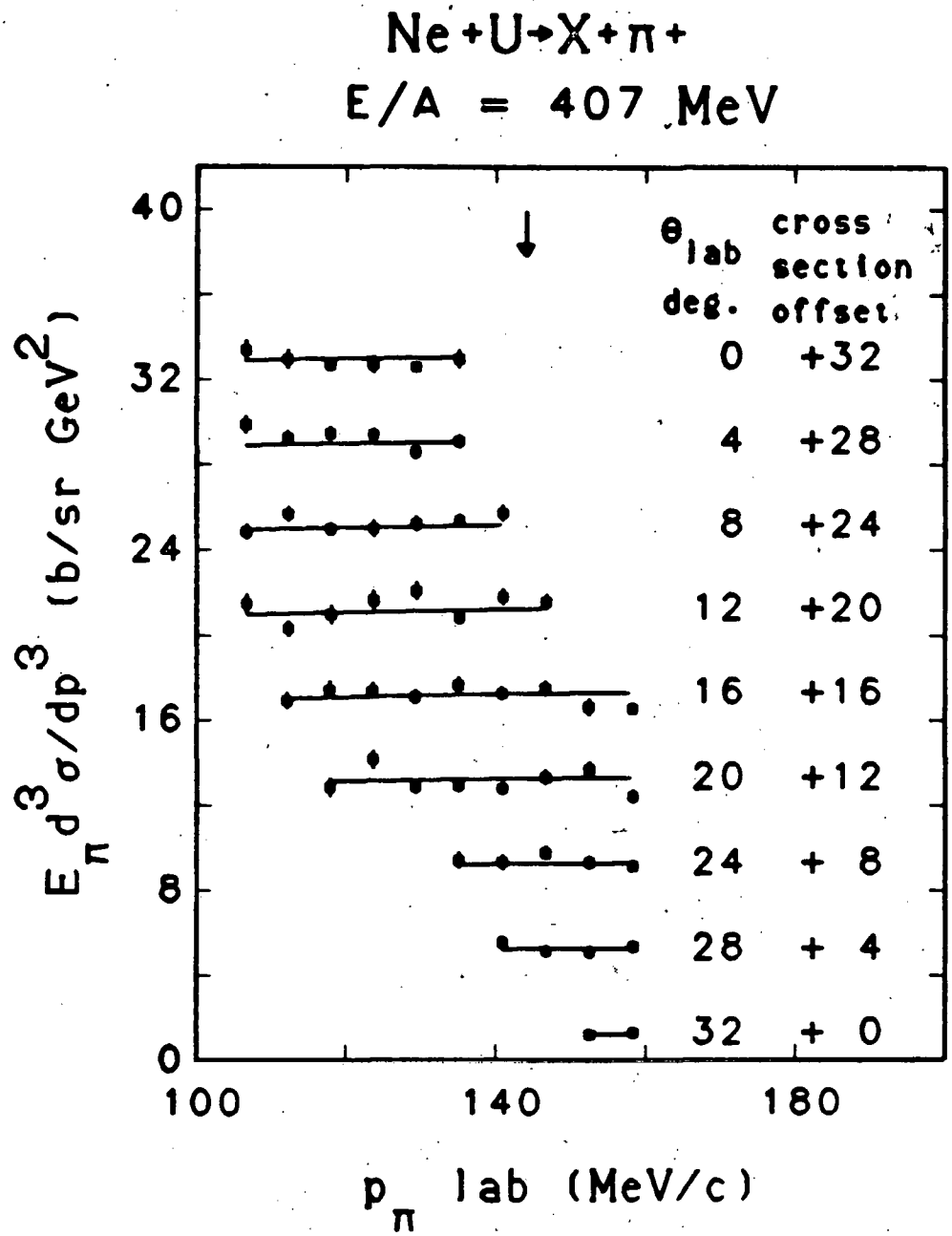

Fig. 24B -- Lorentz invariant cross section vs. lab momentum for Ne+U → π^+ at E/A = 407 MeV. See also the caption for figure 16A.

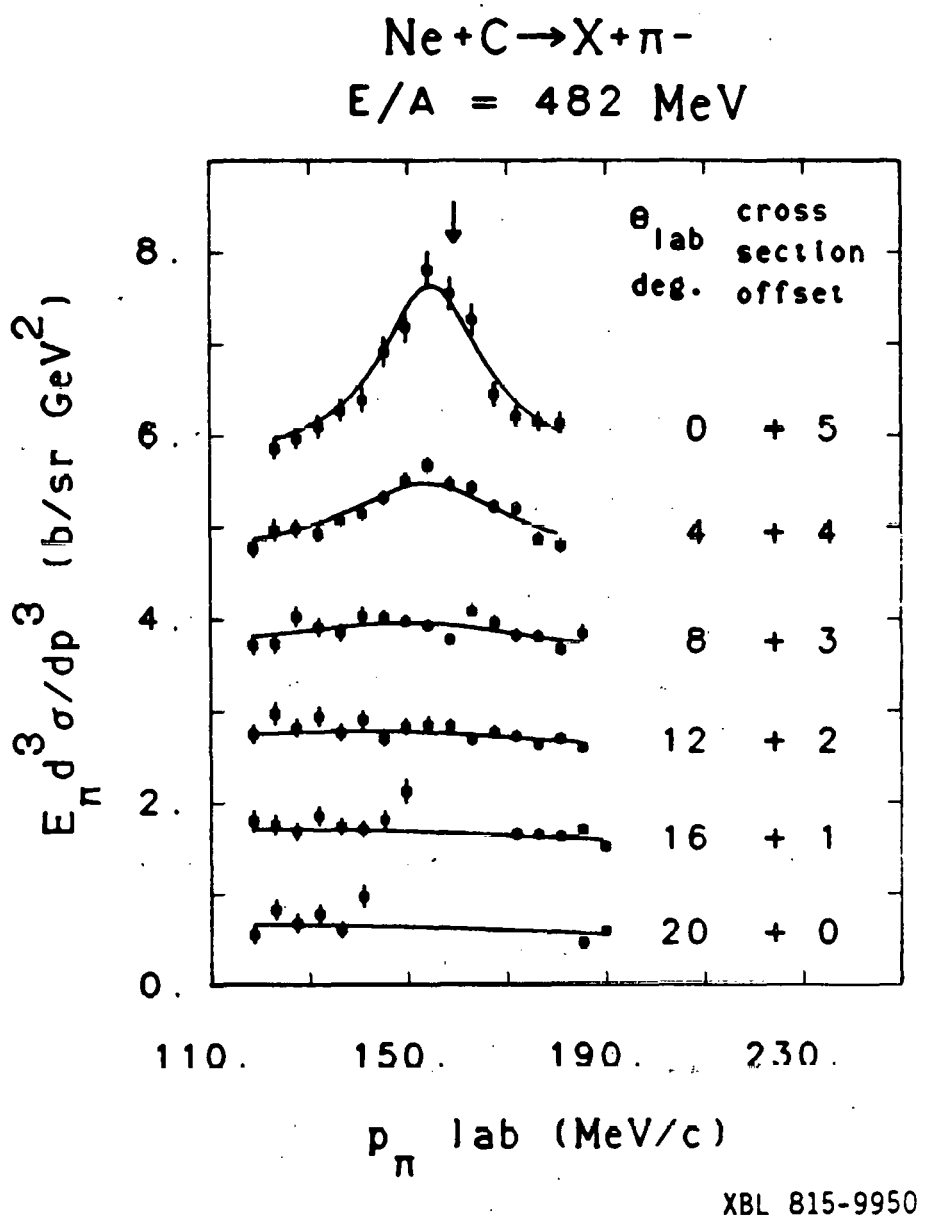

Fig. 25A -- Lorentz invariant cross section vs. lab momentum for Ne+C $\rightarrow \pi^-$ at E/A = 482 MeV. See also the caption for figure 16A.

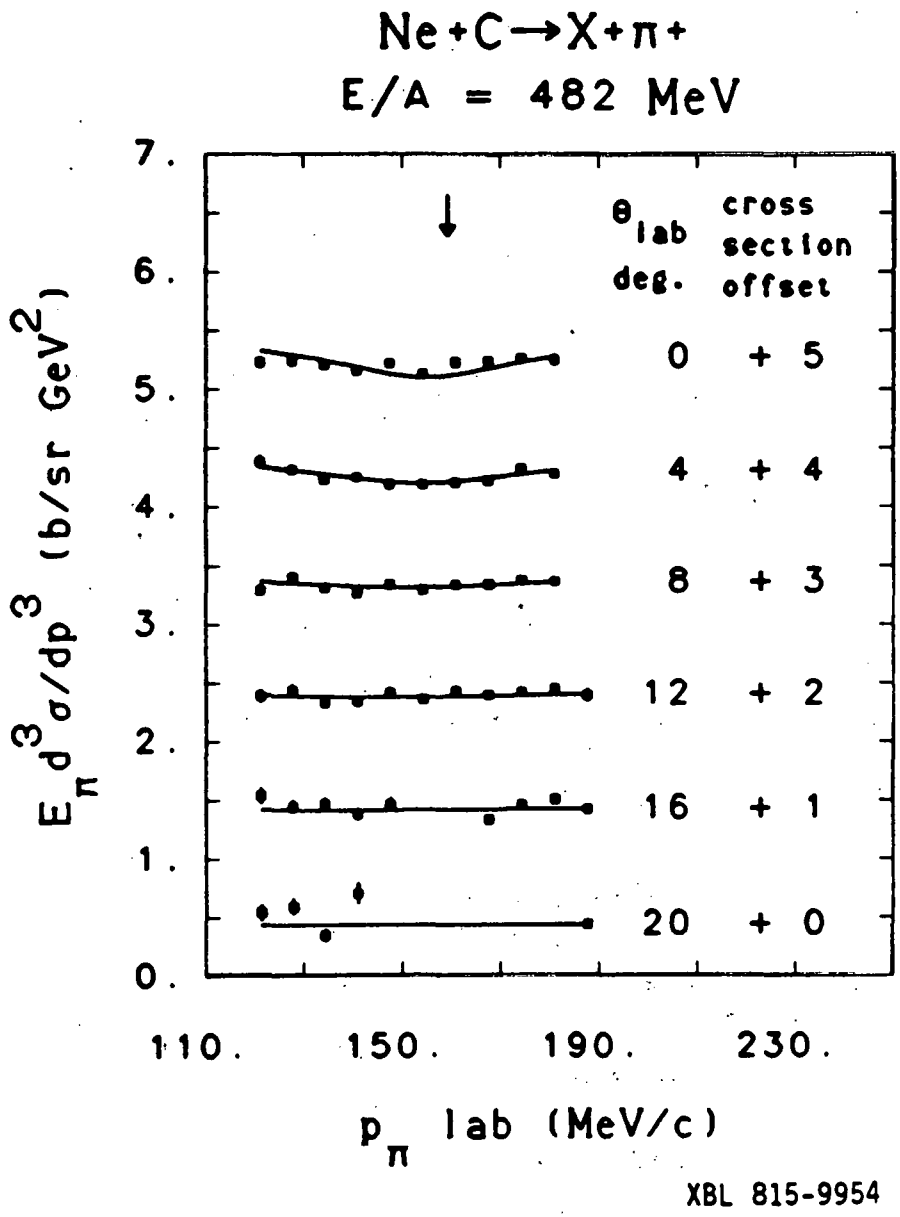

Fig. 25B -- Lorentz invariant cross section vs. lab momentum for Ne+C → π^+ at E/A = 482 MeV. See also the caption for figure 16A.

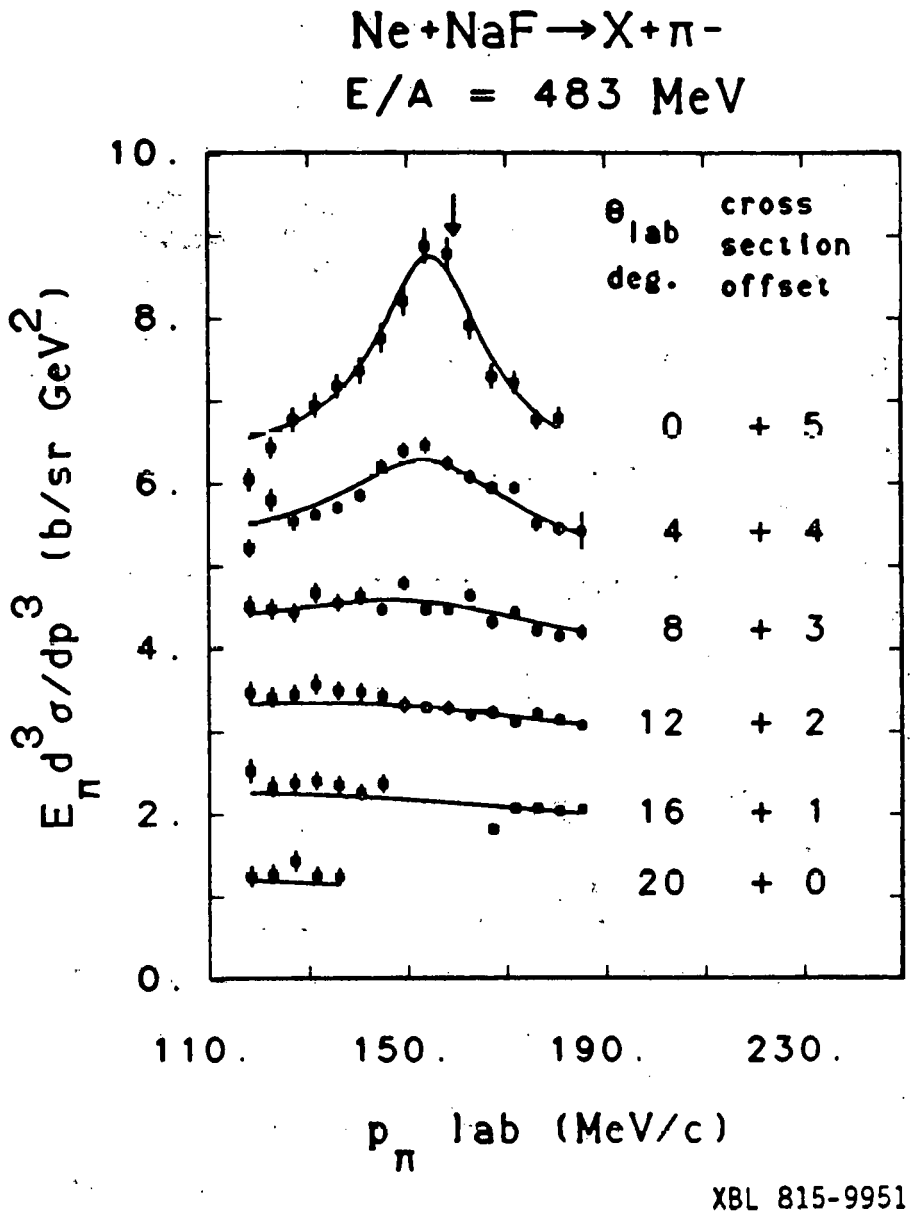

Fig. 26A -- Lorentz invariant cross section vs. lab momentum for Ne+NaF → π^- at E/A = 483 MeV. See also the caption for figure 16A.

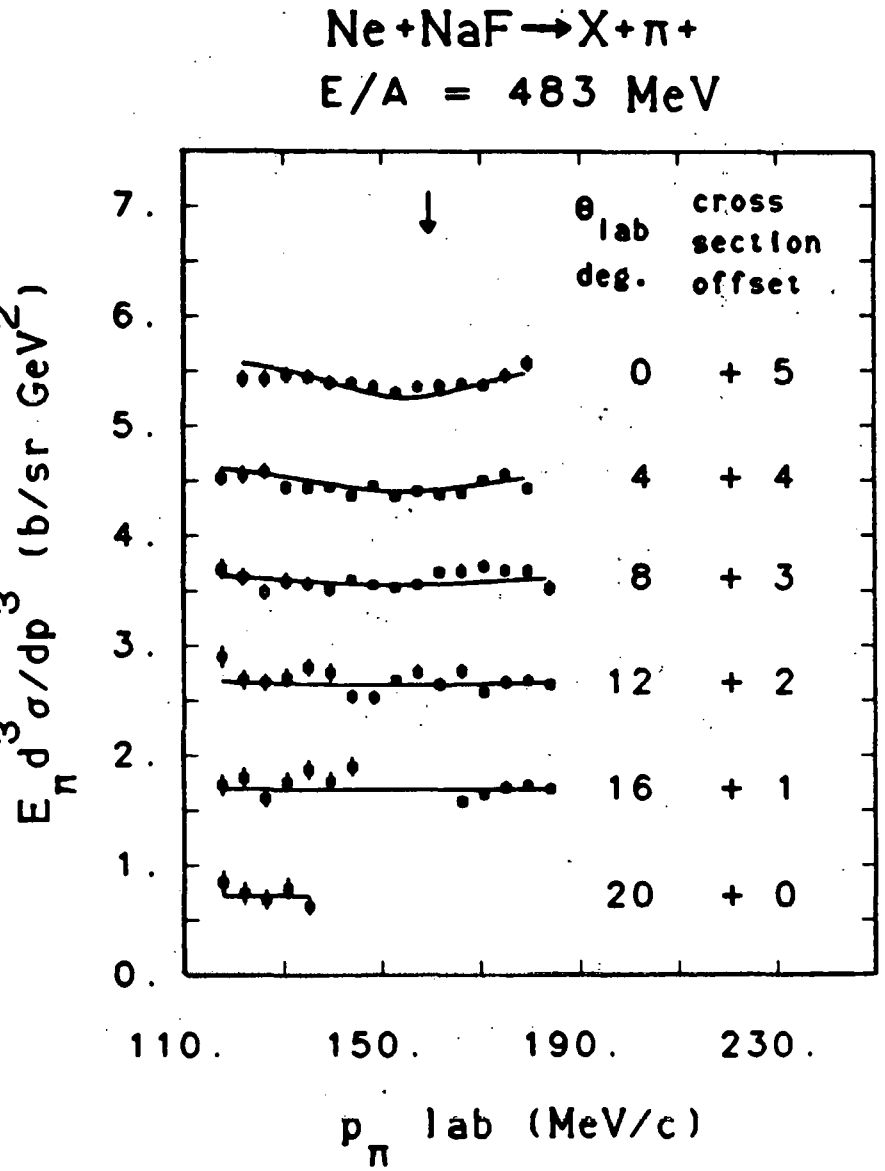

Fig. 26B -- Lorentz invariant cross section vs. lab momentum for Ne+NaF → π^+ at E/A = 483 MeV. See also the caption for figure 16A.

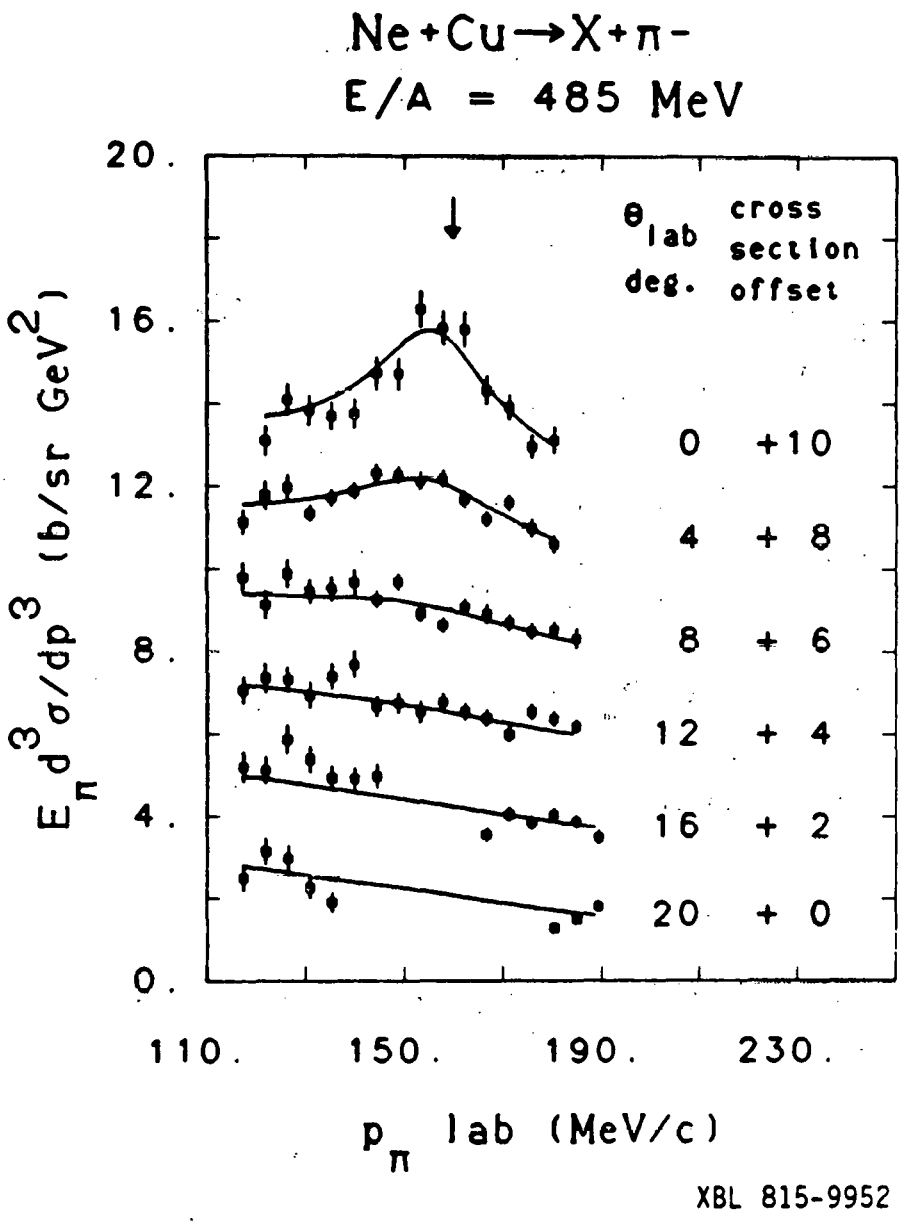

Fig. 27A -- Lorentz invariant cross section vs. lab momentum for Ne+Cu → π^- at E/A = 485 MeV. See also the caption for figure 16A.

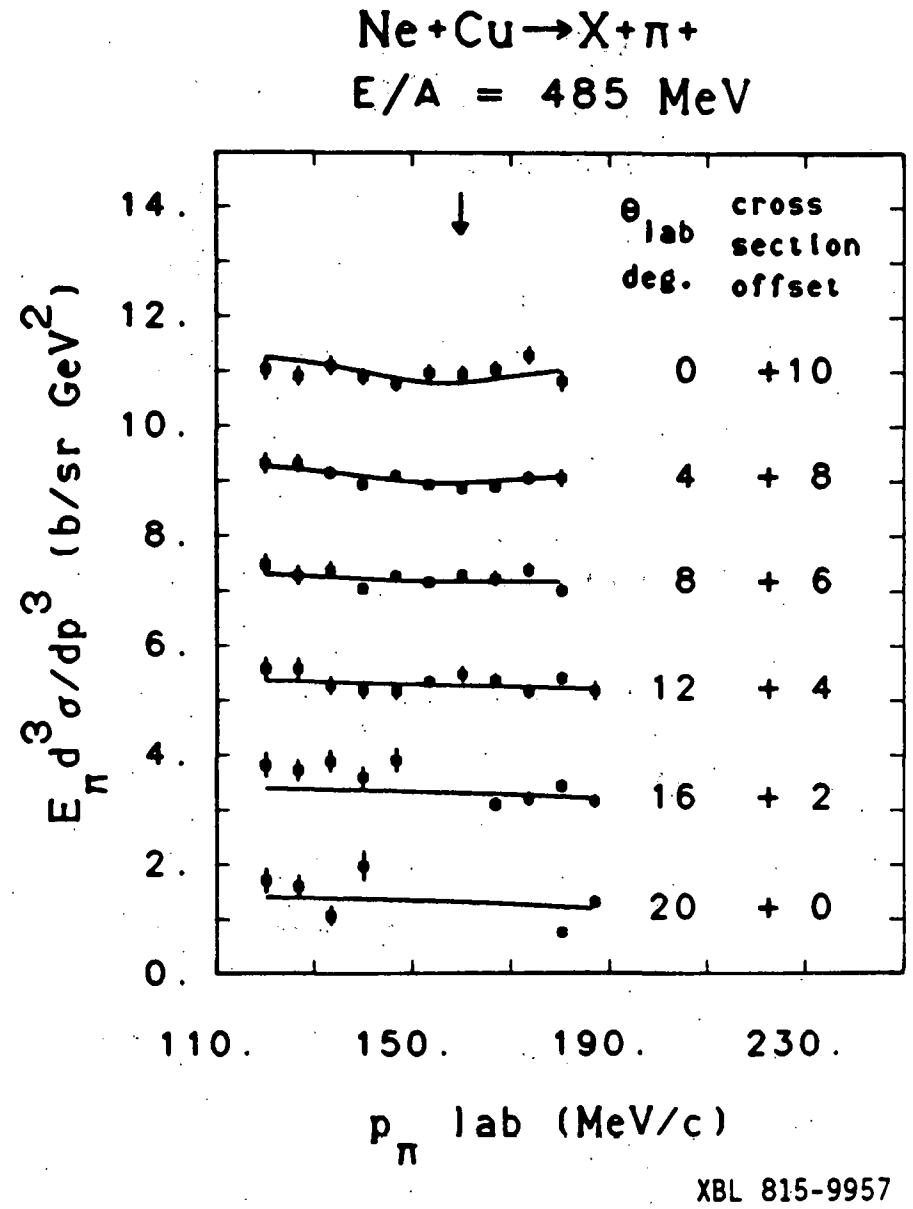

Fig. 27B -- Lorentz invariant cross section vs. lab momentum for Ne+Cu → π^+ at E/A = 485 MeV. See also the caption for figure 16A.

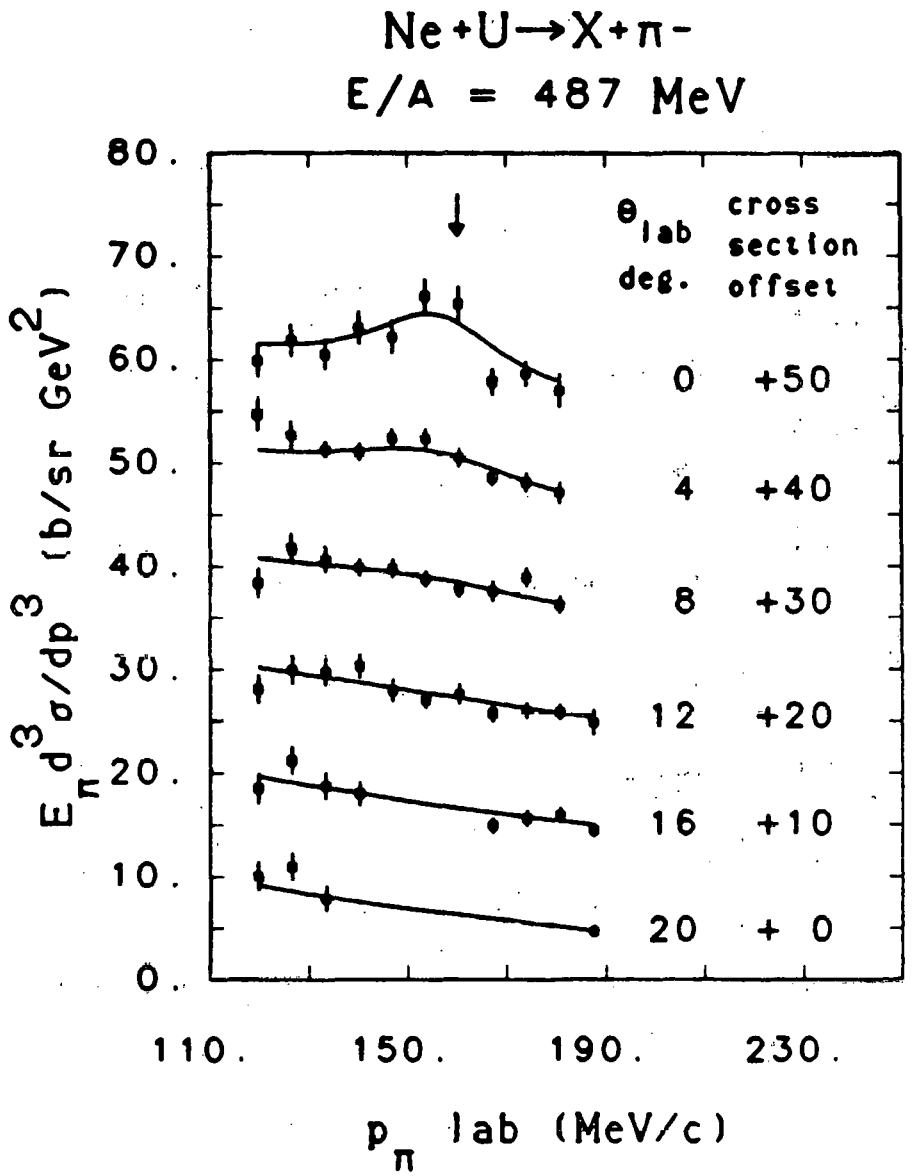

Fig. 28A -- Lorentz invariant cross section vs. lab momentum for Ne+U → π^- at E/A = 487 MeV. See also the caption for figure 16A.

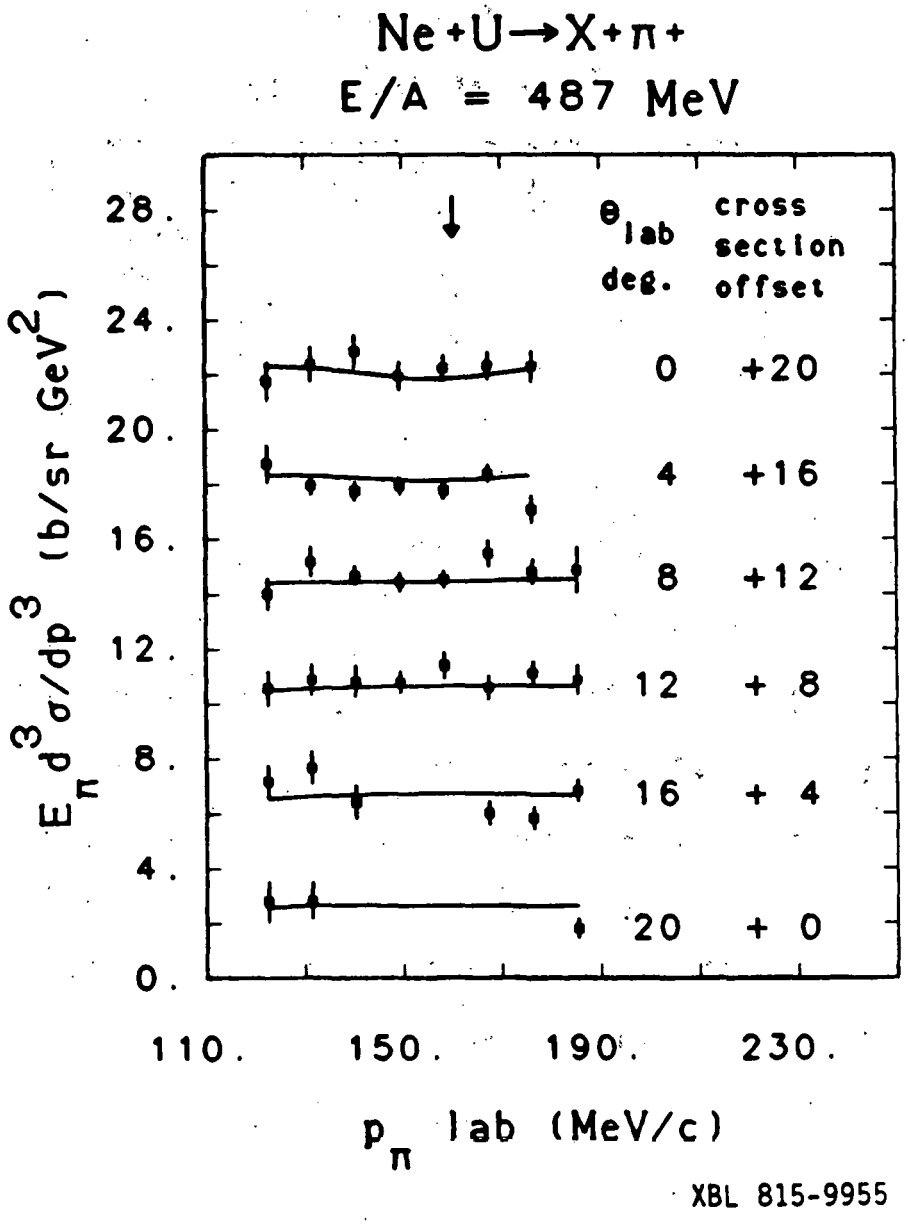

Fig. 28B -- Lorentz invariant cross section vs. lab momentum for Ne+U → π^+ at E/A = 487 MeV. See also the caption for figure 16A.

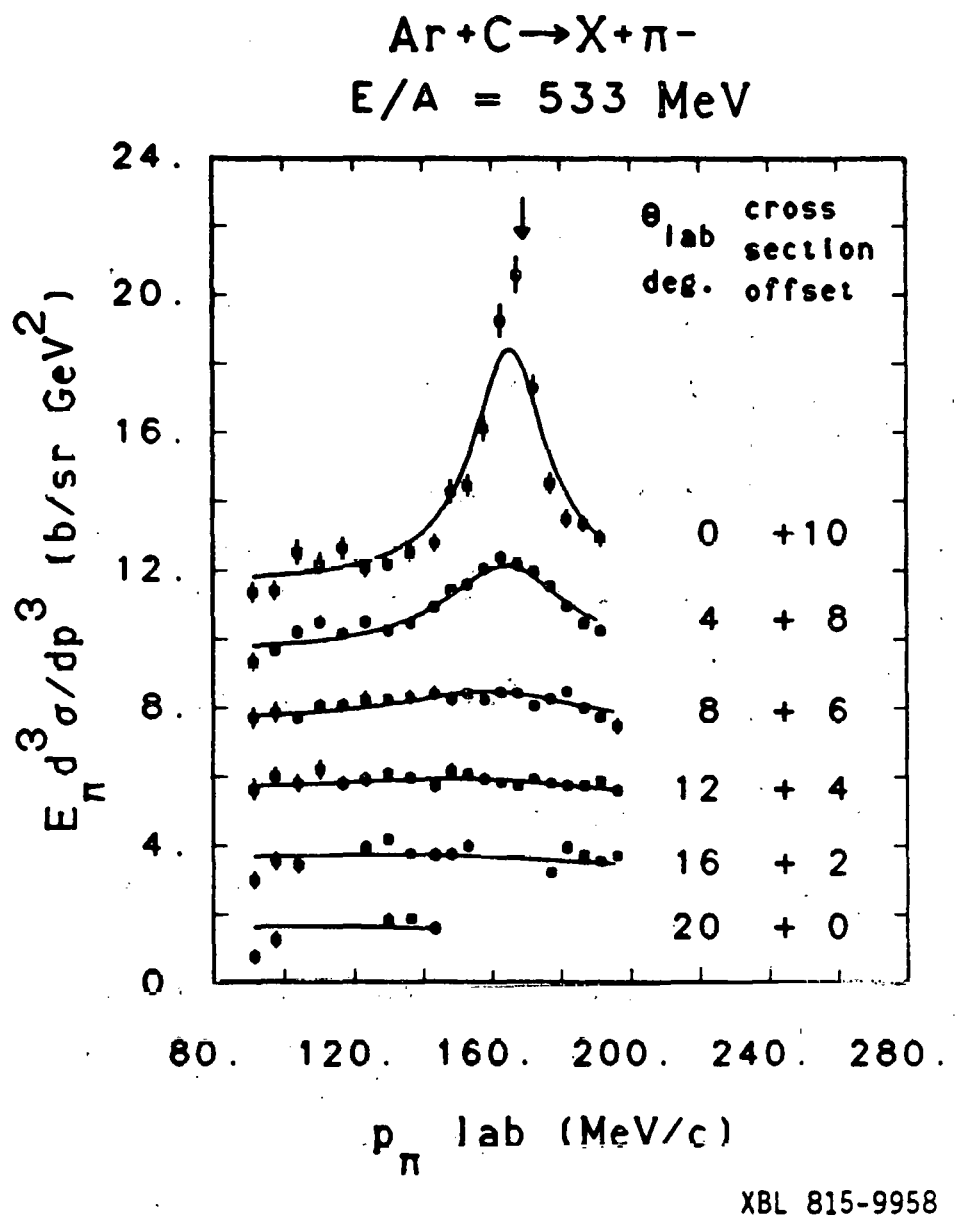

Fig. 29A -- Lorentz invariant cross section vs. lab momentum for Ar+C → π^- at E/A = 533 MeV. See also the caption for figure 16A.

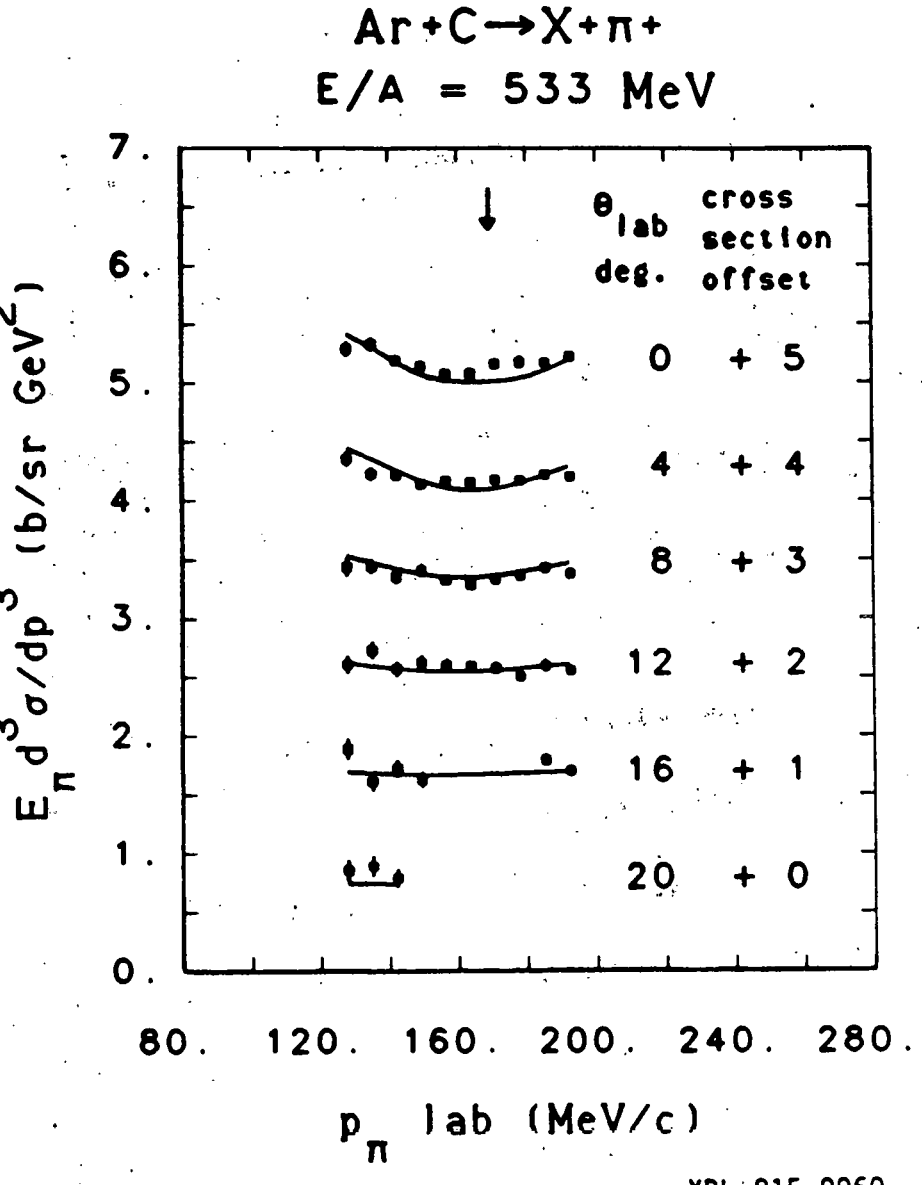

Fig. 29B -- Lorentz invariant cross section vs. lab momentum for Ar+C → π^+ at E/A = 533 MeV. See also the caption for figure 16A.

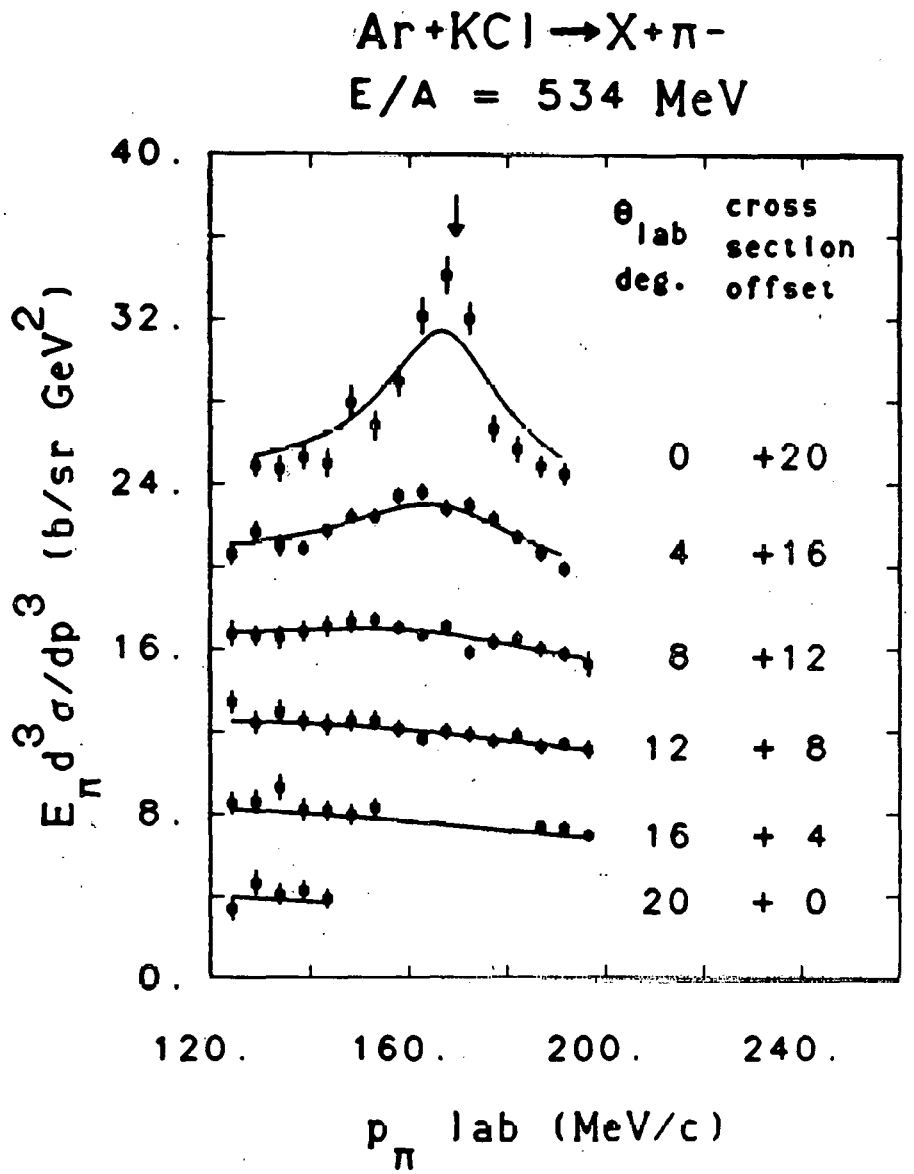

Fig. 30A -- Lorentz invariant cross section vs. lab momentum for Ar+KCl → π^- at E/A = 534 MeV. See also the caption for figure 16A.

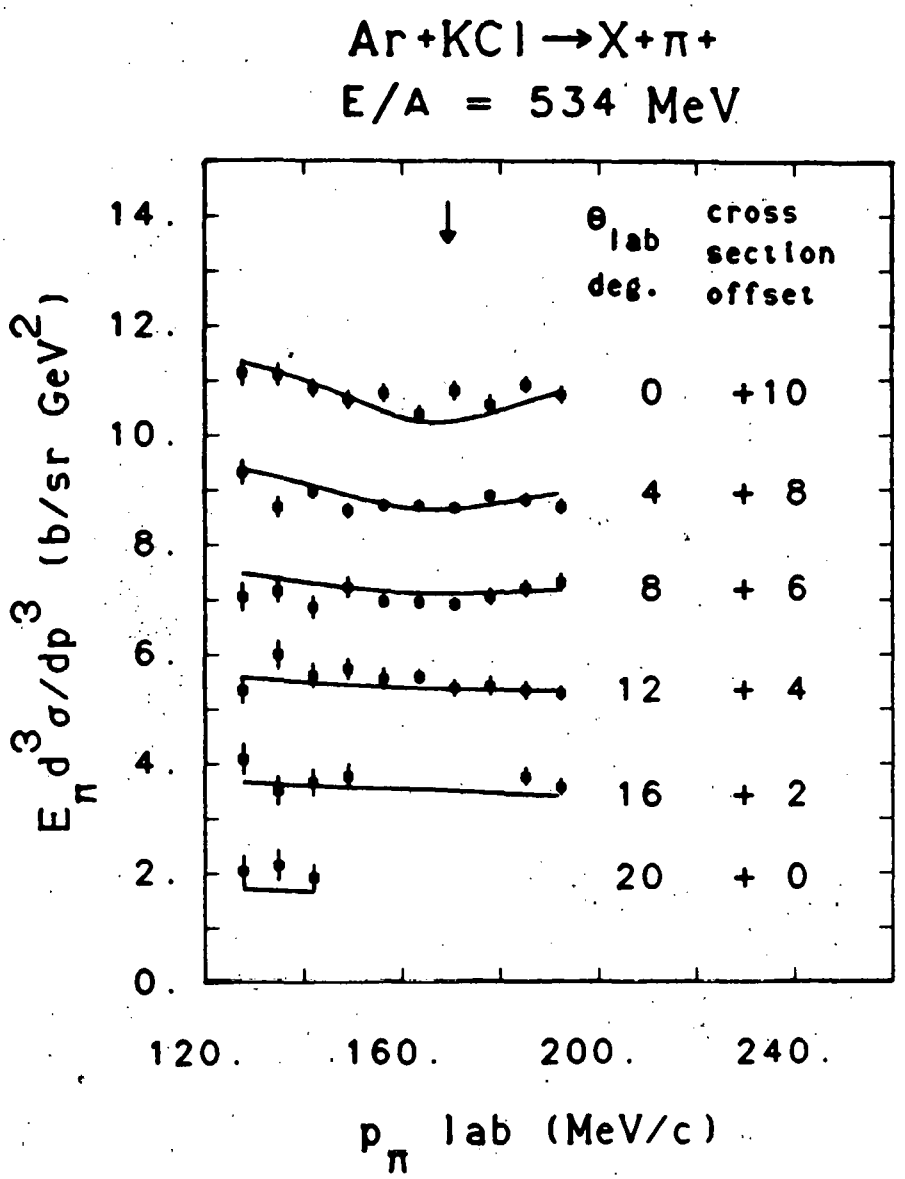

Fig. 30B -- Lorentz invariant cross section vs. lab momentum for Ar+KCl → π^+ at E/A = 534 MeV. See also the caption for figure 16A.

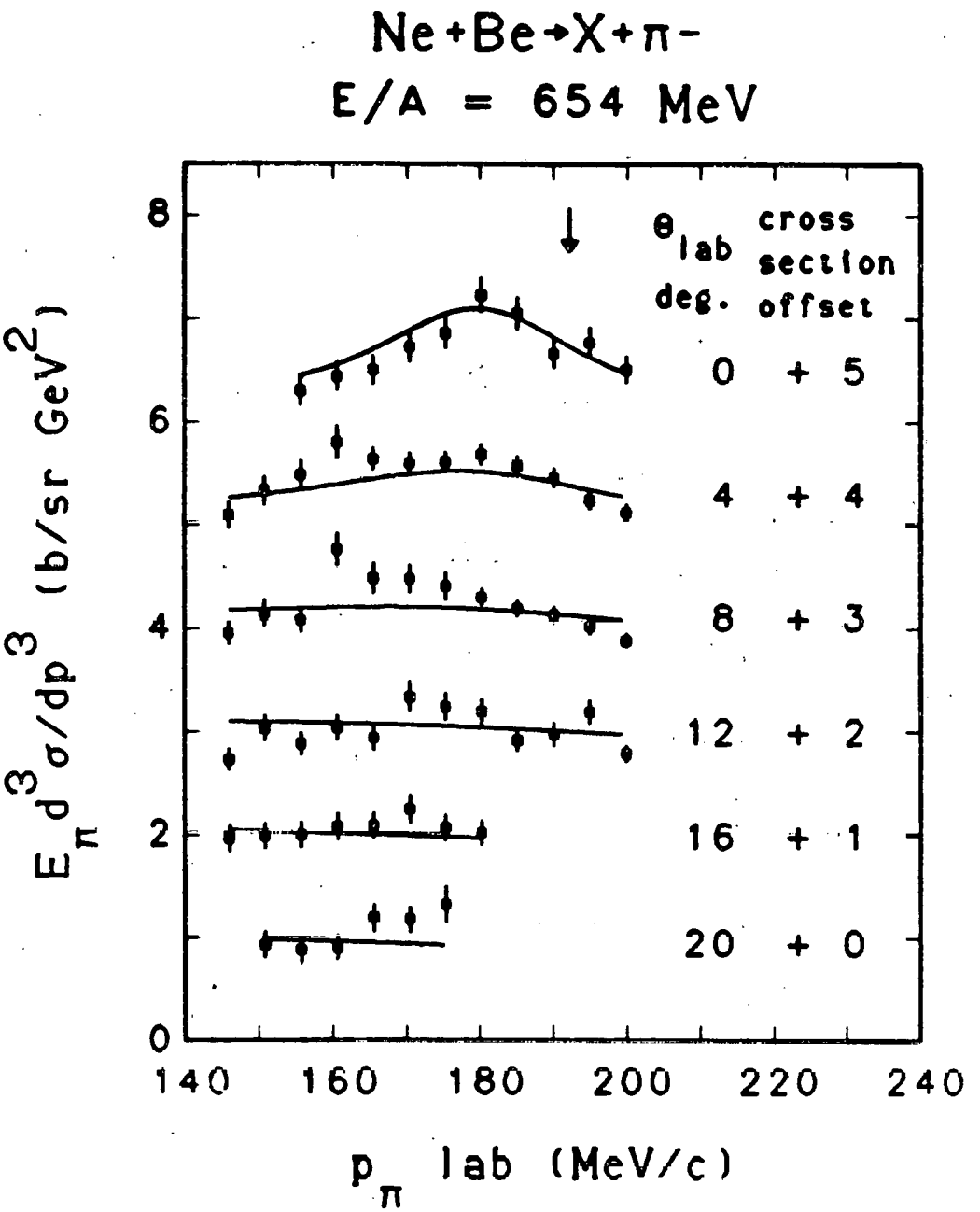

Fig. 31A -- Lorentz invariant cross section vs. lab momentum for Ne+Be → π^- at E/A = 654 MeV. See also the caption for figure 16A.

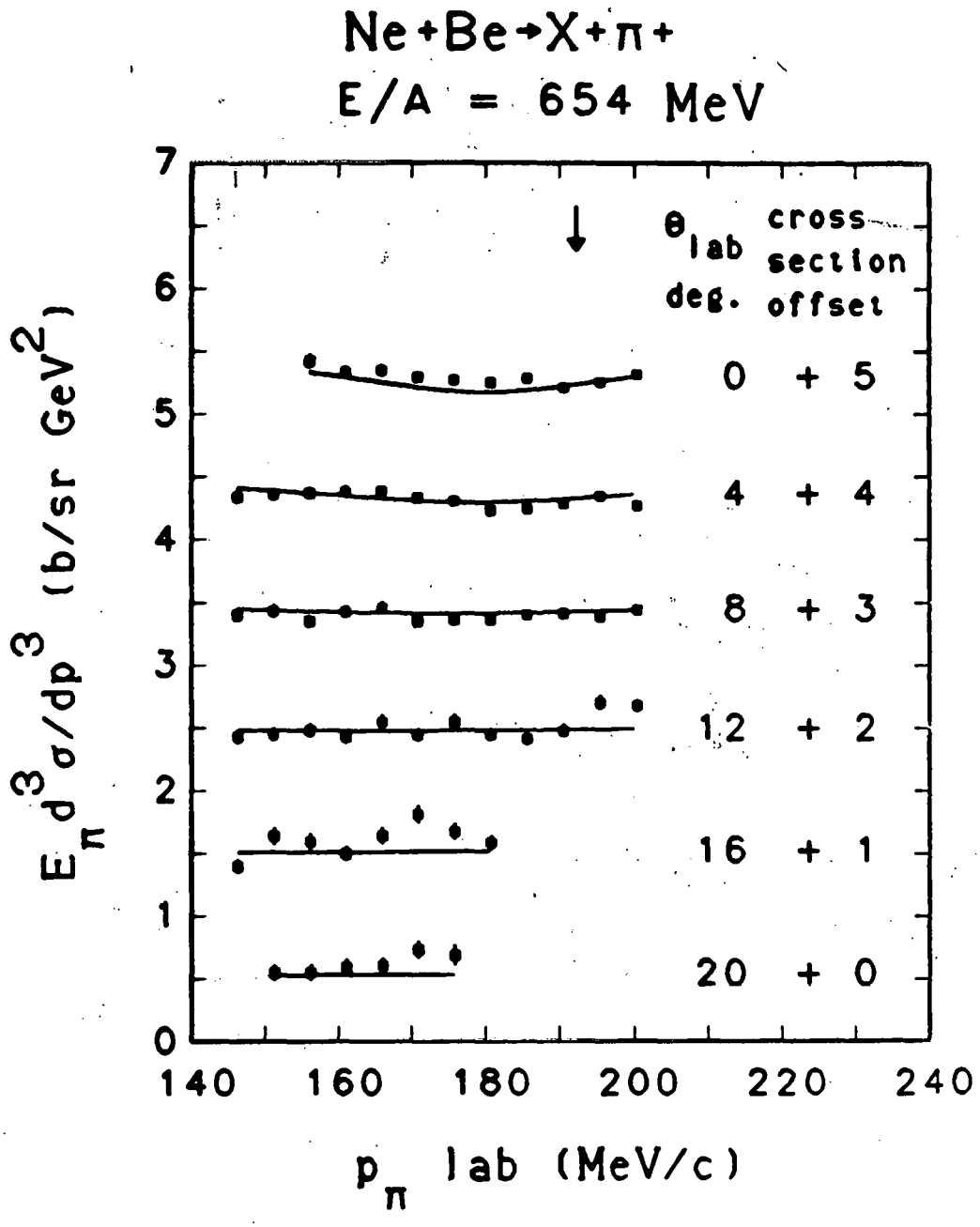

Fig. 318 -- Lorentz invariant cross section vs. lab momentum for Ne+Be → π^+ at E/A = 654 MeV. See also the caption for figure 16A.

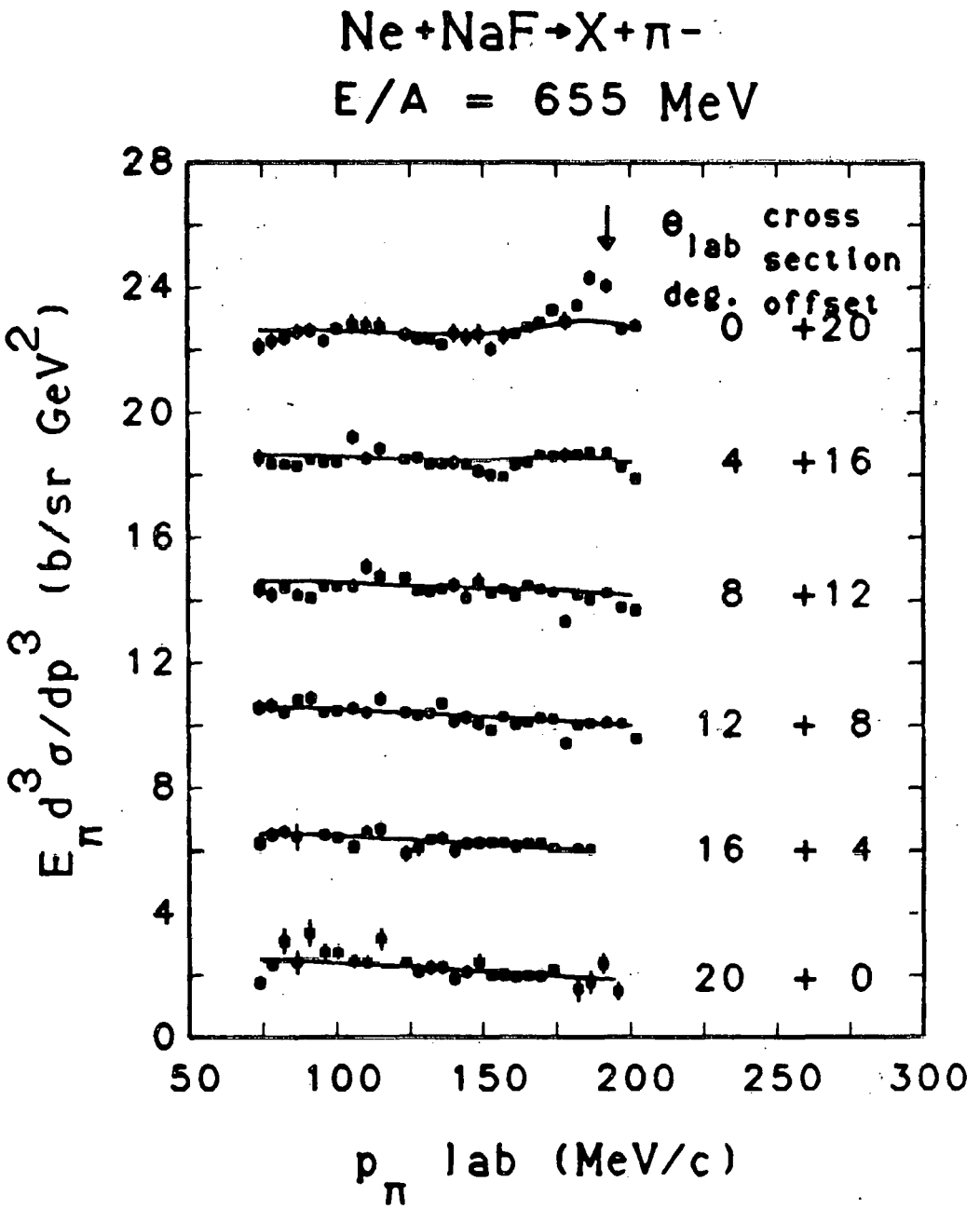

Fig. 32A -- Lorentz invariant cross section vs. lab momentum for Ne+NaF → π^- at E/A = 655 MeV. This figure shows the data from 0 to 20 degrees, figure 32B shows the data from 24 to 44 degrees. See also the caption for figure 16A.

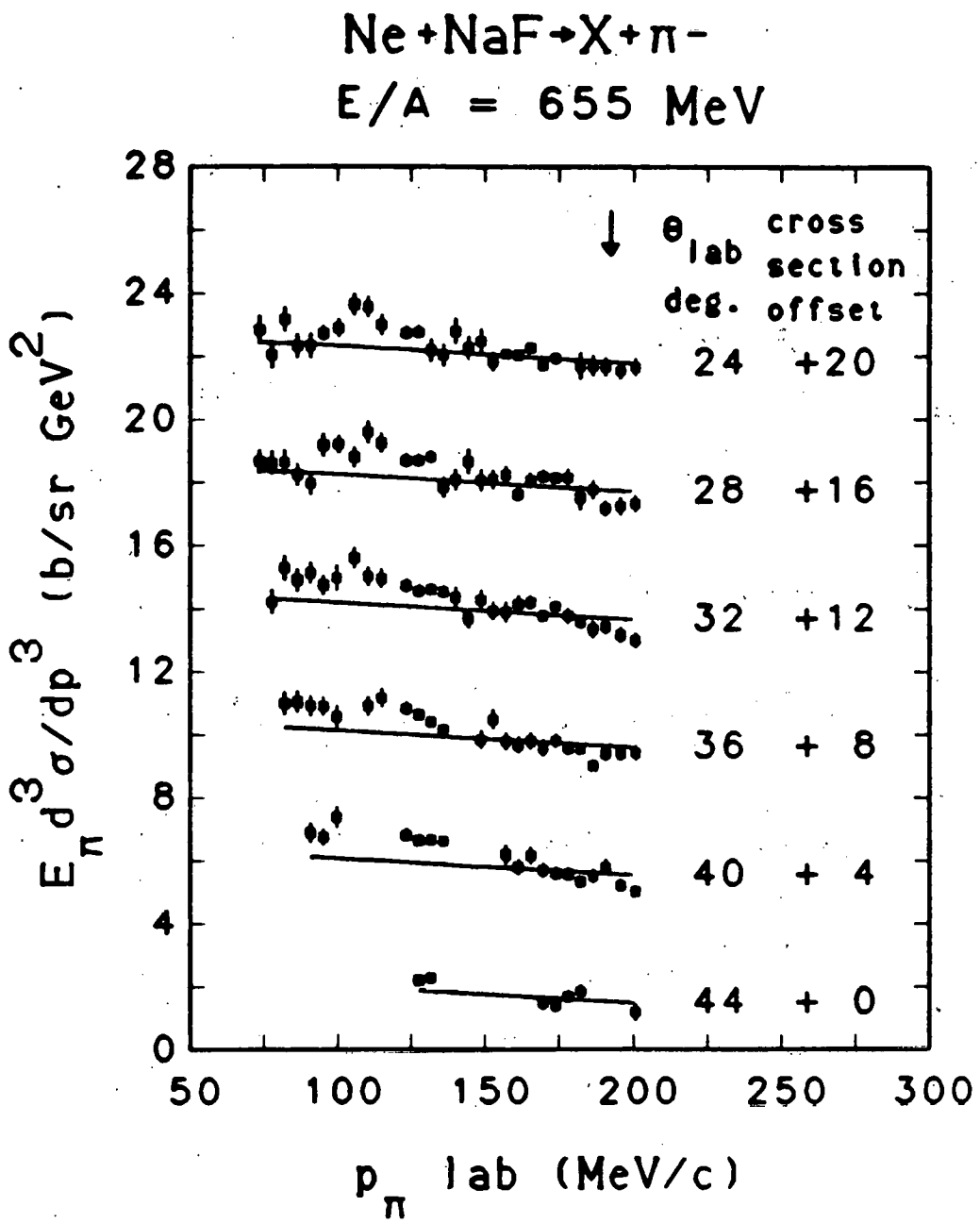

Fig. 32B -- Lorentz invariant cross section vs. lab momentum for Ne+NaF → π^- at E/A = 655 MeV. This figure shows the data from 24 to 44 degrees, figure 32A shows the data from 0 to 20 degrees. See also the caption for figure 16A.

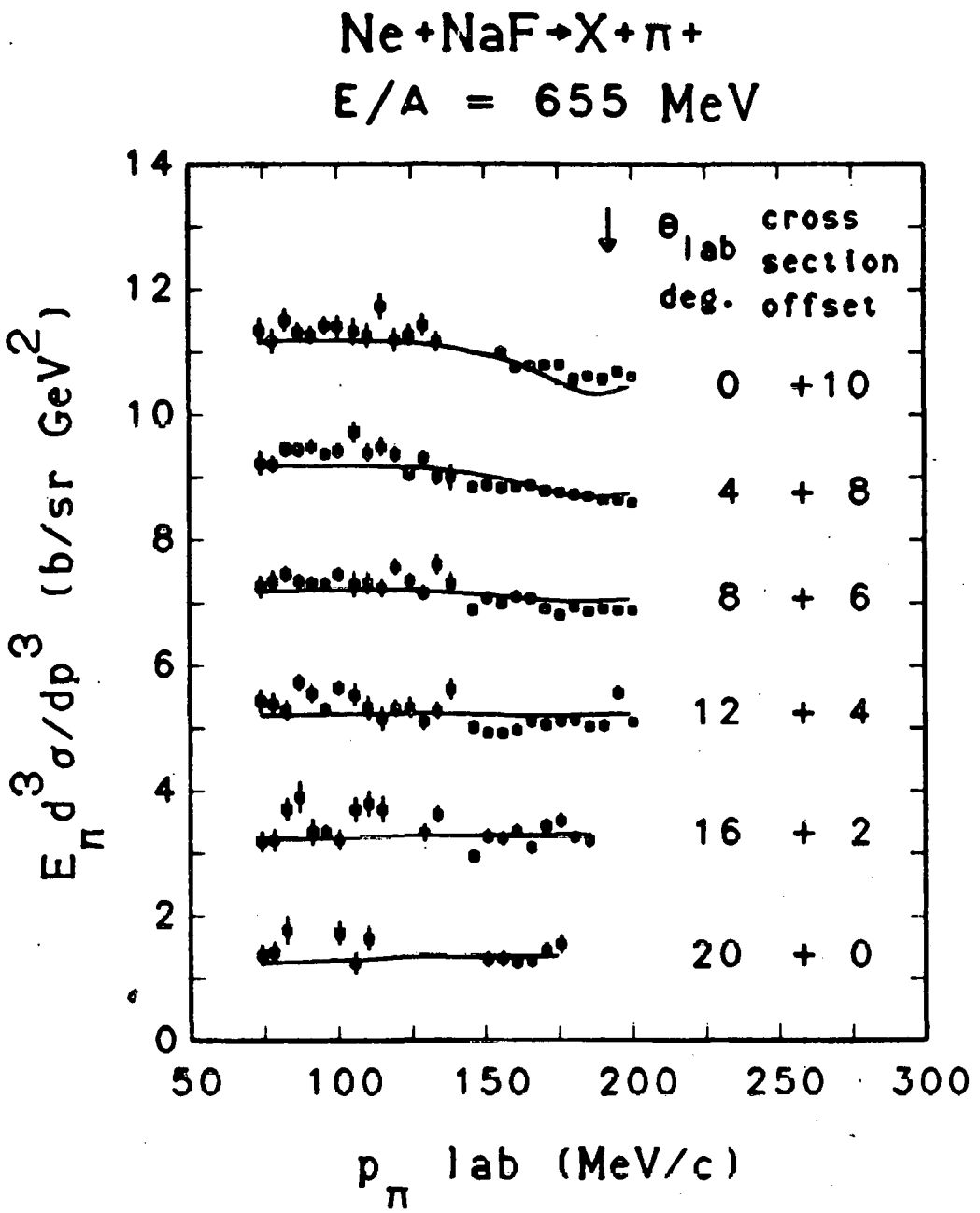

Fig. 32C -- Lorentz invariant cross section vs. lab momentum for Ne+NaF → π^+ at E/A = 655 MeV. See also the caption for figure 16A.

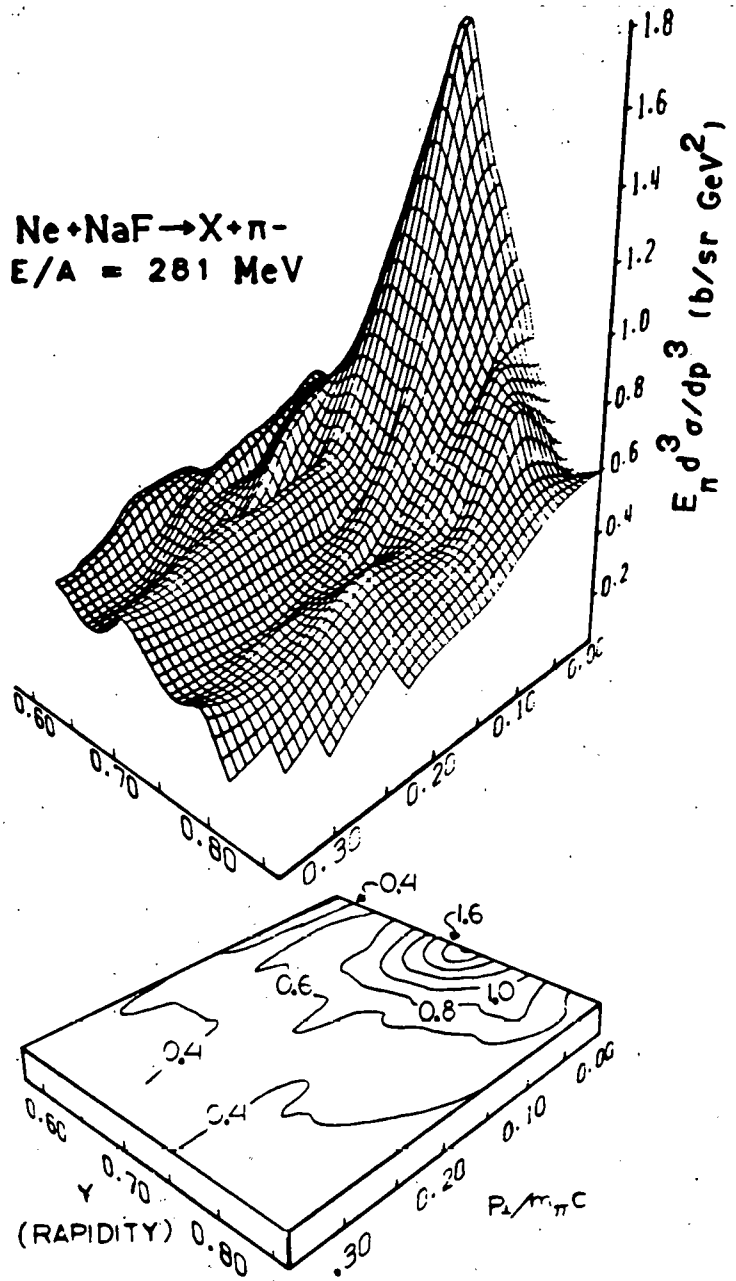

Fig. 33A -- The top part of the figure shows a perspective representation of the surface defined by the Lorentz invariant cross section ($Ed^3\sigma/dp^3$, units of $\mu b/sr\ MeV^2$) as a function of rapidity ($y=\tanh^{-1}(p_{||}/E)$) and $p_\perp$ for Ne+NaF $\rightarrow \pi^-$ at E/A = 281 MeV. The bottom part of the figure is a contour plot of the same surface with the same scales for the y and $p_\perp$ axes.

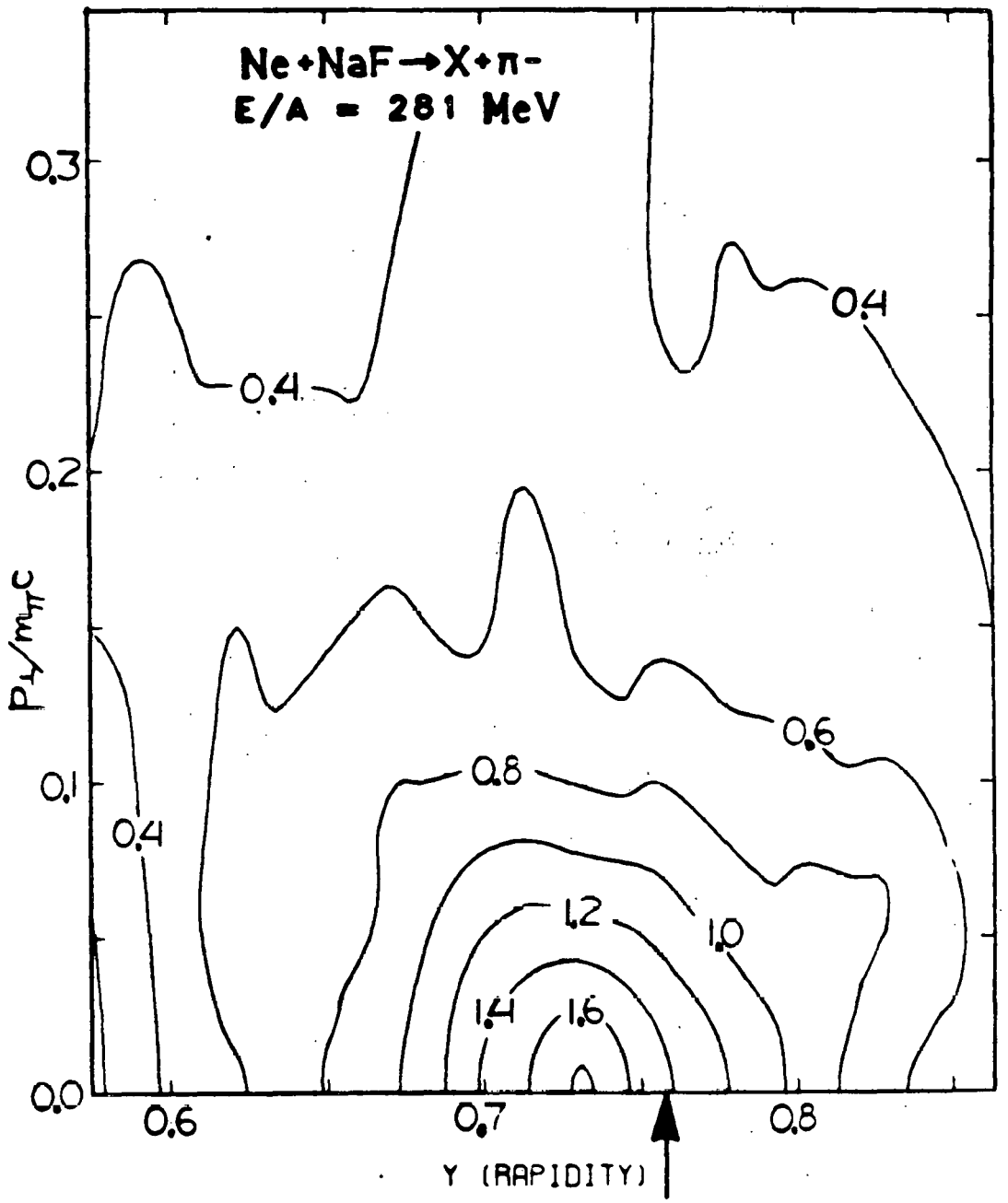

Fig. 33B -- A contour plot of the Lorentz invariant cross section ($Ed^3\sigma/dp^3$, units of $\mu b/sr\ MeV^2$) as a function of rapidity and $p_\perp$ for Ne+NaF → π^- at E/A = 281 MeV. The arrow marks the velocity of the incident beam. This contour plot is the same as the one shown in figure 33A, except that it is not drawn in perspective and a more conventional orientation of the axes has been used.

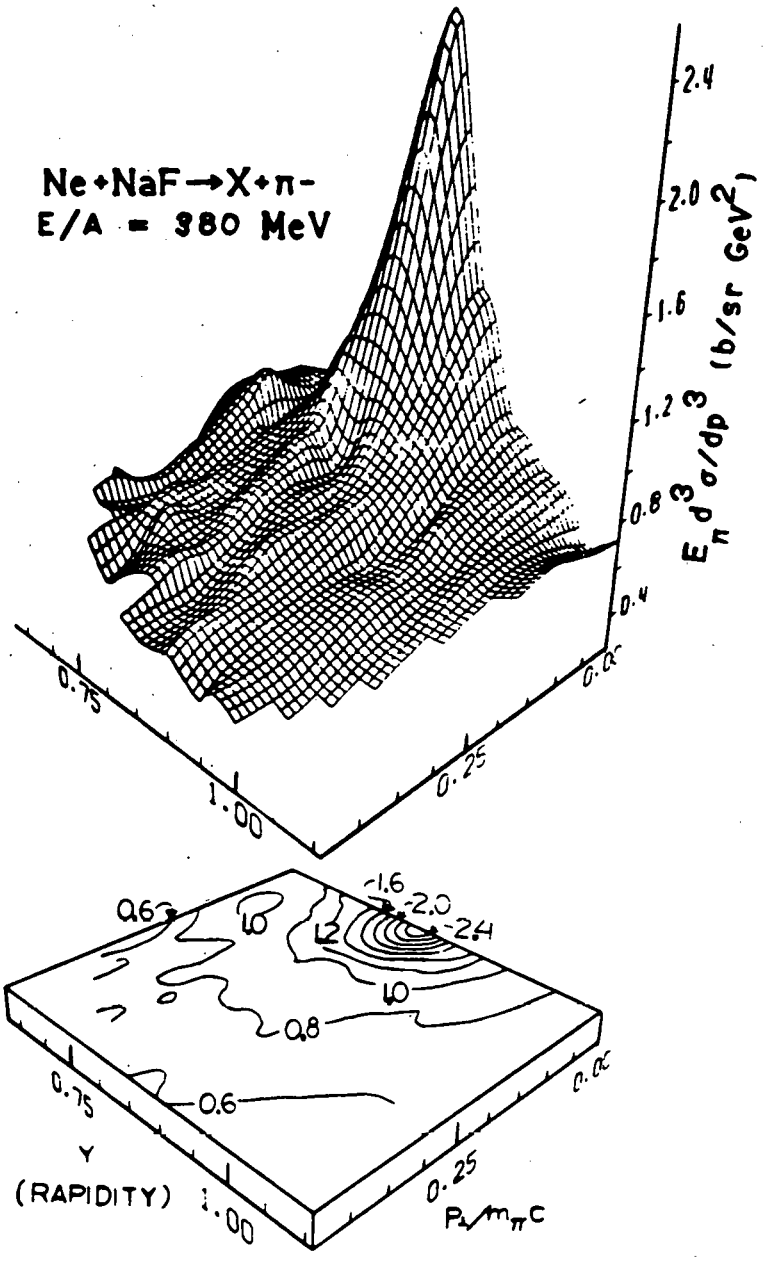

Fig. 34A -- The top part of the figure shows a perspective representation of the surface defined by the Lorentz invariant cross section ($Ed^3\sigma/dp^3$, units of $\mu b/sr\ MeV^2$) as a function of rapidity ($y=\tanh^{-1}(p_\parallel/E)$) and $p_\perp$ for Ne+NaF → π^- at E/A = 380 MeV. The bottom part of the figure is a contour plot of the same surface with the same scales for the y and $p_\perp$ axes.

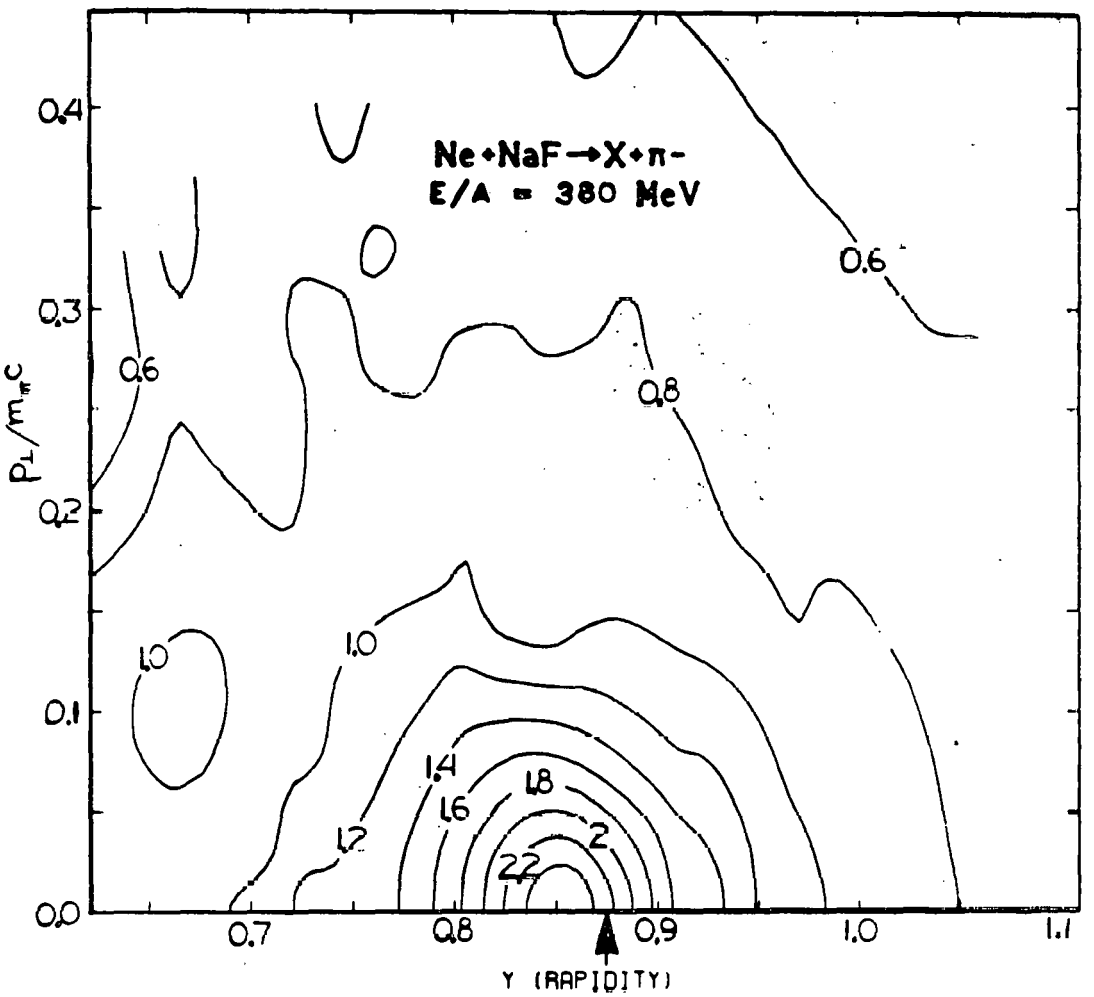

Fig. 34B -- A contour plot of the Lorentz invariant cross section ($Ed^3\sigma/dp^3$, units of $\mu b/sr\ MeV^2$) as a function of rapidity and $p_\perp$ for Ne+NaF → π^- at E/A = 380 MeV. The arrow marks the velocity of the incident beam. This contour plot is the same as the one shown in figure 34A, except that it is not drawn in perspective and a more conventional orientation of the axes has been used.

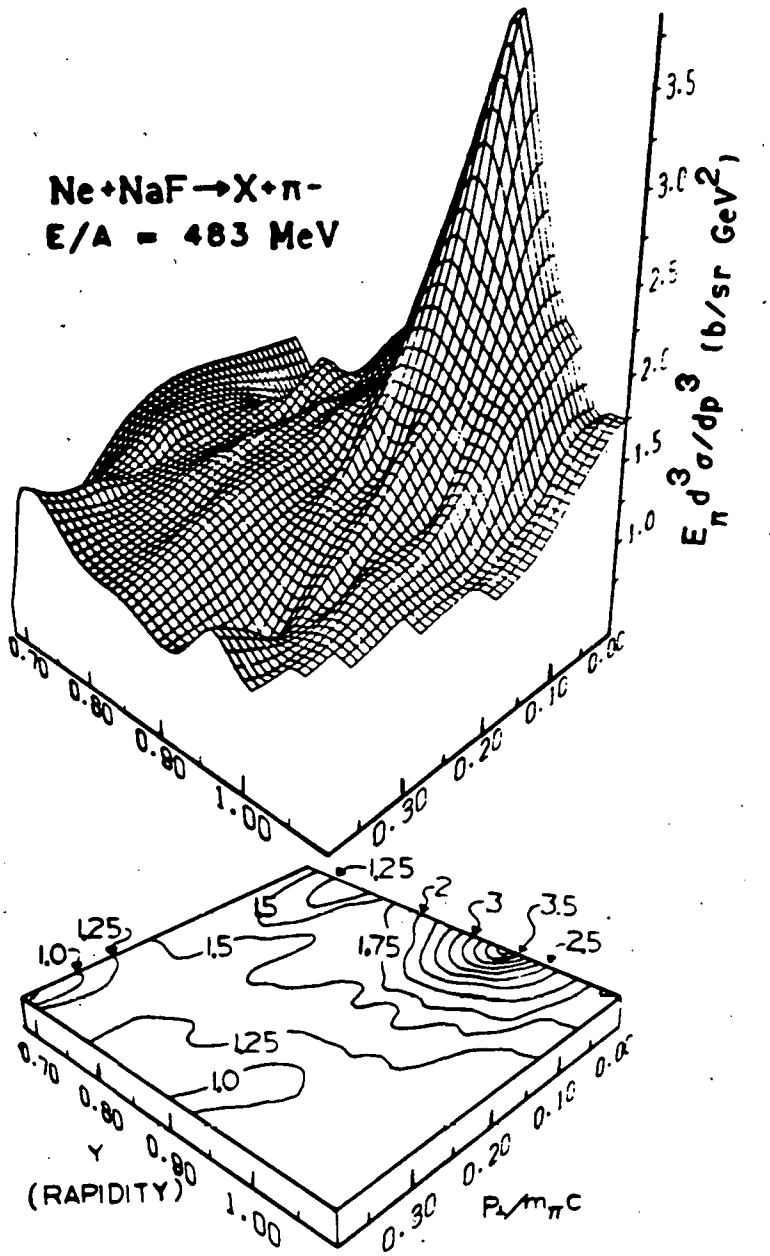

Fig. 35A -- The top part of the figure shows a perspective representation of the surface defined by the Lorentz invariant cross section ($Ed^3\sigma/dp^3$, units of $\mu b/sr\ MeV^2$) as a function of rapidity ($y=\tanh^{-1}(p_\parallel/E)$) and $p_\perp$ for Ne+NaF $\rightarrow \pi^-$ at E/A = 483 MeV. The bottom part of the figure is a contour plot of the same surface with the same scales for the y and $p_\perp$ axes.

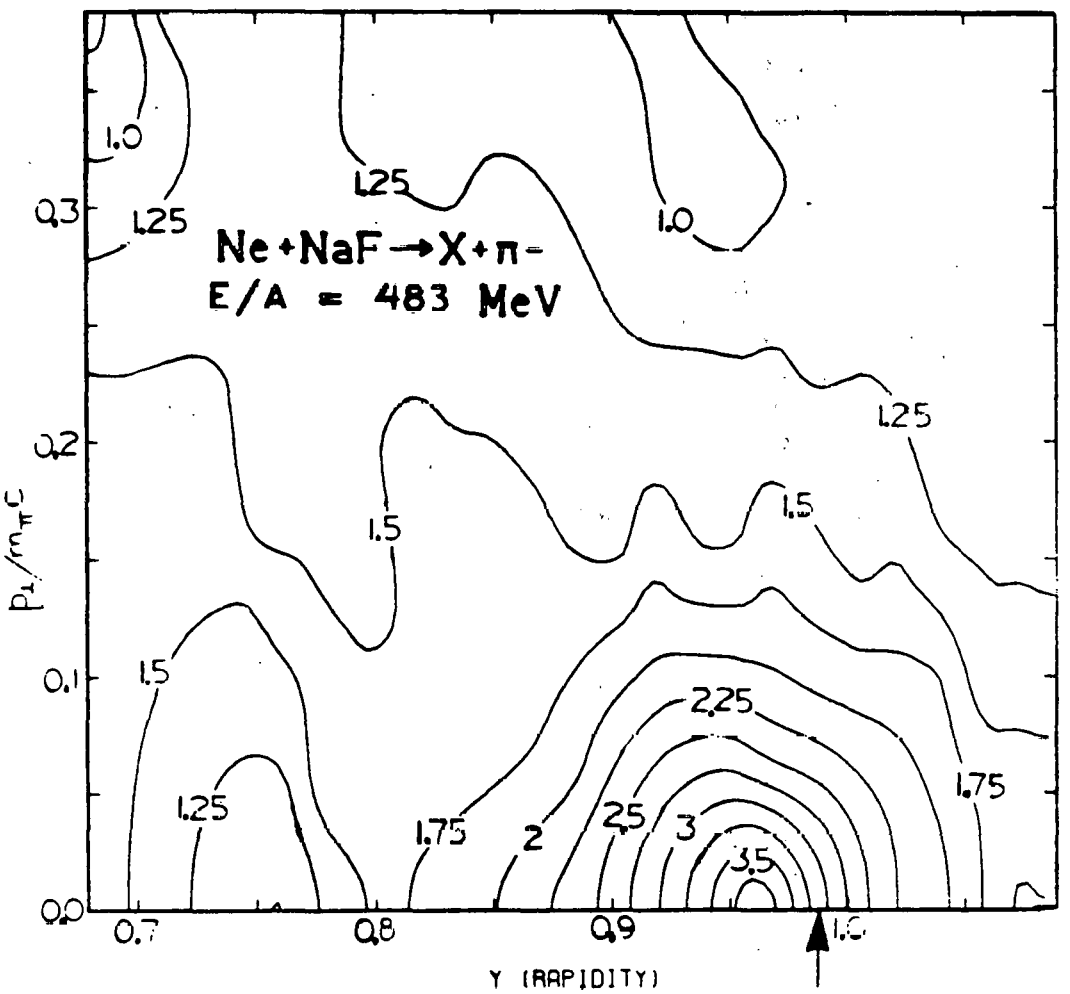

Fig. 35B -- A contour plot of the Lorentz invariant cross section ($Ed^3\sigma/dp^3$, units of $\mu b/sr\ MeV^2$) as a function of rapidity and $p_\perp$ for Ne+NaF → π^- at E/A = 483 MeV. The arrow marks the velocity of the incident beam. This contour plot is the same as the one shown in figure 35A, except that it is not drawn in perspective and a more conventional orientation of the axes has been used.

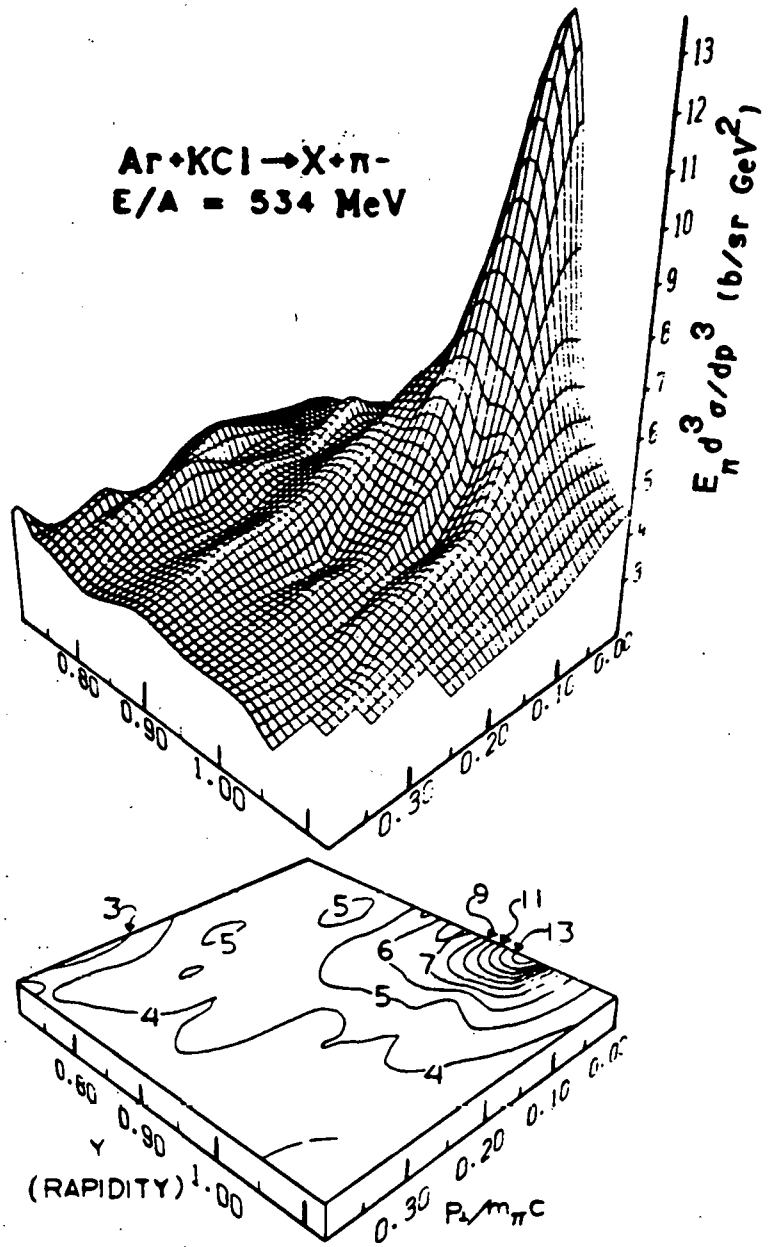

Fig. 36A -- The top part of the figure shows a perspective representation of the surface defined by the Lorentz invariant cross section ($Ed^3\sigma/dp^3$, units of $\mu b/sr\ MeV^2$) as a function of rapidity ($y=\tanh^{-1}(p_{\parallel}/E)$) and $p_\perp$ for Ar+KCl→ π^- at E/A = 534 MeV. The bottom part of the figure is a contour plot of the same surface with the same scales for the y and $p_\perp$ axes.

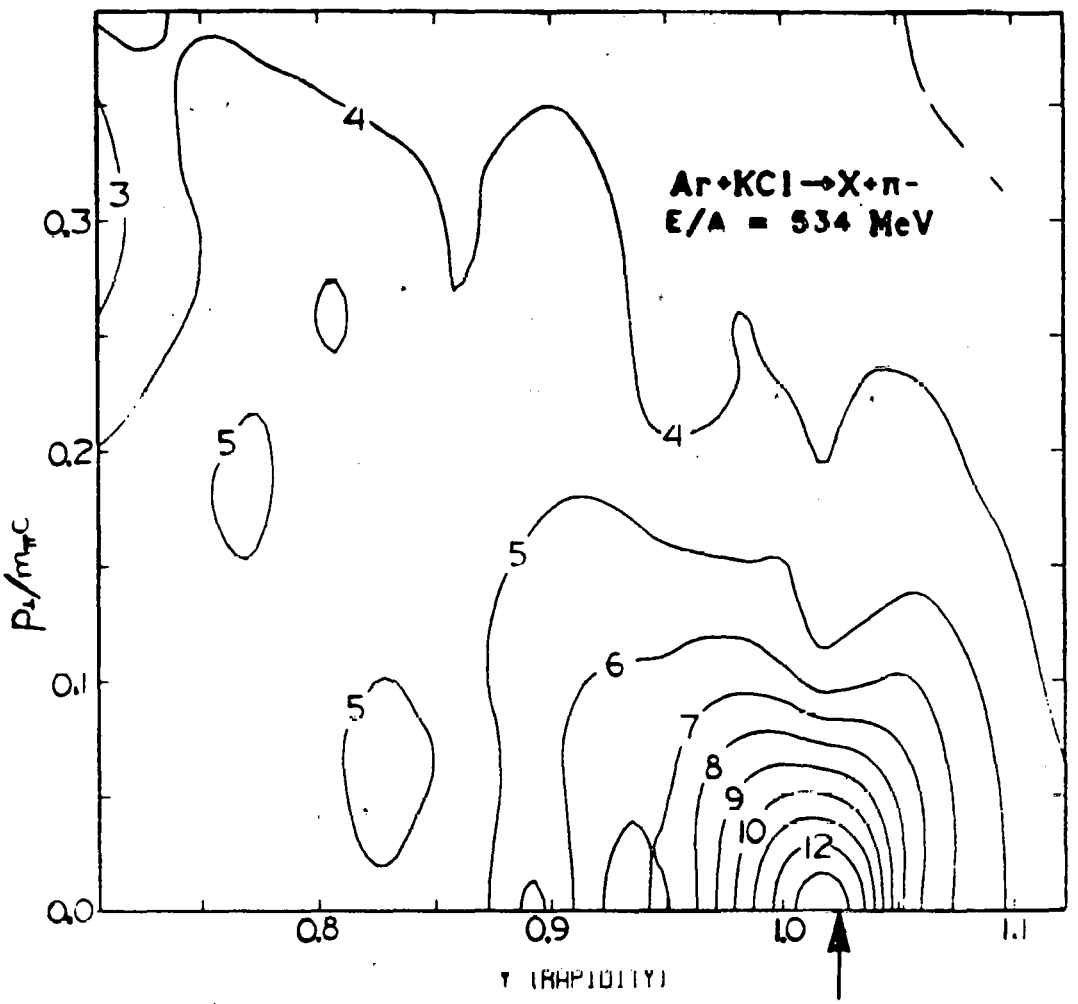

Fig. 36B -- A contour plot of the Lorentz invariant cross section ($Ed^3\sigma/dp^3$, units of $\mu b/sr\ MeV^2$) as a function of rapidity and $p_\perp$ for Ar+KCl $\rightarrow \pi^-$ at E/A = 534 MeV. The arrow marks the velocity of the incident beam. This contour plot is the same as the one shown in figure 36A, except that it is not drawn in perspective and a more conventional orientation of the axes has been used.

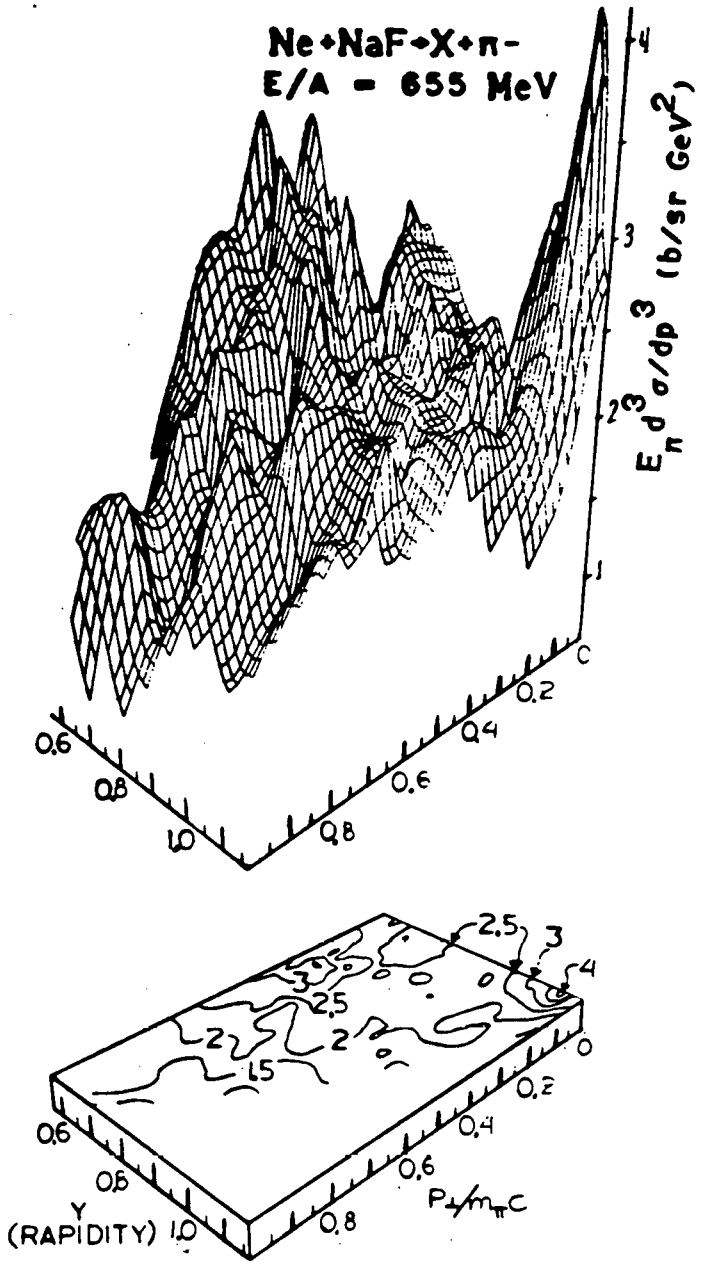

Fig. 37A -- The top part of the figure shows a perspective representation of the surface defined by the Lorentz invariant cross section ($Ed^3\sigma/dp^3$, units of $\mu b/sr\ MeV^2$) as a function of rapidity ($y=\tanh^{-1}(p_{\parallel}/E)$) and $p_\perp$ for Ne+NaF $\rightarrow \pi^-$ at E/A = 655 MeV. The bottom part of the figure is a contour plot of the same surface with the same scales for the y and $p_\perp$ axes. The data were assumed to be symmetric about the center of mass rapidity and all points have been reflected about the center of mass. Only the part of the data on the projectile side of the center of mass has been shown.

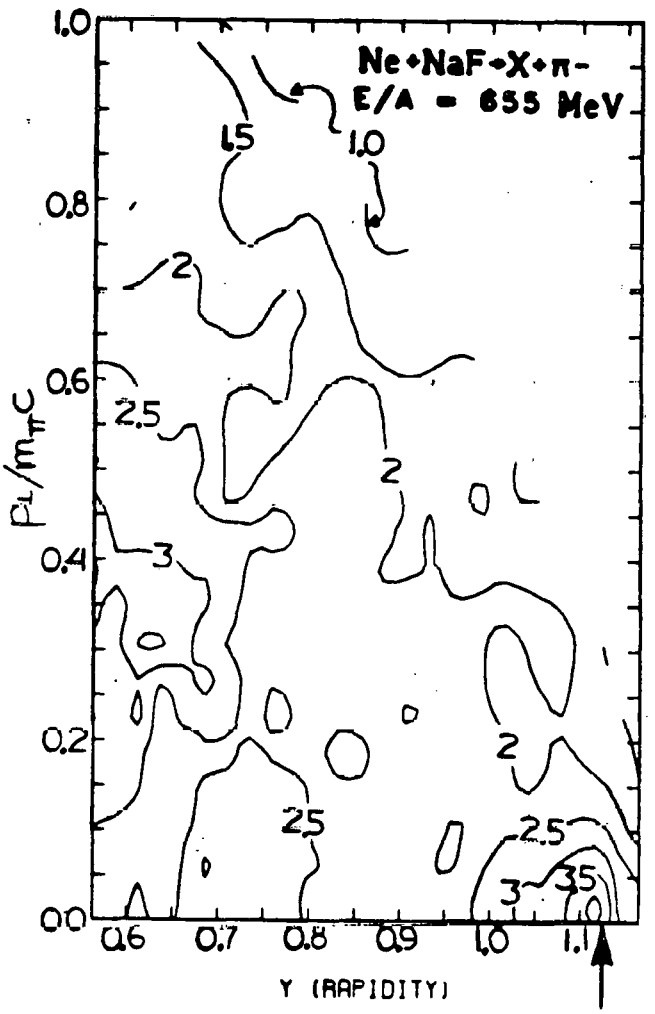

Fig. 37B -- A contour plot of the Lorentz invariant cross section ($Ed^3\sigma/dp^3$, units of $\mu b/sr\ MeV^2$) as a function of rapidity and $p_\perp$ for Ne+NaF $\rightarrow \pi^-$ at E/A = 655 MeV. The arrow marks the velocity of the incident beam. This contour plot is the same as the one shown in figure 37A, except that it is not drawn in perspective and a more conventional orientation of the axes has been used. The data were assumed to be symmetric about the center of mass rapidity and all points have been reflected about the center of mass. Only the part of the data on the projectile side of the center of mass has been shown.

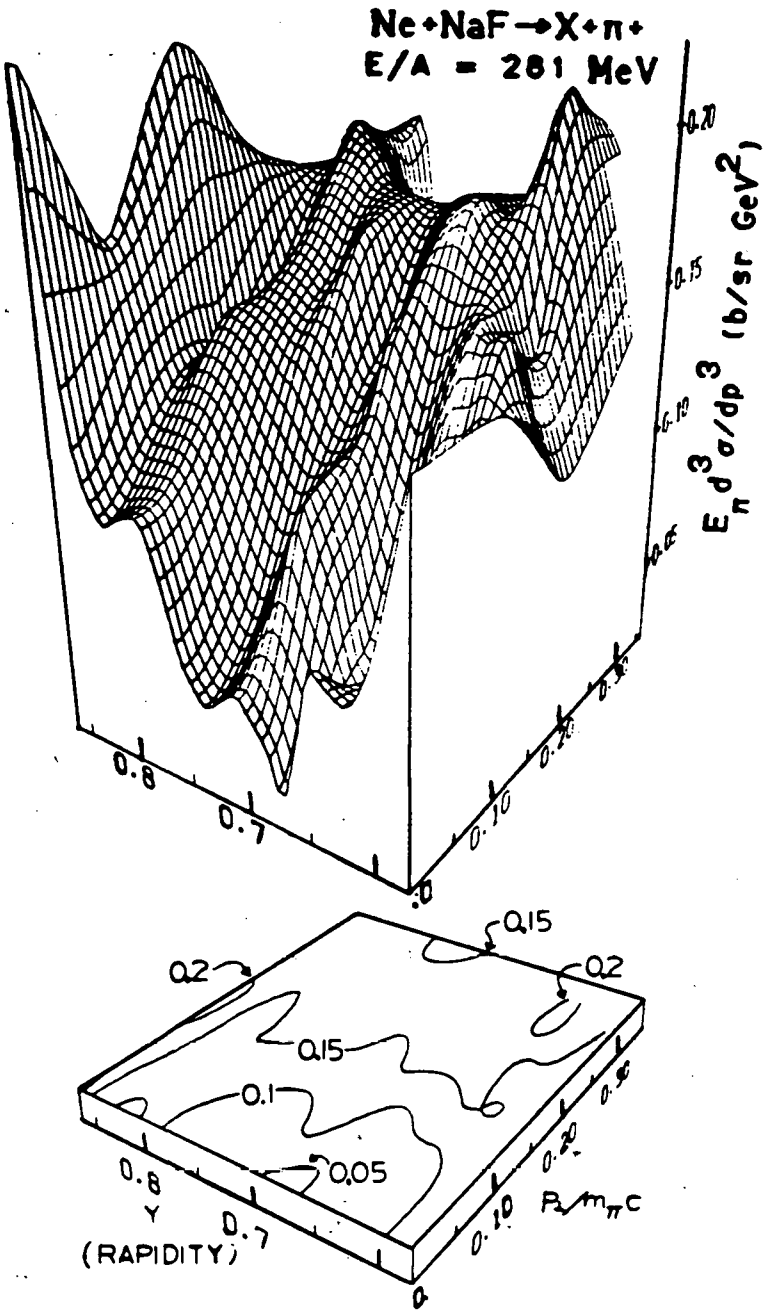

Fig. 38A -- The top part of the figure shows a perspective representation of the surface defined by the Lorentz invariant cross section ($Ed^3\sigma/dp^3$, units of $\mu b/sr\ MeV^2$) as a function of rapidity ($y=\tanh^{-1}(p_{\parallel}/E)$) and $p_\perp$ for Ne+NaF $\rightarrow \pi^+$ at E/A = 281 MeV. The bottom part of the figure is a contour plot of the same surface with the same scales for the y and $p_\perp$ axes.

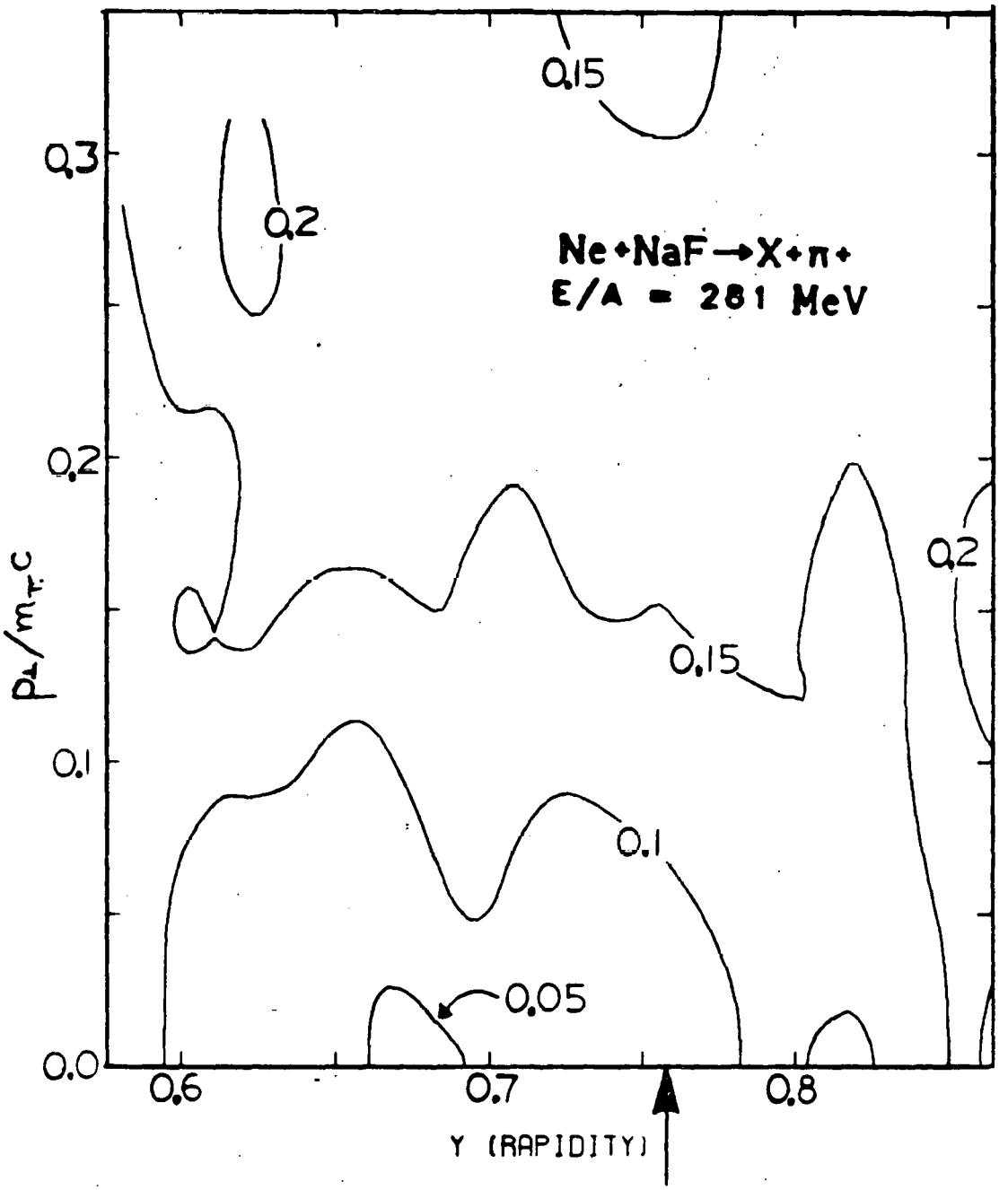

Fig. 38B -- A contour plot of the Lorentz invariant cross section ($Ed^3\sigma/dp^3$, units of μb/sr MeV^2) as a function of rapidity and $p_\perp$ for Ne+NaF → π^+ at E/A = 281 MeV. The arrow marks the velocity of the incident beam. This contour plot is the same as the one shown in figure 38A, except that it is not drawn in perspective and a more conventional orientation of the axes has been used.

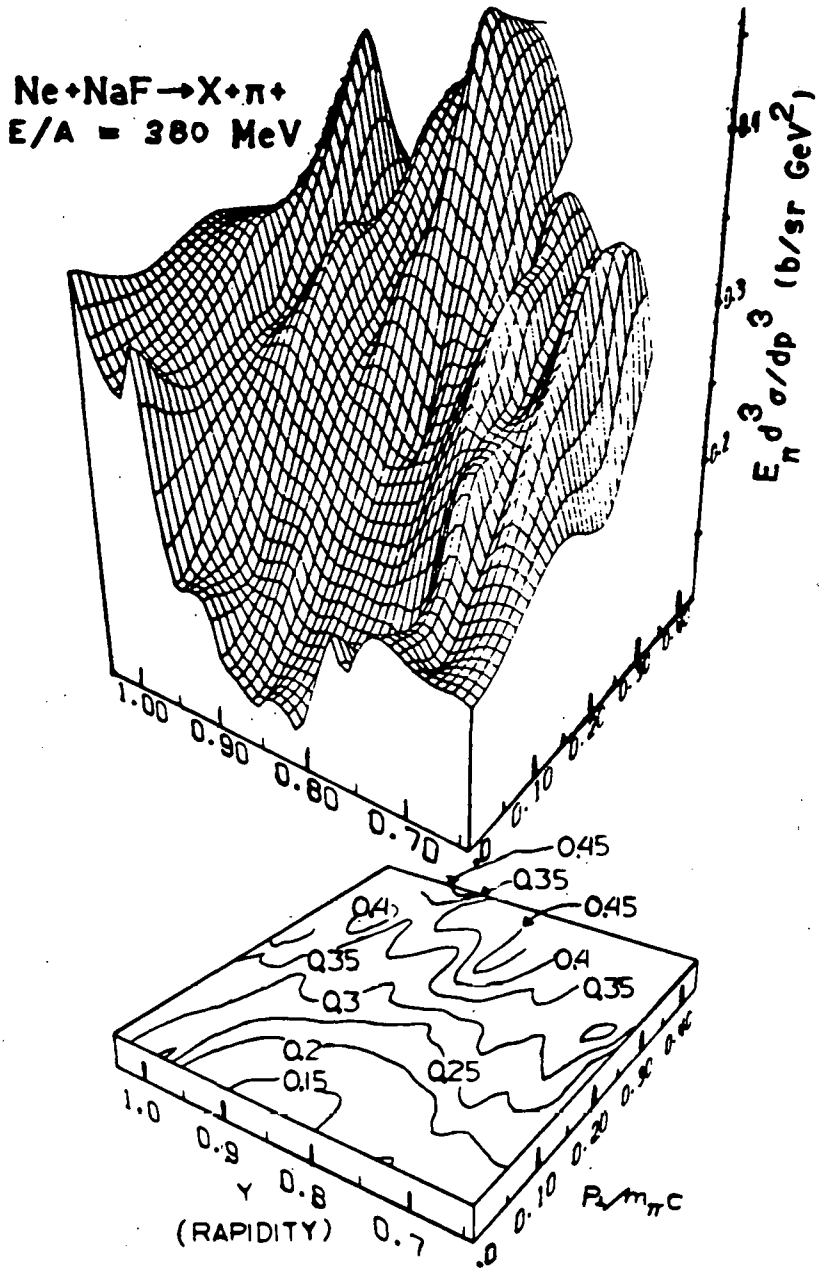

Fig. 39A -- The top part of the figure shows a perspective representation of the surface defined by the Lorentz invariant cross section ($Ed^3\sigma/dp^3$, units of $\mu b/sr\ MeV^2$) as a function of rapidity ($y=\tanh^{-1}(p_{\parallel}/E)$) and $p_\perp$ for Ne+NaF $\rightarrow \pi^+$ at E/A = 380 MeV. The bottom part of the figure is a contour plot of the same surface with the same scales for the y and $p_\perp$ axes.

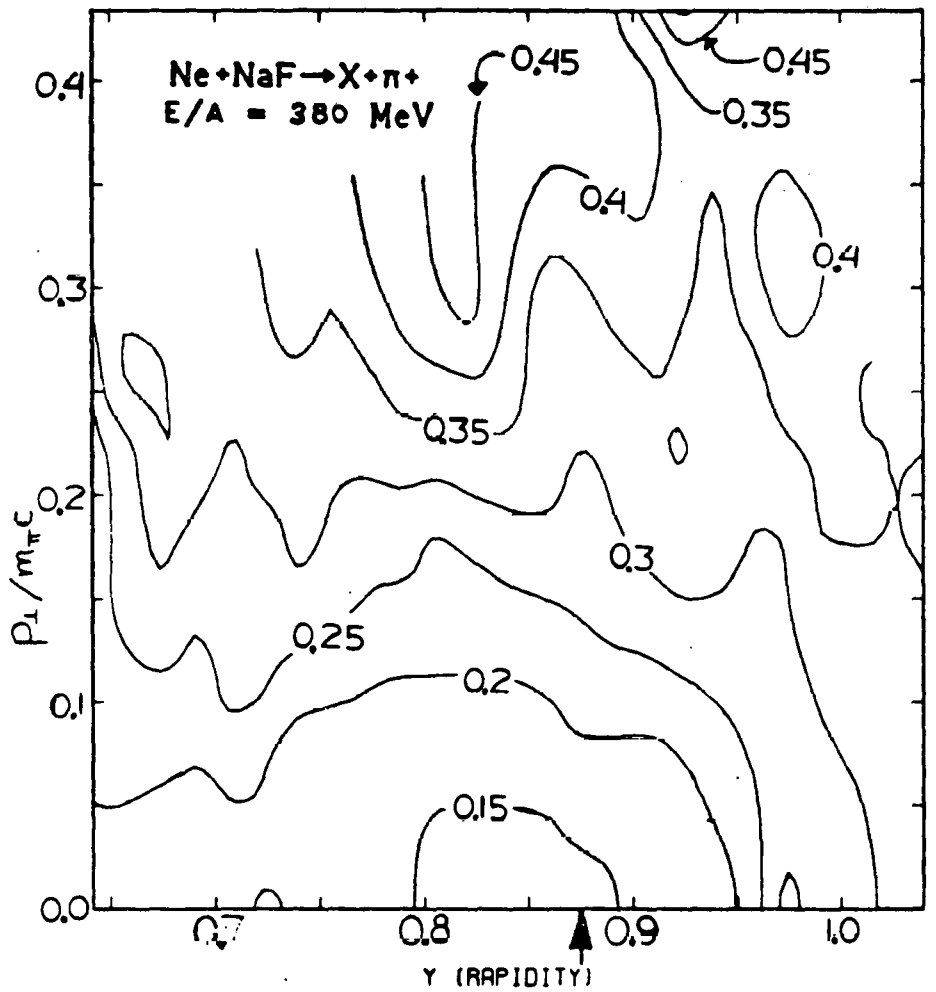

Fig. 39B -- A contour plot of the Lorentz invariant cross section ($Ed^3\sigma/dp^3$, units of $\mu b/sr\ MeV^2$) as a function of rapidity and $p_\perp$ for Ne+NaF $\rightarrow \pi^+$ at E/A = 380 MeV. The arrow marks the velocity of the incident beam. This contour plot is the same as the one shown in figure 39A, except that it is not drawn in perspective and a more conventional orientation of the axes has been used.

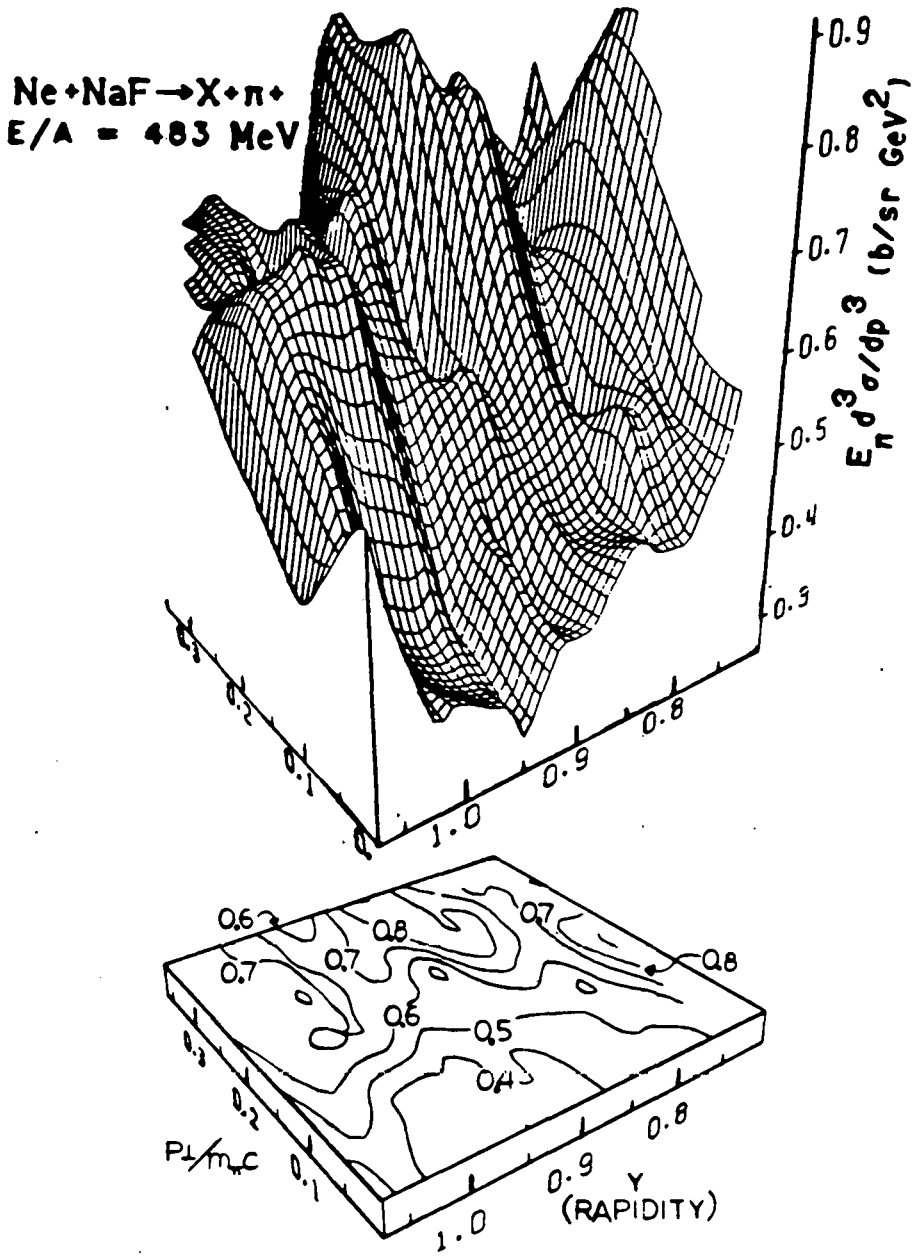

Fig. 40A -- The top part of the figure shows a perspective representation of the surface defined by the Lorentz invariant cross section ($Ed^3\sigma/dp^3$, units of $\mu b/sr\ MeV^2$) as a function of rapidity ($y=\tanh^{-1}(p_{||}/E)$) and $p_\perp$ for Ne+NaF $\rightarrow \pi^+$ at E/A = 483 MeV. The bottom part of the figure is a contour plot of the same surface with the same scales for the y and $p_\perp$ axes.

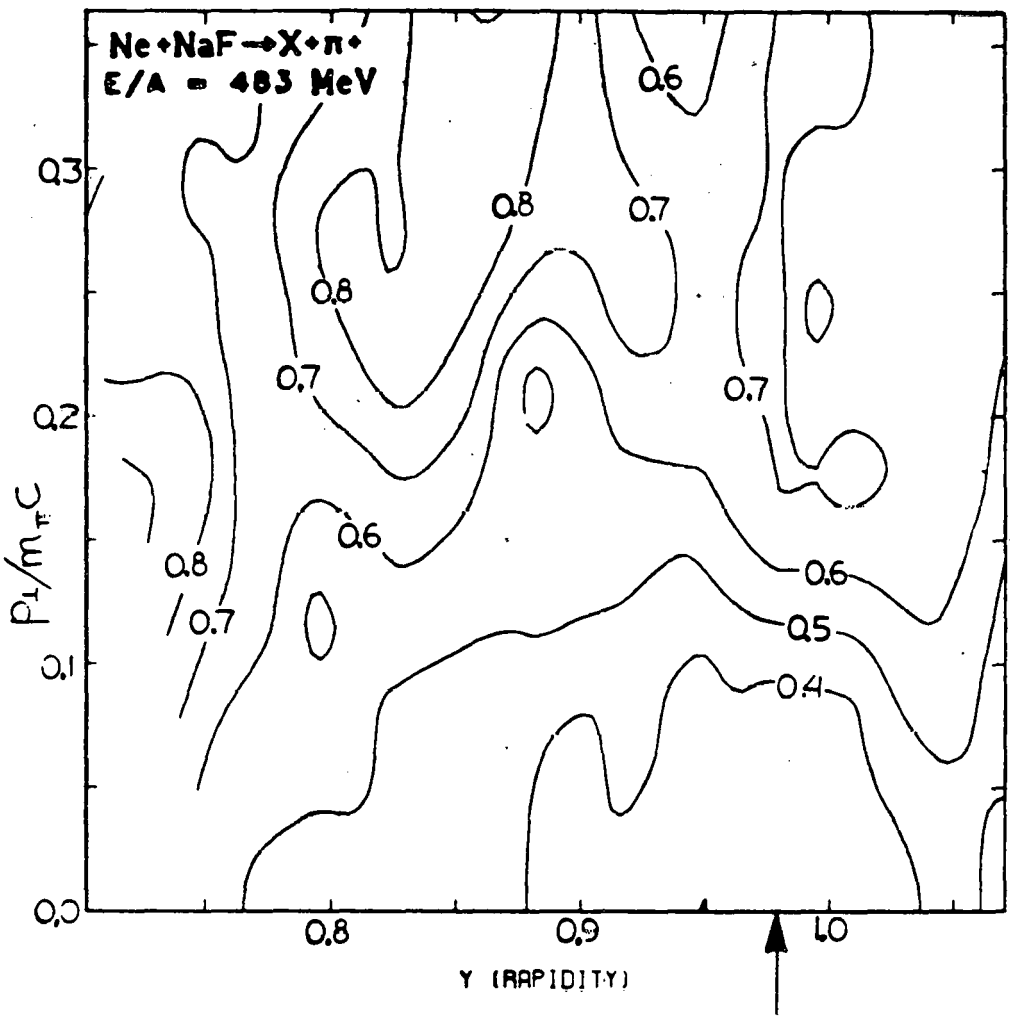

Fig. 40B -- A contour plot of the Lorentz invariant cross section ($Ed^3\sigma/dp^3$, units of μb/sr MeV^2) as a function of rapidity and $p_\perp$ for Ne+NaF → π^+ at E/A = 483 MeV. The arrow marks the velocity of the incident beam. This contour plot is the same as the one shown in figure 40A, except that it is not drawn in perspective and a more conventional orientation of the axes has been used.

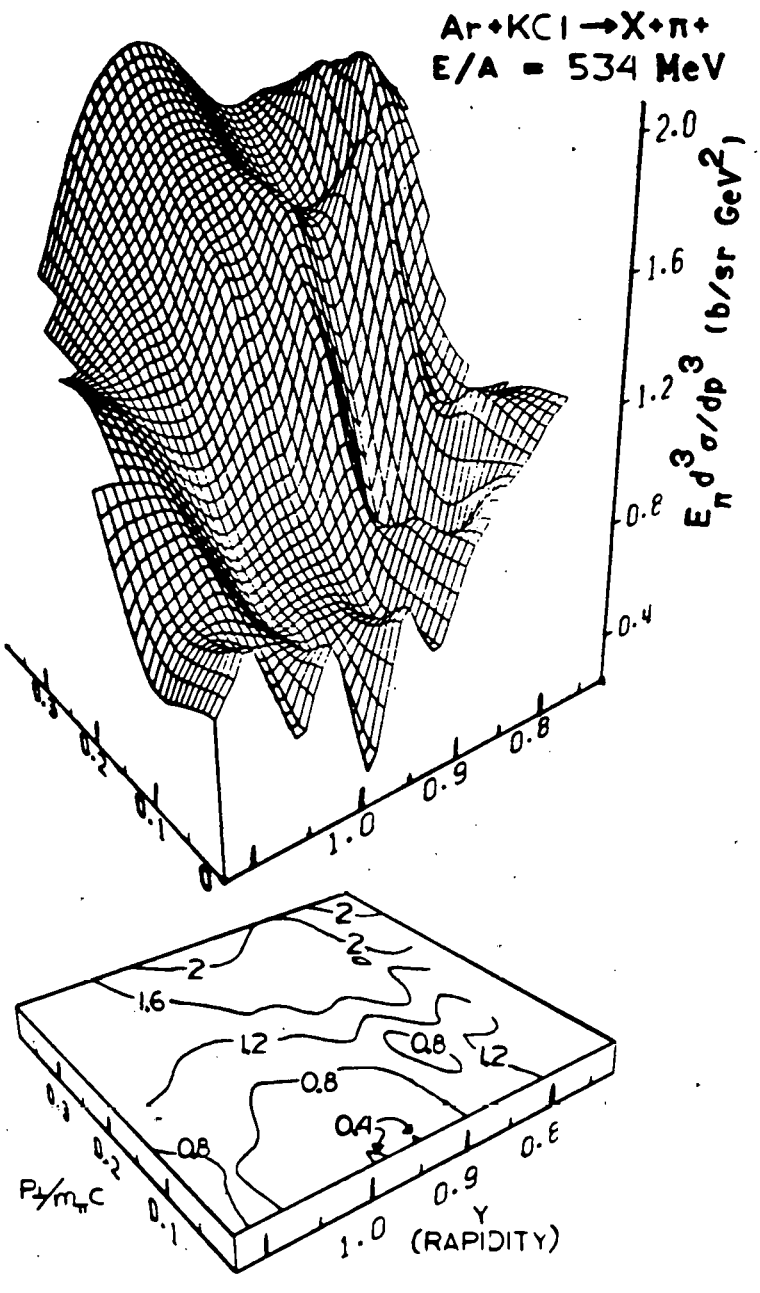

Fig. 41A -- The top part of the figure shows a perspective representation of the surface defined by the Lorentz invariant cross section ($Ed^3\sigma/dp^3$, units of μb/sr MeV^2) as a function of rapidity ($y=\tanh^{-1}(p_{\parallel}/E)$) and $p_\perp$ for Ar+KCl $\rightarrow \pi^+$ at E/A = 534 MeV. The bottom part of the figure is a contour plot of the same surface with the same scales for the y and $p_\perp$ axes.

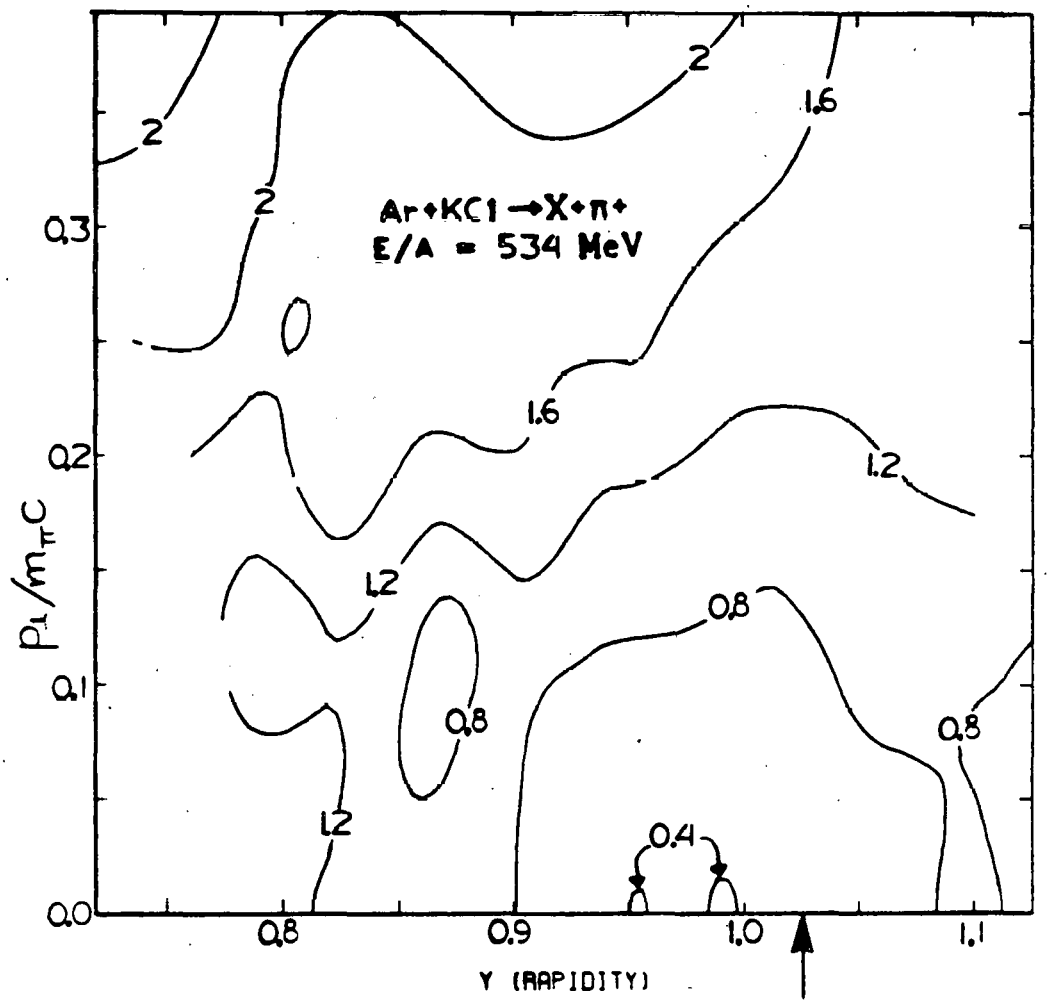

Fig. 41B -- A contour plot of the Lorentz invariant cross section ($Ed^3\sigma/dp^3$, units of $\mu b/sr\ MeV^2$) as a function of rapidity and $p_\perp$ for Ar+KCl → π^+ at E/A = 534 MeV. The arrow marks the velocity of the incident beam. This contour plot is the same as the one shown in figure 41A, except that it is not drawn in perspective and a more conventional orientation of the axes has been used.

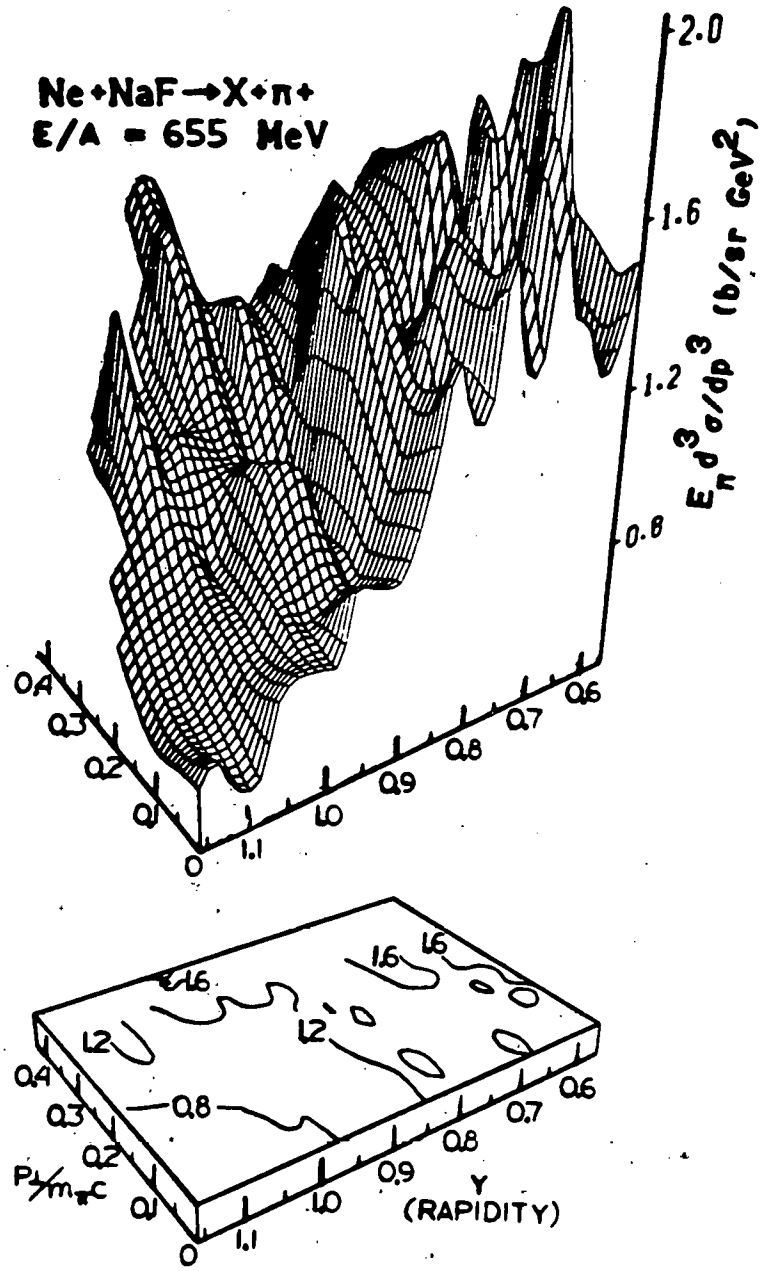

Fig. 42A -- The top part of the figure shows a perspective representation of the surface defined by the Lorentz invariant cross section ($Ed^3\sigma/dp^3$, units of μb/sr MeV^2) as a function of rapidity ($y=\tanh^{-1}(p_\parallel/E)$) and $p_\perp$ for Ne+NaF → π^+ at E/A = 655 MeV. The bottom part of the figure is a contour plot of the same surface with the same scales for the y and $p_\perp$ axes. The data were assumed to be symmetric about the center of mass rapidity and all points have been reflected about the center of mass. Only the part of the data on the projectile side of the center of mass has been shown.

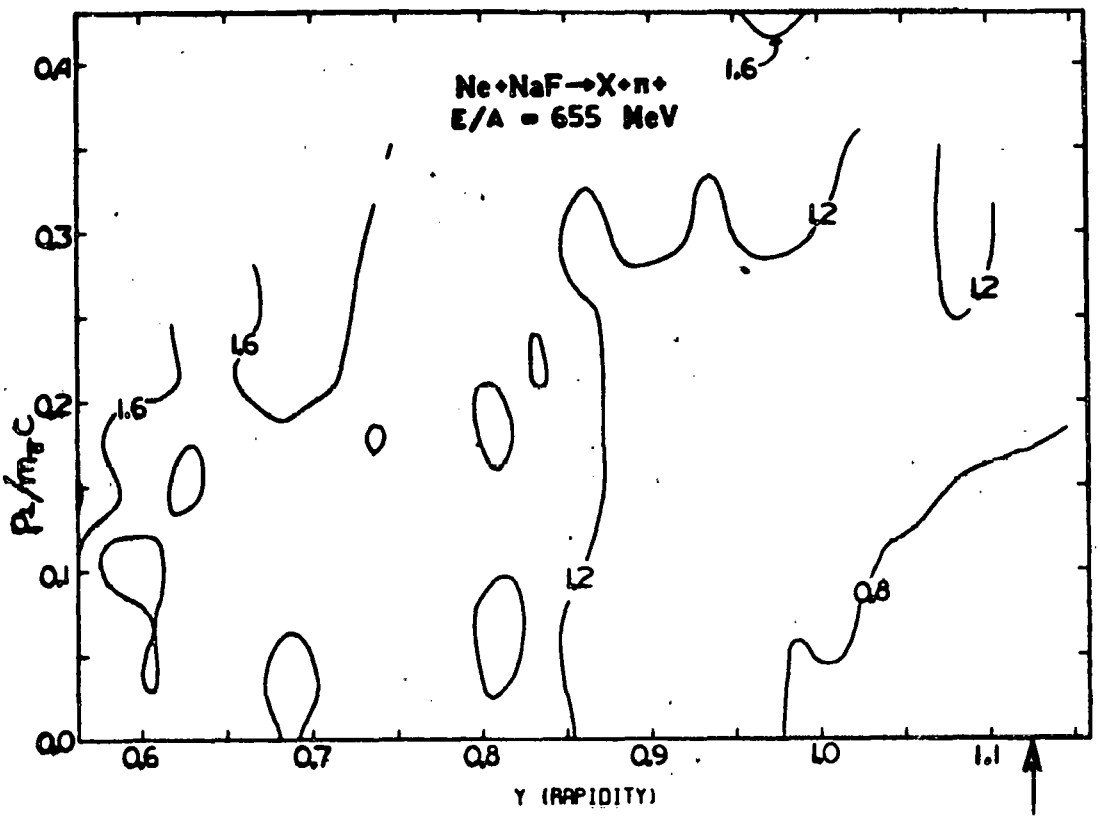

Fig. 42B -- A contour plot of the Lorentz invariant cross section ($Ed^3\sigma/dp^3$, units of $\mu b/sr\ MeV^2$) as a function of rapidity and $p_\perp$ for Ne+NaF $\rightarrow \pi^+$ at E/A = 655 MeV. The arrow marks the velocity of the incident beam. This contour plot is the same as the one shown in figure 42A, except that it is not drawn in perspective and a more conventional orientation of the axes has been used. The data were assumed to be symmetric about the center of mass rapidity and all points have been reflected about the center of mass. Only the part of the data on the projectile side of the center of mass has been shown.

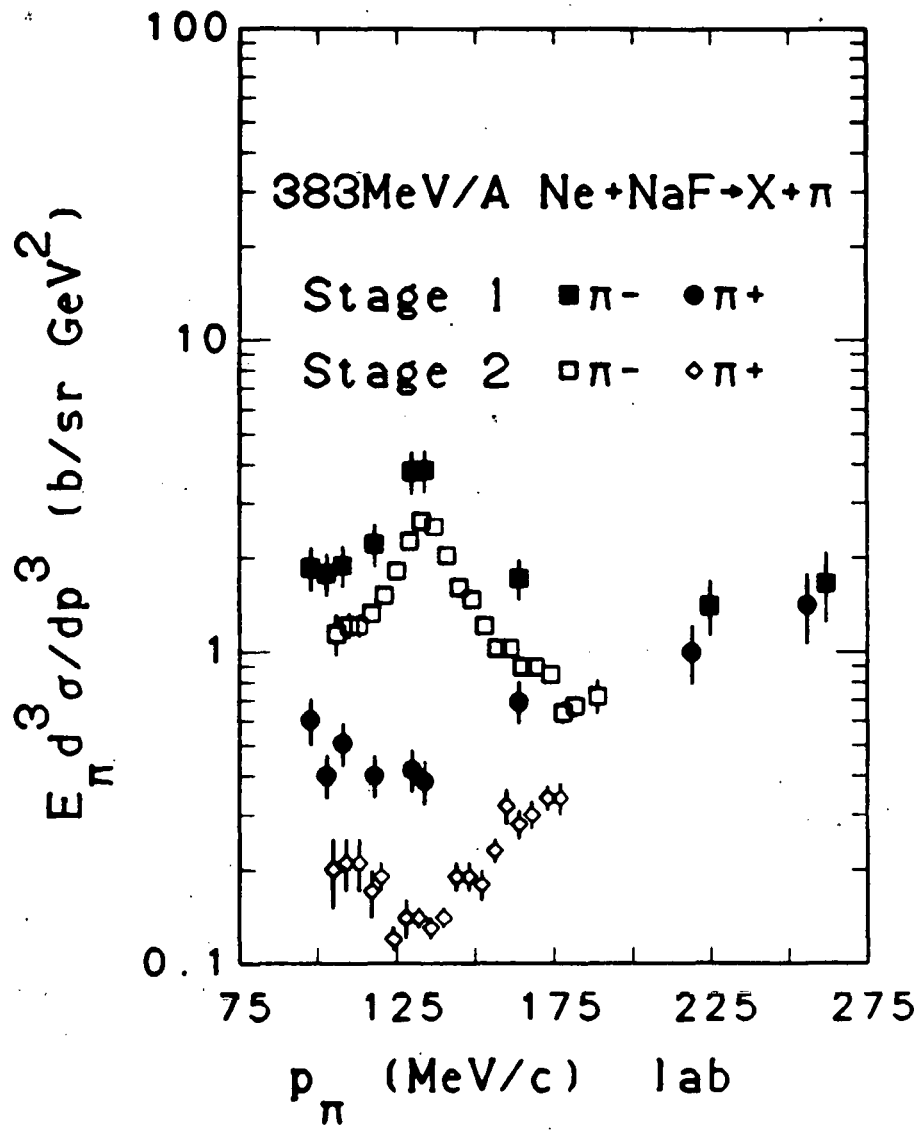

Fig. 43 -- Comparison of the Ne+NaF → $\pi^{\pm}$ data at E/A = 383 MeV from the lead slit spectrometer (the stage 1 data) and from the upgraded spectrometer (the stage 2 data).

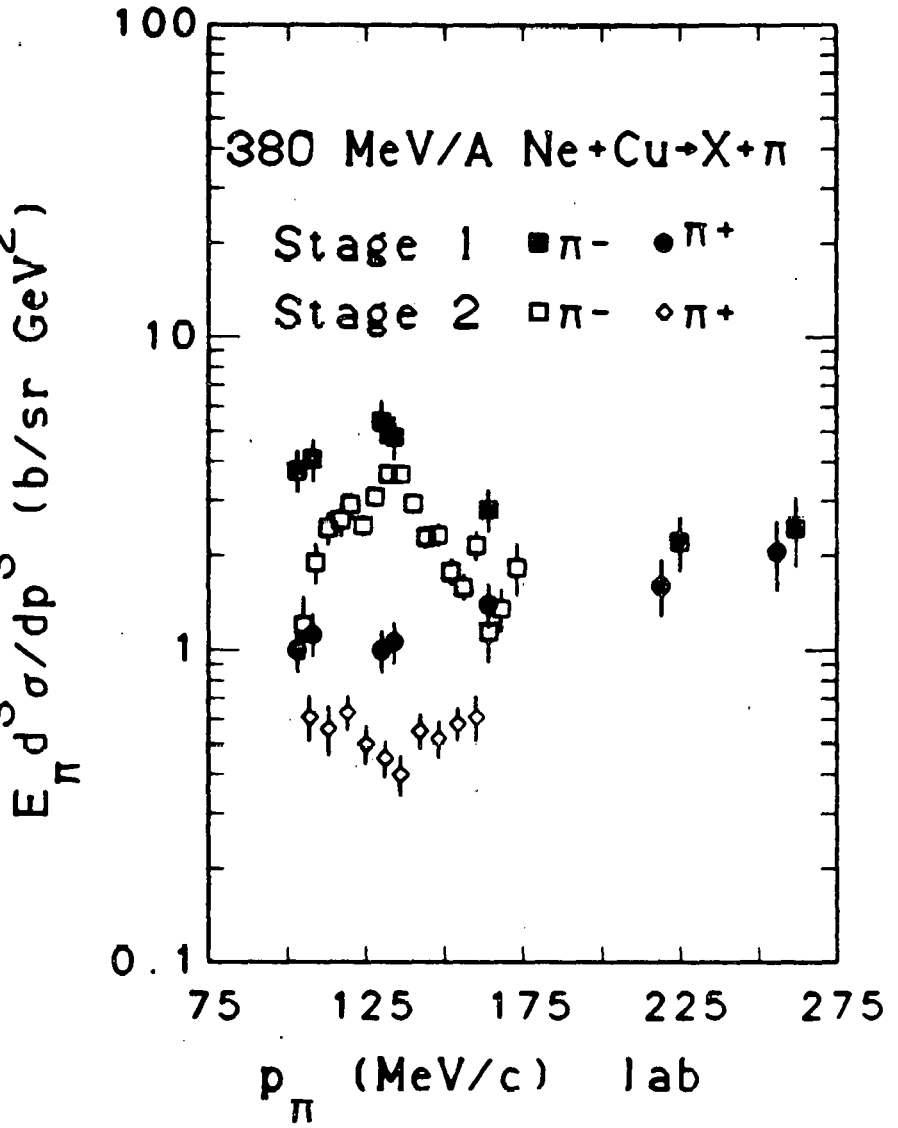

Fig. 44 -- Comparison of the Ne+Cu → $\pi^\pm$ data at E/A = 380 MeV from the lead slit spectrometer (the stage 1 data) and from the upgraded spectrometer (the stage 2 data).

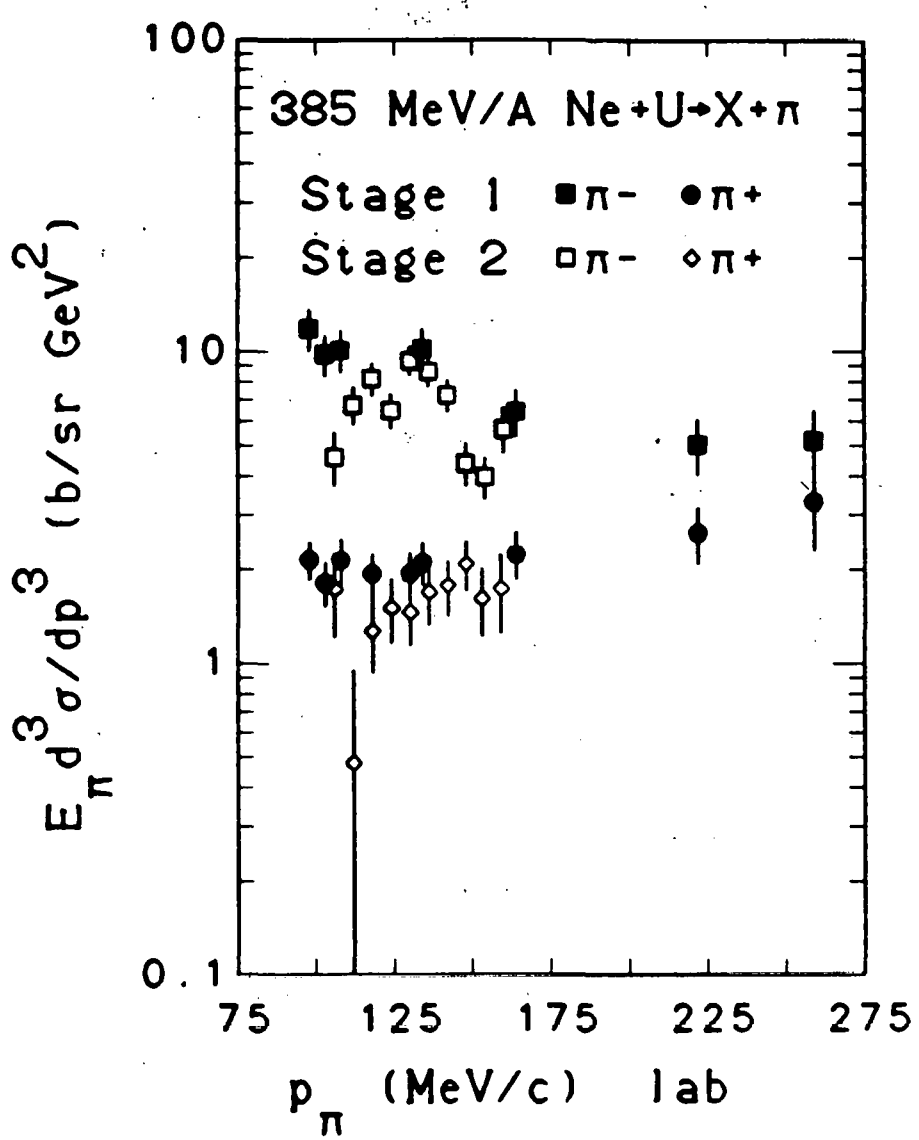

Fig. 45 -- Comparison of the Ne+U → $\pi^\pm$ data at E/A = 385 MeV from the lead slit spectrometer (the stage 1 data) and from the upgraded spectrometer (the stage 2 data). The Lorentz invariant cross section is plotted as a function of the lab momentum of the pion.

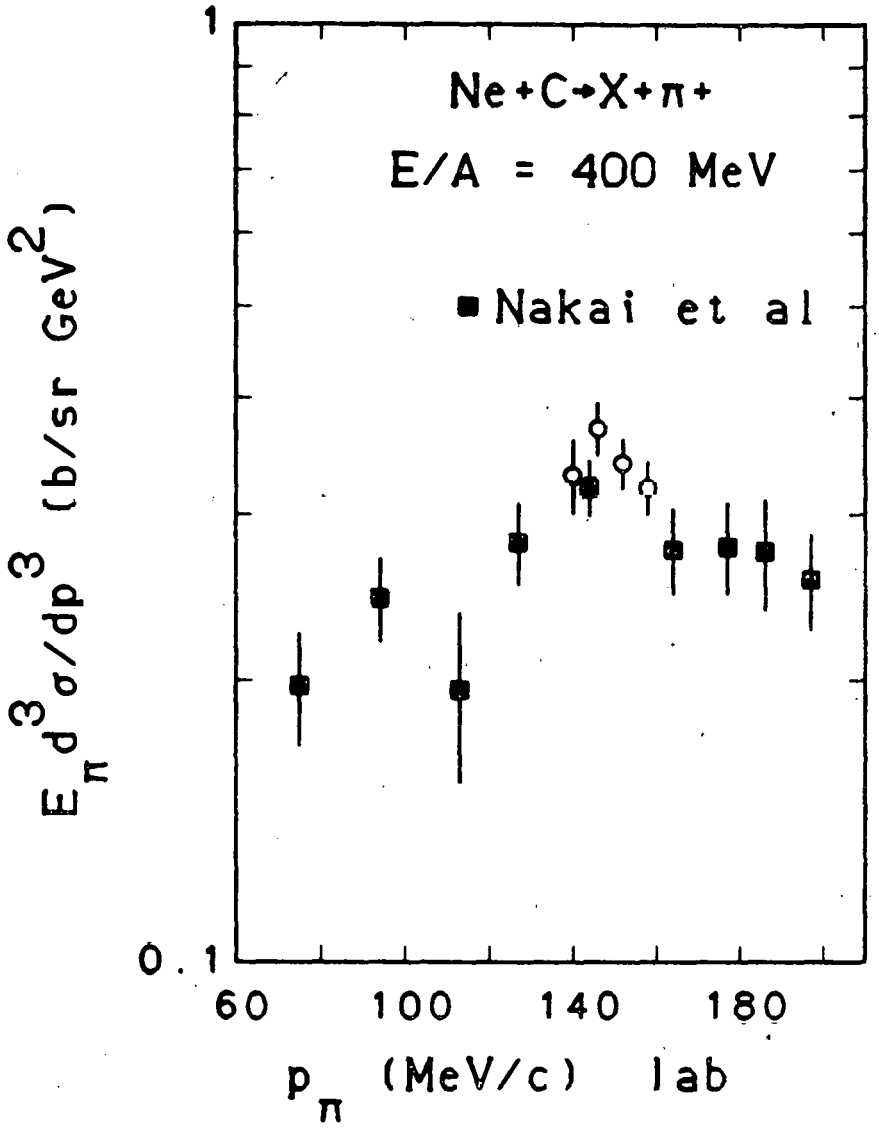

Fig. 46 -- Comparison of the Ne+C → π^+ data at E/A ≃ 400 MeV and a lab angle of 30 degrees from Nakai *et al*.[11] (solid squares) with the present results (open circles). The beam energies are probably slightly different since the beam energies for the present results have been corrected to the values at the center of the target, while those of Nakai *et al*. probably have not been corrected. The error bars are statistical.

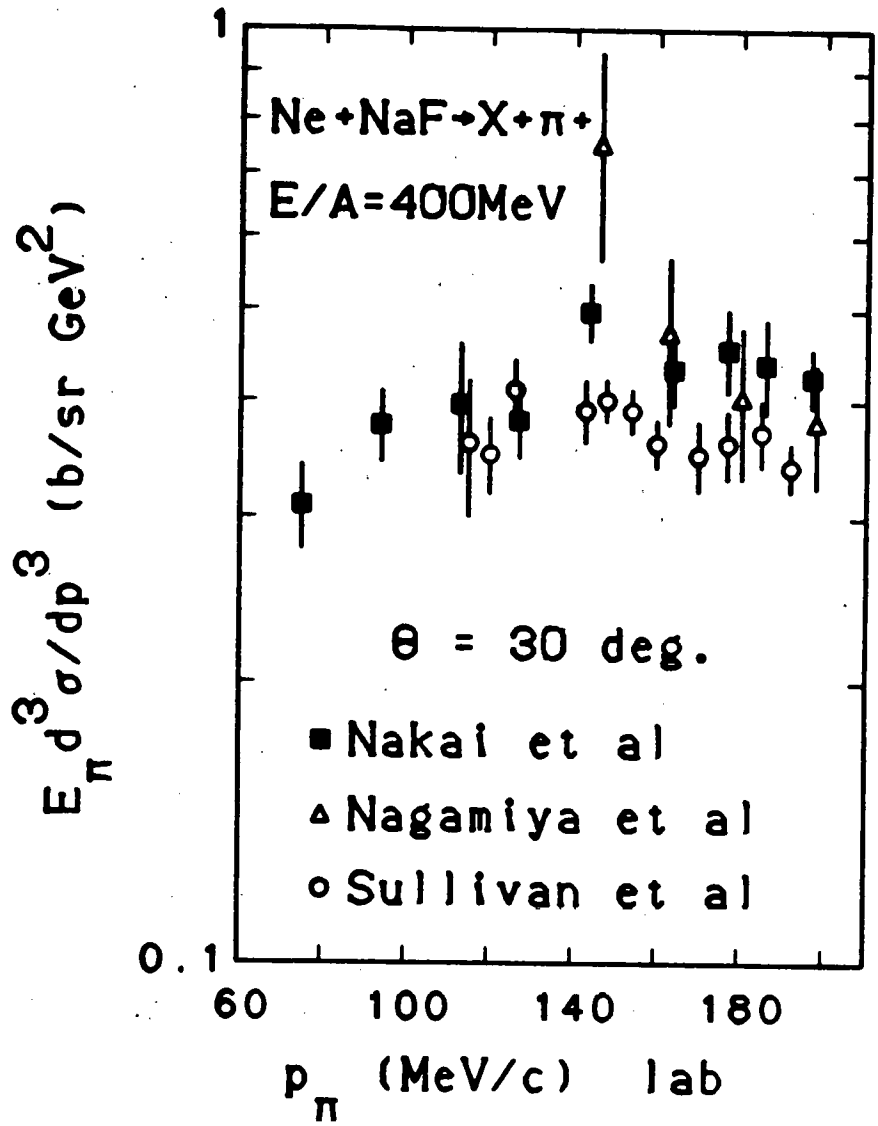

Fig. 47 — Comparison of the Ne+NaF → π^+ data at E/A ≃ 400 MeV and a lab angle of 30 degrees from Nakai et al.[11] (solid squares) and from Nagamiya et al.[13,63] (open triangles) with the present results (open circles). The beam energies are probably slightly different since the beam energies for the present results have been corrected to the values at the center of the target, while those of the other groups probably have not been corrected. The error bars are statistical. The data from reference 63 are preliminary.

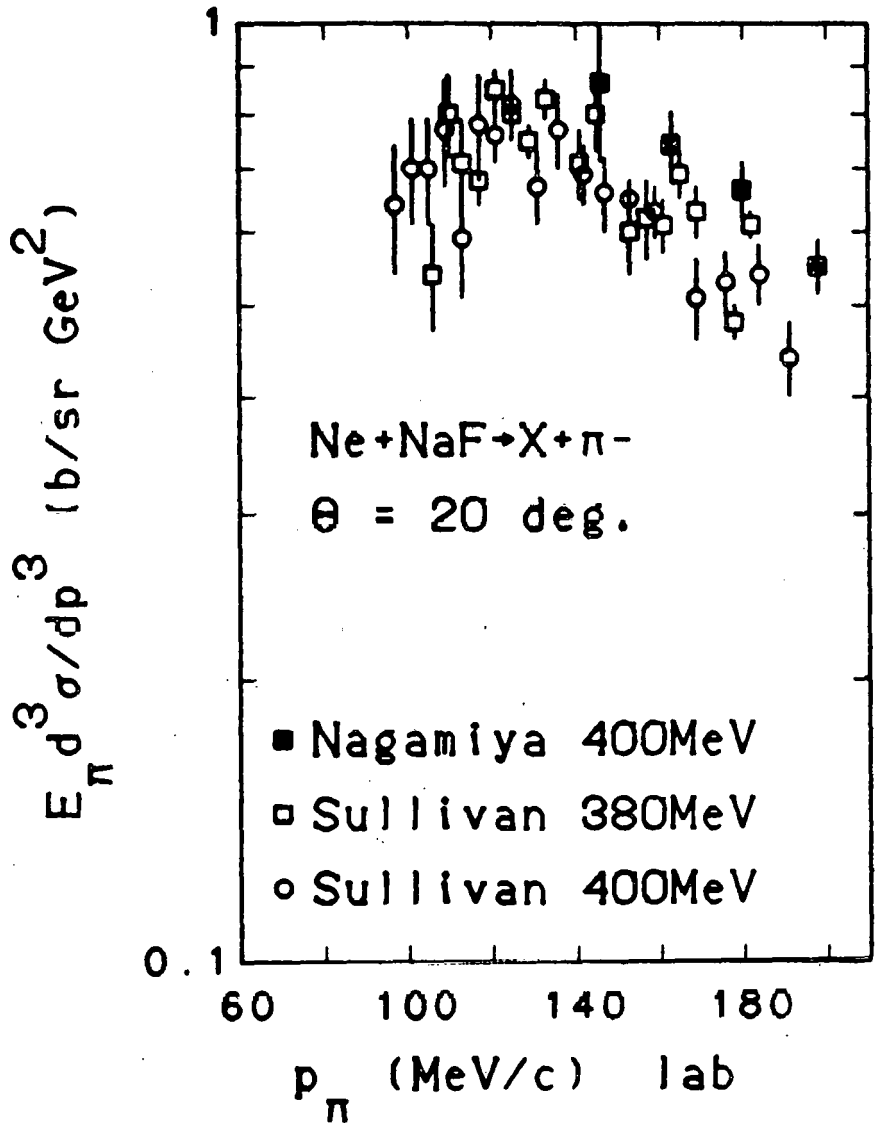

Fig. 48 — Comparison of the Ne+NaF $\rightarrow\pi^-$ data at E/A $\simeq$ 400 MeV and a lab angle of 20 degrees from Nagamiya et al.[13,63] (solid squares) and the present results (open circles) at two slightly different beam energies. The beam energies are given at the center of the target in the case of the present results, while those of Nagamiya et al. probably have not been corrected. The error bars are statistical. The data from reference 63 are preliminary.

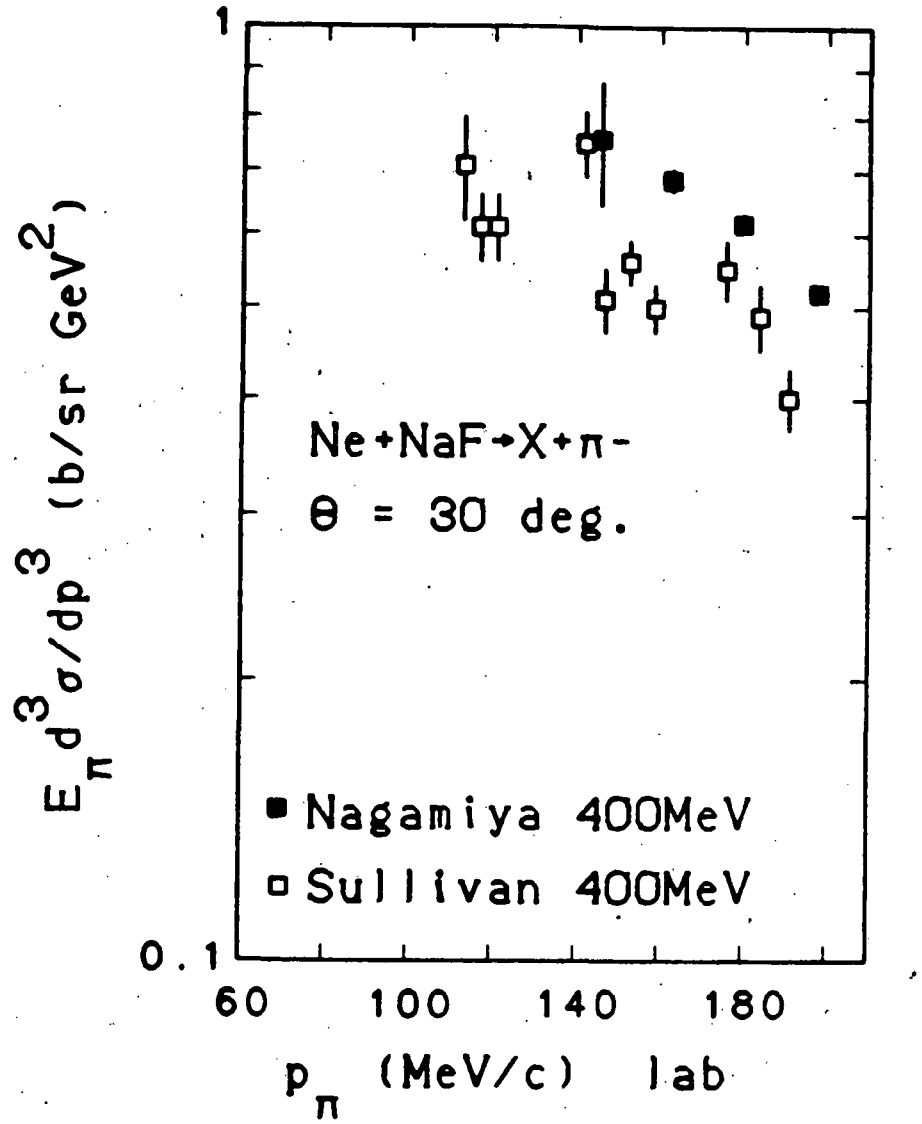

Fig. 49 -- Comparison of the Ne+NaF $\rightarrow\pi^-$ data at E/A $\simeq$ 400 MeV and a lab angle of 30 degrees from Nagamiya et al.[13,63] (solid squares) and the present results (open squares). The beam energies are probably slightly different since the beam energies for the present results have been corrected to the values at the center of the target, while those of Nagamiya et al. probably have not been corrected. The error bars are statistical. The data from reference 63 are preliminary.

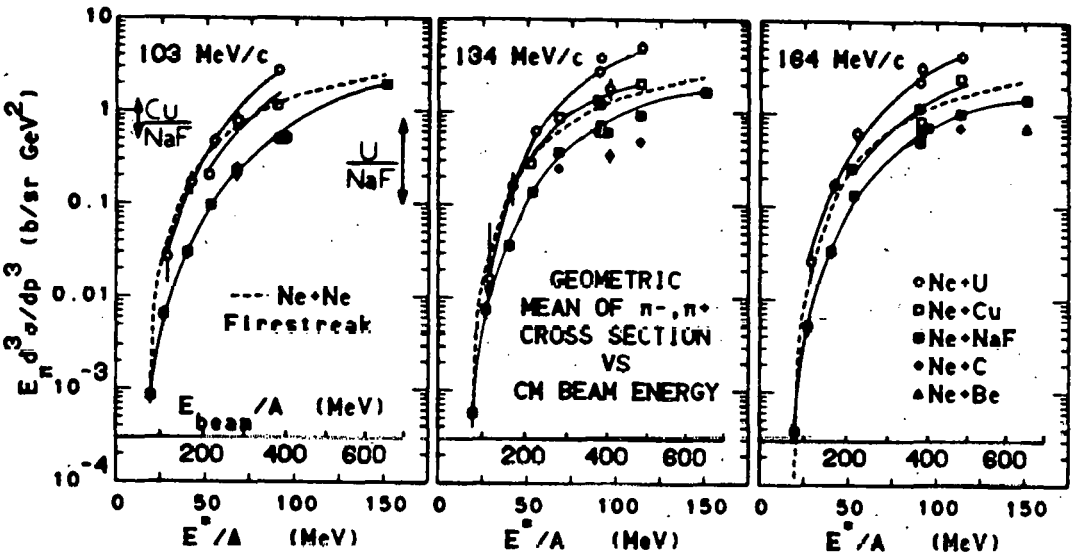

Fig. 50 -- The Lorentz invariant cross section at three different pion lab momenta as a function of the neon beam energy per nucleon in the nucleon-nucleon center of mass. In order to approximately remove the Coulomb effects, the geometric mean of the π^- and π^+ cross sections has been plotted. The data from the lead slit spectrometer have been divided by 1.7 in order to bring the normalization into agreement with the normalization of the data from the upgraded spectrometer. The arrows on the left hand side of the figure show the expected separation of the curves for Cu/NaF and U/NaF targets if the cross sections scaled according to equations 6.8 and 6.10. The solid lines are to guide the eye. The dashed lines show the predictions of the firestreak model[23] for Ne+Ne. The error bars on the data points do not include the uncertainty on the overall normalization. This figure is an updated version of figure 7.

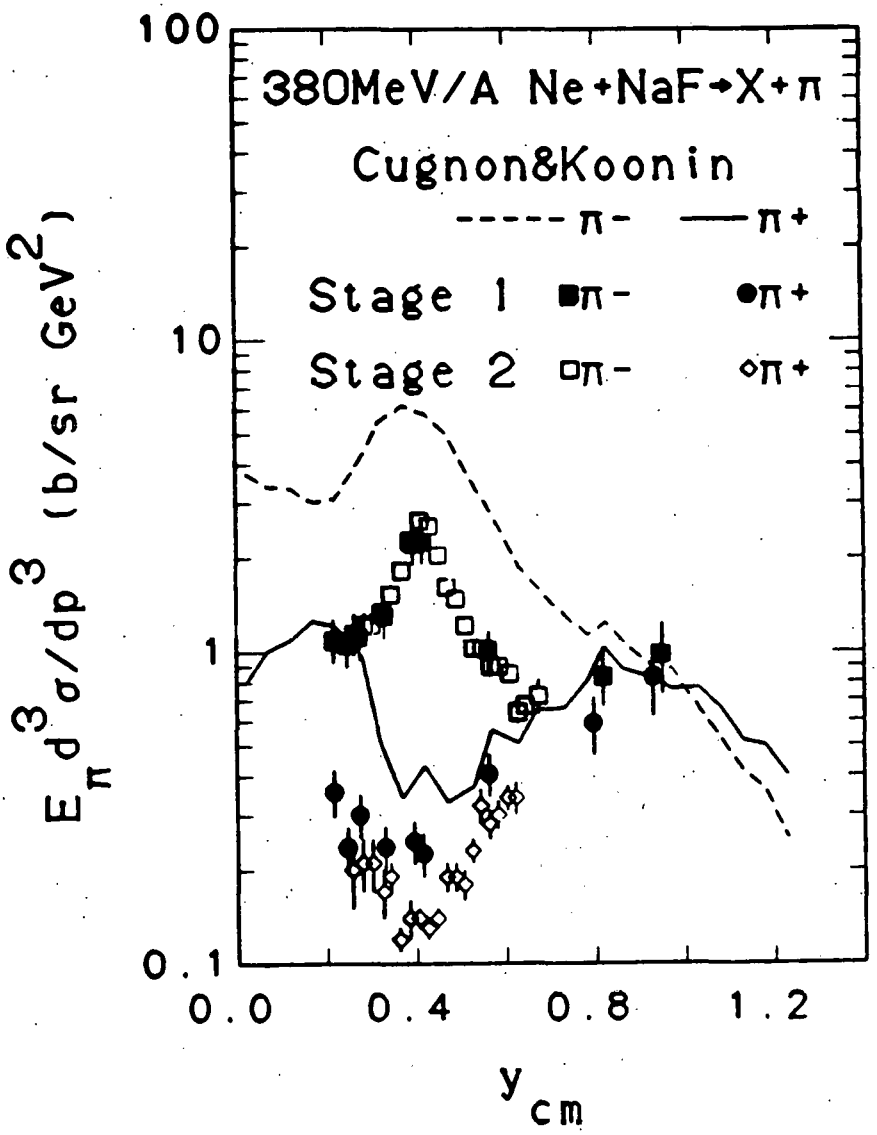

Fig. 51 -- A comparison of the measured cross sections for Ne+NaF $\rightarrow \pi^{\pm}$ at E/A = 380 MeV and the predictions of Cugnon and Koonin[30]. The cross sections from the lead slit, or stage 1, spectrometer (solid points) have been divided by 1.7 in order to bring them into agreement with the normalization of the data from the upgraded, or stage 2, spectrometer (open points). The error bars on the data points do not include the uncertainty on the overall normalization.

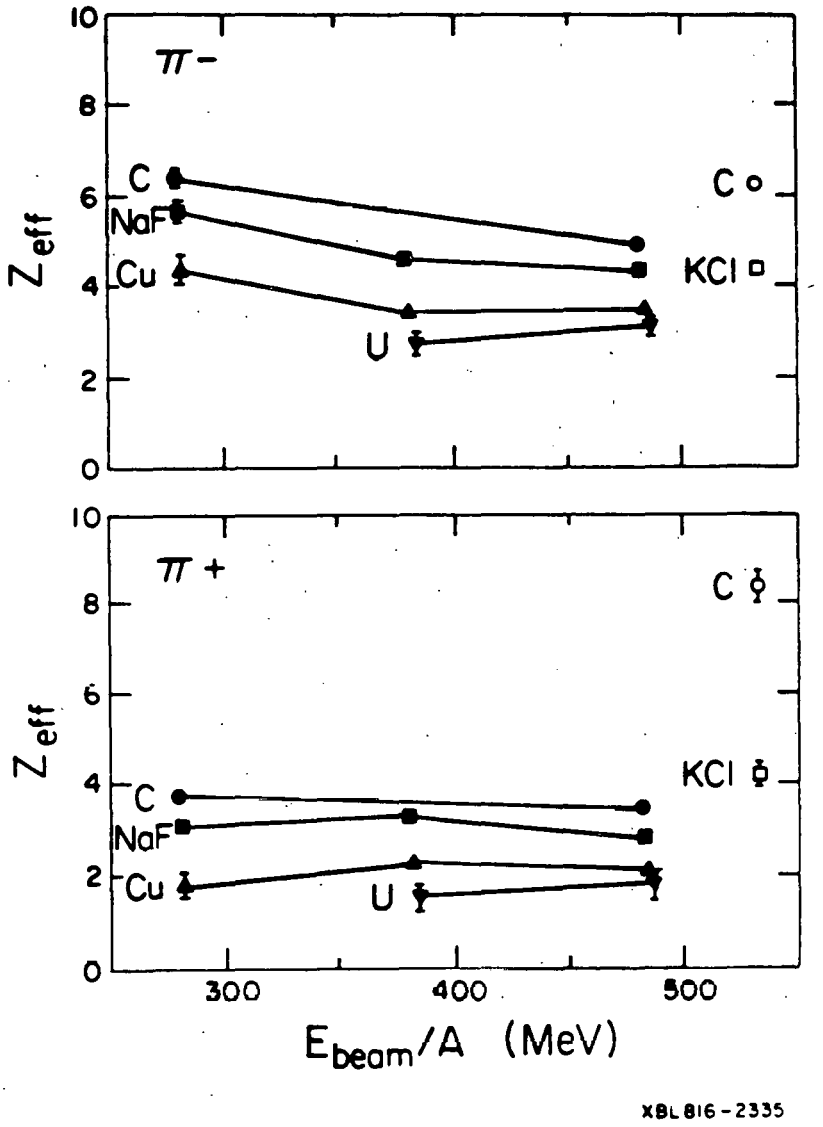

Fig. 52 -- Effective charge of the projectile fragment from the least squares fits of the Coulomb correction formulas[42] to the π^- (top) and π^+ (bottom) data. The closed symbols are from the data with Ne beams and the open symbols with an Ar beam. The lines are to guide the eye. Tne target is shown next to each point or set of points. Some of the data have been omitted because the fits to the data were poor.

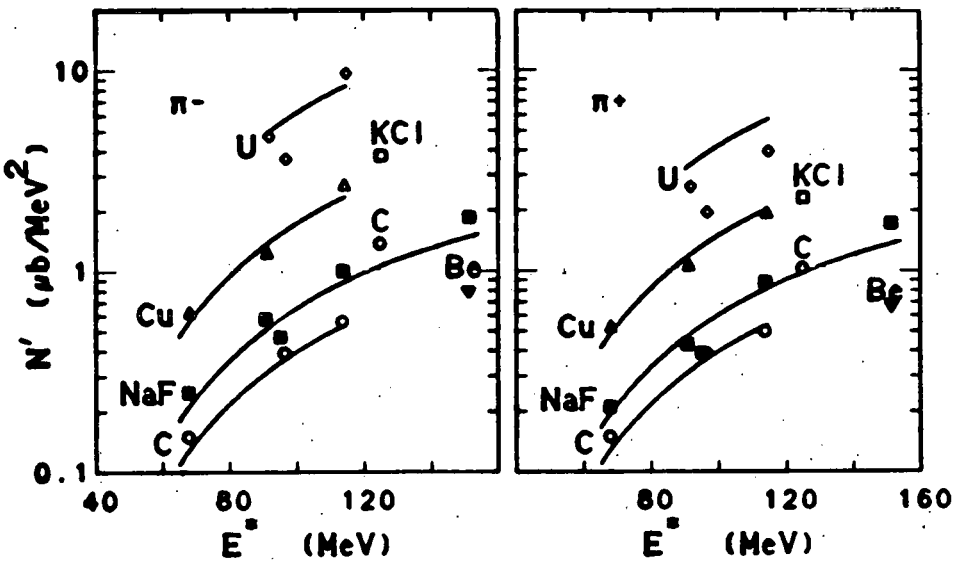

Fig. 53 -- The values of the Lorentz invariant form of the uncharged pion source function (see eq. 6.14) evaluated for pions at rest in the center of mass [$N' = m_\pi \sigma_0(p_{cm}=0) = Nm_\pi \exp(-m_\pi/T)$] vs. the beam energy per nucleon in the nucleon-nucleon center of mass. The right side of the graph is from the fits to the π^+ data and the left side is from the π^- data. The closed symbols are for a Ne beam and the open symbols are for an Ar beam. The lines are from a semi-empirical parameterization of these values (see eq. 6.18). The target is shown next to each point or set of points.

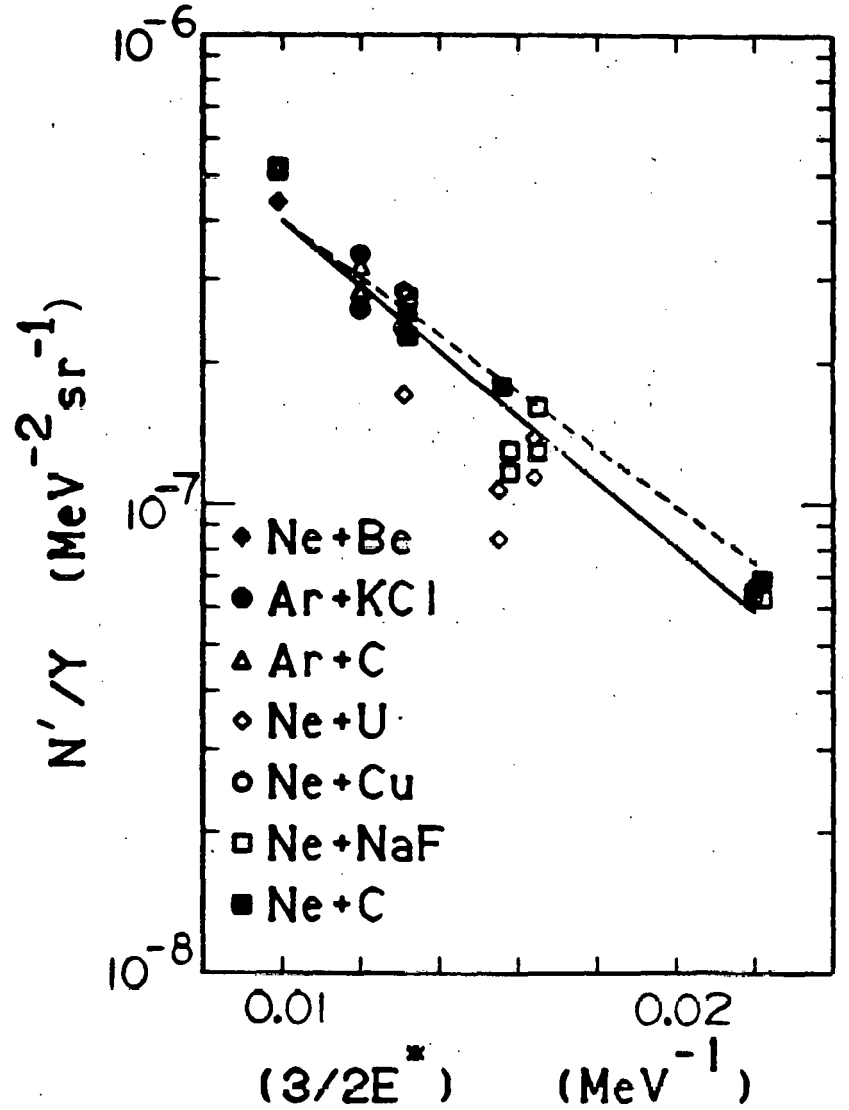

Fig. 54 -- A plot based on equation 6.18 showing N', the value of the source function (eq. 6.14) evaluated for pions at rest in the nucleon-nucleon center of mass, divided by Y, the geometric scaling of the pion cross sections predicted by equations 6.8 and 6.10, versus $3/2E^*$. $2E^*/3$ is (roughly) the temperature in the fireball model[22]. The solid line is a least squares fit to all of the data points. It has a slope of -160 MeV. The dashed line has a slope of $-m_\pi c^2$, which is (again roughly) what would be expected from the fireball model. The data from all projectile-target combinations studied have been combined on this graph. Many of the points have been obscured because they lie on top of one another.

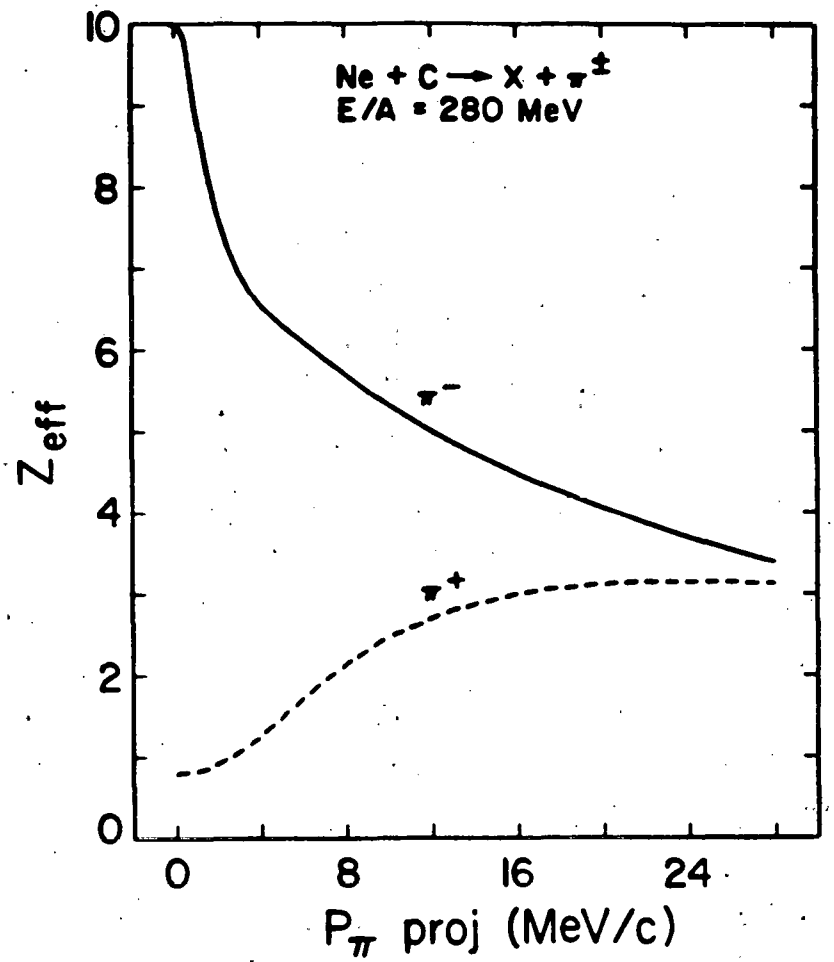

XBL 816-10171

Fig. 55 -- The average effective projectile fragment charge (Z_{eff}) that would give the same theoretical $\pi^{\pm}$ cross sections as the detailed averaging procedure of Radi et al.[72]. The data points are plotted as a function of pion momentum in the rest frame of the projectile for Ne+C at E/A = 280 MeV.

REFERENCES

(1) W. Benenson, G. Bertsch, G.M. Crawley, E. Kashy, J.A. Nolen, Jr., H. Bowman, J.G. Ingersoll, J.O. Rasmussen, J. Sullivan, M. Koike, M. Sasao, J. Péter, T.E. Ward, Phys. Rev. Lett. 43, 683 (1979) ; errata : 44, 54 (1980).

(2) J.P. Sullivan, J.A. Bistirlich, H.R. Bowman, R. Bossingham, T. Buttke, K.M. Crowe, K.A. Frankel, C.J. Martoff, J. Miller, D.L. Murphy, J.O. Rasmussen, W.A. Zajc, O. Hashimoto, M. Koike, J. Péter, W. Benenson, G.M. Crawley, E. Kashy, J.A. Nolen, Jr., LBL Report #11971 (1981); to be published in Phys Rev. C.

(3) W. Schimmerling, K.G. Vosburgh, K. Koepke, W.D. Wales, Phys. Rev. Lett. 33, 1170 (1974); K.G. Vosburgh, W. Schimmerling, K. Koepke, W.D. Wales, Phys. Rev. D11, 1743 (1975).

(4) J. Papp, J. Jaros, L. Schroeder, J. Staples, H. Steiner, S. Wagner, J. Wiss, Phys. Rev. Lett. 34, 601 (1975). ; J. Papp, Ph.D. Thesis, University of California, Berkeley, LBL Report 3633 (1975), unpublished.

(5) P.J. McNulty, G.E. Farrell, R.C. Filz, W. Schimmerling, K.G. Vosburgh, Phys. Rev. Lett. 38, 1519 (1977) ; generally discredited, their results are not consistent with the results of references 1,6,7.

(6) P.J. Lindstrom, H.J. Crawford, D.E. Greiner, Ray Hagstrom, H.H. Heckman, Phys. Rev. Lett. 40, 93 (1978).

(7) R. Kullberg, A. Oskarsson, I. Otterlund, Phys. Rev. Lett. 40, 289 (1978).

(8) S.Y. Fung, W. Gorn, G.P. Kiernan, F.F. Liu, J.J. Lu, Y.T. Oh, J. Ozawa, R.T. Poe, L. Schroeder, H. Steiner, Phys. Rev. Lett. 40, 292 (1978).

(9) K.L. Wolf, H.H. Gutbrod, W.G. Meyer, A.M. Poskanzer, A. Sandoval, R. Stock, J. Gosset, C.H. King, G. King, Nguyen Van Sen, G.D. Westfall, Phys. Rev. Lett. 42, 1448 (1979).

(10) J. Chiba, K. Nakai, I. Tanihata, S. Nagamiya, H. Bowman, J. Ingersoll, J.O. Rasmussen, Phys. Rev. C20, 1332 (1979).

(11) K. Nakai, J. Chiba, I. Tanihata, M. Sasao, H. Bowman, S. Nagamiya, J.O. Rasmussen, Phys. Rev. C20, 2210 (1979).

(12) L.S. Schroeder, S.A. Chessin, J.V. Geaga, J.Y. Grossiord, J.W. Harris, D.L. Hendrie, R. Truehaft, K. Van Bibber, Phys. Rev. Lett. 43, 1787 (1979).

(13) S. Nagamiya, M.-C. Lemaire, E. Moeller, S. Schnetzer, G. Shapiro, H. Steiner, I. Tanihata, Phys. Rev. C24, 971 (1981).

(14) K.A. Frankel, J.A. Bistirlich, R. Bossingham, H.R. Bowman, K.M. Crowe, C.J. Martoff, D. Murphy, J.O. Rasmussen, J.P. Sullivan, W.A. Zajc, J.P. Miller, O. Hashimoto, M. Koike, J. Péter, J. Quebert, LBL Report #12585 (1981); submitted to Phys. Rev. C, Rapid Communications.

(15) W. Scheid, H. Müller, W. Greiner, Phys. Rev. Lett. 32, 741 (1974).

(16) M.I. Sobel, P.J. Siemens, J.P. Bondorf, H.A. Bethe, Nucl. Phys. A251, 502 (1975).

(17) V. Ruck, M. Gyulassy, W. Greiner, Z. Phys. A277, 391 (1976).

(18) H. Orland and R. Schaeffer, J. Phys. (Paris) Lett. 37, L327 (1976).

(19) G.F. Bertsch, Phys. Rev. C15, 713 (1977).

(20) J. Hüfner and J. Knoll, Nucl. Phys. A290, 460 (1977).

(21) I.A. Schmidt and R. Blankenbecler, Phys. Rev. D15, 3321 (1977).

(22) J.I. Kapusta, Phys. Rev. C16, 1493 (1977).

(23) W.D. Myers, Nucl. Phys. A296, 177 (1978); J. Gosset, J.I. Kapusta, and G.D. Westfall, Phys. Rev. C18, 844 (1978); Note that some of the data to which the model was compared have been revised.

(24) H.J. Pirner and B. Schürmann, Nucl. Phys. A316, 461 (1979).

(25) R.H. Landau and M. Gyulassy, Phys. Rev. C19, 149 (1979).

(26) P.J. Siemens and J.O. Rasmussen, Phys. Rev. Lett. 42, 880 (1979).

(27) Y. Yariv and Z. Fraenkel, Phys. Rev. C20, 2227 (1979); Phys. Rev. C24, 488 (1981).

(28) J. Cugnon, Phys. Rev. C22, 1885 (1980).

(29) S. Das Gupta and A.Z. Mekjian, Phys. Rep. 72, 131 (1981).

(30) J. Cugnon and S.E. Koonin, Nucl. Phys. A355, 477 (1981).

(31) G.E. Brown and W. Weise, Phys. Rep. 27C, 1 (1976).

(32) G. Baym and E. Flowers, Nucl. Phys. A222, 29 (1974).

(33) R.F. Sawyer and D.J. Scalapino, Phys. Rev. D7, 953 (1973).

(34) A.B. Migdal, Rev. Mod. Phys. 50, 107 (1978).

(35) T.D. Lee, Rev. Mod. Phys. 47, 267 (1975).

(36) J.I. Kapusta, Nucl. Phys. B148, 461 (1979).

(37) E.M. Friedländer, Phys. Lett. 2, 38 (1962); N.I. Kostanashvili, G.I. Lebedevich, D.S. Nabichvrishvili, Yad. Fiz. 13, 1243 (1971). [Sov. J. Nucl. Phys. 13, 715 (1971).]

(38) H. Yagoda, Phys. Rev. 85, 891 (1952).

(39) J. Burfening, E. Gardner, C.G.M. Lattes, Phys. Rev. 75, 382 (1949).

(40) K.G. Libbrecht and S.E. Koonin, Phys. Rev. Lett. 43, 1581 (1979).

(41) G. Bertsch, Nature 283, 280 (1980).

(42) M. Gyulassy and S.K. Kauffmann, Nucl. Phys. A362, 503 (1981).

(43) C.M. Ko and P.J. Siemens, Nucl. Phys. A367, 496 (1981).

(44) R. Wada and J.R. Alonso, IEEE Trans. Nucl. Science NS-28, 2276 (1981).

(45) A.S. Carroll, I-H. Chiang, C.B. Dover, T.F. Kycia, K.K. Li, P.O. Mazur, D.N. Michael, P.M. Mockett, D.C. Rahm, R. Rubinstein, Phys. Rev. C14, 635 (1976).

(46) C. Wilkin, C.R. Cox, J.J. Domingo, K. Gabathuler, E. Pedroni, J. Rohlin, P. Schwaller, and N.W. Tanner, Nucl. Phys. B62, 61 (1973).

(47) A.S. Clough, G.K. Turner, B.W. Allardyce, C.J. Batty, D.J. Baugh, W.J. McDonald, R.A.J. Riddle, L.H. Watson, M.E. Cage, G.J. Pyle, G.T.A. Squier, Nucl. Phys. B76, 15 (1974).

(48) J.F. Amann, P.D. Barnes, M. Doss, S.A. Dytman, R.A. Eisenstein, A.C. Thompson, Phys. Rev. Lett. 35, 426 (1975).

(49) M.A. Moinester, R.L. Burman, R.P. Redwine, M.A. Yates-Williams, D.J. Malbrough, C.W. Darden, R.D. Edge, T. Marks, S.H. Dam, B.M. Preedom, F.E. Bertrand, T.P. Cleary, E.E. Gross, C.A. Ludemann, M. Blecher, K. Gotow, D. Jenkins, F. Midler, Phys. Rev. C18, 2678 (1978).

(50) M. Blecher, K. Gotow, D. Jenkins, F. Milder, F.E. Bertrand, T.P. Cleary, E.E. Gross, C.A. Ludemann, M.A. Moinester, R.L. Burmann, M. Hamm, R.P. Redwine, M. Yates-Williams, S. Dam, C.W. Darden III, R.D. Edge, D.J. Malbrough, T. Marks, B.M. Preedom, Phys. Rev. C20, 1884 (1979).

(51) G. Molière, Z. Naturforsch 2a, 133 (1947) and 3a, 78 (1948); H.A. Bethe, Phys. Rev. 89, 1256 (1953).

(52) M. Abramowitz and I.A. Stegun, Handbook of Mathematical Functions, p538 (U.S. Government Printing Office, Washington D.C., 1964).

(53) R. Vandenbosch and J.R. Huizenga, Nuclear Fission, p382 (Academic, New York, 1973).

(54) J.C. Alder, B. Gabioud, C. Joseph, J.F. Loude, N. Morel, A. Perrenoud, J.P. Perround, M.T. Tran, B. Vaucher, E. Winkelmann, D. Renker, H. Schmitt, C. Zupančič, H. Von Fellenberg, A. Frischknecht, F. Hoop, G. Strassner, P. Truöl, Nucl. Inst. and Meth. 160, 93 (1979).

(55) M. Crozen, Ph. Chavanon, A. Courau, Th. Leray, J.L. Narjoux, and J. Tocqueville, Nucl. Phys. 64, 567 (1965).

(56) F. Binon, P. Duteil, J.P. Garron, J. Gorres, L. Hugon, J.P. Peigneux, C. Schmit, M. Spighel, and J.P. Stroot, Nucl. Phys. B17, 168 (1970).

(57) J.F. Marshall, M.E. Nordberg Jr., R.L. Burman, Phys. Rev. C1, 1685 (1970).

(58) H. Dollard, K.L. Erdman, R.R. Johnson, H.R. Johnston, T. Masterson, P. Walden, Phys. Lett. 63B, 416 (1976).

(59) R.R. Johnson, T.G. Masterson, K.L. Erdman, A.W. Thomas, R.H. Landau, Nucl. Phys. A296, 444 (1978).

(60) I. Navon, D. Ashery, G. Azuelos, H.J. Pfeiffer, H.K. Walter, F.W. Schleputz, Phys. Rev. Lett. 42, 1465 (1979).

(61) E. Bellotti, D. Cavalli, C. Matteuzzi, Nuovo Cimento 18A, 75 (1973).

(62) These computer routines were originally written by Dynamic Graphics Inc., 2150 Shattuck Ave., Berkeley, California, 94704. The versions used here were obtained from the LBL Computer Center. The original documentation was modified at LBL and is available from the Computer Center. Ask for the User Manual for the Surface Gridding Library and the User Manual for the Surface Display Library.

(63) E. Moeller, M.-C. Lemaire, S. Nagamiya, S. Schnetzer, H. Steiner, I. Tanihata, LBL Report #12257 (1981); This report is still in preparation so the numerical data which are used here are preliminary.

(64) M.M. Sternheim and R.R. Silbar, Phys. Rev. D6, 3117 (1972).

(65) G. Friedlander, J.W. Kennedy, E.S. Macias, and J.M. Miller, Nuclear and Radiochemistry, 3rd ed., p81, (John Wiley & Sons, New York, 1981).

(66) P. Marmier and E. Sheldon, Physics of Nuclei and Particles, Vol. I, p360 (Academic, New York, 1969).

(67) A. deShalit and H. Feshbach, Theoretical Nuclear Physics Volume I: Nuclear Structure, p778 (John Wiley & Sons, New York, 1974).

(68) D.E. Greiner, P.J. Lindstrom, H.H. Heckman, Bruce Cork, F.S. Bieser, Phys. Rev. Lett. 35, 152 (1975).

(69) Y.P. Viyogi, T.J.M. Symons, P. Doll, D.E. Greiner, H.H. Heckman, D.L. Hendrie, P.J. Lindstrom, J. Mahoney, D.K. Scott, K. Van

Bibber, G.D. Westfall, H. Wieman, H.J. Crawford, C. McParland, C.K. Gelbke, Phys. Rev. Lett. 42, 33 (1979).

(70) K. Van Bibber, D.L. Hendrie, D.K. Scott, H.H. Weiman, L.S. Schroeder, J.V. Geaga, S.A. Chessin, R. Treuhaft, Y.J. Grossiord, J.O. Rasmussen, C.Y. Wong, Phys. Rev. Lett. 43, 840 (1979).

(71) Both the fitting and the error analysis were done with the MINUIT program (version 2.77) written at CERN. A description of this program, the minimization methods used (see the section on MIGRAD), the error analysis (see the section on MINOS) are available from: Program Library, Division DD, CERN, CH 1211 Geneve 23, Switzerland. Ask for the long writeup on MINUIT, D506.

(72) H.M.A. Radi, J.O. Rasmussen, J.P. Sullivan, K.A. Frankel, O. Hashimoto, LBL Report #12591 (1981); to be published in Phys. Rev. C.

TECHNICAL INFORMATION DEPARTMENT
LAWRENCE BERKELEY LABORATORY
UNIVERSITY OF CALIFORNIA
BERKELEY, CALIFORNIA 94720